OPTICAL FIBRE SENSORS AND THEIR INTERROGATION

Alexander George Simpson

Doctor of Philosophy

ASTON UNIVERSITY

January 2005

ABSTRACT

OPTICAL FIBRE SENSORS AND THEIR INTERROGATION

Alexander George Simpson

Doctor of Philosophy

January 2005

This thesis describes novel developments in the fabrication and understanding of type IA fibre Bragg gratings, the uses of said gratings as optical sensors and the interrogation of optical sensors using tilted fibre Bragg gratings.

Modern methods of construction for composite structures such as marine vessels, aircraft, and high performance cars require detailed feedback of loading and deformation. As structural complexity increases, so does the required number of measurements and measurement sites. Fibre sensors are capable of fulfilling these demanding roles due to their small size, low cost and ease of multiplexing.

The main contributions to the knowledge of the subject documented by this thesis are in related subtopics which together form two of the most common issues with optical sensor networks; the cross-sensitivity of optical sensors to more than one measurand, and the interrogation of optically encoded measurand data produced by fibre sensors using equipment which is both compact and rugged.

This thesis presents the most detailed study of type IA gratings performed to date and provides the basis of a dual grating optical sensor capable of independently measuring strain and temperature. Until this work it was not known how to reliably fabricate type IA gratings or how they would react to high ambient temperatures, nor was it known what effect external parameters such as fibre type, dopant levels, inscription laser intensity, or hydrogenation levels would have on the physical properties of the grating. This comprehensive study has yielded answers to all of these unknowns and produced several unexpected uses for type IA gratings, such as the use of the previously unreported strong loss band at 1400nm to locally heat fibres by optical absorption and thereby fabricate optically tuneable gratings which do not affect directly adjacent standard gratings.

Blazed fibre Bragg gratings have been studied in detail and used to produce several high quality prototype sensor interrogation systems yielding stability and accuracy values unsurpassed by similar devices reported in literature. An accurate distribution map of light radiated by blazed gratings is shown for the first time and has been studied in respect of polarisation state showing that for certain easily achievable conditions a blazed grating spectrometer may be deemed to be polarisation insensitive. In a novel implementation of the system, it is shown that the dynamic wavelength range of a blazed grating spectrometer may be at least doubled by superimposing blazed gratings.

INDEXING TERMS: fibre optic sensors, fibre Bragg gratings, photosensitivity, type IA gratings, self compensating temperature and strain sensors.

ACKNOWLEDGMENTS

Profound acknowledgment is due to those the author has worked most closely with; they include Ian Bennion, Kyriacos Kalli, Lin Zhang, and Kaiming Zhou. Further acknowledgment is due to Bert Biggs whose considerable skill as laboratory manager ensured that the experimental work described within this thesis was performed with the minimum of distress to its author.

Acknowledgement is due to all members of the Photonics Research Group for their numerous contributions with special mention due to at least, Yicheng Lai, Kate Sugden, David Webb and John Williams.

Acknowledgement is due to the partners of the DTI-Link project, *EMPIRE* (BAE-Systems, Deutsch LTD, Insensys LTD and Indigo Photonics).

This work would not have been possible without the generous funding of the Engineering and Physical Sciences Research Council (EPSRC), BAE-Systems, Indigo Photonics and Mum & Dad.

CONTENTS

DOCUMENT REVISION NUMBER: 2

TABLE OF FIGURES

Chapter 3:

Chapter 4:

Chapter 5:

Chapter 1

Introduction

1. INTRODUCTION

PREAMBLE

The subject of this thesis is developments in the field of fibre Bragg grating (FBG) based optical sensors. FBGs are reflective optical filters which may be fabricated in sections of optical fibre by exposure to spatially modulated ultraviolet radiation. Figure 1.1 shows the structure of an FBG in the core of an optical fibre.

FBGs find their origin from the work of Kenneth Hill and co-workers at the Canadian Communications Research Centre (CRC) [1]. Fibre gratings were discovered when a fibre sample doped with germanium was used in an experiment concerning Raman lasers.

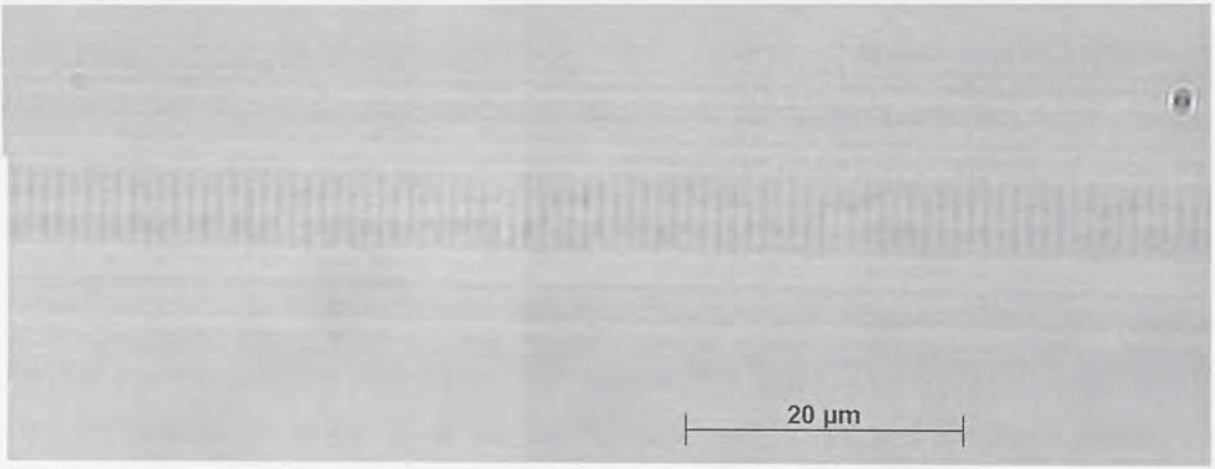

Figure 1.1 An image of a fibre Bragg grating showing the grating structure within the core of the fibre.

OPTICAL SENSING

Optical sensing is simply the act of encoding measurand data by some optical means. An early example is *Moiré Fringes* which are used in many optical rotational or linear displacement sensors. More recently it has become common place to encode measurand data such as temperature or strain (and many derivatives thereof) in terms of colour or wavelength. Devices such as fibre Bragg gratings reflect a narrow bandwidth of light at a central wavelength (termed the *Bragg wavelength*) determined by the period of the

grating and the refractive index of the fibre core. In operation, elongation of the fibre through applied strain results in a measurable shift in the Bragg wavelength of the device through an increase in the period of the grating. Temperature changes may be detected through the thermo-optic effect which is a change in the refractive index of the fibre proportional to temperature (thermal expansion also accounts for ~10% of the measurable shift in Bragg wavelength).

Optical sensing has grown in popularity as a result of the need for larger numbers of sensors complying to more stringent weight limits. Historically it has not been possible to achieve such targets with electrical sensors; the final Concorde prototype, Concorde 101, flew with more than 12,000kg of test equipment, chiefly comprising traditional wire-film strain gauges and their associated instrumentation equipment. This massive weight accounted for almost the entire payload of the aircraft and all but filled the available cabin space. The problem with this type of sensor system is that each sensor requires an individual set of measurement circuitry, and more significantly, an individual wiring loom from the sensor to the measurement circuitry. Although many techniques exist for reducing the wiring requirements in such systems, it is not possible to multiplex such devices at the most basic level.

Optical sensors, however, may be easily multiplexed in terms of time (TDM), wavelength (WDM) or both, leading to large numbers of sensors in a single fibre. For a system of given bandwidth, it is clearly possible to optically space a finite number sensors such that the signal reflected by each device does not interfere with any of its neighbours during transit. A TDM topology may be achieved by taking account of the transit time between points within a length of fibre. By combining the two multiplexing regimes large arrays of sensors may be built within a single low-loss fibre of considerable length. The result of this technology is that a modern day equivalent of Concorde, probably requiring an order of magnitude more sensors, would be implemented optically and would require only a small number of arrays. An additionally beneficial aspect of optical fibre sensors is that the fibres are sufficiently small (having an un-clad external diameter of only 125μm) to be embedded within composite structures. This property has lead to the practical reality

of *smart structures* with bridges and d aircraft alike being able to react in real time to different loading conditions.

In the case of fibre Bragg grating optiotical sensors, the measurand information is usually encoded as a derivative of the fundammental sensitivities, strain and temperature. Because these sensitivities coexist, unless a serensor is exposed to only one type of environmental change it is not possible for a decodiding system to distinguish strain from temperature. Unfortunately, such situations are commmon and provision must be made for de-coupling the information. Another drawbackk of FBG based optical sensors is that the instrumentation required to convert wavavelength shifts to measurand data is often delicate and extremely expensive.

This thesis suggests viable solutions t to these problems using novel implementations of FBG based devices and demonstratates their use. It shows the development of an interrogation system that is compact, l, low-cost and rugged and also shows a method of fabricating a sensor capable of decouplpling temperature and strain. In doing so, this thesis documents substantial findings in the e field of fibre photosensitivity known as type IA photosensitivity.

In order that the reader may gain a hisistorical perspective of this thesis, a timeline of the key milestones leading to this work is s shown below:

1915	*Sir William Henry Bragg (1862 to 1942) and William Lawrence Bragg (1890 to 1971) were jointly awarded the Nobel Prize for Physics.*	
1978	Hill *et al* discovered fibre gratings during experiments using 488nm radiation and germanosillicate optical fibre. This was the first report of fibre photosensitivity and the gratings produced later became known as *Hill gratings*.	[1]
1981	Lam and Garside determined that Hill gratings had been the result of two photon absorption. Their work led to the prediction that photons at 5eV (244nm) could be used to induce refractive index changes by absorption of a single photon thereby significantly increasing writing efficiency.	[2]
1989	Meltz and Morey reported the successful side writing of FBGs through the cladding of an optical fibre using a transverse holographic method. This discovery enabled the inscription of gratings at a wavelength determined by the angle of the interfering beams and was instrumental to the beginning of widespread research interest in the topic.	[3]
1993	Hill *et al* and Anderson *et al* published independent reports of FBG inscription using a phasemask. The use of a phasemask has enabled near identical gratings to be manufactured on a large scale and has been largely responsible for the commercialisation of FBG based devices.	[4, 5]
1990	Meltz *et al* reported the fabrication of a *fibre optic tap*. This was a tilted grating structure that radiated light guided in the core.	[6]
2001	Liu reported the discovery of a regenerated grating with a significantly reduced thermo-optic effect and large mean index shift.	[7]

Since Hill *et al*'s discovery, the subject has evolved such that there is a sufficiently large body of information to produce several review articles on FBGs (e.g. [8-11]), on FBG sensors (e.g. [12-16]) and a further selection of books encompassing the subject as a whole (e.g. [17, 18]).

THESIS OUTLINE

Chapter 2: Theoretical Basis

Chapter 2 provides the relevant theoretical background for the remainder of the thesis. The photosensitivity of fibres to UV radiation and the associated decay is discussed at length giving an important insight into the work of all chapters, particularly Chapters 5 & 6. Fibre gratings are discussed; including a mathematical explanation for the "fibre optic tap" reported by Meltz *et al* [6], pertinent to Chapter 4, and the operation of FBG sensors, pertinent to Chapters 5 & 6. Sensor cross-sensitivity is shown mathematically and a means by which solutions may be compared like-for-like is provided.

Chapter 3: Optical Fibre Sensors

Chapter 3 serves largely as a review of literature available in the subject relevant to this thesis. It provides a vital basis for Chapters 4 to 6 by setting the work in context and giving the reader a reference for alternative solutions to problems solved and developments made therein.

Optical fibre sensors are discussed in general, leading to a detailed review of FBGs, their operation, manufacture and uses. This in turn leads to a review of temperature-strain cross-sensitivity and a direct comparison of the published methods for overcoming this. Finally, the interrogation of optical sensors is discussed in relation to spectroscopic methods using blazed FBGs.

Chapter 4: Blazed Fibre Grating Spectroscopy

Chapter 4 gives a detailed account of the experimental work performed on the subject of blazed FBG spectrometers. The chapter shows accurately profiled radiation mode patterns and demonstrates how these modes move and change with wavelength, blaze angle and fibre type. From this work a spectrometer pre-prototype is developed and system testing information is provided indicating a successful spectrometer design. A novel design is then provided wherein blazed FBGs are superimposed to increase the bandwidth of the system. The pre-prototype is then formally prototyped yielding significant gains in system stability, accuracy and resolution.

Chapter 5: Type IA Fibre Bragg Gratings, Fabrication and Applications

Chapter 5 details the fabrication and application of type IA gratings. In doing so it draws several conclusions relating to the photosensitivity effects and reactions underlying their formation. A detailed report of the unique characteristics of IA gratings is provided and best-practice is suggested for the inscription of these regenerated gratings. This discussion is expanded to include important fabrication parameters, such and the need for uniformity of exposure along the length of the inscription site. This chapter concludes

with a description of how best to use the properties of IA gratings to manufacture a self-referencing independent temperature and strain sensor head.

Chapter 6: Type IA Fibre Bragg Gratings, Fundamental Investigation

Chapter 6 discusses the parameters which affect the growth of IA gratings and the physical properties of the mature grating. This chapter provides a substantial body of information on gratings formed in several fibre types with varying dopant levels and differing hydrogenation saturation levels within the fibres. A previously unreported (in relation to IA gratings) absorption band at 1400nm is reported and shown to be useable for selective grating tuning by optical means. Finally, considerable experimental data is provided on the annealing properties of IA gratings and their longevity at elevated temperatures.

Chapter 7: Thesis Conclusions

Chapter 7 provides a concluding overview of the thesis.

Chapter 2

Theoretical Basis

2. THEORETICAL BASIS

2.1. PREAMBLE

Fibre Bragg gratings have been the subject of intense research for several years, their small size, ease of multiplexing and reliability have made them indispensable to the telecommunication and optical sensing markets. This chapter introduces the fundamental theoretical concepts which must be outlined to enable the reader to understand the content of the later chapters. This chapter introduces and discusses the photosensitivity of silica fibres to ultraviolet radiation, the mechanism by which Bragg gratings may be inscribed within silica fibres, and the decay of these gratings at elevated temperatures. Following this, fibre geometrics are discussed and the concept of blazing grating fringes such that light guided by the core of the fibre may be radiated from the side of the fibre is introduced. A mathematical description of in-fibre Bragg gratings as optical sensors is presented and followed by a discussion of sensor cross-sensitivity.

2.2. PHOTOSENSITIVITY IN OPTICAL FIBRES

Photosensitivity of optical fibres manifests itself as a change in refractive index following exposure to UV radiation. It is fundamental to the inscription of fibre gratings and an understanding of current thinking is essential for this work.

It is extremely well known that Hill *et al* were the first researchers to report the UV photosensitivity of optical fibres in 1978 [1] in the paper which spawned intense worldwide research into the subject of fibre Bragg gratings (FBGs). However, despite the widespread academic interest photosensitivity has received, there is still no one theory which can explain photosensitivity in all cases; indeed there is still much disagreement on the subject. There is consensus, however, that photosensitivity is a combination of several effects and that the relative contributions from each differ according to fibre type, fibre preparation (hydrogenation, flame brushing, etc) and inscription details.

There are currently at least six published theories which interleave significantly. These are set out for completeness in Table 2.1.

Photosensitivity model	Author	Year	Reference
Compaction / densification	Fiori & Devine	1986	[19]
Ionic migration	Lawandy	1989	[20]
Colour-centre	Hand & Russell	1990	[21]
Electron charge migration	Attard	1992	[22]
Stress relief	Sceats	1993	[23]
Permanent electric dipole	Williams *et al*	1993	[24]

Table 2.1 A summary of some of the current models for UV photosensitivity in silica fibres

2.2.1. Point defects (colour centres)

It is believed that the mechanism of photosensitivity is linked to the UV absorption band resulting from oxygen deficiencies in the crystal structure of the fibre [25].

2.2.1.1. Silicon glass

Point defects are responsible for (for example) unwanted absorption bands affecting telecommunication transmission over fibres, non-linear optical fibre transmission and the fibre fuse effect. Point defects are also believed to be responsible for the phenomenon of photosensitivity in optical fibres, to this end, extensive research using electron spin resonance (ESR) techniques has identified a number of point defects in silica glass. Three intrinsic defects in silica glass are now known: the E' centre, the nonbonding [or nonbridging] oxygen hole centre (NBOHC), and the peroxy centre [18]. Although widely accepted as constituting one of the fundamental mechanisms behind photosensitivity, their structure, role and photochemistry are still uncertain.

2.2.1.2. Germanosillicate glass

Germanium has two stable oxides and thus can be expected to occur as both GeO and GeO_2. GeO may also exist as discrete molecules; however, it is believed to be more likely to exist as Ge-Si wrong bonds which themselves are believed to be point defect forerunners. Thermodynamic analysis predicts that a defect centre known as a germanium-oxygen deficiency centre (GODC) exists at a level proportional to that of GeO_2. A characteristic of GeO defect centres is a luminescence at 400nm seen as a blue glow at the inscription site when inscribing gratings with 240nm radiation [26].

Photo-ionisation of GODCs, Ge-Si or Ge-Ge, creates positively charged GeE' hole centres and free electrons. The defect is fixed to the matrix, but the electron has enough energy to escape and so diffuses into neighbouring Ge(1) and Ge(2) sites to form negatively charged traps [24]. Simmons *et al* [25] showed the presence of the GeE' as characterised by a singly charged oxygen vacancy using ESR techniques. They further showed that the number of GeE' sites in the samples had a strong wavelength dependence which was consistent with the two-photon process proposed some ten years earlier [2, 27] and now widely accepted as the mechanism behind the original *Hill gratings* [1]. The result of this work is that GeE' centres are known to form according to a two-photon process with inscription wavelengths of 488nm or a one-photon process when using 244nm radiation [28]. Note that the absorption band at 240nm has a FWHM bandwidth of more than 25nm [26] meaning that sufficient energy may be imparted by lasers within this band.

Williams *et al* reported the first observation of bleaching in the 240nm band under the action of UV radiation [29]. The electrons released during this bleaching and formation of GeE' centres are believed to form further defect centres. This was supported by Atkins *et al*, using UV inscription lasers of 242nm [30] and 248nm [31] who further showed that the resultant defect centres are responsible for changes in the UV absorption spectrum.

Any change in the refractive index may be related to the photo-induced change in absorption through the Kramers-Kronig[1] relation, expressed as [18]:

Equation 2.1 $$\Delta n_{eff}(\lambda) = \frac{1}{2\pi^2} P \int_0^{\infty} \frac{\Delta \alpha_{eff}(\lambda)}{1-(\lambda/\lambda')^2} d\lambda$$

---

[1] It is a general property of complex functions describing a physical reality that under certain conditions the real and imaginary parts are directly related. The relation is called the *Kramers-Kronig* relation. It is a mathematical not a physical property and demands that two conditions are met; causality (no output before an input) and linearity. In this case the Kramers-Kronig technique yields an analysis of the reflection spectrum which allows determination of the experimental dielectric function.

where P is the principal part of the integral, $\Delta n_{eff}(\lambda)$ is the change in refractive index and $\Delta \alpha_{eff}(\lambda)$ is the effective change in the absorption coefficient of the defect. This demonstrates that the index change produced in the IR to visible range of the spectrum by photo-induced processing results from a change in the absorption spectrum of the glass in the UV to far-UV spectrum [21, 27, 32, 33]. Experimental support for the GeE' model is substantial, e.g. [25, 29-31, 34]. This defect centre model, however, yields only an approximation of the change in refractive index and there is evidence that it does not provide a complete explanation for all experimental observations [35-37].

2.2.2. Compaction / densification

A large portion of the UV induced refractive index changes in non-hydrogen loaded fibres is thought to be a result of densification of silica and has experimental accreditation [38]. The densification model is based on laser irradiation induced density increases that result in an increase in the refractive index of the glass. Fiori & Devine [19] originally showed that thermally reversible compaction was possible in amorphous silica grown on Si wafers. The film reduced in thickness by ~16% and returned to its original state after one hour at 950°C in a vacuum. Longer term radiation resulted in a permanent densification. However, Malo *et al* showed [39] that annealing at 1200°C removes the photosensitivity of germanosilicate glass irrecoverably.

Douay *et al* provide a comprehensive review of the photoelastic densification models [40].

2.2.3. Enhancing photosensitivity

2.2.3.1. Co-doping of germanosilicate optical fibres

The inclusion of co-dopants, such as boron [41] or tin [42] in germanosillicate fibres results in the enhancement of the UV photosensitivity. Boron doping in particular has become widely used after its introduction by Williams *et al* [41] and is particularly effective. It can lead to an index change 4 times greater than that obtained in pure germanosillicate fibres (for a given level of Ge doping) and it has been shown that an

index change of 10^{-3} in non-hydrogenated fibres and 10^{-2} in hydrogenated fibres [43, 44] is possible. Absorption measurements suggest that the mechanism responsible is different from the photo-bleaching of GODCs [41].

In addition to increasing the photosensitivity, Section 6.2 of this thesis shows that the addition of boron to germanosillicate fibres has a profound effect on the energy required to fabricate type IA gratings. Gratings in B/Ge fibres are shown to form significantly faster than those in pure Ge doped fibres; indeed the Ge only fibres require more than 5 times more energy to form IA gratings given otherwise identical preparation conditions.

Boron co-doping is often used to alter the refractive index of optical glasses. For example, in order that highly intrinsically photosensitive fibres may be manufactured and used in applications where splicing to standard fibre is necessary, boron is often added as a co-dopant because its presence has the opposite effect of Ge on the refractive index of fused silica in that it reduces it. It is believed that the effect on the refractive index of boron is enhanced by the natural quenching process of optical fibres during the drawing process. Large differences in the thermal properties of the boron doped core and the silica cladding cause a build up of stresses which decrease the refractive index further according to the stress-optic effect. By balancing the B and Ge levels, fibre manufacturers are able to make fibres which are highly photosensitive, without the requirement of costly hydrogenation, and which possess NA values extremely close to that of standard fibre.

It is from knowledge of the stress related index reducing properties of boron that the current understanding of the mechanism by which boron enhances photosensitivity is deduced. Heating caused by the absorption of UV causes stress relaxation to occur. It is postulated that the refractive index increases through photo-induced stress relaxation initiated by the breaking of wrong-bonds by UV light [45].

2.2.3.2. Hydrogenation of germanosilicate optical fibres

Hydrogenation was introduced as a method to increase the intrinsic photosensitivity of optical fibres by Lemaire *et al* in 1993 [43, 44]. The technique is a simple one, and requires that the fibres be soaked in hydrogen at pressures of typically 150-225bar at

temperatures of 25°C to 80°C. In non-hydrogenated germanosillicate glasses, the number of GODCs in the lattice is dependent on the number of naturally occurring defects. It is believed that the process of hydrogenating germanosillicate optical fibres enhances photosensitivity because the hydrogen has the capability to turn all Ge atoms in the lattice into GODCs and that these GODC and OH species are formed by thermally driven reactions of H_2 and Si-O-Ge glass sites. The photosensitivity mechanism of hydrogenated fibre is dependent on the interactions between germanium, silica and hydrogen molecules, coupled with the UV exposure conditions. Under UV exposure, an OH band is formed at ~1400nm which comprises two peaks at 1390nm and 1410nm. This is attributed to OH groups of Si and Ge respectively that do not form in fibres which have not been first loaded with H_2. This absorption band is shown in Figure 2.1 [11, 18, 46]. Figure 2.1b shows the growth of the OH band with increasing fluence for a fully hydrogen loaded B/Ge co-doped fibre. Canning *et al* [46] showed that the level of hydrogen present in the fibre is proportional to the size of the absorption band at 1400nm. They further showed that pre-sensitisation of the fibre by hydrogen loading followed by hydrogen outgassing may be used to enhance the photosensitivity without forming a large OH band. Section 6.2.2.1 shows, however, that type IA gratings do not form in pre-sensitised optical fibres and that they require the presence of hydrogen.

Figure 2.1 (a) (left) Reproduced from [11]. The absorption spectrum changes in the IR region for a hydrogenated germanosilicate optical fibre. (b) (right) Reproduced from [46]. Spectra of OH and near-IR attenuation bands for a fully H_2 loaded B/Ge co-doped fibre.

Viswanathan *et al* [47] recently reported a noteworthy development in the procedure of hydrogenating optical fibres. They used an ultra-high pressure setup and diluted H_2 with only 1atm partial pressure of H_2. In their method, the H_2 is diluted with gasses such as argon, carbon dioxide, methane or ethane at pressures >1000atm. They showed that these high pressure mixtures enhanced the photosensitivity of the fibre above that achievable using the equivalent H_2 partial pressure because the diluent gasses have the ability to enhance the fugacity of the H_2 in the mixture. The fugacity of the gas depends on the temperature, pressure and selection of diluent gas. However, the need for a pressure vessel capable of safely containing such large pressures has prevented this method being widely adopted by research or industrial facilities thus far.

Note that although some evidence exists that low level hydrogenation can increase the rate at which type IIA photosensitivity occurs [48] it is not widely experimentally supported, being contradicted even by its own authors [40]. This becomes important when considering the similarities between IA and IIA gratings.

2.2.3.3. Hydrogen saturation levels

The concentration of hydrogen molecules and the rate at which these molecules diffuse into the core of the optical fibre depend on the temperature and pressure at which the fibre is soaked. The concentration of H_2 molecules in the core of an optical fibre at saturation (the equilibrium solubility), κ_{sat}, is given by [49]:

Equation 2.2 $$\kappa_{sat} = 3.3481 p \exp\left[\frac{8670 J/mol}{RT}\right] \text{ [ppm] (1 ppm = } 10^{-6} \text{ moles } H_2 \text{ / mole } SiO_2\text{)}$$

where p is the pressure of the hydrogen in atmospheres, T is the temperature in Kelvin, and R is the gas constant (8.31451 $JK^{-1}mol^{-1}$). The saturated hydrogen concentration increases linearly with pressure and decreases as the temperature increases. The variance in κ_{sat} for changes of p and T is shown in Figure 2.2a. The diffusivity of hydrogen molecules in silica is given by [49]:

Equation 2.3 $$d_{H_2} = 2.83*10^{-4}\, p \exp\left[\frac{-40190 J/mol}{RT}\right] \text{ [cm}^2\text{s}^{-1}\text{]}$$

and increases with both pressure and temperature.

The variance in d_{H_2} for changes of p and T is shown in Figure 2.2b. Figure 2.2 shows the trade off which must be made when hydrogenating optical fibres; higher temperatures mean that it is possible to hydrogenate fibres relatively quickly, but only at the expense of the final concentration of hydrogen in the core of the fibre.

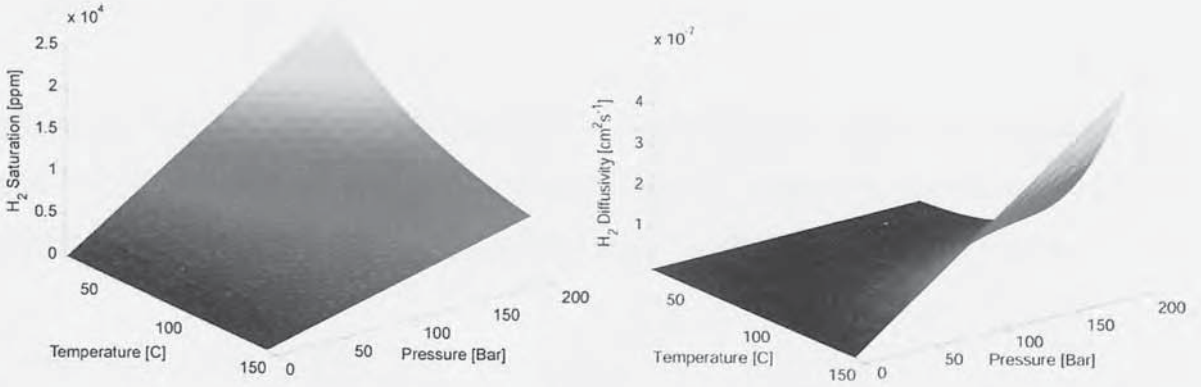

Figure 2.2 (a) (left) The variance in the hydrogen saturation levels of a silica fibre core for changes of p and T, and (b) (right) The variance in the diffusivity of hydrogen in silica for changes of p and T.

The solution on the axis for outward diffusion in cylindrical geometry is conveniently given by Crank [50] as:

Equation 2.4 $$\frac{C}{\kappa_{sat}} = 1 - \exp\left(-\frac{a^2}{4 d_{H_2} t}\right)$$

where C is the concentration of hydrogen in the fibre and a is the fibre radius.

2.2.3.4. Flame brushing of germanosilicate optical fibres

The intrinsic photosensitivity of germanosilicate optical fibres may be increased by flame brushing. Flame brushing requires the fibre to be immersed in the flame of a hydrogen-oxygen burner at a temperature ~1700°C for around 20 minutes [51]. This method

induces a strong absorption band in the 240nm UV band, typically reaching 700dB.mm^{-1}) [18]. The effect is localised to the germanium doped fibre core leaving the cladding properties unaffected. It has been shown that this technique is capable of increasing the UV photosensitivity of the fibre by a factor of 10 and that it is possible to achieve >10^{-3} changes in the refractive index of the core [51].

2.2.4. Multi-photon absorption

It is extremely well known that the energy of a photon was defined by Niels Bohr as:

Equation 2.5 $$E = hf = \frac{hc}{\lambda}$$

where h is Planck's constant (6.63x10^{-34} J.s^{-1}), f is the frequency of the photon and c is the speed of light (2.998x10^{8} m.s^{-1}). Bohr showed that the energy of a photon emitted by the transition of an atom from an excited energy state (E_1) to the ground state (E_0) is:

Equation 2.6 $$hf = \frac{hc}{\lambda} = E_1 - E_0$$

Similarly, the energy required to raise an electron from E_0 to E_1 is equal to $|E_1 - E_0|$.

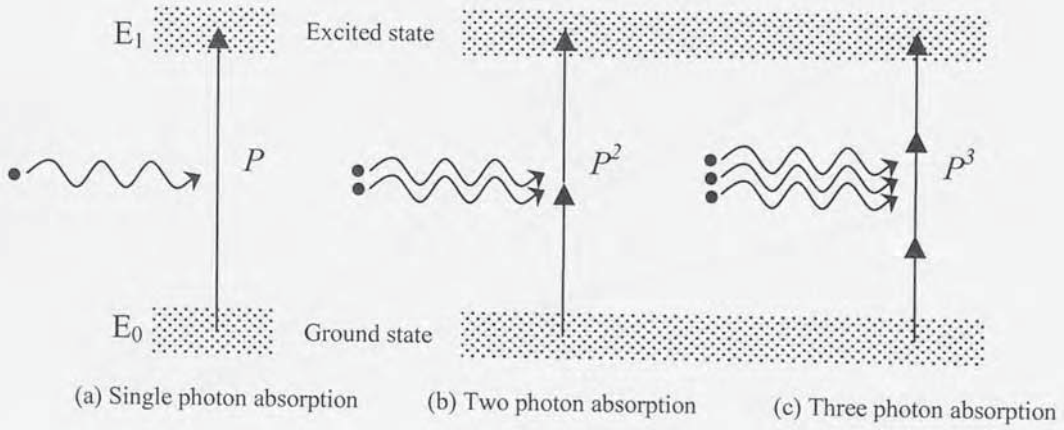

Figure 2.3 A schematic demonstration of multi-photon absorption. The figure shows the energy requirements of a photon, or multiple photons absorbed quasi-simultaneously, to move an atom from state E_0 to E_1.

It is now widely accepted that the original *Hill gratings* [1] were formed by a 2-photon process at 488nm, which is shown schematically in Figure 2.3b. The photon energy at this wavelength is 2.54eV (1eV = 1.602×10^{-34}J); to perform the transition with a single absorbed photon, the photon must have twice the energy, as shown in Figure 2.3a. The wavelength of light having 5.08eV per photon is 244nm; thus UV lasers at this wavelength are now used to inscribe gratings. The associated absorption band has a FWHM bandwidth of >25nm; thus gratings within this spectral region are commonly used, such as the Ar^+ lasers at 244nm used in this thesis.

In the single photon case, transitions will occur when a photon excites an electron in the ground state; this will occur with a probability P which is related to the density of photons at the site. Clearly then, the two photon case requires two photons to quasi-simultaneously excite an electron and the probability is therefore P^2. It follows that a three photon transition has probability P^3 (and so on). If we plot photon density against atomic transitions, the gradient will be equal to the number of photons required to move the electron to the excited state, as shown in Figure 2.4.

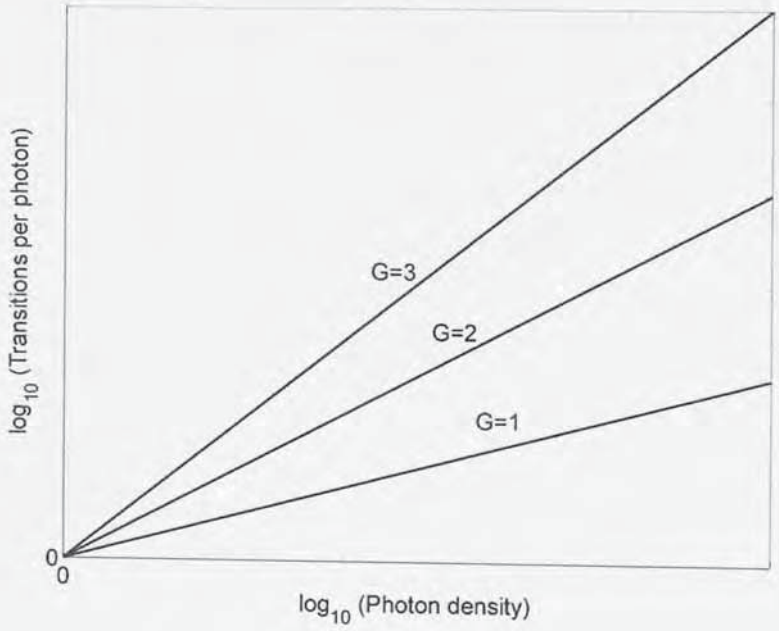

Figure 2.4 Plotting photon density against atomic transitions, showing the gradients of multi-photon processes. By plotting this figure using experimental data it is possible to determine the number of photons which must be quasi-simultaneously absorbed for an atomic transition to take place.

2.2.5. Photosensitivity / photosensitisation summary

There are three widely recognised types of photosensitivity observable in germanosilicate fibres under UV inscription; type I, II and IIA. These are summarised below in Table 2.2, which also shows the lesser known IA index changes.

Type	Description	Photosensitisation	Refractive index change
I	Standard grating, written in both hydrogenated and non-hydrogenated fibre of all types.	None	$n_{mod} = 1x10^{-4}$
		B doping	$n_{mod} = 1x10^{-3}$
		Flame brushing	$n_{mod} = 1x10^{-3}$
		Hydrogenation (H_2)	$n_{mod} = 3x10^{-3}$
IA	Regenerated grating written after erasure of a type I grating in hydrogenated germanosilicate fibre of all types.	H_2	$n_{mod} = 1x10^{-3}$, $n_{mean} = 1.8x10^{-2}$
		H_2 & B doping	$n_{mod} = 3x10^{-3}$, $n_{mean} = 1.8x10^{-2}$
II	Damage written gratings	(pulsed UV, not CW)	$n_{mod} = 2x10^{-3}$
IIA	Regenerated grating written after erasure of a type I grating in hydrogen-free germanosilicate fibres.	B co-doping (no H_2)	
		Strain	$n_{mod} = 1x10^{-3}$, $n_{mean} = -3x10^{-4}$

Table 2.2 A summary of the refractive index changes associated with various fibre treatments. The table shows modulated (grating strength) and mean (grating offset) index changes.

2.3. DECAY OF UV INDUCED GERMANOSILICATE GRATINGS

The index change achieved by exposure to UV radiation is not permanent. Standard fibre gratings are widely accepted as having a lifetime of 25 years at room temperature. Sensor gratings are often required to operate for prolonged periods of time at elevated temperatures and it is therefore necessary to study the decay of FBGs in order that safe working constraints may be imposed.

Williams and Smith [52] studied the thermal stability of strong and weak gratings. They showed that proper stabilisation by annealing ensures that the gratings remain extremely stable and may be expected to last at least 25 years. This result was confirmed by Kannan *et al* [53] among others. Ishikawa *et al* [54] proposed a model by which the proper annealing time may be calculated. Patrick *et al* [55] compared the stability of hydrogenated and non-hydrogenated germanosilicate fibres and concluded that gratings written in hydrogen-free fibre were significantly more stable at elevated temperatures. Aslund *et al* [56] showed that pre-sensitised fibres (refer to Section 2.2.3.2) are more thermally stable than hydrogenated fibres. Niay *et al* [37] showed that UV grating inscription using either CW or pulsed sources resulted in gratings possessing the same elevated temperature stability properties (for the same grating types, and after proper annealing).

2.3.1. Modulated index changes during annealing

The modulated index change may be represented by the integrated coupling constant (ICC) in preference to reflectivity or peak transmission loss because this quantity is proportional to the UV-induced refractive index change, even for cases where the gratings are non-uniform. This quantity may be calculated according to [57]:

Equation 2.7 $$ICC = \tanh^{-1}\sqrt{1-T_{min}}$$

where T_{min} is the transmission minimum, i.e. the grating peak reflectance 1-T=R. It is possible to normalise ICC plots according to grating length, i.e. $ICC' = \frac{ICC}{L}$, or initial

amplitude, i.e. $ICC''(t) = \frac{ICC_{t=0}}{ICC(t)} = \eta$, or both which enables the direct comparison of gratings with different lengths or initial reflectances.

Erdogan *et al* showed that initially gratings decay extremely quickly which is followed by a substantial decrease in the rate of decay at longer times. They concluded that this behaviour was indicative of a *power law* dependence on time and could be fitted according to [57]:

Equation 2.8 $$\eta = \frac{1}{1 + A\left(t/t_1\right)^{\alpha}}$$

where the factor A and exponent α depend on temperature and are dimensionless, whilst t_1 = 1min in order to keep dimensions consistent. Baker *et al* [58] confirmed the power law thermal decay model holds well for non-hydrogenated fibres but went on to suggest that for hydrogenated fibres it was a poor fit.

2.3.2. Mean index changes during annealing

A study of the wavelength shift of FBGs manufactured in hydrogenated germanosilicate (Corning SMF28) fibre by Masuda *et al* [59] showed that the wavelength shift during annealing was solely due to the outgassing of H_2 from the fibre. This was shown by annealing a specimen grating then re-hydrogenating it and then annealing it again. During both annealing processes the wavelength evolution was shown to be the same, and hence they concluded their result. However, Chisholm *et al* [60] showed that for boron-germanium co-doped silica fibres, the wavelength decay even occurred after the hydrogen had out gassed. Pal *et al* [61] showed that the power law model used to model modulated index decay may be modified to model the decay in mean index.

2.4. FIBRE BRAGG GRATINGS

Fibre Bragg gratings (FBGs) are periodic perturbations in the refractive index of the core of an optical fibre core and were first reported by Hill *et al* [1]. The fundamental principle behind FBGs is that of Bragg reflection. When light propagates through regions of periodically modulated refractive index (known as fringes), small reflections take place at each boundary. If the spacing between the reflections is such that their round trip is an integral number of wavelengths, then these reflections add in-phase and the reflection can grow to almost 100%.

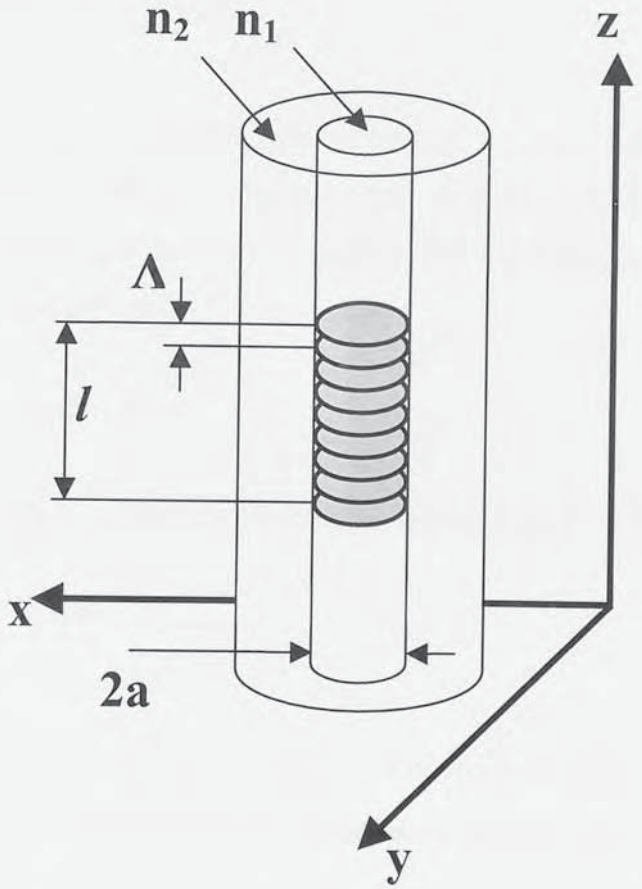

Figure 2.5 A schematic diagram showing the structure of a fibre Bragg grating of a given period in a step index optical fibre.

It follows that this in-phase condition must only be possible for specific wavelengths since the round trip distance is determined by the spacing of the index modulations. Consequently, all other wavelengths result in cancellation and high transmission results.

It is this condition for high reflection, known as the Bragg condition, which determines the Bragg wavelength (λ_{BR}) of an FBG and is given by [62]:

Equation 2.9 $$\lambda_{BR} = 2n_{eff}\Lambda$$

where n_{eff} is the effective (average) refractive index of the guided mode and Λ is the period of the refractive index perturbation maxima. The refractive index profile of a fibre Bragg grating is shown schematically in Figure 2.5 and may be described according to the following equation [18]:

Equation 2.10 $$n(z) = n_{eff} + \left|\Delta n \cos\left(\frac{2\pi z}{\Lambda}\right)\right|$$

where, Δn is the amplitude of the induced refractive index perturbation from peak-to-peak. The coupled mode theory analysis of Lam *et al* [2] (which is well documented by, for example [17, 18]) may be used to predict that the reflectivity, R, of an FBG with sinusoidal fringes and of length, l, is given by:

Equation 2.11 $$R = \tanh^2(\kappa l)$$

where κ is the coupling coefficient of the fibre and is given by [18]:

Equation 2.12 $$\kappa = \frac{\pi \Delta n \eta}{\lambda_{BR}}$$

where η is an efficiency giving a measure of how much optical power guided by the fibre is within the core at the physical location of the grating. It may be approximated according to $\eta \approx 1 - \frac{1}{V^2}$ where V is the so called V-parameter of the fibre, given by [62]:

Equation 2.13 $$V = \frac{2\pi}{\lambda} aNA = \frac{2\pi}{\lambda} an_1\sqrt{2\Delta}$$

where *NA is the numerical aperture of the fibre. The V-parameter* is <2.405 for single mode fibres..

The modulated refractive index may be approximated according to [18]:

Equation 2.14 $$\Delta n_{\mathrm{mod}} = \left({}^{\lambda_{BR}}\!/_{\pi l} \right) \tanh^{-1}\left(\sqrt{1 - T_{\min}} \right)$$

where T_{min} is the transmission loss at the Bragg wavelength.

2.5. BLAZED FIBRE BRAGG GRATINGS

Blazing (or tilting[1]) the index perturbations shown in Figure 2.5 results in modes which were previously confined to the core being coupled to loosely bound guided-cladding or radiation modes. This principle forms the basis of the spectrometers designed and documented in Chapter 4. The bandwidth of radiated light and the efficiency at which these core modes are out-coupled is dependent on the strength and angle of the index perturbations.

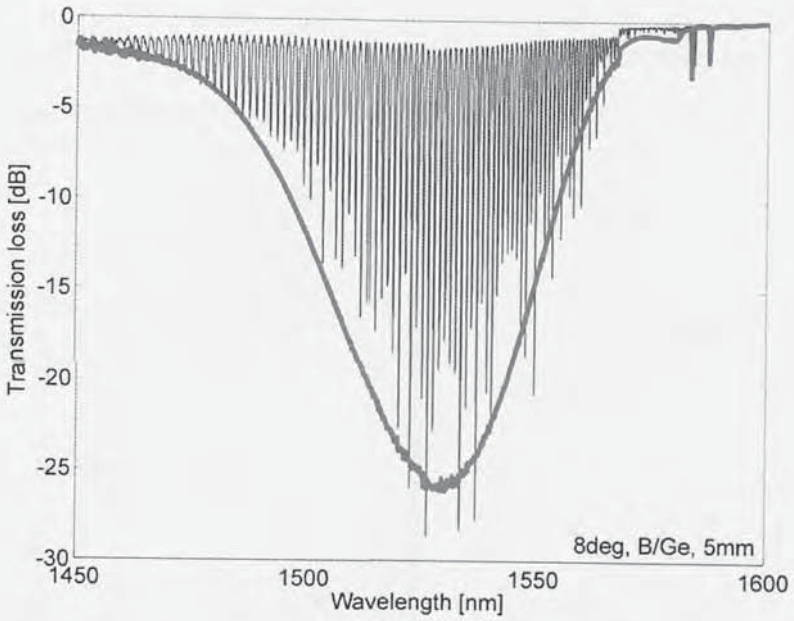

Figure 2.6 The transmission spectra of an example BFBG shown in air (blue) and immersed in index matching gel (red). The trace in air shows the resonant structure caused by the cladding-air interface of the fibre and may be removed by simulating the infinite cladding condition by immersion in index matching gel.

Figure 2.6 shows the transmission profile of a typical BFBG. This particular specimen is a 5mm grating manufactured by the phasemask method (refer to Section 3.3.1) in B/Ge

[1] The terms "blazed" and "blazing" have been widely adopted in place of the more accurate terms "tilted" and "tilting" in common literature. Speaking strictly, a tilted fibre Bragg grating may only be described as *blazed* if the angle of incidence is equal to the angle of reflection. This is not the case for the majority of so called *blazed* fibre Bragg gratings. However, this thesis accepts convention and will refer to *blazed gratings*.

co-doped fibre. The blue trace shows a resonant structure which is caused by reflections at the cladding-air boundary. These may be removed by immersing the grating in index matching gel which simulates the infinite cladding condition. The result of so doing is shown in red.

The refractive index distribution in a BFBG structure is given by:

Equation 2.15 $$n(z,x) = \Delta n \cos\left[\frac{2\pi}{\Lambda}\cos\xi z - \frac{2\pi}{\Lambda}\sin\xi x\right]$$

where z and x are the coordinate axes defining the fibre orientation and ξ is the internal fringe tilt angle, as depicted in Figure 2.7.

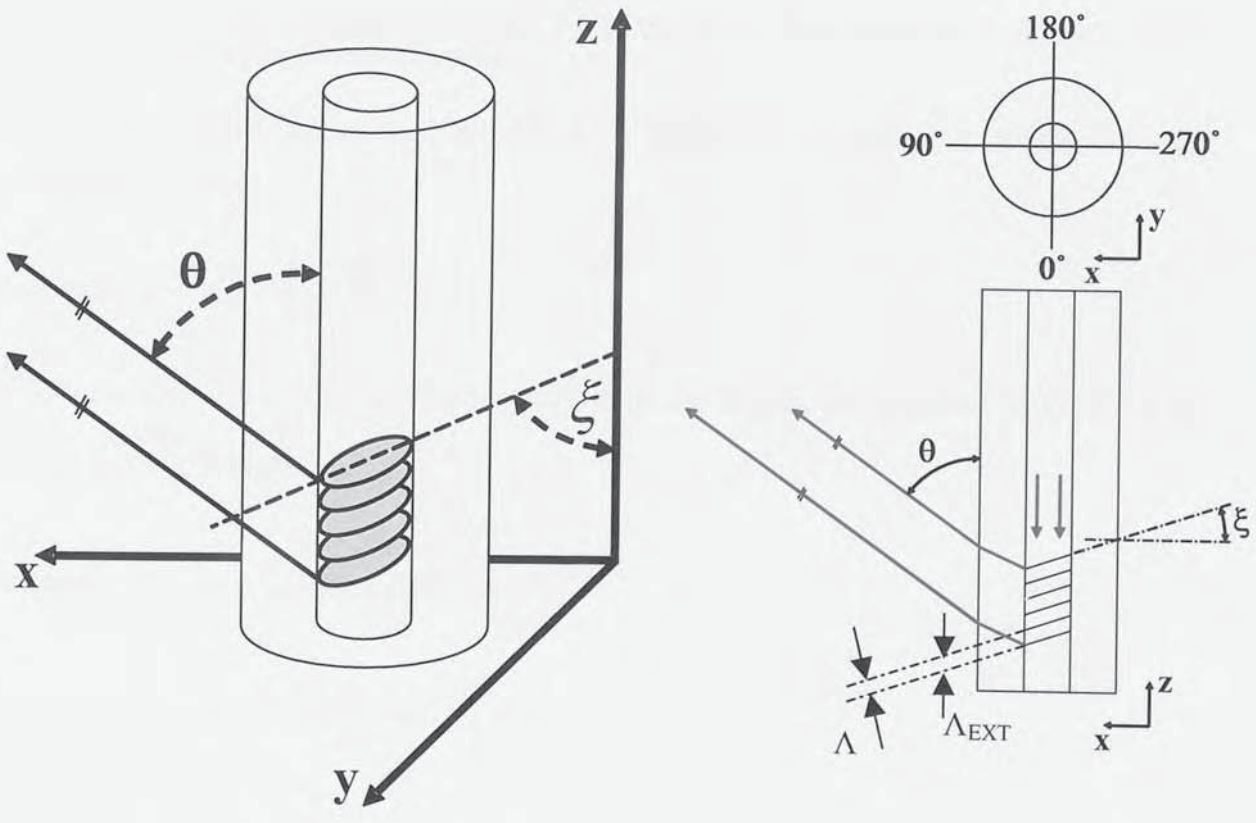

Figure 2.7 A schematic diagram showing the structure of a fibre Bragg grating of a given period in a step index optical fibre whose fringes have been tiled (or blazed) with respect to the fibre normal. Also shown in the coordinate system which is used throughout this thesis.

The radiation mode vector is highly directional and its exit angle is related to the fringe angle. This may be modelled using the volume current method suggested by Li *et al* [63].

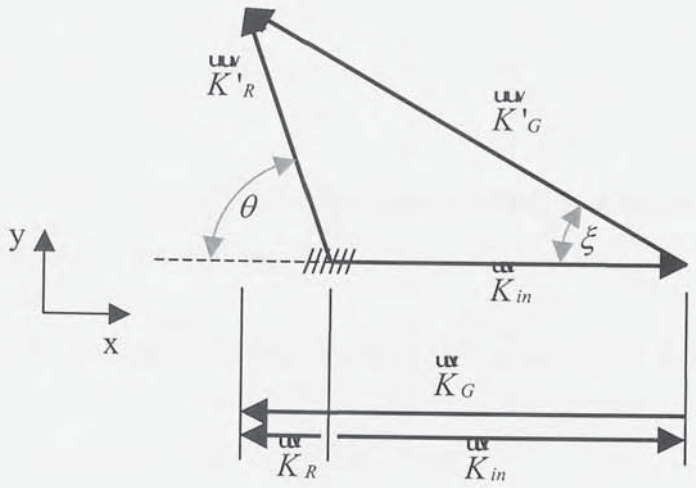

Figure 2.8 (a) (upper) The vector diagram of a BFBG for the Bragg condition (b) (lower) and the vector projection on the x-axis.

Figure 2.8a shows the vector diagram of a BFBG at the phase matching (Bragg) condition, we have:

Equation 2.16 $$\vec{K}_R = \vec{K}_G + \vec{K}_{in}$$

it follows that if we consider the projection on the x-axis, as indicated in Figure 2.8b where $k = \left|\vec{K}\right|$, we have:

Equation 2.17 $$k_{in} = k_G \cos(\xi) - k_R \cos(\theta)$$

where, $k_{in} = n_{eff} k_0$, $k_G = \dfrac{2\pi}{\Lambda}$, and $k_R = n_2 k_0$

so Equation 2.17 becomes

Equation 2.18 $$\cos(\theta) = \frac{\dfrac{2\pi}{\Lambda}\cos(\xi) - n_{eff} k_0}{n_2 k_0}$$

where $k_0 = \frac{2\pi}{\lambda}$, thus Equation 2.18 reduces to:

Equation 2.19 $$\cos(\theta) = \frac{\frac{\lambda}{\Lambda}\cos(\xi) - n_{eff}}{n_2}$$

This analysis shows that the angle of radiation from a BFBG is a function of wavelength, blaze angle and the period of the grating.

The peak wavelength of the light radiated by a BFBG is given by Li *et al* [63] as:

Equation 2.20 $$\lambda_{MAX} = n_{eff}\Lambda_{EXT}(1+\cos 2\xi) = 2n_{eff}\Lambda\cos(\xi)$$

where Λ_{EXT} is defined in Figure 2.7.

For a uniform period grating, Equation 2.19 tells us that the radiation modes are parallel in the x-z elevation, but divergent in the azimuthal direction due to the circular geometry of the core and cladding. It is therefore possible to manufacture a chirped BFBG having different solutions of Equation 2.19 along the z-axis. This was first reported by Wagner *et al* [64] who showed that radiation modes converge at a point determined by the chirp rate. They approximated that the focal length, f, of a chirped BFBG to be:

Equation 2.21 $$f \approx \frac{\Lambda^2 \sin(\xi_{PM})\tan(\xi)}{\lambda\cos(\xi)C}$$

where C is the uniform chirp rate in nm/cm.

Side-detection of radiation modes offers many application-specific advantages ascribable to its highly predictable spectral-spatial relationship; for example, in conjunction with a CCD detector array, the function of side-tapping light with high spatial resolution may be utilised to implement a spectrometer function or to form the basis for low-cost WDM devices. The wavelength component is the basis by which BFBGs may be used as spectrometers or WDM add-drop components (for example).

2.5.1. Inscription considerations

The operation of tilting the grating has an effect upon the period of the inscribed grating. A comprehensive study by Mihailov *et al* [65, 66] shows that the internal grating period of a BFBG (Λ) is related to the UV interference fringe period (Λ_{EXT}) according to:

Equation 2.22 $$\Lambda = \frac{\Lambda_{EXT}\cos(\xi)}{\cos(\xi_{EXT})}$$

in both the phasemask and the holographic cases (see Section 3.3 for a discussion of the two manufacture techniques) where ξ_{EXT} is the angle of the fringes externally incident to the fibre.

2.5.1.1. Phasemask inscription

Owing to the cylindrical geometry of the fibre, the internal fringe angle (ξ) is not the same as the external phasemask angle (ξ_{PM}). This is effect is shown in Figure 2.9.

Figure 2.9 Reproduced from [66]. A demonstration of the difference between the internal and external fringe angles of a BFBG using a glass rod.

The relation between internal and external fringe angles is given by [65, 66]:

Equation 2.23 $$\xi = \frac{\pi}{2} - \tan^{-1}\left[\frac{1}{n\tan(\xi_{PM})}\right]$$

where n is the refractive index of the fibre.

In the case of the phasemask inscription method, the normal period of the grating is solely determined by the period of the mask, that is:

Equation 2.24 $$\Lambda_{EXT} = \frac{1}{2}\Lambda_{PM}$$

The grating period is thus independent from the tilting operation.

2.5.1.2. Holographic inscription

In the case of holographic fabrication, the fibre is rotated within the region of interference of the two inscribing beams. In this case, the internal fringe angle, ξ, is described by [67]:

Equation 2.25 $$\xi = \frac{1}{2}\left[\arcsin\left(\frac{1}{n}\sin\left(\alpha + \xi_{EXT}\right)\right) - \arcsin\left(\frac{1}{n}\sin\left(\alpha - \xi_{EXT}\right)\right)\right]$$

where α is the angle between the two interfering beams and ξ_{EXT} is the fibre tilt angle. Simple geometry shows that the grating period is a function of ξ_{EXT} and may be expressed as [67]:

Equation 2.26 $$\Lambda = \frac{\lambda_{uv}}{2n\sin\left(\frac{1}{2}\left[\arcsin\left(\frac{1}{n}\sin\left(\alpha + \xi_{EXT}\right)\right) + \arcsin\left(\frac{1}{n}\sin\left(\alpha - \xi_{EXT}\right)\right)\right]\right)}$$

Thus, in contradiction to the phasemask case, the period of blazed gratings formed using the holographic technique is related to the tilt angle of the grating.

2.5.2. Polarisation considerations

Theoretical simulations of the far-field image formed by light radiated from a BFBG performed by Zhou [68] have shown that the polarisation sensitivity of BFBGs is insignificant for wavelengths close to the Bragg resonance of the grating, when the blaze

angle is <~10°. However, when the incident radiation is at a wavelength which is sufficiently separated from the grating, the polarisation dependency becomes significant.

Figure 2.10 Reproduced from [68]. The simulated far-field images for 0° and 90° polarised 633mn and 1560nm radiation, as indicated. The figure shows that at wavelengths close to the Bragg resonance the polarisation sensitivity is negligible, but at wavelengths distant from this value the radiated image is heavily polarisation dependant.

Figure 2.10a&b show the large difference in radiation profile for a 7° grating with central Bragg resonance of 1540nm for polarisation states of 0° and 90° illuminated with a 630nm He-Ne laser source. It shows that at this wavelength, the radiation profile is extremely sensitive to polarisation state. However, as the radiated light approaches the Bragg resonance (Figure 2.10c&d) the polarisation sensitivity becomes negligible, and the radiated strength becomes significantly (5 orders of magnitude) higher. Further theoretical study by Zhou [69] has shown that when the blaze angle approaches 45° the

polarisation characteristics are significant for wavelengths close to the Bragg wavelength and it is possible to fabricate an in-fibre polariser.

2.5.2.1. 45° BFBGs

As an alternative to coupled mode theory, the spectrum of a BFBG may be simulated using the volume current method (also known as Green's Function) [63]. The loss of core mode in a small section (δl) of a BFBG in single mode fibre can thus be expressed as [69]:

Equation 2.27 $$\text{Loss} = -\chi \cdot \delta l$$

where χ is the loss coefficient and can be calculated using [69]:

Equation 2.28 $$\chi = -\frac{k_0^{\,3}\delta n^2}{4n} \cdot \frac{1}{1+\frac{u^2}{w^2}} \cdot \frac{K_1^{\,2}(a.w)}{K_0^{\,2}(a.w)} \cdot F$$

where $k_0 = \frac{2\pi}{\lambda_0}$ is wave vector of the light in vacuum, δn and n are the perturbation and original refractive indexes of the core respectively, a is the radius of the core and u and w are the fibre waveguide parameters as defined by Green's function, extensively discussed in [69], and not repeated here. The integration parameter F in Equation 2.28 is defined as [69]:

Equation 2.29 $$F = \int_0^{2\pi} \left(1 - sin^2(\theta) cos^2(\xi - \phi)\right) \left(\frac{K_{new} J_0(a.u) J_1(aK_{new}) - uJ_0(aK_{new}) J_1(a.u)}{K_{new}^{\,2} - u^2} \right)^2 d\phi$$

where $K_{new} = \sqrt{K_t^{\,2} + k_0^{\,2} n_{cl}^{\,2} sin(\theta^2) + 2K_t k_0 n_{cl} sin(\theta) cos(\phi)}$ and angle θ denotes the polarisation of the core mode [69].

Using the above equations it is possible to calculate the transmission spectra for light bound within the core after a BFBG [69]. Figure 2.11 shows the simulated transmission spectra for BFBGs of period 542nm at varying blaze angles (as indicated) for 0° polarised

(solid line) and 90° polarised (dashed line) incident modes. Figure 2.11 shows that although the trends are similar for both polarisation states, the change in amplitude for 90° light is most noticeable. However, at ξ = 45° almost all 0° polarised light is transmitted, whereas the 90° polarised light undergoes significant attenuation. This characteristic provides a mechanism through which an in-fibre polariser may be manufactured.

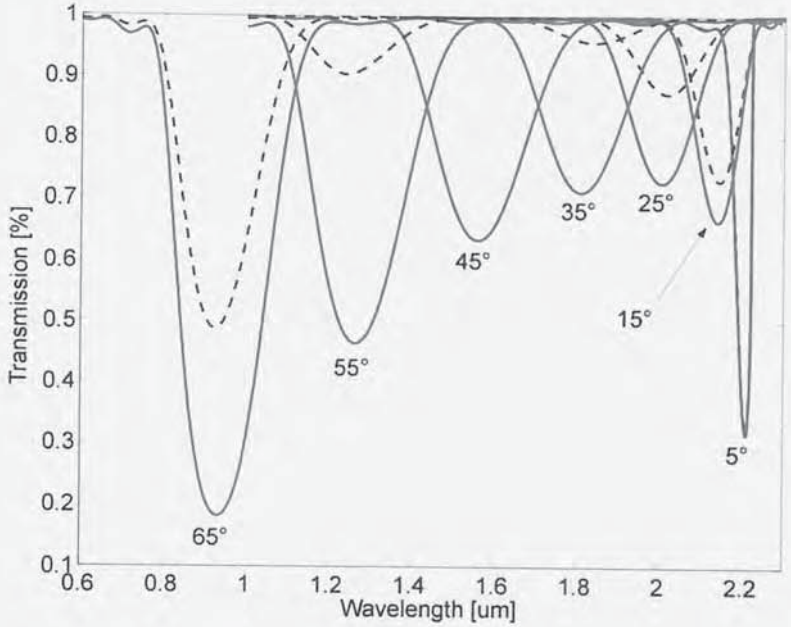

Figure 2.11 The simulated transmission spectrum of BFBGs with different tilting angles. The dashed blue lines show the transmission spectra for 90° polarised light and the solid red lines show 0° polarised light. This figure shows that 45° gratings have a strong transmission loss for 90° polarised light but almost no attenuation for 0° polarised light. It is this phenomenon which makes it possible to use 45° BFBGs as fibre polarisers.

The null transmission loss of 90° light in 45°-tilted BFBGs may be explained using Brewster's law. The grating comprises a periodic structure of two-layer materials with slightly different refractive indexes, n_a and n_b. The Brewster angle for the interface is determined by:

Equation 2.30 $$tan(\xi) = \frac{n_a}{n_b}$$

Since n_a and n_b are almost identical (typically, $\Delta n < 0.01$), ξ is very close to 45°. So when the index fringes of the grating are oriented at 45°, the 90° light component in the

core mode will propagate through the BFBG structure whereas the 0° light will be reflected by the 45°-fringes and coupled into cladding and radiation modes.

2.6. FBG SENSORS

FBG sensors are a comparatively new and exciting alternative to traditional sensor techniques. They are inherently sensitive to temperature and strain and may be implemented such that these sensitivities are utilised for encoding measurands other than strain or temperature.

2.6.1. Axial strain and ambient temperature response

The shift in Bragg wavelength for an FBG with period Λ and core refractive index n in an axial strain ($\varepsilon = \Delta l / l$) and temperature (T) field may be expressed using [15]:

Equation 2.31

$$\Delta\lambda = 2\left(\Lambda\frac{\partial n}{\partial \varepsilon} + n\frac{\partial \Lambda}{\partial \varepsilon}\right)\Delta\varepsilon + 2\left(\Lambda\frac{\partial n}{\partial T} + n\frac{\partial \Lambda}{\partial T}\right)\Delta T$$

$$\Delta\lambda = \lambda\left(\frac{1}{n}\frac{\partial n}{\partial \varepsilon} + 1\right)\Delta\varepsilon + \lambda(\varsigma + \alpha)\Delta T$$

where $\alpha = \frac{1}{\Lambda}\frac{\partial \Lambda}{\partial T}$ and is the thermal expansion coefficient of the fibre and $\varsigma = \frac{1}{n}\frac{\partial n}{\partial T}$ is the thermo-optic coefficient. The thermo-optic effect may be either positive or negative in optical fibres [70]. For plastic optical fibres (POF), e.g. polymethylmethacrylate fibres (PMMA), $dn/dT < 0$ and a negative change in refractive index is observed, but for silica fibres $dn/dT > 0$ and a positive change in n is observed. Table 2.3 provides a summary of the contributions of the two competing processes:

Fibre type	n	α	ς
SiO_2	1.5	$0.55\text{x}10^{-6}$	$1\text{x}10^{-5}$
POF	1.3-1.7	$0.93\text{x}10^{-5}$	$-1\text{x}10^{-4}$ to $-4\text{x}10^{-4}$

Table 2.3 A summary of values for the thermo-optic effect and the thermal expansion coefficients of polymethylmethacrylate and silica fibre. This table shows that PMMA fibres have a negative temperature coefficient and that they are an order of magnitude more sensitive than silica fibres.

Thus the temperature sensitivity of FBG sensors is predominantly a result of the thermo-optic effect rather than thermal expansion. POF optical sensors provide a substantially more sensitive medium for thermal sensing applications.

If we expand the analysis to consider more closely the effect of axial strain on the Bragg resonance of the sensor, we may describe it accordingly [12, 71, 72]:

Equation 2.32 $$\Delta\lambda_{BR} = 2n\Lambda\varepsilon\left(1-\left(\frac{n^2}{2}\right)\left(P_{12}-v\left(P_{11}+P_{12}\right)\right)\right)$$

where $P_{i,j}$ coefficients are the Pockel's coefficients of the stress-optic tensor and v is Poisson's ratio. The strain response of an FBG is governed by the physical elongation of the grating's period and also by a change in the refractive index as a result of the Pockel coefficients (strain-optic effect). The photoelastic effect comprises coefficients of the refractive index, Poisson's ratio and the Pockel coefficients and is described by [73]:

Equation 2.33 $$\left(\frac{n^2}{2}\right)\left(P_{12}-v\left(P_{11}+P_{12}\right)\right)\approx 0.21$$

which equates to a reduction in the strain sensitivity of silica gratings of ~21% as compared to the response based on elongation of the grating alone [74]. The measured strain response is thus given by $\frac{1}{\lambda_{BR}}\frac{\partial\lambda_{BR}}{\partial\varepsilon}$ and the thermal response by $\frac{1}{\lambda_{BR}}\frac{\partial\lambda_{BR}}{\partial T}$ (at constant temperature and constant strain respectively). The exact figures for these values are dependent on fibre and grating types; this is discussed extensively in Chapters 5 and 6. However, the following approximations for type I (standard) gratings are widely accepted and give a good insight to the properties of fibre sensors:

$\frac{1}{\lambda_{BR}}\frac{\partial\lambda_{BR}}{\partial\varepsilon}$ ➔ 1 pm shift per 1 με of axial strain

$\frac{1}{\lambda_{BR}}\frac{\partial\lambda_{BR}}{\partial T}$ ➔ 10 pm shift per 1 °C change in the ambient temperature

There is also a component of the strain response which is dependent on temperature; however, James *et al* [75] report that the strain coefficient of an FBG sensor is temperature invariant over a wide temperature range from cryogenic levels to room

temperature. Additionally, Maier *et al* [74] report that there are no incidences in literature where the strain-optic effect is said to be strongly temperature variant. This is supported by O'Dwyer *et al* [76] who carried out a comprehensive investigation in to the effect, consolidated with theoretical discussion. Their results showed only a $0.03 fm\mu\varepsilon^{-1}{}^{\circ}C^{-1}$ variation over the temperature range 100°C to 400°C. Maier *et al* do, however, report that the stress (force / area) response of an FBG has a thermal dependence of $1.22x10^{-4}K^{-1}$ in the temperature range of -38°C to 110°C. This may be explained because the value is approximately equal to the increase in Young's Modulus of the fibre over the same temperature excursion. Flockhart *et al* [77] report that the temperature response of an FBG is non-linear over the extended range of -70°C to 80°C (they report a ~35pm deviation from linear) having used a Fourier-transform spectroscopy technique to measure the absolute Bragg wavelength.

2.7. SENSOR CROSS-SENSITIVITY

Because temperature and strain sensitivities of FBGs co-exist, it is necessary to devise a method for decoupling them. Equation 2.31 shows that the effect of a change in the axial strain or ambient temperature fields produces an indistinguishable change in the Bragg resonance. The issue of cross-sensitivity will be discussed at length later in this thesis. For now, we will consider only the simple underlying mathematics.

For an ideal optical sensor arrangement which is sensitive to strain and temperature (ε, T) such that each measurand induces a change in the observables ϕ_1 and ϕ_2 respectively with no cross-sensitivity, we have [78]:

Equation 2.34
$$\begin{pmatrix} \phi_1 \\ \phi_2 \end{pmatrix} = \begin{pmatrix} K_{1T} & 0 \\ 0 & K_{2\varepsilon} \end{pmatrix} \begin{pmatrix} T \\ \varepsilon \end{pmatrix}$$

where K_{nT} and $K_{n\varepsilon}$ are the temperature and strain responses of the sensors respectively. Equation 2.34 is plotted in the (ε, T) plane in Figure 2.12a for specific values of observables ϕ_1 and ϕ_2. The intersection of these loci yield the values of ε and T.

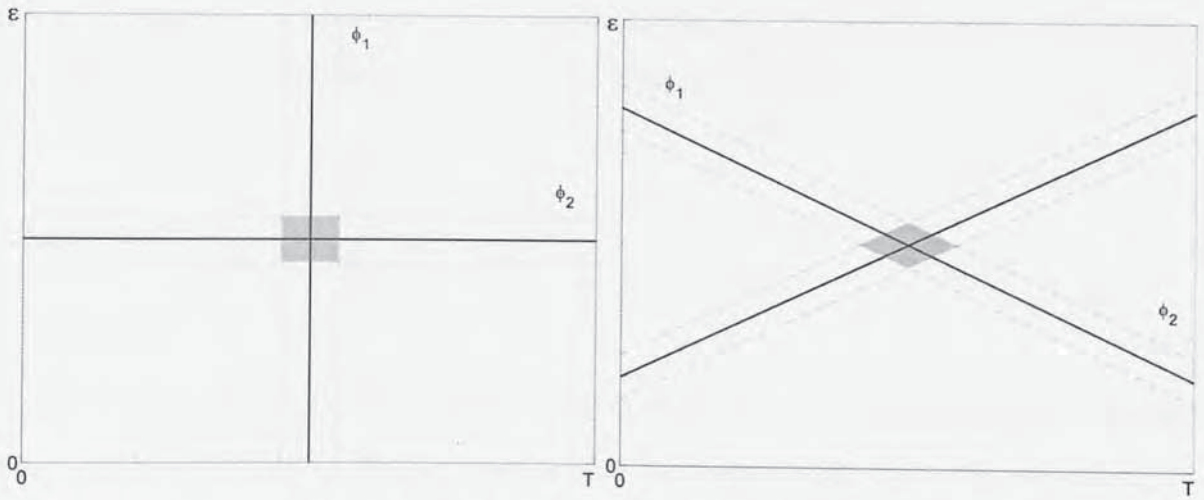

Figure 2.12 (a) (left) The loci ϕ_1 and ϕ_2 in the (ε,T) plane for the ideal case of zero cross-sensitivity. (b) (right) The loci ϕ_1 and ϕ_2 in the (ε,T) plane for the non-ideal case when cross-sensitivity exists between the two observables. The dashed lines represent the uncertainty in the measurement of the observables. The grey shaded areas represents the corresponding uncertainty in the recovery of the measurands.

In practice, however, it is most common for the ideal case to be unrealisable and cross-sensitivity exists such that the observables ϕ_1 and ϕ_2 have a response to both ε and T. In this instance we must rewrite Equation 2.34 as follows:

Equation 2.35
$$\begin{pmatrix} \phi_1 \\ \phi_2 \end{pmatrix} = \begin{pmatrix} K_{1T} & K_{1\varepsilon} \\ K_{2T} & K_{2\varepsilon} \end{pmatrix} \begin{pmatrix} T \\ \varepsilon \end{pmatrix}$$

such that:

Equation 2.36
$$\begin{pmatrix} T \\ \varepsilon \end{pmatrix} = \frac{1}{(K_{1T}K_{2\varepsilon} - K_{2T}K_{1\varepsilon})} \begin{pmatrix} K_{2\varepsilon} & -K_{1\varepsilon} \\ -K_{2T} & K_{1T} \end{pmatrix} \begin{pmatrix} \phi_1 \\ \phi_2 \end{pmatrix}$$

Equation 2.35 is plotted in the (ε, T) plane in Figure 2.12b for specific values of observables ϕ_1 and ϕ_2. Again, the loci intersection point yields the values of ε and T. The practical determination of ε and T results from the inversion of matrix following accurate measurement of ϕ_1 and ϕ_2, as per Equation 2.36. As the angle between the loci tends to zero, then the condition where $K_{1T}/K_{2T} = K_{1\varepsilon}/K_{2\varepsilon}$ will exist and the result of Equation 2.36 will tend to infinity thus invalidating the measurement.

We can compare errors in the derived measurements with those of the ideal case. Ideally, the errors in strain ($\delta\varepsilon$) and temperature (δT) are given by [79]:

Equation 2.37
$$\begin{pmatrix} \delta T \\ \delta\varepsilon \end{pmatrix} = \begin{pmatrix} \delta\phi_1 / K_{1T} \\ \delta\phi_2 / K_{2\varepsilon} \end{pmatrix}$$

where $\delta\phi_1$ and $\delta\phi_2$ are the measurement errors of ϕ_1 and ϕ_1 as indicated by the dashed lines of Figure 2.12. The shaded areas around the intersections show the uncertainty of the determined measurements. The error increases when the case is non-ideal and the loci are not orthogonal, such that [80]:

Equation 2.38
$$|\delta\varepsilon| = \frac{|K_{2T}||\delta\phi_1| + |K_{1T}||\delta\phi_2|}{|K_{1T}K_{2\varepsilon} - K_{2T}K_{1\varepsilon}|}$$

and,

Equation 2.39 $$|\delta T| = \frac{|K_{2\varepsilon}||\delta\phi_1| + |K_{1\varepsilon}||\delta\phi_2|}{|K_{2T}K_{1\varepsilon} - K_{1T}K_{2\varepsilon}|}$$

An alternative description has been provided in [81] where the errors in ϕ_1 and ϕ_1 have been converted to an error ellipse in the (ε, T) plane.

A useful mathematical tool for quickly assessing the accuracy of a dual sensor arrangement is to calculate the condition number of the sensor matrix. The condition number of a matrix measures the sensitivity of the solution of a system of linear equations to errors in the data. It gives an indication of the accuracy of the results from matrix inversion and the linear equation solution. This is easily calculated in Matlab using *cond(c,1)* or MathCad using *cond1(c)* where *c* is the sensor matrix in question. For the ideal case shown in Figure 2.12a, the matrix is given by Equation 2.34. The condition number of this matrix is therefore 1 indicating a perfectly conditioned matrix. For a mathematical explanation for the procedure of calculating the condition numbers of matrices see, for example, [82, 83].

Refer to Section 3.4.2.5 for a summary of the condition numbers for published results.

2.8. CHAPTER CONCLUSIONS

The theoretical study of fibre gratings has progressed significantly in recent years and is now the sole focus of many research groups and individuals alike. As a consequence of this dedicated study it is now possible to produce fibre gratings for a plurality of diverse applications with a good degree of fundamental understanding.

Unfortunately, despite this intense research the topic of photosensitivity is still widely accepted as lacking a cohesive model applicable to all instances. Fortunately, however, in many practical situations it is not always necessary to completely understand the atomic or molecular transitions taking place such that the photochemistry of a particular fibre type is wholly understood; it is often possible to simply accept the results of the exposure of a certain fibre to certain ultraviolet conditions. It is likely that a breakthrough will soon occur in the study of photosensitivity and will therefore enable pre-dating experimental results to be revisited and more completely understood.

This chapter predominantly and deliberately shows the results of theoretical study which are useful to an experimentalist. For example, Section 2.2.3.3 gives equations for the diffusion rate of hydrogen gas in silica fibres later used in Section 6.2.2.2 to calculate the saturation levels differently prepared samples and Section 2.2.4 provides the theoretical background for the discussion of multi-photon absorption in Section 5.4.1.

This chapter, in conjunction with Chapter 3, serves as the basis for the following experimental chapters and is referred to frequently.

Chapter 3

Optical Fibre Sensors

3. OPTICAL FIBRE SENSORS

3.1. PREAMBLE

This chapter builds upon the theoretical concepts introduced by Chapter 2, concentrating on the operation of optical fibre sensor systems. Optical fibre sensors are discussed at length, including their inscription, the different types of fibre Bragg grating and their associated properties, and an in-depth review of current solutions to sensor cross-sensitivity. The concept of embedding photonic sensors in composite structures is also discussed. An introduction to sensor interrogation using blazed fibre Bragg grating spectroscopy includes a review of previous descriptions and prepares the reader for Chapter 4.

3.2. OPTICAL FIBRE SENSORS

A recent survey of OFS15 by Lee [16] showed that the predominant measurands for optical fibre sensors are strain and temperature and that the vast majority of fibre sensors are Bragg gratings, or variants thereof. The results of this survey are shown for completeness in Figure 3.1.

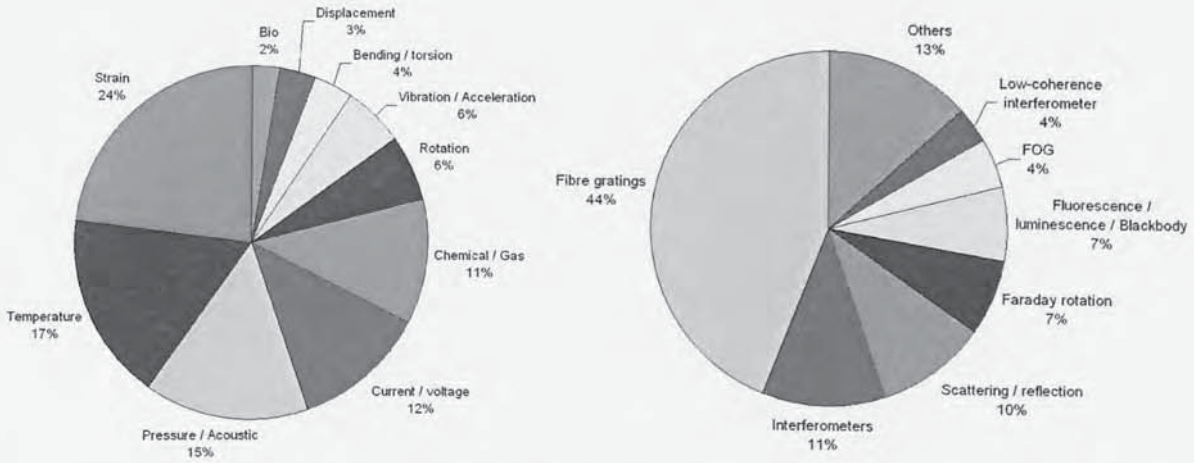

Figure 3.1 (a) (left) The distribution of OFS15 papers according to measurand and (b) (right) according to technologies used. This figure shows that strain and temperature are the most commonly measured physical entities and that Bragg gratings are by far the most used sensor. After [16].

3.2.1.1. Benefits of optical fibre sensors

The principal benefits of optical fibre sensors are threefold:

- They can be easily multiplexed into large arrays, either in terms of wavelength or time, or both making them ideal for applications requiring multi-point measurement.
- They have a very small cross-sectional area, typically 250um for acrylate jacketed fibres, or 130um for polyimide jacketed fibres making them ideal for embedment in composite materials.
- They are electrically passive and so are both immune to electromagnetic interference and do not present an ignition hazard making them ideal for sensing applications in explosive environments.

3.3. *Fibre Bragg Gratings*

3.3.1. FBG manufacture

The original *Hill gratings* [1] were fabricated during an experiment that saw light from an Ar^+ laser being guided by a fibre. Fresenel reflections (typically of ~4%) from the ends of the fibre created a standing wave within the fibre and a grating was formed at the wavelength of the Ar^+ laser (488nm). This arrangement inscription is extremely simple, but also very limited as there is no convenient way to select the resonant wavelength of the inscribed grating.

Side inscription in glass optical fibres by holographic exposure through the cladding was reported by Meltz and Morey in 1989 [3]. They followed the findings of Lam and Garside [2] who demonstrated that *Hill gratings* were inscribed according to a 2-photon absorption process at 488nm by observing that grating strength increased as the square of the inscription laser intensity. It followed, therefore, that use of an inscription with twice the photon energy would result in a 1-photon process; thus Meltz and Morey [3] used a 244nm laser. Further developments that result in generally higher quality gratings were proposed in 1993 by Hill *et al* [5] and Anderson *et al* [4]. The two techniques are now widely known as the holographic (or interferometric) and phasemask techniques respectively. There are many custom variations of each method published, but the base concepts are clear in all cases.

3.3.1.1. Holographic inscription

The first technique for side writing in-fibre gratings was patented by Meltz and Morey [84] shortly before their 1989 paper [3] describing the technique.

Figure 3.2 An early diagram showing the familiar holographic inscription apparatus [85]. The diagram shows a compensator plate whose purpose is to ensure that the optical path is similar in both arms of the interferometer which is particularly important when dealing with sources with poor coherence. The Bragg wavelength of the inscribed gratings is related to the interfering angle.

Figure 3.2 shows the now well known holographic inscription technique as pictured by Moran *et al* [85]. The holographic equipment used in this thesis is shown below in Figure 3.3.

The holographic inscription method is extremely versatile and represents a convenient way to inscribe gratings over a wide range of wavelengths – typically a holographic setup may be used to inscribe gratings with central resonances from 600nm to 1600nm. The system operates by passing the UV inscription beam through a 50:50 beam splitter; these beams are then reflected at two similar mirrors and focused on to the fibre core using similar cylindrical lenses, as shown in Figure 3.3. In order to ensure that each beam is of the same intensity, a ½ wave plate may be placed in front of the 50:50 beam splitter; by rotating the polarisation of the input beam, it is possible to balance the intensities in each arm of the interferometer.

Figure 3.3 An annotated photo of the holographic FBG inscription system used throughout this thesis. Photo: David Birkin.

Interference of the two beams governs the period of the UV fringes and the central reflecting wavelength of the inscribed grating is selected according to the angle at which these beams interfere. This angle, 2θ, is related to grating period as follows [18]:

Equation 3.1 $$\Lambda = \frac{\lambda_{UV}}{2\sin(\theta)}$$

for non-tilted gratings where λ_{UV} is the wavelength of the inscribing laser. This may be re-written for Bragg wavelength as follows [18]:

Equation 3.2 $$\lambda_{BR} = \frac{n_{eff}\lambda_{UV}}{\sin(\theta)}$$

It is often desirable to produce gratings that are longer than the length of the interfering UV beams. This is achieved by expanding the UV beam by means of a beam expanding telescope. Usually, an aperture is used to select the central portion of the expanded beam thereby approximating a uniform intensity profile along the length of the interference pattern. An additional compensator plate, as shown in Figure 3.2, is required for inscription lasers with poor coherence (e.g. excimer lasers) but is almost always omitted in setups using Ar^+ lasers such as Coherent FRED and SABRE FRED lasers. The inclusion of such a plate (or additional mirror) insures a similar optical path for both arms of the interferometer and thereby eliminates different lateral orientations of the interfering beams. There are other configurations which achieve this, such as using an extra mirror in place of the compensator plate; although Ar^+ lasers do not usually require such measures. A number of prism based (also referred to as wavefront-splitting interferometers) techniques have also been proposed (prism interferometer [86, 87], and Lloyd interferometer [88]), which generally offer improved stability at the expense of the wavelength versatility of a free-space approach.

The main disadvantage to the interferometric approach is the susceptibility of the grating fringe visibility to mechanical vibrations. Due to the large mechanical distances involved, any submicron displacements in the position of any of the optical components will result in poor fringe visibility of the inscribed grating.

3.3.1.2. Phasemask fabrication

Phasemask exposure [4, 5] is widely regarded as the most effective method for inscribing gratings. A phasemask is a one dimensional diffractive optical element which spatially modulates the inscribing laser thereby determining the period of the UV fringe pattern. Usually constructed in fused silica, phasemasks are manufactured either holographically or by electron-beam lithography. Lithographically produced phasemasks have the advantage that the period of the phasemask may be varied along its length. This is useful for producing chirped or Moiré patterns. Electron-beam lithography is usually performed in sub-millimetre sections which are joined to form the entire relief grating. Errors in the alignment of the sections are commonly referred to as *stitching errors* which clearly does not affect holographically produced phasemasks. The effects of stitching errors form a large body of literature in their own right; however, it has been shown (e.g. [89]) that the consequence of stitching errors in uniform period gratings is minimal compared with chirped gratings.

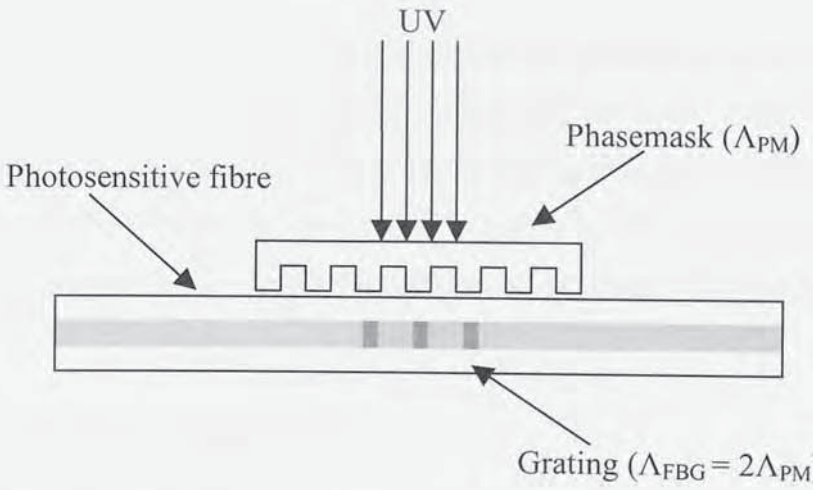

Figure 4.1 A schematic diagram showing the operation of a static phasemask inscription system. The UV laser is passed through a surface relief phasemask and the resulting fringe pattern is projected on to the optical fibre core, thereby inscribing a grating with period equal to twice that of the phasemask.

The period of a phasemask can clearly not be altered post manufacture; although it is common for manufacturers to produce masks with multiple sections of differing period, it

us often desirable to tune the wavelength of the inscribed fibre grating. To this end, several techniques have been proposed.

Prohaska *et al* [90] proposed a system wherein the inscribed wavelength was shortened by means of a magnifying optic arrangement prior to the phasemask. A biconvex lens was positioned such that the light emerging from the phasemask was a converging sphere, magnified by 0.9987. However, this method is not particularly successful; their results showed a shift in the Bragg wavelength of only approximately -2nm.

Zhang *et al* [91] showed that it was possible to strain the fibre prior to inscription thereby shifting the Bragg resonance upon relaxation of the fibre relative to that inscribed in an unstrained grating. The wavelength tuning range of this method is only limited by the level of strain one may apply to a fibre before failure; typically it is possible to tune the Bragg resonance by up to -5nm to -7nm. Byron *et al* [92] showed that by varying the applied strain during inscription it was possible to fabricate complex grating structures, such as chirped gratings, using a uniform period phasemask.

Simpson *et al* [93] have shown that it is possible to tune the resonance of a grating written in hydrogenated germanosilicate fibre by tailoring the mean refractive index using prolonged exposure to UV radiation. The absolute tuning range is governed by the fibre type and hydrogen saturation levels; typically it is possible to tune a grating in SMF28 by up to 8nm and in highly B/Ge co-doped fibre by up to 19nm. This work is discussed extensively in Chapters 5 and 6.

3.3.2. Types of fibre Bragg grating

The four currently published types of photosensitivity have already been described in Chapter 2. A summary of the resultant grating types is provided below in Table 3.1:

Designation	Description
I	Standard grating, written in both hydrogenated and non-hydrogenated fibre of all types.
IA	Regenerated grating written after erasure of a type I grating in hydrogenated germanosilicate fibre of all types.
II	Damage written gratings
IIA	Regenerated grating written after erasure of a type I grating in hydrogen-free germanosilicate fibres.

Table 3.1 A summary of the types of fibre Bragg grating reported to date.

Figure 3.4 shows the spectra of types I, IA and IIA gratings written in B/Ge co-doped fibre before annealing. Each grating has the same period but they are separated in wavelength due to the different mean index changes associated with each type.

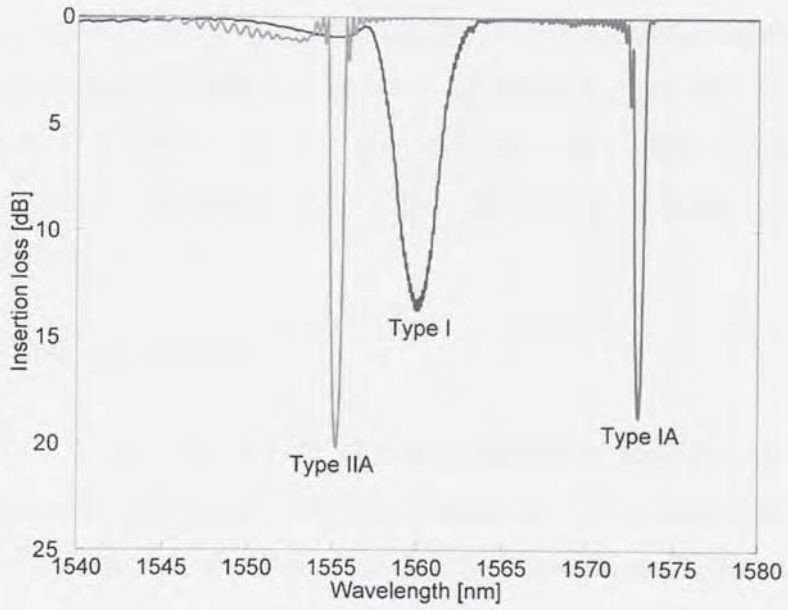

Figure 3.4 The spectra of type I (blue), IA (red), and IIA (green) gratings prior to annealing written in B/Ge fibre. Each grating has the same period and the spectral separation of their peaks demonstrates the differences in the mean index of the three gratings.

3.3.2.1. Type I gratings

Type I gratings are usually known as standard gratings and are manufactured in fibres of all types under all hydrogenation conditions. Typically, the reflection spectra of a type I grating is equal to (1-T) where T is the transmission spectra. This means that the

reflection and transmission spectra are complementary and there is negligible loss of light by reflection into the cladding or absorption. Type I gratings are the most commonly used of all grating types.

3.3.2.2. Type II gratings

Archambault *et al* showed that it was possible to inscribe gratings of 100% (>99.8%) reflectance with a single UV pulse in fibres on the drawing tower [94] and, more importantly, by the holographic technique in fibres doped with 15mol% Ge [95]. The resulting gratings were shown to be stable at temperatures as high as 800°C. The gratings were inscribed using a single 40mJ pulse from an eximer laser at 248nm. It was further shown that a sharp threshold was evident at ~30mJ; above this level the index modulation increased by more than two orders of magnitude, whereas below 30mJ the index modulation grew linearly with pulse energy. For ease of identification, and in recognition of the distinct differences in thermal stability, they labelled gratings fabricated below the threshold as *type I gratings* (known as standard gratings, see above) and above the threshold as *type II gratings*. Microscopic examination of these gratings showed a periodic damage track at the grating's site within the fibre [95]; hence type II gratings are also known as *damage gratings*.

3.3.2.3. Type IIA gratings

Later research by Xie *et al* [35, 37] showed the existence of another type of grating with similar thermal stability properties to the type II grating. This grating exhibited a negative change in the mean index of the fibre; this new type was termed *type IIA*. The gratings were formed in germanosilicate fibres with pulses from a frequency doubled XeCl pumped dye laser. It was shown that initial exposure formed a standard (type I) grating within the fibre which underwent a small red shift before being erased. Further exposure showed that a grating reformed which underwent a steady blue shift whilst growing in strength; this is shown in Figure 3.5 below [96]. It is believed that the photosensitivity mechanism is related to the UV photo-bleaching of a GODC absorption band near 5eV, although the exact mechanism is not well understood [97].

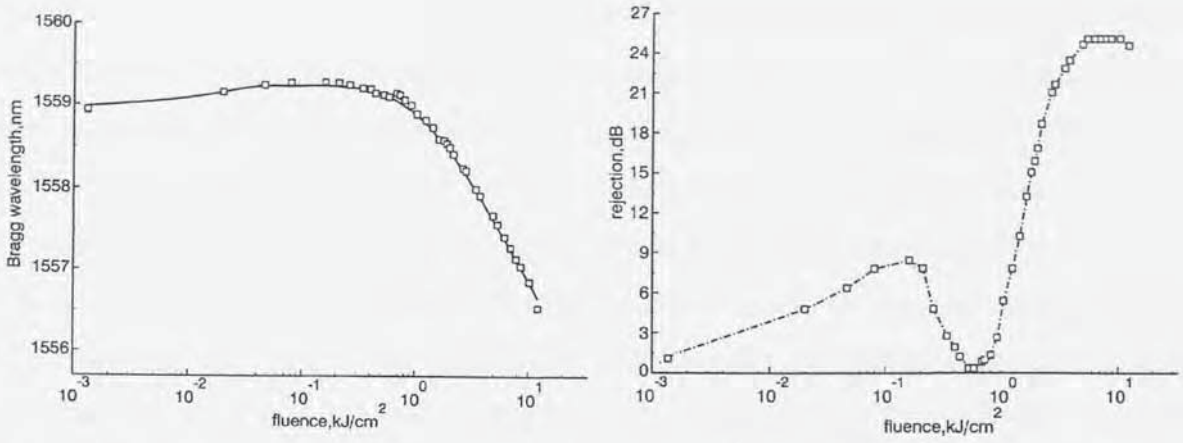

Figure 3.5 Reproduced from [96]. (a) (left) The index change with exposure for a type IIA grating shown in terms of the Bragg resonance of the grating, and (b) (right) the peak transmission loss of the grating. This figure shows the well known negative index shift of IIA gratings, and that they decay to zero reflectivity before reaching a maximum reflectivity at the end of the inscription process.

A three energy-level model has been proposed by Dong *et al* [98]. It suggested that a positive index change is obtained when level 2 is populated by depletion of the ground level, and a negative index occurs when level 3 is populated by the depletion of level 2. This is an extremely simplified model, but it can be used to support the experimental observation of Dyer *et al* [99, 100] that a grating can be amplified in terms of its reflectance using uniform post exposure to a 193nm ArF laser.

Canning *et al* [96, 101, 102] showed a direct correlation of type IIA grating growth and an increase in the compressive stress orthogonal to the core. This correlation was explained by structural change through expansion of the glass in the regions of peak irradiation. They concluded that a large negative contribution to the refractive index came from the structural change in the exposed regions which formed a less dense glass. However, it has further been shown [11], that axial stress during the inscription process retards the formation of type I gratings, and increases the efficiency of the IIA grating formation.

3.3.2.4. Type IA gratings

Type IA gratings were first published by Yu Liu in 2001 during experiments designed to determine the effects of hydrogen loading on the formation of IIA gratings in

germanosilicate fibre [7]. In contrast to the anticipated blue shift of the peak Bragg wavelength, a large positive wavelength shift was measured, as shown in Figure 3.6a; it was noted that 8nm and 18nm red shifts were achieved in hydrogenated SMF28 and highly B/Ge co-doped fibre respectively. This type IA grating appeared once the conventional type I FBG had reached saturation followed by subsequent complete or partial erasure, and was therefore labelled as *regenerated*. It was also noted that the temperature coefficient of the regenerated grating was lower than a standard grating written under similar conditions. In keeping with the rationale of Archambault *et al* [94], gratings formed before this threshold were labelled as type I gratings, and those which evolved after were labelled type IA gratings. There is a clear relationship between type IA and IIA gratings insomuch as their fabrication conditions are identical in all but one aspect: they both form in B/Ge co-doped fibre but IAs form only in hydrogenated fibres and IIAs do not. As shown in Figure 3.6b, type IA gratings do not decay completely in a similar way to IIA gratings and their peak reflectivity is a result of the initial type I grating formed before the IA grating grows.

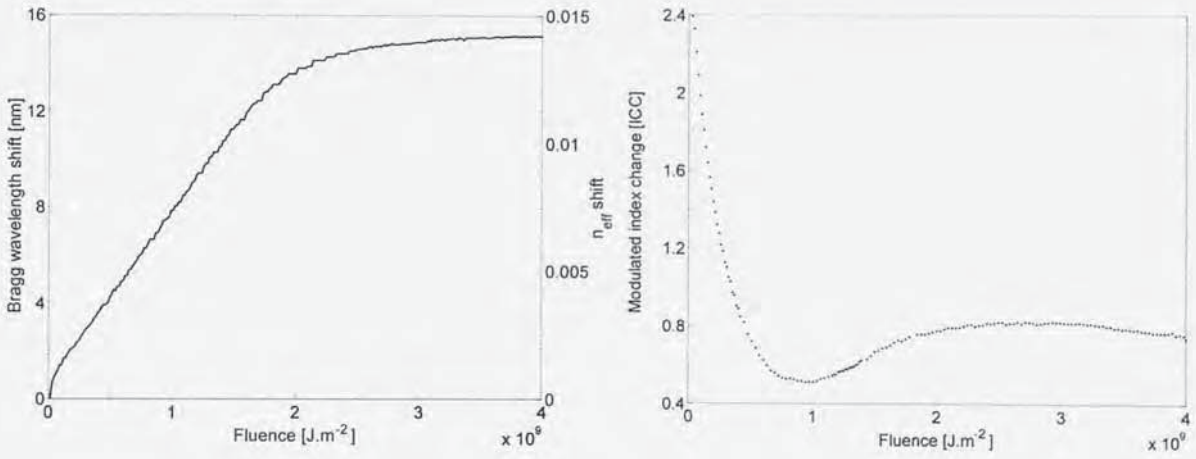

Figure 3.6 An example of the characteristic red shift displayed during prolonged UV exposure of hydrogenated germanosilicate fibre shown in terms of the spectral red-shift and associated refractive index change (a) (left) and the modulated index change (b) (right). This figure is in marked contrast to Figure 3.5.

Further work highlighted the potential application of these gratings for temperature compensated dual grating sensors [103-108]. The largest temperature difference was achieved between type IIA and IA gratings [106].

Although Liu *et al* were the first to identify the large IA mean index change as a significant growth characteristic of fibre Bragg gratings and moreover that IA gratings have a substantially lower thermal coefficient than all other grating types; there are several examples in literature [109-112] of the IA growth characteristics which pre-date Liu's initial publication [7].

Brennan *et al* [109-111] studied the high pressure hydrogenation of Ge doped (~9 mol%) silica fibres. They hydrogenated the fibres at pressures of 140, 1035, 1400 and 1930bar at 60°C until saturation. A 1dB grating was then written using a KrF excimer laser at 248nm and phasemask. Following the initial inscription, the phasemask was removed and the samples were exposed to 30mins of uniform radiation whilst the peak Bragg resonance was monitored. They showed that for the pressures listed above, the Bragg wavelength shifted 3.5, 9, 11 and 12.5nm respectively. Kawano *et al* [112] have also shown the large IA mean index change is possible for long period gratings. An interesting study by Poignant *et al* [48] was performed which showed that small levels of hydrogen in the core speeded up the formation of IIA gratings. It is unclear why they did not show the formation of IA gratings during this work and was soon contradicted by at least one author [40].

3.4. TEMPERATURE-STRAIN DUALITY OF FBG SENSORS

Almost all sensors are cross-sensitive in some way. The well known wire film resistive strain gauge is used to detect strain as a function of resistance. Unfortunately, the resistance of the device changes as a result of elongation or as a result of temperature fluctuation. This problem is easily solved; strain gauges have two axes, only one of which is sensitive to strain. By placing two devices at the same sensor location but orientated at 90° to each other, one will detect temperature and strain, whilst the other detects only temperature. The application of a simple circuit, the Wheatstone bridge (described by Christie in 1833 but used extensively by Wheatstone), yields a temperature invariant reading of strain. Unfortunately, such a straightforward approach to the cross-sensitivity of fibre sensors has yet to be found, because it is not commonly possible to exploit the passive axis technique with optical fibres due to the type of sensing applications they are usually employed in. The more popular solutions to strain, temperature cross-sensitivity are reviewed below.

3.4.1. Reference grating

This is the simplest solution to the cross-sensitivity problem; were it not for practical considerations this approach would have solved the problem with similar ease to the wire film strain gauge method. In the reference grating approach an extra grating is included in the sensor array which is isolated from either strain or temperature; its response is monitored and subtracted from the sensor data thus isolating temperature and strain e.g. [113-116]. Strain isolation is the most common since it can be achieved by having one grating which is simply not bonded to the structure, or which is mounted inside a sufficiently rigid structure. Temperature isolation is a little more complex but is achievable by mounting the grating within a package that expands with temperature such that it applies a strain exactly (and oppositely) mimicking the increase in Bragg wavelength caused by temperature [117]. It has also been shown that packaging the grating in liquid crystal has significant success [118].

However, despite the general effectiveness of this technique, it has additional costs involved since it usually requires an additional grating and associated interrogation electronics. In addition to the financial aspect, the technique can only compensate for general temperature changes – it can not compensate for temperature changes at each sensor location. If the sensor array was monitoring (for example) the stress distribution on the engine casing of a gas-turbine aircraft engine, the temperature gradient could be as much as 2000°C from the near frozen air-scoops to the extremely hot exhaust. In this situation, a single temperature monitoring grating would not give suitable thermal compensation. Of course any temperature above 1200°C would erase the sensors, but that is another issue.

3.4.2. Two FBGs with different temperature / strain responses

The problem of temperature gradients can be solved by manufacturing sensor heads which are self referencing. This can be done by inscribing two adjacent gratings with markedly different temperature and strain responses. In doing this, it is possible to decouple temperature and strain at each sensor location.

3.4.2.1. Markedly different Bragg wavelengths

The thermo-optic and photo-elastic effects both have wavelength dependencies, which result in a slight difference in the strain and temperature response of gratings written at different wavelengths. Xu *et al* [119] exploited this by superimposing two gratings in the same location within the fibre providing reflective peaks at 850nm and 1300nm. A theoretical and experimental study by Sivanesan *et al* [83] investigated the optimal wavelength pair selection and the accuracy of the technique using Corning Flexcor-980 fibre. They showed that a wavelength pair including a member in the shorter wavelength range yields a better conditioned matrix than pairs with both are in the upper wavelength range. They concluded that the measurement accuracy of a 1300nm - 660nm grating pair was almost twice as accurate as a 1550nm – 780nm grating pair.

Kalli *et al* demonstrated this approach using a single grating [81, 120]. Under certain writing conditions, it is possible to inscribe a grating that reflects equally at the 1st and 2nd

harmonics of the Bragg resonance. In doing so, the manufacture of a dual or superimposed grating sensor head is not required since the single grating provides all the information required.

The practical drawback of this technique is that the interrogation electronics must be capable of operating at two wavelengths; this usually requires two light sources and two photodiodes.

3.4.2.2. Photo-induced differences in the thermal responses of two gratings

Liu *et al* [103-108] proposed a revolutionary approach to this problem using type IA and type IIA gratings which have substantially different temperature coefficients, typically 6pm°C^{-1} and 12pm°C^{-1} respectively. By monitoring these gratings, which are separated by 15-20nm if inscribed using the same phasemask, the temperature change is determined by the distance between the two peaks and the strain is determined by the relative shift from the relaxed state. Simpson *et al* [93] showed that there is a small, but measurable, difference between the strain responses of the two gratings caused by the difference in wavelength. They further showed that the manufacturability of the devices may be significantly improved by using a IA-I combination which, although yielding a slightly less well conditioned sensor matrix, does not require the fibre to be annealed in between the inscriptions of the gratings. Frazao *et al* showed a similar sensor head utilising a I-IIA grating pair [121].

The beauty in the approach of using two different grating types is that each grating pair can be interrogated using the same photodiode / light source due to the close spectral proximity of the reflective peaks and that every sensor in the array is capable of independent strain-temperature measurement. Refer to Chapters 5 and 6 for a more detailed discussion of this work.

3.4.2.3. Different thermal responses of two joined fibres

Another approach is to splice two different fibres and write a grating over the join. Proper choice of fibre insures that the two gratings have different central wavelengths and that

the thermal and/or strain responses are different. Cavalerio *et al* [122] used hydrogenated Siecor SMF1528 and Fibercore PS1250/1500. They inscribed gratings using two different phasemasks to give sufficient distance between the grating peaks. Their results showed that the strain coefficients were $0.97pm\mu\varepsilon^{-1}$ and $0.95pm\mu\varepsilon^{-1}$ and the temperature coefficients were $8.43pm^{\circ}C^{-1}$ and $7.37pm^{\circ}C^{-1}$. Their estimated error was $18.4\mu\varepsilon$ and $2.2^{\circ}C$.

Guan *et al* [123] manufactured a dual grating sensor head (although they describe it as a single grating approach) with similar strain coefficients and dissimilar temperature coefficients. They used Corning SMF28 and Er,Yb co-doped hydrogenated fibres. Their results showed that the strain coefficients were $1.05pm\mu\varepsilon^{-1}$ and $1.04pm\mu\varepsilon^{-1}$ and the temperature coefficients were $10.6pm^{\circ}C^{-1}$ and $9.2pm^{\circ}C^{-1}$. Their estimated error was $8.5\mu\varepsilon$ and $1.6^{\circ}C$.

Although Guan *et al* [123] claim significantly improved results over Cavalerio *et al* [122], it is likely that, since the percentage differences in the thermal response of their sensor heads are approximately the same, this claim stems from assuming a more accurate interrogation system and that the results are comparable.

3.4.2.4. Different strain responses between fibres of different diameters

In this technique, two fibres of similar core diameter but different cladding diameters, usually standard 125um and 80um suppressed cladding fibres are spliced together [124]. Since strain is related to Young's Modulus by stress and stress is a function area, the strain experienced by the grating in the wider fibre is smaller than that in the narrower fibre.

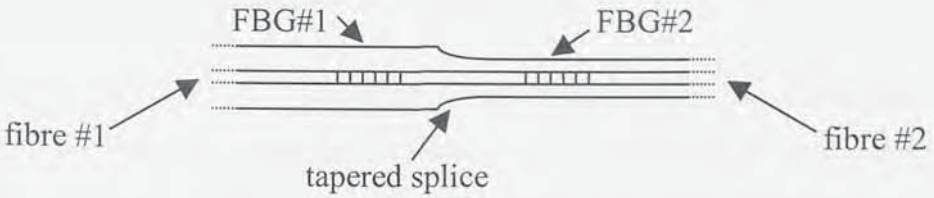

Figure 3.7 Illustration of a grating written either side of the splice between two fibres of different diameters which may be used to discriminate between temperature and strain changes because the fibre in the narrower fibre will experience more strain than the grating in the wider fibre.

If the two gratings are given a different period, strain changes are given by the separation of the peaks and temperature is given by the shift of both peaks from their resting state.

An interferometer has been designed which directly measures the difference between the peaks, thus measuring the strain changes and ignoring temperature variations [125].

3.4.2.5. Dual grating summary

In order to compare and contrast the dual grating approaches labelled above, the matrix condition number has been calculated as per Section 2.7 using the published values of K_{nT} and $K_{n\varepsilon}$ for each method. The results are shown below in Table 3.2 and offer a unique contrasting compilation.

Method	Reference	Condition Number
Strain or temperature isolated reference grating	(K_T = 10pm°C^{-1}, K_ε=1pmμε^{-1})	10
Different diameter fibres	James *et al*, [124].	48
Type IIA and type IA grating pair	Shu *et al*, [105].	68
Superimposed grating pair	Xu *et al*, [119].	123
First and second order Bragg resonances	Sivanesan *et al*, [83].	161
Germanosilicate and Er,Yb doped germanosilicate	Guan *et al*, [123].	169
Germanosilicate and B doped germanosilicate	Cavalerio *et al*, [122].	173
Type IA and type I grating pair	Simpson *et al*, [93].	188
First and second order Bragg resonances	Kalli *et al*, [81, 120].	203
Type IIA and type I grating pair	Frazao *et al*, [121].	272

Table 3.2 Matrix condition numbers of dual grating temperature-strain isolation configurations outlined in this section. The table is ordered with the most effective method (as defined by the lowest condition number) first.

3.4.3. FBG and a chirped FBG in a fibre taper

In a uniform period FBG, the spectral bandwidth has a negligible dependence on strain and temperature. If a strain gradient is introduced along the length of a grating, then the spectral bandwidth term becomes significant and may be used to compensate for changes in the strain of a sensor. Xu *et al* applied a strain gradient by tapering the fibre and then inscribing a chirped grating over the taper, a uniform grating was inscribed adjacent to the taper [126]. The taper was designed such that the grating was linearly chirped when tension was applied. The average strain was measured as a change in the spectral bandwidth of the grating. Temperature changes induce a change in both central reflecting wavelengths, but only strain altered the effective bandwidth of the tapered grating; thus temperature and strain may be decoupled. A schematic of this system is shown below in Figure 3.8.

Figure 3.8 Reproduced from [126]. A schematic showing the arrangement by which independent temperature and strain measurement may be used using a chirped grating in a tapered fibre and a uniform reference grating.

3.5. EMBEDDED PHOTONICS

One of the most attractive aspects of fibre sensors is that they have an extremely small diameter. This combined with the ability to multiplex many sensors into a single length of fibre make them am obvious choice for engineers wishing to manufacture so called *smart structures*. A smart structure is a structure with feedback that indicates its current state and enables action to be taken to maintain an equilibrium state. However, the very fact which makes fibres ideal for embedding in to composite structures is also their Achilles heel; fibres are extremely susceptible to damage at the ingress / egress point within the structure. If we consider a commonly sited example of a large passenger aircraft it is easy to understand the financial implications of a large wing structure which relied heavily on embedded fibres for structural health monitoring being irreparably damaged by a trivial accident at the fibre access point. For this reason, there is currently a great deal of research in to the manufacture of reliable, re-configurable fibre connectors for use with composite materials.

3.5.1. Composite connectors

Research into composite fibre connectors is almost entirely carried out by aerospace research groups rather than optical fibre research groups, which is an indicator of the potential market for such technology. An early solution to the problem was proposed by Lu *et al* wherein they suggested the incorporation of slightly adapted standard FC:PC connectors at the desired entry point of the structure [127]. This solution relied on the inclusion of bulky metal components within the composite material which would require extensive qualification in order to be permitted by either civil or military aerospace regulatory authorities. However, this solution represents an extremely cost effective solution to the problem and whilst finding use primarily in laboratory based applications, it does provide a simple and reconfigurable solution. Talat *et al* [128] proposed a hybrid concept wherein a silica capillary tube was used to terminate the fibre at the edge of the composite material with a section of Teflon tubing used to guide a similarly terminated fibre to be glued into position with index matching adhesive. The problems associated with index matching adhesive not withstanding, this approach has two primary draw

backs, namely ruggedness and re-configurability. A narrow silica capillary tube does not represent a significant defence against accidental damage and the use of an optical adhesive makes the de-mating and re-mating of such a connector extremely impractical. Additionally, it is not possible to machine the edge of the composite panel when using this method since the fibre must be cleaved post-curing and the Teflon tube is required to protrude from the surface. Morgan *et al* [129] proposed a progression of Talat's method which incorporated two GRIN lenses to minimise coupling losses. Unfortunately, Morgan's method has the same drawback of Lu and Talat's; the solution required a fibre to protrude from the composite during the curing process. This is when the fibre is most susceptible to damage. Similar solutions have been suggested by Kang *et al* [130] but are little more than reinforcing methods for standard fibre pig-tales exiting the composite structure. More recent work has begun to address the issues of the practical incorporation and use of composite connectorisation. Sjogren [131], for example, proposed several options including a flush mounting dual channel fibre connector with the potential to be incorporated such that the panel edge might be machined post-curing. The device was also extremely compact having a cross section of only 3mm by 7mm. An additional study into the effects on the static strength of the composite structure following the embedment of the connector was also performed [132]. This work showed that the impact on the composite strength was significant in both tension and compression. It further showed that smaller connectors which could be embedded by simply overlaying the plies had reduced structural impact compared to those requiring the cutting of the plies.

Green *et al* [133, 134] have studied resin flow during the curing process and highlighted that resin can flow along the exposed fibres at the point they exit the structure. This may lead to fibre breakage due to the comparatively poor elastic properties of epoxy resin. Resin flow is also a problem for embedded connectors since flow into the connector shell usually results in damage to the highly polished end-faces of the fibre.

The ideal solution, therefore, is a completely sealed connector shell that is totally embedded within the composite material during the curing process. The connectors may be accessed by machining the edge of the composite and revealing the connector. This

has been successfully prototyped by Deutsche Connectors as their contribution to the DTI EMPIRE project, for which the work detailed in this thesis was produced.

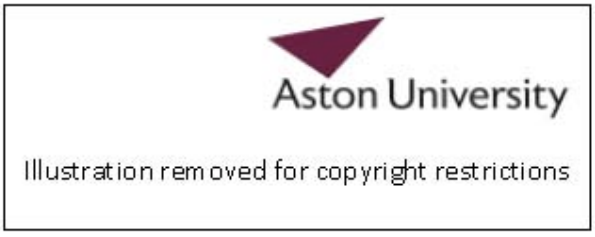

Figure 3.9 A sample of the composite connectors designed by Deutsche Ltd as part of the DTI-Link EMPIRE project. Shown are designs for edge and surface connectors. The edge connectors are buried in the composite during lay-up and curing and are exposed by post-machine. This approach represents the most reliable method for ensuring the integrity of the connector during composite manufacture.

3.6. BFBG SPECTROSCOPY

Since their first report in 1990 by Meltz *et al* [6], blazed fibre Bragg gratings (BFBGs) have been demonstrated for applications including WDM channel monitoring [135], WDM add-drop multiplexers [136-138], macro bending sensors [139], refractomerty [140], erbium doped fibre amplifier (EDFA) gain flattening [141], polarisation discrimination [142], comb-filters [143], narrow-band rejection filters [144] and edge filters [145] etc. Several reports have been published showing that BFBGs may be used to outcouple light from the core of a fibre which may be used as the basis of a diffractive spectrometer [64].

Spectroscopy using diffraction gratings is a simple concept: light is diffracted according to wavelength such that a detector may be used to relate the spatial distribution to the optical spectrum; widely used commercial systems include the low cost, miniature spectrometer by Ocean Optics. It is beneficial to use all fibre components since this has an impact in both insertion loss and the overall size of the unit. BFBGs have already been discussed theoretically in Chapter 2; they act as diffraction gratings because the fringes allow coupling of core modes to radiation modes.

The first BFBG patent was filed by Meltz and Morey [146] following their 1990 publication of the potential applications of BFBGs as optical taps [6]. Since then, two similar patents have been filed by Koeppen *et al* and Perez *et al* [147, 148]. Wagner *et al* [64] also published a BFBG spectrometer design. They used an index matching prism to remove cladding-air resonances and focus radiated light on to a 256 element InGaAs detector array. They achieved focusing of the beam along the fibre axis by chirping the grating, as discussed in Chapter 2. Other applications include the novel use of BFBGs in planar waveguides as optical interconnects [149] and as waveguide grating couplers [150].

Figure 3.10 Reproduced from [151]. A schematic diagram showing the setup of the BFBG sensor interrogation system proposed by Jauregui et al.

Jauregui *et al* [151-155] have demonstrated a BFBG interrogation system which exploits the resonant structure of the radiated light form the grating. They placed a BFBG, which was not covered in an index matching medium, approximately 5mm from a 512 element array as indicated by Figure 3.10 [151]. In doing so, a resonant structure caused by partial radiation of core modes (refer to Section 2.5 for a discussion of the resonant structure) was detected by the array which corresponded to the convolution of the spectra of the reflective gratings in the sensor array. A moderately complicated deconvolution is required with this setup since each sensor grating contributes to the final spectrum. The authors report large bandwidth (>150nm) although the system accuracy was reported to be only 25pm and operated in the 1300nm range.

Wielandy & Dunn [156] proposed another compact system which used a superstructure grating, an index matching prism and a 512 element array, as shown in Figure 3.11.

Figure 3.11 After [156]. The schematic diagram showing the operation of the BFBG spectrometer proposed by Wielandy and Dunn which uses an index matching prism and a 512 element photodetector array.

The design uses a tilted superstructure grating which couples light out of the fibre and produces an interference pattern on the detector array. The Fourier transform of the interference pattern serves as a direct measurement of the optical input spectrum. They report picometer resolution over an 80nm bandwidth and more coarse resolution over a 160nm bandwidth.

Feder *et al* [157] proposed a system which used three BFBGs separated in wavelength and three photodetectors. The system operated by measuring the ratio of the optical power radiated by each grating. However, this system was designed for coarse spectroscopy of WDM systems. The reported resolution of 7nm would not be sufficient for most sensing applications.

Figure 3.12 Reproduced from [157]. The multi-element BFBG spectrometer proposed by Feeder et al which uses the relative intensities of the light radiated from 3 different BFBGs to calculate an approximate wavelength for light incident to the device.

3.7. CHAPTER CONCLUSIONS

Optical fibre sensors are now enjoying more commercial popularity than ever before. This is predominantly market driven; for example, the aerospace composite industry requires the ability to take large numbers of measurements within strict weight limits and the undersea drilling markets require intrinsically safe sensors for use within oil or gas fields.

Optical fibre sensors have emerged as the most common optical sensor element largely due to extremely repeatable fabrication techniques such as the phasemask method which enables medium-skilled operators to fabricate identical or near-identical gratings. As with all sensors, measurand cross-sensitivity is frequently a problem for FBG sensors. To this end there are a large number of published solutions to the problem with varying effectiveness and individual drawbacks. This chapter reviews many of the most successful methods and provides a basis for direct comparison in the form of Table 3.2 which orders them in terms of accuracy derived from the matrix condition number defined in Section 2.7.

This chapter also provides the reader with an insight in to the current state-of-the-art optical connectors, as designed by the Embedded Photonic Infrastructure project (EMPIRE). The connector solutions shown represent the next generation of fibre connectors that will be used in the aerospace and auto-sport industries and which will facilitate the growth of optical sensor technology beyond the current level.

A crucial element of optical sensing is the recovery of information encoded by the sensor using spectroscopy techniques. In recent years, attention has been paid to the use of blazed fibre Bragg gratings as diffractive elements for spectrometers. This chapter provides a review of the first such devices and the current embodiments of the concept.

Chapter 4

Blazed Fibre Bragg Grating Spectroscopy

4. BLAZED FIBRE BRAGG GRATING SPECTROSCOPY

4.1. PREAMBLE

Fibre optic sensors are of enormous interest because their small size, immunity from electromagnetic interference, potential low cost and ease of multiplexing make them ideal for embedding in composite materials. Traditionally, the problem with wavelength encoded optical sensors has been the recovery of information; bulky laboratory equipment cannot be used in the field since it is usually extremely expensive and insufficiently rugged. The most promising systems to date involve variants of tuneable filters to perform the optical interrogation. Common types of tuneable filter include, the Fabry-Perot filter (an interferrometric technique based on a tuneable cavity between two mirrors), the sensor-receiver grating pair (the receiver grating is strained until the two gratings reflect the same wavelength, at condition the measurand may be calculated) and edge filters (the reflected signal from a sensor is passed through a linear intensity filter). This chapter, however, details the development of a sensor interrogation system capable of true spectral measurement which utilises a CCD array and a blazed fibre Bragg grating. It will build on the literary and theoretical introductions of Chapters 1-3 and detail the design of a laboratory demonstration system, an industrial prototype and several novel uses of BFBGs.

4.2. BFBG RADIATION MODES

BFBGs may be UV inscribed using the phasemask or the holographic interference techniques. Fringes in BFBGs are slanted either by tilting the mask with respect to the fibre or by rotating the fibre in the plane formed by the two interfering beams. In order to examine the characteristics of the radiation mode out-coupling, BFBGs were UV-inscribed in standard telecom, hydrogenated SMF and MMF by both phase-mask and holographic techniques. The tilt angles for gratings written by the phase-mask method were limited by the finite width of the phasemask fringe pattern to 6° whereas the holographic setup was not so constrained and yielded up to 18°.

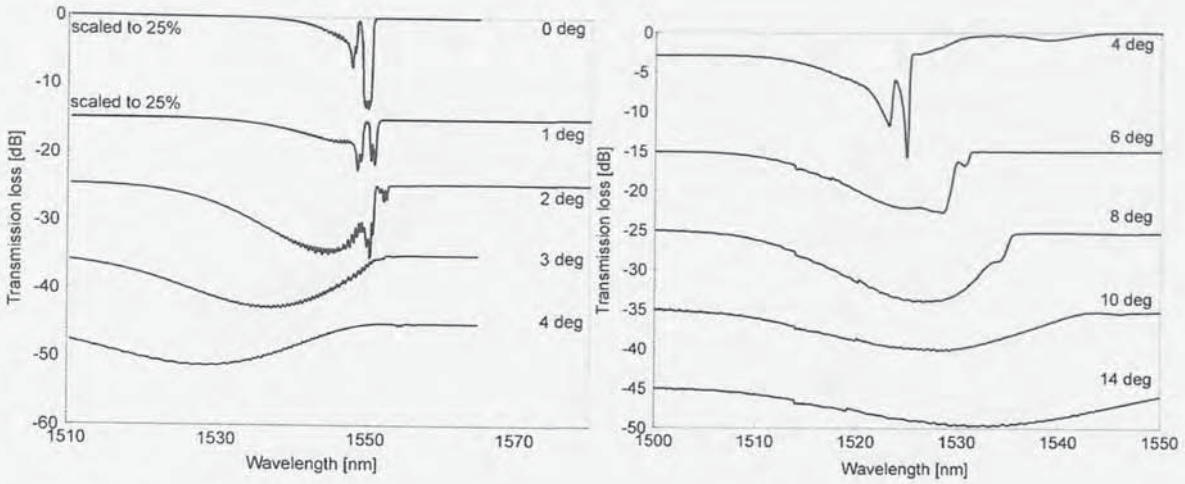

Figure 4.2 The transmission loss profiles of two sets of BFBGs immersed in index matching gel that were manufactured in SMF according to (a) (left) the phase-mask, and (b) (right) the holographic techniques. This figure shows the differences between the Bragg wavelength of the BFBG and the wavelength of the most intense radiation mode which result from the differences in the geometrical arrangements of the two inscription methods. Each plot is offset on the vertical axis.

Figure 4.2a shows the spectra of several gratings written in SMF using the phasemask method. It shows an increase in the wavelength of the Bragg resonance (whilst its strength decreases) and a decrease in the wavelength of the peak radiation mode (whilst its strength increases) with increasing blaze angle. Figure 4.2b shows similar gratings manufactured according to the holographic technique. In this instance, the Bragg resonance experiences an increase in wavelength whilst decreasing in amplitude at a significantly higher rate than the phasemask example. In contrast to the phasemask case, Figure 4.2b shows a steady increase in the wavelength of the peak radiation mode.

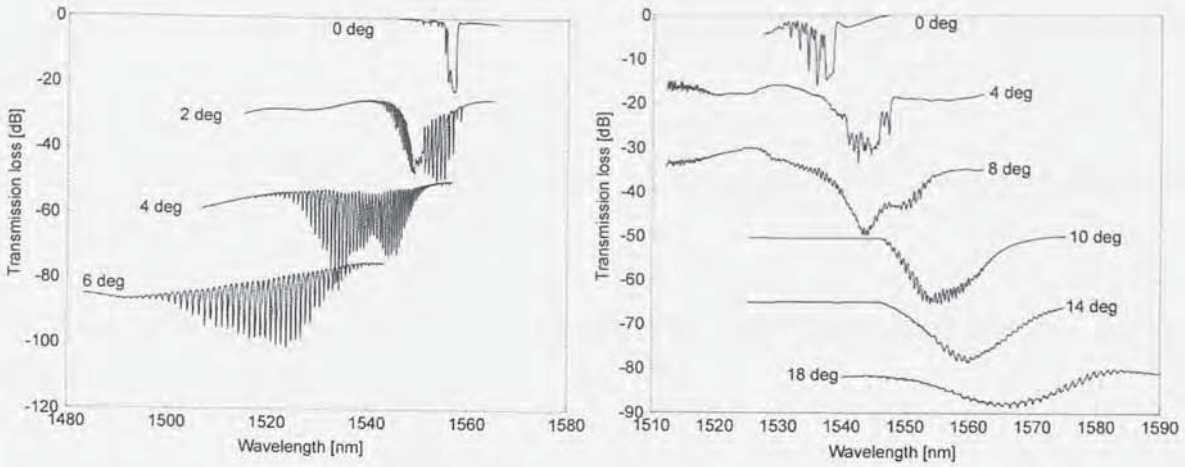

Figure 4.3 The transmission loss profiles of two sets of BFBGs in air that were manufactured in MMF according to (a) (left) the phase-mask, and (b) (right) the holographic techniques. This figure shows that the self-chirping effect of holographic BFBG inscription reduces the resonant structure of the radiation modes. Each plot is offset on the vertical axis.

Figure 4.3 shows the spectra of gratings similar to those in Figure 4.2, but fabricated in hydrogenated multi-mode telecoms fibre. Figure 4.3a shows gratings manufactured by the phasemask method, Figure 4.3b shows those manufactured holographically. Figure 4.3 shows broadly the same spectral characteristics as Figure 4.2, however, the radiation mode out-coupling is significantly stronger and more spectrally confined in MMF than in SMF. For example, gratings with a 10° tilt angle produced by the holographic technique achieved a maximum radiation out-coupling of 14dB in MMF compared with only 4.5dB in SMF. The strong radiation mode out-coupling in MMF may be explained by the comparative fibre core sizes; MMF fibre has a much larger core (50μm) diameter than SMF (9μm). This larger core diameter contains a larger surface area of BFBG fringes than the SMF case resulting in stronger radiation out-coupling.

In order to produce Figure 4.2, the SMF gratings were immersed in index matching gel to enforce the infinite cladding condition. However, it is to be noted that the gratings manufactured holographically had a significantly weaker resonant structure prior to immersion that those fabricated using a phasemask. The MMF gratings used to produce Figure 4.3 were not immersed, by way of demonstration. Figure 4.3 clearly shows the profile smoothing effect which results from the slightly chirped structure of holographic

gratings which is a consequence of rotating the fibre in the slightly diverging inscription beam.

Two trends can be clearly seen from Figure 4.2 and Figure 4.3. They show that with increasing tilt angle:

The peak radiation mode wavelength of gratings fabricated using both methods shift in opposite directions with a similar rate

The Bragg wavelength response shifts toward longer wavelengths at a much higher rate for BFBGs fabricated using the holographic method than those using the phase mask technique

This may be explained using the theory discussed in Chapter 2, Section 2.5. The peak radiated wavelength may be calculated according to Equation 2.20:

Equation 2.20 $$\lambda_{MAX} = n_{eff}\Lambda_{EXT}\left(1+\cos 2\xi\right) = 2n_{eff}\Lambda\cos\left(\xi\right)$$

and is a function of both blaze angle and period. Due to the optical geometry of the inscription conditions in the two BFBG manufacture processes, the period of the grating is a function of blaze angle according to Equation 2.22:

Equation 2.22 $$\Lambda = \frac{\Lambda_{EXT}\cos\left(\xi\right)}{\cos\left(\xi_{EXT}\right)}$$

When manufactured holographically, the external interference fringe period is also a function of blaze angle. This was discussed in Section 2.5.1 where Equation 2.26 defined the relationship mathematically:

Equation 2.26 $$\Lambda = \frac{\lambda_{uv}}{2n\sin\left(\frac{1}{2}\left[\arcsin\left(\frac{1}{n}\sin\left(\alpha+\xi_{EXT}\right)\right)+\arcsin\left(\frac{1}{n}\sin\left(\alpha-\xi_{EXT}\right)\right)\right]\right)}$$

Figure 4.4 shows a plot of the central Bragg resonance and peak radiation mode wavelength as a function of external blaze angle (for fixed interference fringe period, normal to the apparatus).

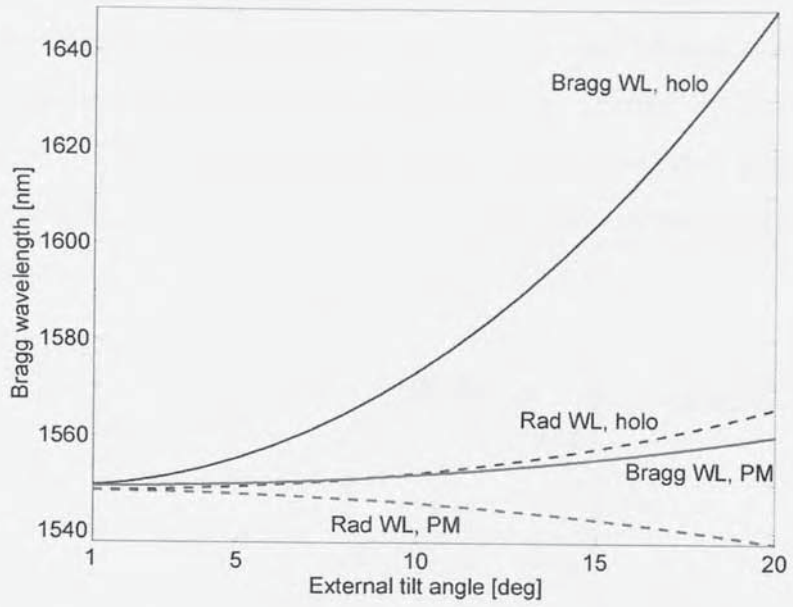

Figure 4.4 The calculated relationship between the Bragg wavelength (solid), the peak radiation wavelength (dashed) and external tilt angles for BFBGs fabricated using the phasemask (red) and holographic (blue) methods. This figure offers a theoretical explanation of the experimental evidence shown by Figure 4.2 and Figure 4.3.

Figure 4.4 shows that the Bragg wavelength increases with external tilt angle in both inscription regimes, but significantly more so in the holographic case where the evolution is enhanced by the increase in grating period due to Equation 2.26.

4.3. BFBG SPECTROMETER PRE-PROTOTYPE

4.3.1. System concept

The BFBG may be used as a dispersive grating which couples light from the core of the fibre to form directional radiation modes which are in turn focused onto a CCD array. Since the radiation angle is wavelength dependent as defined by Equation 2.19, the spatial position of the illuminated pixels on the CCD array becomes a direct function of wavelength and thus the system acts as a spectrometer. The system schematic is shown in Figure 4.5.

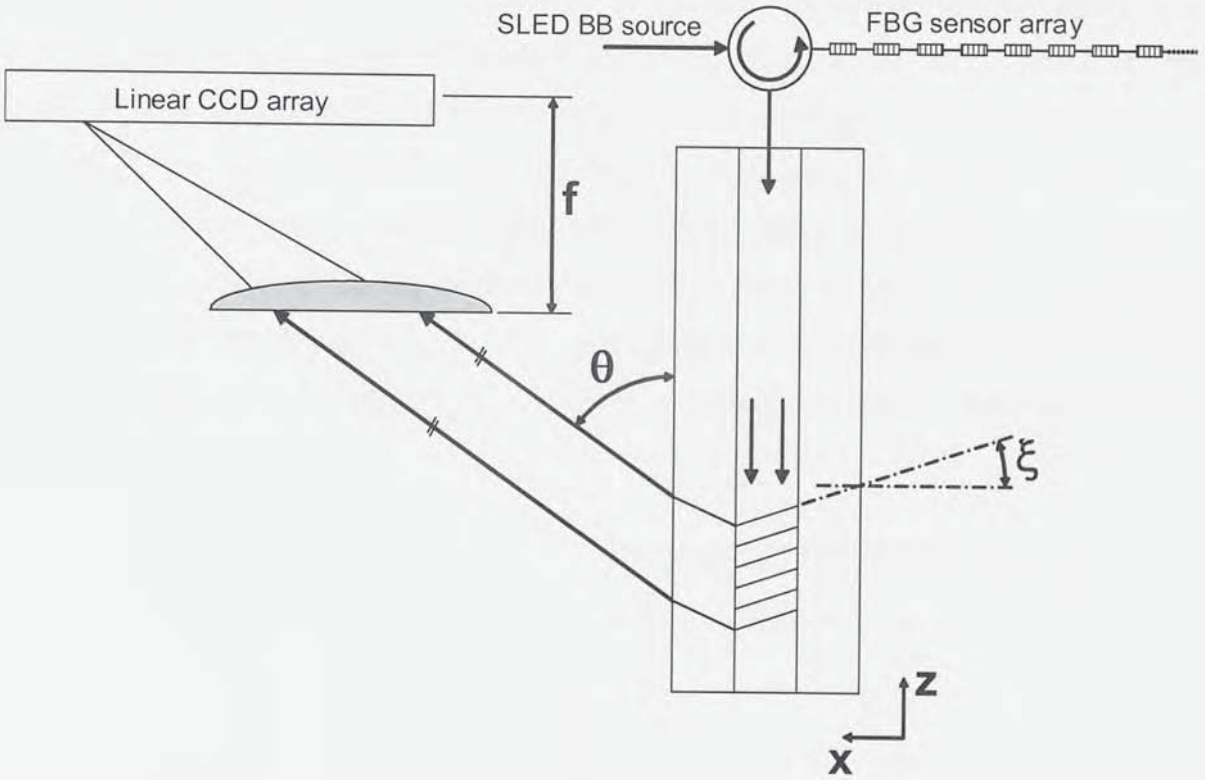

Figure 4.5 Pre-prototype system overview showing the simple concept which makes the design so versatile.

4.3.2. CCD arrays

The detector array used in this series of experiments was a Sony ILX511 linear CCD array, coated with Y_2O_2S:Er,Yb in order to make it responsive to infra-red radiation. The device is comprised of 2048 pixels, 14μm in length, and is shown below in Figure 4.6.

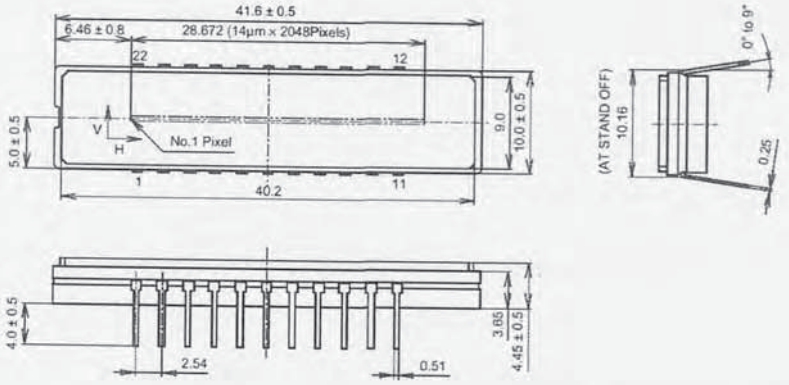

Figure 4.6 The physical dimensions of the CCD array used extensively in this thesis. Sourced from the datasheet for the Sony ILX511 CCD array.

CCD arrays are desirable to use in place of photodiode arrays because they offer longer arrays with smaller pixel size at a fraction of the cost of an InGaAs array. However, this is not without its drawbacks; CCD arrays use CMOS technology which is most sensitive to light in the visible portion of the spectrum. It is possible to coat the array with a substance which emits visible light when illuminated with infra-red radiation. Unfortunately, the responsivity of these coated CCD arrays is highly non-linear; Figure 4.7a shows the responsivity measured using a highly accurate tuneable laser at a constant level of output power. Figure 4.7b shows the manufacturers stated responsivity up to 1µm.

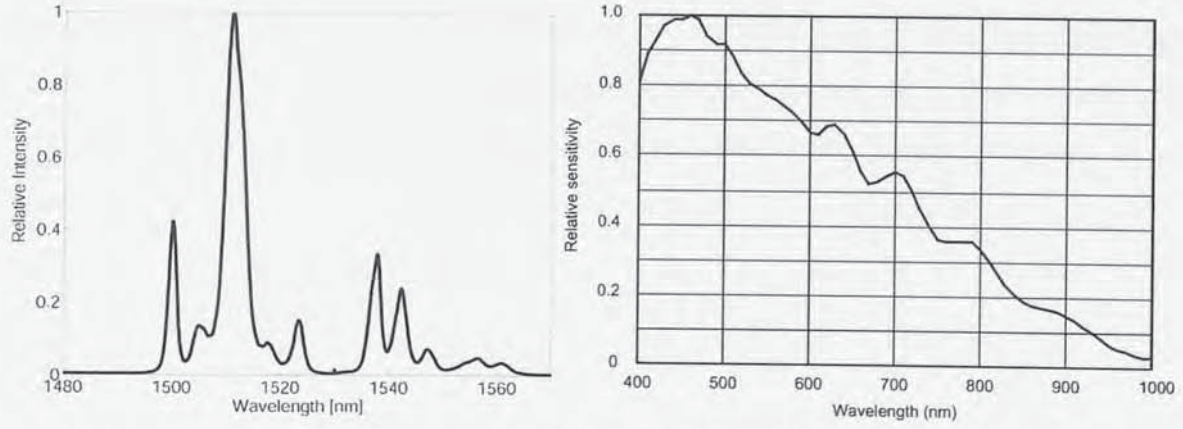

Figure 4.7 (a) (left) The responsivity of the CCD to IR radiation after coating with an IR sensitive compound and (b) (right) the manufacturers stated responsivity up to 1µm stated in the Sony ILX511 datasheet.

CCD arrays essentially count photons for a period of time, termed the integration period (sometimes known as the shutter time in analogy to photography). The integration period

is usually controlled by software and is typically of the order of 1-500ms and represents the lower limit at which the CCD may be sampled.

4.3.3. Pre-prototype description

For this prototype, a 7° BFBG was inscribed by the phasemask method in hydrogenated B/Ge fibre (Verillion IF01001410101) with a 244nm Sabre Fred laser. The grating was then annealed at 80°C for 48 hours to stabilise the grating. The fibre was clamped such that the radiation direction could be controlled by rotating the clamp within its holder, to aid initial alignment. Application of Equation 2.19,

Equation 2.19

$$\cos(\theta) = \frac{\frac{\lambda}{\Lambda}\cos(\xi) - n_{eff}}{n_2}$$

yields a radiation angle of ~22°. The BFBG was immersed in index matching gel to remove cladding-air resonances from the radiation spectrum which would otherwise have caused significant attenuation at multiple wavelengths. An IR coated Sony ILX511 CCD array was mounted on a motorised stage in the plane of the outcoupled light (refer to Section 4.3.2). This enabled the CCD array to be scanned across the far-field image of the light radiated from the BFBG and by saving CCD images at controlled locations it was possible to build up a highly accurate plot of the far-field image. This beam profiling technique was used to monitor the focusing of the system and thereby improve performance. The pre-prototype is shown in Figure 4.8 wherein all major components are annotated.

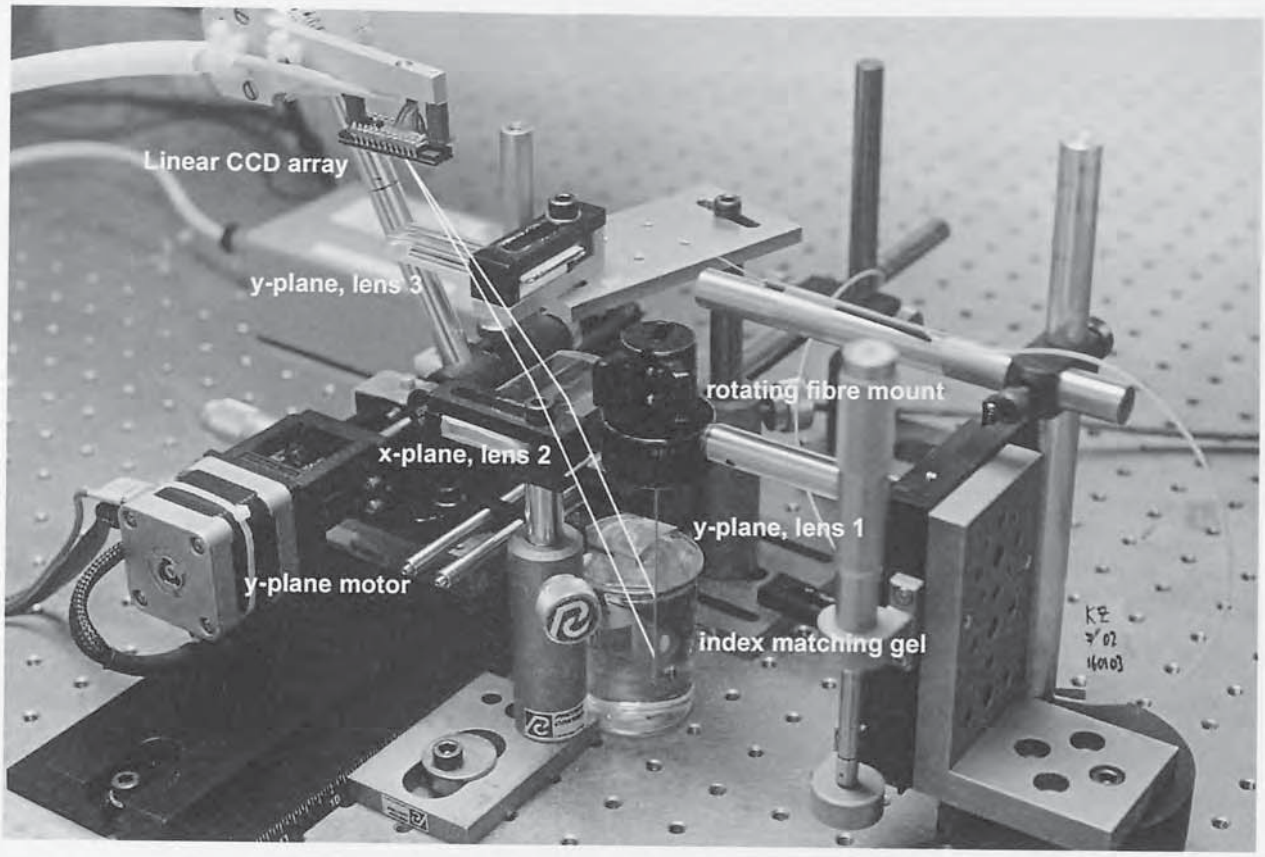

Figure 4.8 The pre-prototype of the BFBG/CCD spectrometer system pictured with annotations indicating the important features. Photo: David Birkin.

Focusing was achieved in the x- and y-planes using cylindrical lenses. Two lenses were used in the y-plane (since the beam is heavily divergent in this plane due to the circular geometry of the fibre) and one in the x-plane.

4.3.3.1. System alignment

In order that the system may be initially aligned, a 633nm He-Ne laser was coupled to the BFBG input and thereby radiated outwards by the grating. A screen was placed over the equipment and the orientation of the BFBG and CCD were approximately placed using the visible output. Subsequent alignment and focusing was achieved with real-time feedback from the CCD array and beam profiling techniques outlined above using a tuneable laser at 1511.2nm.

Figure 4.9 shows the beam profile for the system both in terms of a contour plot indicating the spot size and an intensity plot showing the significant improvement

achievable with only one lens. In each case, the leftmost plot shows the radiation profile without any collimation, the right hand trace shows the radiation profile with collimation in the x-plane. The CCD array needs to be placed with its long axis directly parallel to the x-axis and positioned on the y-axis to bisect the point of maximum intensity. Clearly the addition of a lens in the y-plane will increase the signal detected by the CCD array further.

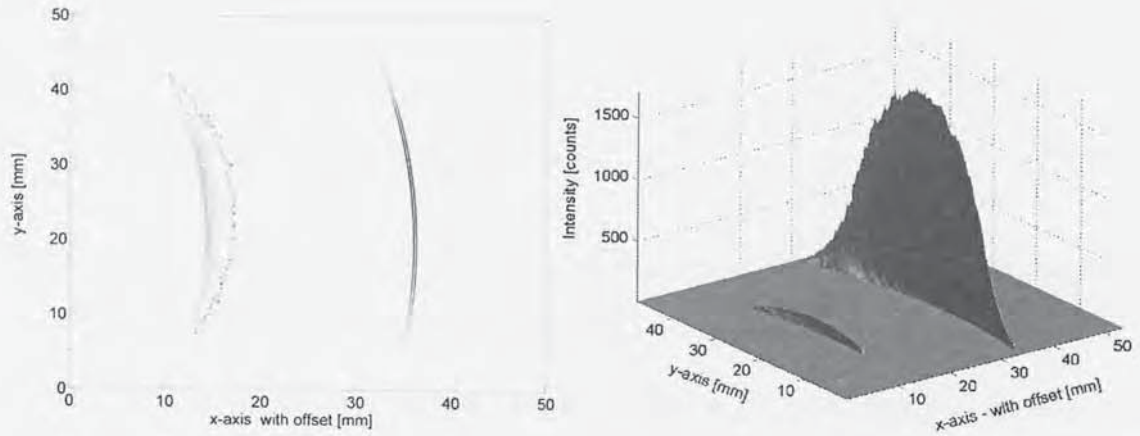

Figure 4.9 Far field images showing the increase in spatial resolution and intensity achievable with the use of only one lens in the x-plane. The leftmost peak of each plot shows the unfocused beam, whereas the rightmost peak represents the focused result. The surface plot clearly demonstrates the increase in intensity as a result of the focusing in only one plane.

4.3.4. Pre-prototype operation

4.3.4.1. Transfer function

In order to determine the function of the system, it is first necessary to calibrate it in terms of wavelength by means of a tuneable laser. This was done by connecting the BFBG input to a tuneable laser. For each discrete wavelength a distinct peak is detected by the CCD array, as indicated in Figure 4.10a. A computer program was written to control the tuneable laser and monitor the output of the CCD array.

Figure 4.10b shows the evolution of the far-field image for 1500nm to 1520nm in 2nm steps. This plot clearly shows how the diffractive operation of the BFBG and is the first indication of wavelength dependent signal to noise ratio (refer to Section 4.3.5.3) wherein

wavelengths closer to 1511.2nm appear distinctly brighter than wavelengths around 1502nm where a dip in the responsivity plot exists (refer to Figure 4.7).

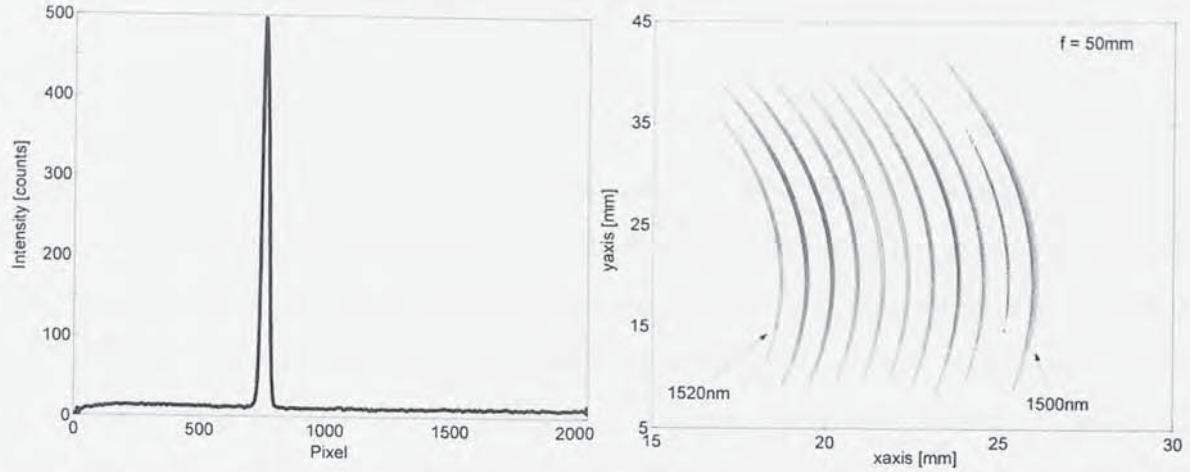

Figure 4.10 (a) (left) An example of a peak received by the CCD for the output of a tuneable laser. (b) (right) A contour plot showing the distribution of the far-field images at discrete wavelengths. Higher intensities are represented by 'brighter' colours.

In order that the system may be used as a spectrometer, it is necessary to create a transfer function, or look up table, which converts the wavelength units from 'pixels' to the more usual 'nm'. This was done by instructing the tuneable laser to scan across the working range in 5pm steps. By plotting wavelength against illuminated pixel one may quickly see that the relationship is linear, as depicted in Figure 4.11a.

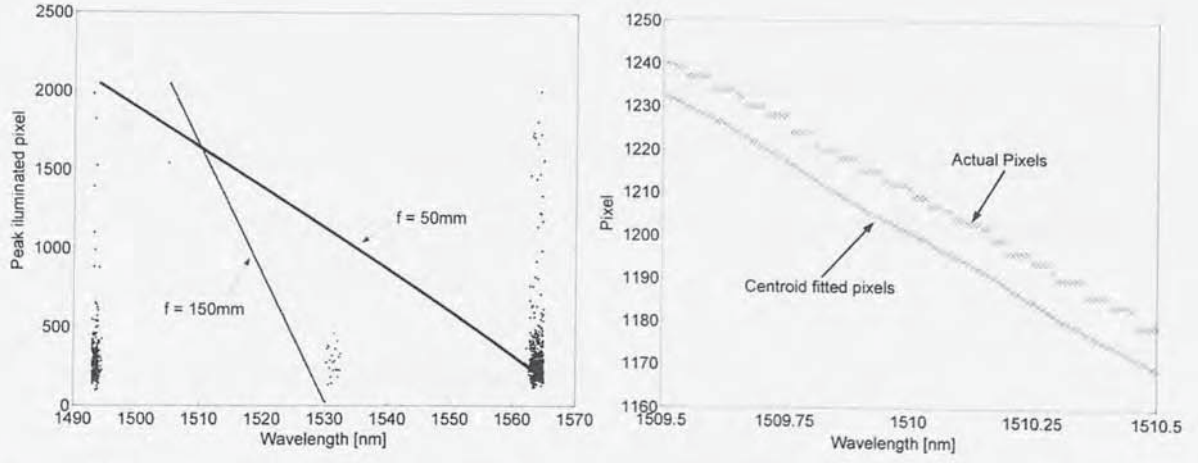

Figure 4.11 (a) (left) The system transfer function relating wavelength to illuminated pixel, shown for two systems of different focal length. (b) (right) A closer view of the difference between plotting the most intense pixel and the centroid fitted pixel values which shows the improvement to the system resolution achievable with software interpretation of the data.

In practice, it may not be necessary to convert pixels to true wavelength units; since the relationship is linear, if the system is being used to decode a WDM sensor array the conversion may be made from pixels straight to strain.

4.3.4.2. Pixilation

Figure 4.11b shows the effect of pixilation on the detected peak of the CCD array. Pixilation is a simple consequence of the finite width (14μm) of the pixels used in the CCD array and represents the minimum physical resolution of the system. This problem may be addressed in software and greatly reduced with simple techniques which significantly improve the system performance. There are many different algorithms which one may apply to a dataset in order to improve the resolution (see for example [82]) and there would be little worth in reviewing them in this thesis; suffice to say that one of the simplest approaches yields excellent results and requires only minimal computation time. The Centroid Detection Algorithm (CDA) takes an amplitude weighted mean of the data according to Equation 4.1 [158]:

Equation 4.1
$$\hat{i} = \frac{\sum_{1}^{2048} x_i . y_i \left(> y_{\min} \right)}{\sum_{1}^{2048} y}$$

where $\hat{i}$ is the centroid fitted peak value, x_i is the wavelength of the i^{th} element and $y_i \left(> y_{\min} \right)$ is the amplitude of the y^{th} element greater than the noise floor $y_{\min}$. The result of this equation may be seen in Figure 4.11b which unequivocally demonstrates the benefit of software data enhancement.

4.3.4.3. Bandwidth and resolution

Figure 4.11 shows the trade off which must be made between resolution and bandwidth, that is that the wider the bandwidth of the system, the lower the resolution will be. Ultimate system bandwidth is limited by the length of the CCD array and the bandwidth of the BFBG's radiation modes. For a CCD array of a given length and BFBG of given

spectra; the bandwidth of the system is a function of the distance from the grating to the array. The physical resolution may then be simply calculated as the bandwidth divided by the number of pixels. Note that data interpolation techniques may be used to significantly improve the resolution, as indicated in Section 4.3.4.2. For the two lenses used in Figure 4.11, the system parameters may be summarised as per Table 4.1:

Focal length mm	Bandwidth nm	Gradient nm/mm	Max Intensity counts	Physical resolution pm/pixel
50	70	2.71	3720	38
150	25	0.89	2587	12

Table 4.1 System parameter summary for two lenses of different focal length

In addition to the trade off between bandwidth and resolution, it is also necessary to consider the effect of altering the focal length of the system on the intensity of the light falling on the CCD array. In the simplest arrangements, it is only necessary to use one lens focusing the radiation modes onto the CCD array in the x-plane. Since the radiation modes diverge heavily in the y-plane due to the cylindrical geometry of the fibre core and cladding (refer to Chapter 2, Section 2.5), the beam will be significantly less intense. This is shown diagrammatically in Figure 4.12 and numerically in Table 4.1.

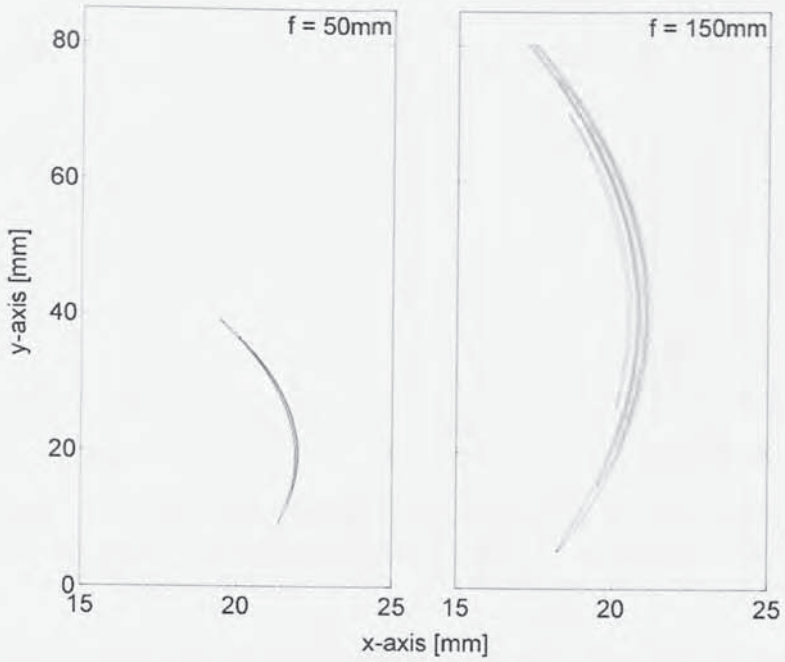

Figure 4.12 A contour plot showing the far-field images of 1511.2nm light radiated from the BFBG. This plot shows the difference in spot sizes (and therefore intensity) with different focal length lenses.

4.3.5. Sensor interrogation

In order to demonstrate the utility of the system as a sensor interrogation system, a WDM sensor array of nominally 4 elements was fabricated in SMF with Bragg resonances chosen to coincide with the peak responsivities indicated in Section 4.3.2.

4.3.5.1. Sensor interrogation using a tuneable laser

Initial experiments utilised the simplest arrangement possible with this system using only one lens in the x-plane to focus the light onto the CCD array. Since much of the light was lost due to poor focusing of the radiated beam, it was necessary to scan a powerful tuneable laser across the spectral regions associated with the WDM grating array. This yielded significantly more effective optical power than a broadband source.

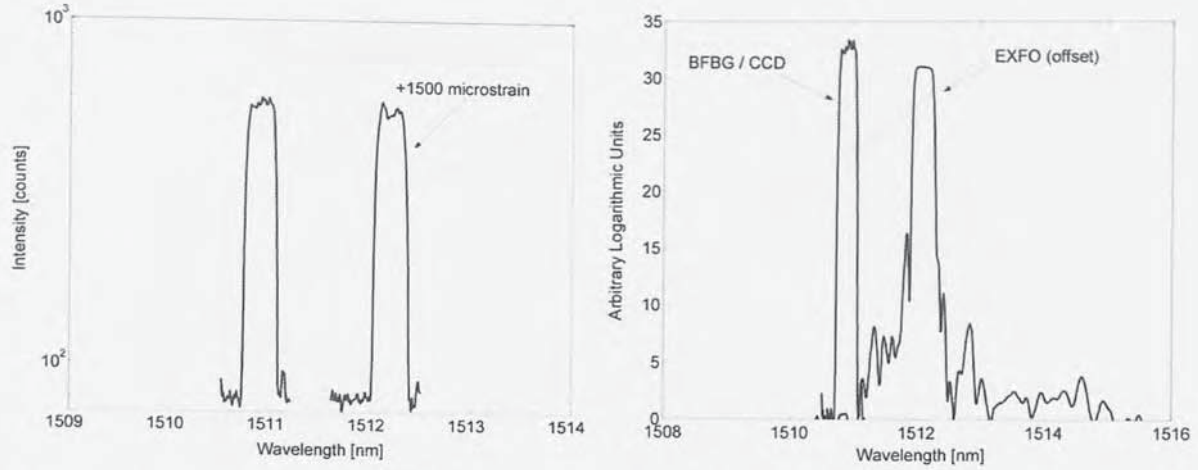

Figure 4.13 (a) (left) The plot of the spectrum detected by the BFBG/CCD spectrometer with illuminated with a tuneable laser and (b) (right) a comparison of the detected spectra from the BFBG/CCD spectrometer and a laboratory spectroscopy system.

Figure 4.13a shows the spectrum of one sensor grating in two states of stress (at rest and at 1500με). It clearly shows good representation of a reflective sensor grating. Figure 4.13b shows a comparison between the BFBG/CCD system and a spectrometer system comprising a tuneable laser, wavemeter and power meter array. The tuneable laser apparatus detects significantly more of the reflected features from the grating, but both systems show the peak of the grating to a similar extent.

By way of demonstration, Figure 4.14 shows the result of an experiment to strain a sensor grating incrementally up to 1500με.

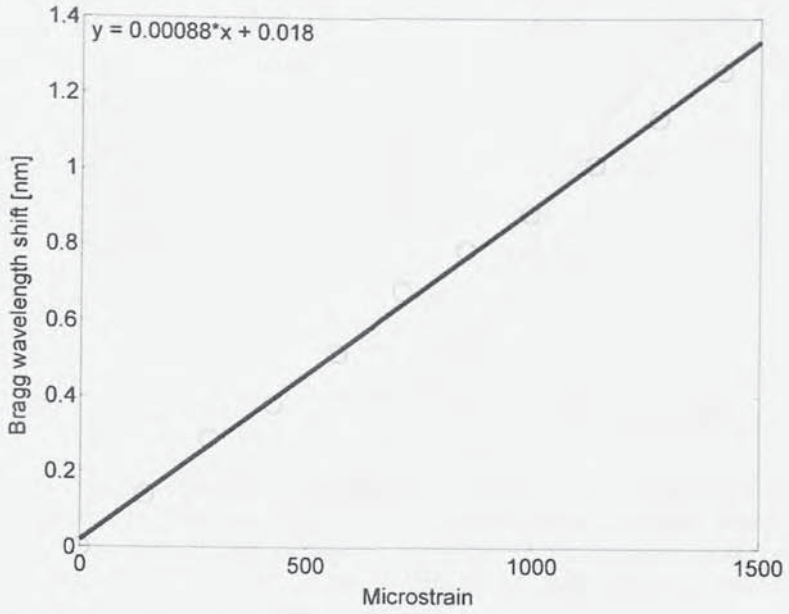

Figure 4.14 A plot showing the example data of a sensor FBG being strained and interrogated using the BFBG/CCD spectrometer.

4.3.5.2. Sensor interrogation using a broadband source

In order that the system become a practical reality, it was necessary to reduce the losses surrounding the coupling of the radiation modes from the BFBG to the CCD array. This was achieved by inserting two lenses in the y-plane as indicated in Figure 4.8, thus narrowing the radiation profiles seen in Figure 4.12 to those shown by Figure 4.15a which shows the far field image of radiation modes from a BFBG focused to a uniform 1mm diameter spot. The plot shows a series of contours representing discrete intensity levels. Clearly this has profound implications on the intensity of the radiation modes detected at the CCD array and enables the use of a broadband source to illuminate the WDM sensor array.

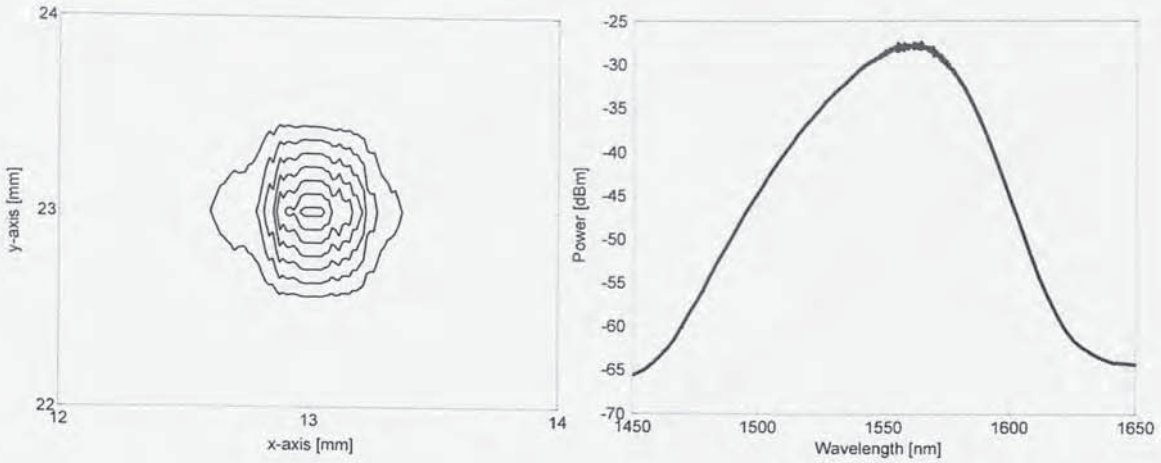

Figure 4.15 (a) (left) The far-field image of radiation modes, shown as a contour plot of discrete intensity levels, from a BFBG/CCD spectrometer system when focused in two planes. This shows the excellent collimation achievable with properly designed optics. (b) (right) The spectrum of the SLED light source used to illuminate the sensor demonstration system.

The BBS chosen for the demonstration of the system was a superluminescent light emitting diode (SLED). The output spectrum of this source is shown in Figure 4.15b. The grating array was connected to the output of an optical circulator as shown in Figure 4.5, and illuminated by the SLED operating at maximum bias current (refer to Figure 4.15b). The return port of the circulator (port 3) was connected to the BFBG, enabling the sensor spectral data to be radiated onto the CCD array and the waveform captured by software.

Sensor gratings from the array were monitored in strain and in temperature varying environments. For each discrete change of measurand, 10 readings of Bragg wavelength were calculated using the CDA, and their average plotted. Figure 4.16a shows the results for an increase in strain of up to 1400με, whilst Figure 4.16b shows the results for a temperature shift of 30°C. They show an RMS deviation from a linear trend of 3.7pm and 1.7pm respectively.

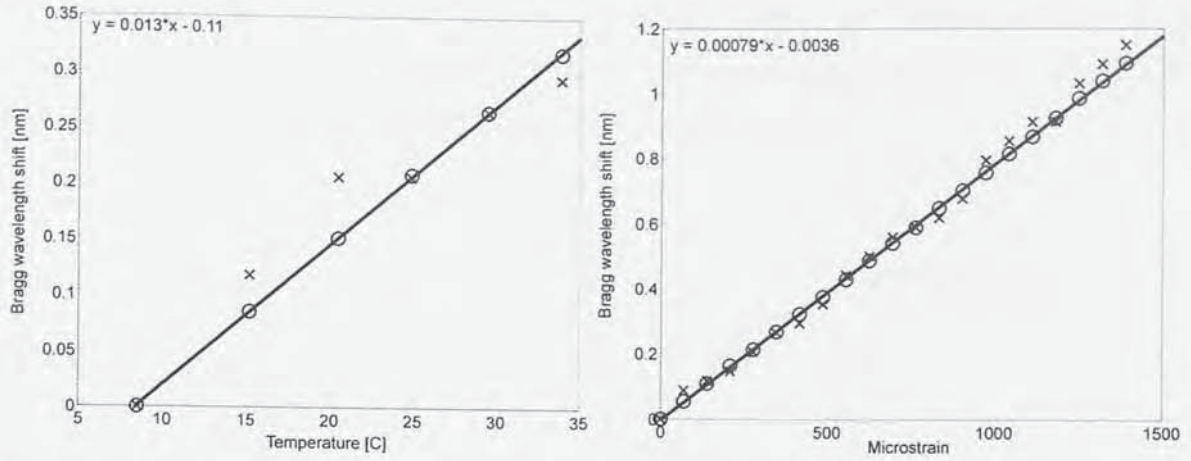

Figure 4.16 Detected strain (a) (left) and temperature (b) (right) induced wavelength shifts using the BFBG-CCD apparatus and a SLED broadband light source. This shows excellent system accuracy. The points marked with 'O' show the result of software interpretation of the physical data which is marked with 'X'.

The points marked with 'o' in Figure 4.16 represent the shift in the Bragg wavelength calculated by the Centroid Detection algorithm, whilst those marked with 'x' are the value calculated simply by looking for the point of maximum optical reflection. The difference in accuracy between the two data collection techniques is clearly demonstrated by these two datasets.

4.3.5.3. Signal-to-noise ratio

Figure 4.17a shows the spectrum of one of the sensor FBGs used to produce the results in Section 4.3.5.2 above. The signal to noise ratio was calculated from the relative intensities of the FBG peak and the maximum noise level of the system (after correction in software for dark current, as detailed in Section 4.3.2). However, the SNR of the system is a function of the integration time of the CCD array by virtue of the fact that longer shutter times result in more photons being absorbed by the array. In order that this may be demonstrated graphically, the system was set up to monitor the reflection from the sensor grating which was held at a constant temperature with a constant illumination level from the SLED light source shown in Figure 4.15b. The integration time was then steadily increased in 1ms steps. At each integration time, 20 readings of the grating were taken and their average plotted against integration time. This is shown in Figure 4.17b where the SNR is plotted on a dB scale. At approximately t=120ms, the SNR begins to

decay because the signal from the sensor grating becomes too intense and the CCD saturates. At this point the noise floor continues to rise resulting in the decay shown. This represents the maximum possible SNR for this configuration.

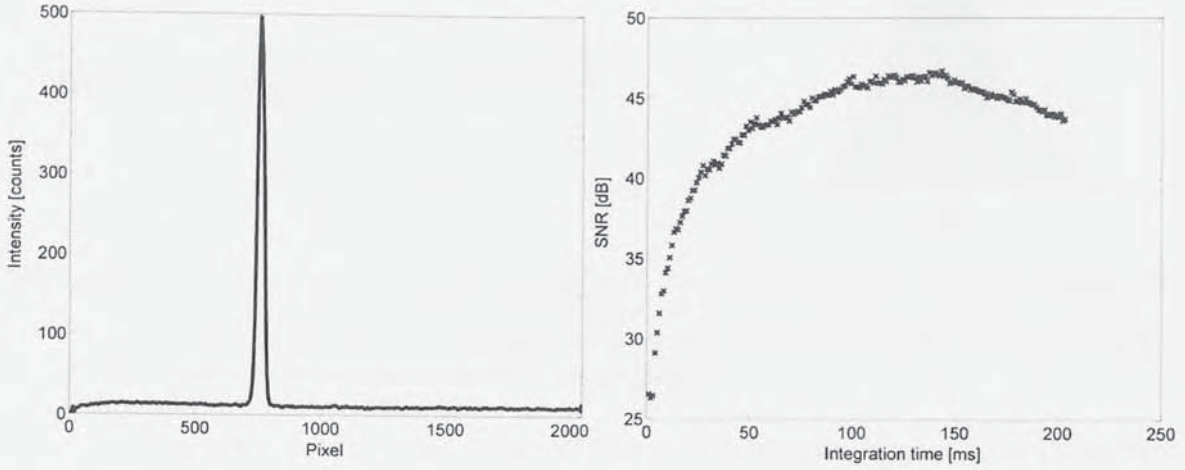

Figure 4.17 (a) (left)The CCD output spectrum when illuminated with a sensor FBG and SLED broadband source indicating the excellent signal to noise ratio. (b) (right) A plot of the signal to noise ratio measured in dB for increasing integration times showing the saturation point at ~140ms.

4.3.5.4. System drift

Drift is an extremely important factor to consider when designing a sensor interrogation system. Values which should remain constant over time but show change through system drift are a large contributing factor to overall system error. To model this, the system was used to monitor the reflected spectrum of a sensor FBG held at constant temperature for a period of 45 minutes at a sample rate of 1Hz.

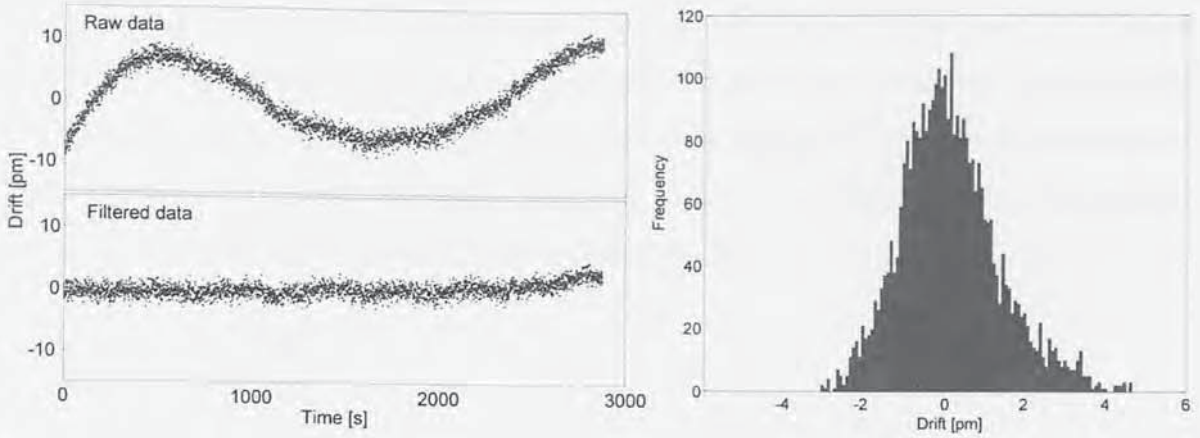

Figure 4.18 (a) (left) (upper) The drift over time of the recorded λ_{BR} value of a sensor FBG measured with the BFBG-CCD system and (lower) filtered for external temperature variations. (b) (right) A histogram showing the distribution of the recorded values of the Bragg wavelength over a 45-minute period.

Figure 4.18a shows the recorded value of Bragg wavelength against time. The large variations may be attributed to temperature changes in the Peltier controlled sensor. In order to ascertain the fluctuations in the reading made by the system, these large variations have been mathematically filtered out and are shown in the lower portion of Figure 4.18a. Figure 4.18b shows the approximately normal distribution of the data from Figure 4.18a. The RMS deviation from the mean of this histogram is a 1.2pm thus indicating that the system is inherently stable.

4.3.5.5. Polarisation sensitivity

Polarisation sensitivity affects the performance of a sensor interrogation system because random changes in polarisation state may be interpreted as a measurand change in a polarisation sensitive system. In order to ascertain the sensitivity of the system to these changes in polarisation state, a tuneable laser was used to simulate the peak formed by the reflection of light from an FBG sensor on the CCD array. This radiation was passed through a PC controlled polarisation state adjuster before reaching the BFBG-CCD system. The polarisation state adjuster was set to scan all possible permutations over a 12 second period. The peak position and amplitude was then logged every 250ms for a 20-minute period. Figure 4.19 clearly shows that although the intensity of the radiation varies according to polarisation state, its spatial position remains constant. This indicates polarisation insensitivity for sensor gratings illuminated with a broadband source since

only a snapshot is required. This may be explained by Chapter 2, Section 2.5.2. Figure 2.10 and its accompanying description show that the position of radiation modes whose wavelength is close to that of the Bragg resonance is negligibly effected by polarisation state. Figure 2.10 further shows that there is, however, a slight polarisation induced variation in the radiation efficiency at these wavelengths.

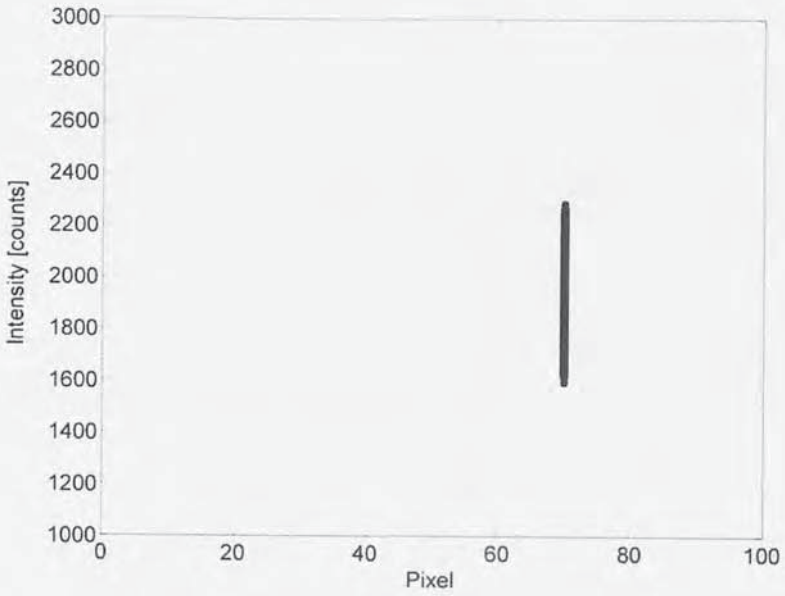

Figure 4.19 The peak position of a sensor for all possible polarisation states. This figure demonstrates the polarisation insensitivity of the BFBG-CCD detection system.

4.3.5.6. WDM channel separation

For a multiplexed system, the minimum possible spacing of sensors is an important factor because it determines the number of sensors per channel. Clearly, as signals begin to overlap, tradeoffs must be made between SNR and WDM spacing. In order to demonstrate the ultimate limit of this system in terms of WDM separation, two tuneable laser sources were used to simulate sensor FBGs with 0.5nm linewidth. One was held at a constant value whilst the second was scanned such that it crossed the first's spectral location. Figure 4.20 shows two frames from this experiment; Figure 4.20a shows the point when the two sources are separated by 100pm, whilst Figure 4.20b shows them at 50pm separation.

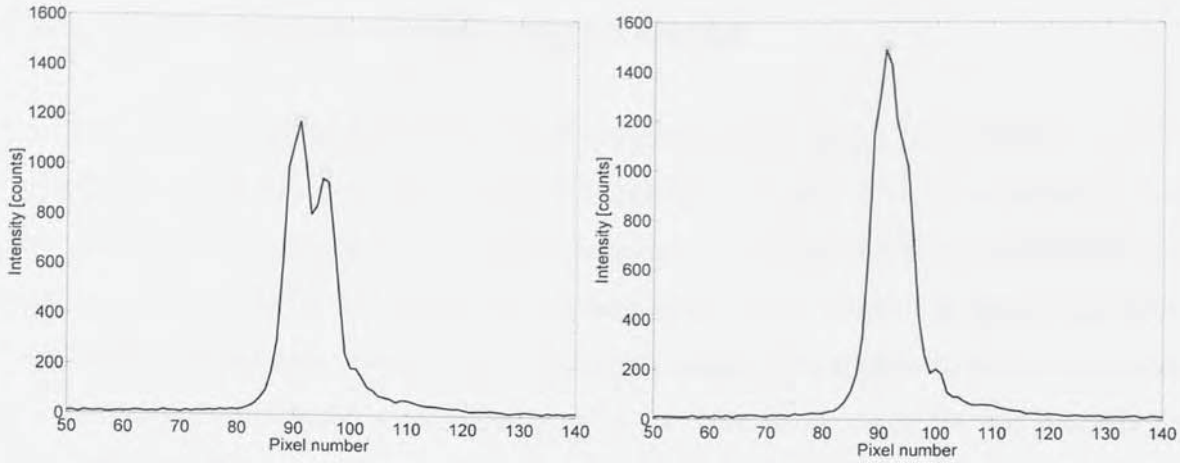

Figure 4.20 This figure shows two received sensors separated by (a) (left) 100pm (WDM separation of 100pm) and (b) (right) 50pm (WDM separation of 50pm).

Note that minimum WDM separation is dependent largely on the linewidth of the FBG and the separation of the CCD detector from the BFBG. For this instance with a linewidth of 0.5nm and f=50mm, the WDM channel separation is shown as a function of SNR in Figure 4.21.

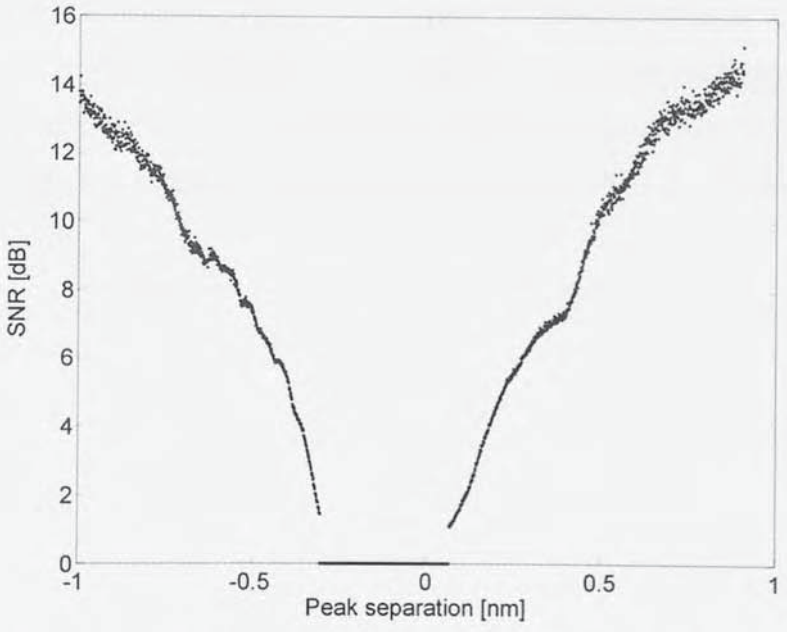

Figure 4.21 This figure shows the SNR of the system as a function of the separation of the WDM sensor channels. The central null position denotes the point wherein the channels became indistinguishable.

4.4. SUPERIMPOSED BFBG SPECTROMETER

A blazed grating couples a portion of forward propagating modes into radiation modes; the spectral width of radiation mode out-coupling is usually tens of nanometres and represents the fundamental limit to the bandwidth of a BFBG/CCD spectrometer. It is possible to use cascaded side detection systems which cover sequential spectral portions and therefore interrogate an extended wavelength range. This approach, however, results in a significantly increased system complexity and cost, since each cascade requires an entire BFBG/CCD setup.

An alternative approach is to combine the cascaded systems into a single piece of apparatus by superimposing blazed gratings upon each other.

4.4.1. Superimposed BFBG Fabrication

In this experiment, the gratings were fabricated according to the normal phasemask method wherein the phasemask is tilted in the plane of the fibre so as to introduce slanted fringes in the core at a predetermined angle. Figure 4.22a shows the transmission spectra of two separate blazed gratings with the same periods at blaze angles of 4° and 8°. It may be clearly seen that the radiation mode envelopes cover 1540 to 1570nm and 1500 to 1550nm respectively.

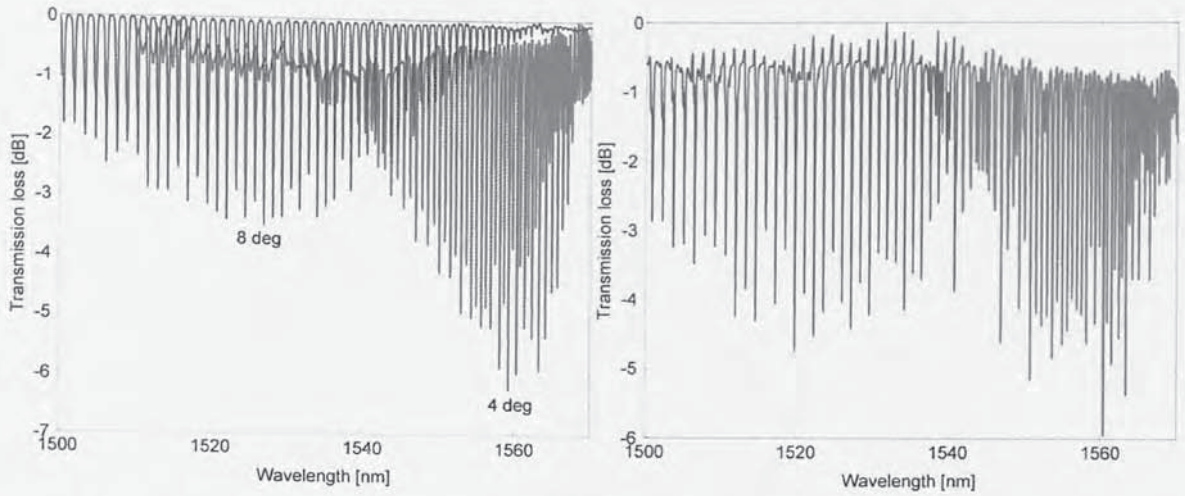

Figure 4.22 The transmission spectra of (a) (left) two individual BFBGs with tilt-angles of 4° and 8° and (b) (right) the spectrum of a superimposed BFBG comprising overlaid 4° and 8° gratings. This figure shows that the convolution of the separate gratings yields the spectrum of the superimposed grating.

The data in Figure 4.22 has been divided for clarity; the red traces denote a contribution from the 4° grating, whilst the blue traces represent the 8° grating. This convention will be carried forward for the remainder of this section.

Superimposed blazed fibre Bragg gratings (SBFBGs) may be fabricated by overlaying gratings with different tilt angles at the same location within the fibre. Figure 4.22b shows the transmission spectrum of a SBFBG consisting of 4° and 8° gratings. The shorter wavelength portion of the spectrum is contributed mainly by the 8° grating and presents a broader, shallower profile with more sparse cladding resonant peaks than the longer wavelength portion which results from the 4° grating. It is clear from Figure 4.22a and Figure 4.22b, that superpositioning the two spectra of the former, one may produce the latter. This technique gives an extended radiation mode spectral bandwidth greater 70nm.

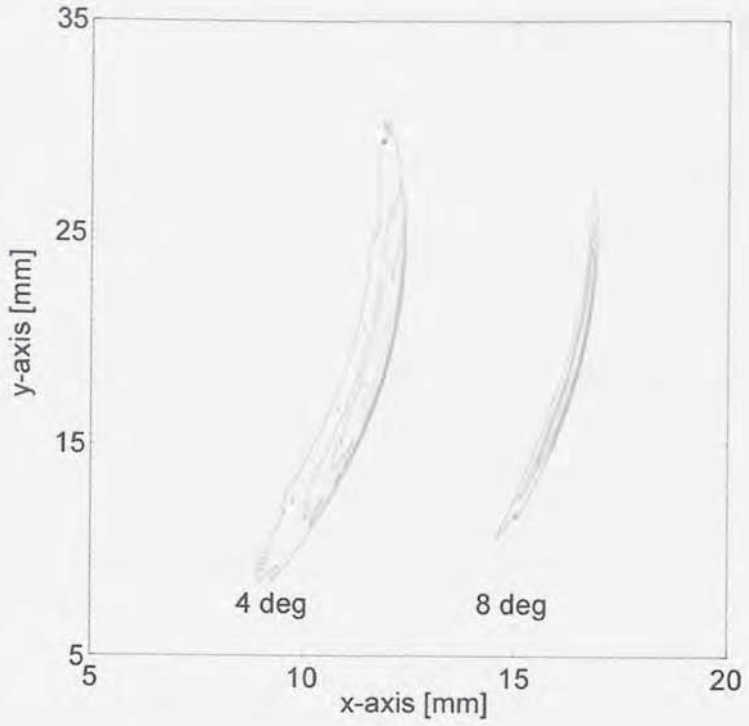

Figure 4.23 The far-field image of the SBFBG system when illuminated with 1546.6nm radiation from a tuneable laser. The two radiation modes are a result of light being radiated at slightly different angles by the constituent gratins in the SBFBG.

There is an obvious region in Figure 4.22 where the spectra from the constituent gratings overlap, this is from approximately 1540nm to 1550nm. In order to better demonstrate this overlap and highlight the significance of the effect of superimposing BFBGs, Figure 4.23 shows the far-filed image of the SBFBG when illuminated with radiation from a tuneable laser at 1546.6nm (chosen to coincide with a peak in the responsivity of the CCD array shown in Figure 4.7 which is within the overlap region of the SBFBG). Although the gratings are superimposed within the same core and illuminated with the same source, they radiate the light at differing angles because they posses different blaze angles. This approach may find uses in a great many applications, such as complex beam splitters for telecom applications.

4.4.2. Radiation mode characterisation of SBFBGs

Before using the SBFBG-CCD spectrometer system to interrogate a sensor array, it was first necessary to calibrate the system so as to produce a transfer function describing the system response to applied wavelength. This was implemented by scanning a tuneable

laser through the working range of the device and a spectral-to-spatial conversion was obtained.

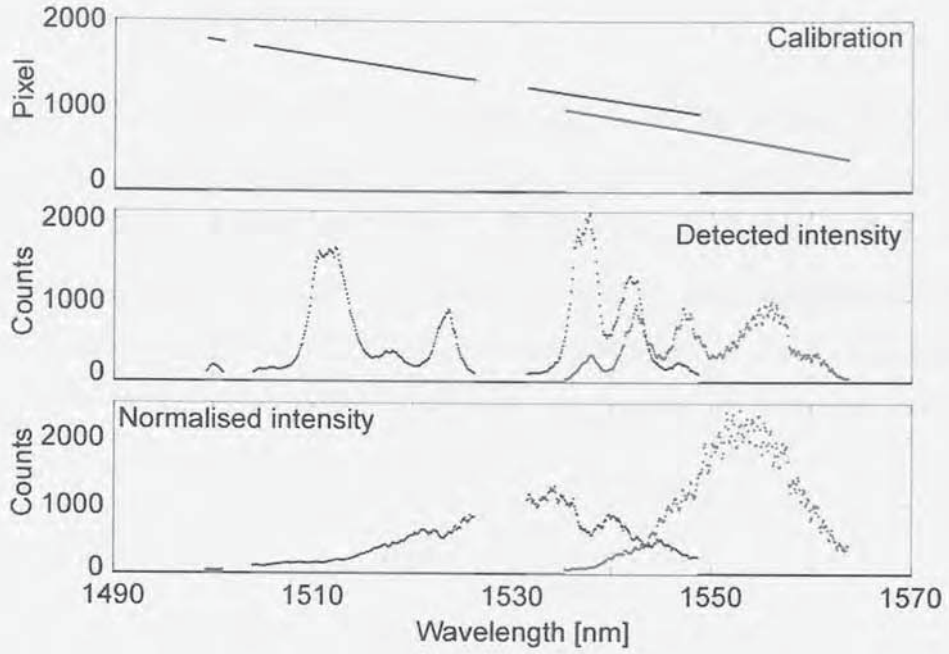

Figure 4.24 A plot of the system calibration data for a SBFBG spectrometer system, showing the wavelength to pixel transfer functions, the detected intensity and the detected intensity normalised for the responsivity of the CCD array. The red traces denote contributions from the 4° grating, whereas the blue traces originate from the 8° grating. This figure shows that the SBFBG may be used to radiate light over an extended bandwidth compared to a conventional BFBG system.

The uppermost plot of Figure 4.24 shows the now familiar transfer function for the system which is used to convert data from units of 'pixel' to more usual 'nm' or 'με'. Note the overlap from the 2 contributing gratings in the 1540nm to 1550nm region; whilst both gratings radiate the same wavelength at this point, they do so at different spatial locations on the CCD. This is the consequence of the superimposed gratings having different blaze angles, as highlighted by Figure 4.23 and explained by Equation 2.19. The central plot of Figure 4.24 shows the detected intensity as a function of wavelength and is difficult to interpret due to the highly non-linear nature of the CCD array, as discussed in Section 4.3.2. This has been clarified in the lower plot which shows the result of normalising the data in accordance with Figure 4.7. One may now see the contributions from the two gratings extremely clearly and recognise the shape of the

radiation intensity profile as an approximate inversion of the spectrum of the SBFBG shown in Figure 4.22b.

4.4.3. Interrogation of sensors

The SBFBG-CCD system was used to interrogate a WDM sensor array consisting nominally of two Bragg gratings, G1 and G2, as shown in figure 2. Their wavelengths (1510nm and 1560nm) were chosen to fall in the first and second spectral portion of the SBFBG. G1 was used to sense strain whilst G2 monitor temperature fluctuations. Due to the relatively weak strength of this SBFBG, it was necessary to use a scanning tuneable laser to simulate a very high power broadband light source, as described previously in Section 4.3.5.1.

Figure 4.25 An example of one of the sensor gratings interrogated using the SBFBG system. The figure shows the grating at rest and strained.

Figure 4.25 shows the measured reflection spectra of sensor G1 at two levels of applied strain. Figure 4.26a shows the wavelength shift of G1 versus applied strain from 0 to 160με. Similarly, Figure 4.26b shows temperature-induced shifts in the Bragg wavelength of G2. From the SBFBG-CCD detection system, we obtained linear strain and temperature responses of 8.87pm/με and 9.4pm/°C with RMS deviations of 5.2pm and 14pm, respectively.

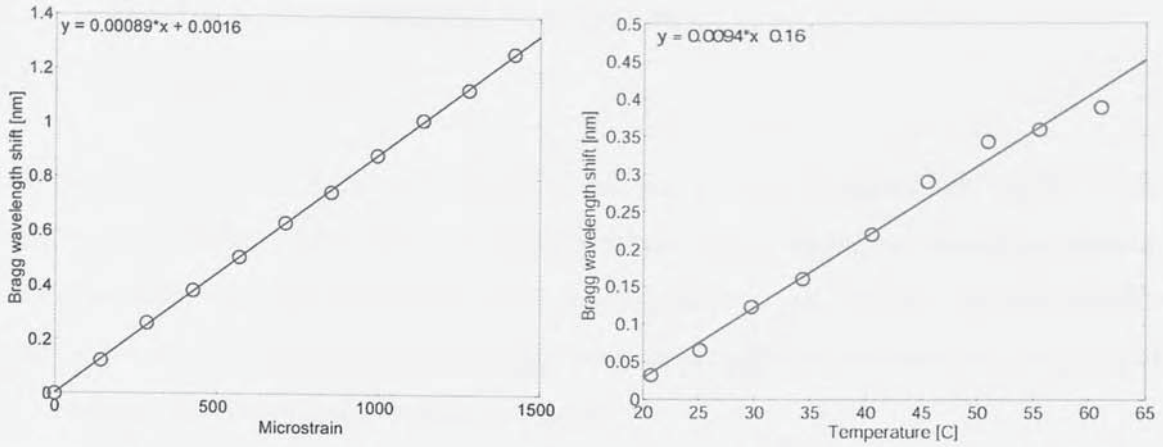

Figure 4.26 The strain coefficient of sensor G1 (a) (left) and the temperature coefficient of sensor G2 (b) (right) as measured by the SBFBG spectrometer system.

This experiment represents the first report that SBFBGs may be used to radiate light from the side of an optical fibre and that they can significantly increase the dynamic range of a BFBG spectrometer system. The distinct advantage of enhanced dynamic range from a low-cost single-device will enhance the functionality and commerciality of BFBG-CCD side detection systems, and is applicable to all variants of such systems.

4.5. BFBG SPECTROMETER PROTOTYPE

4.5.1. Prototype design

The next stage in the development of the blazed grating spectrometer was to built a demonstrator prototype that was sufficiently robust that it might be more than simply a laboratory curiosity. The overriding problem with the practical solution was that the fibre must be immersed in index matching gel to remove air-cladding resonances and to permit the coupling of core modes to radiation modes.

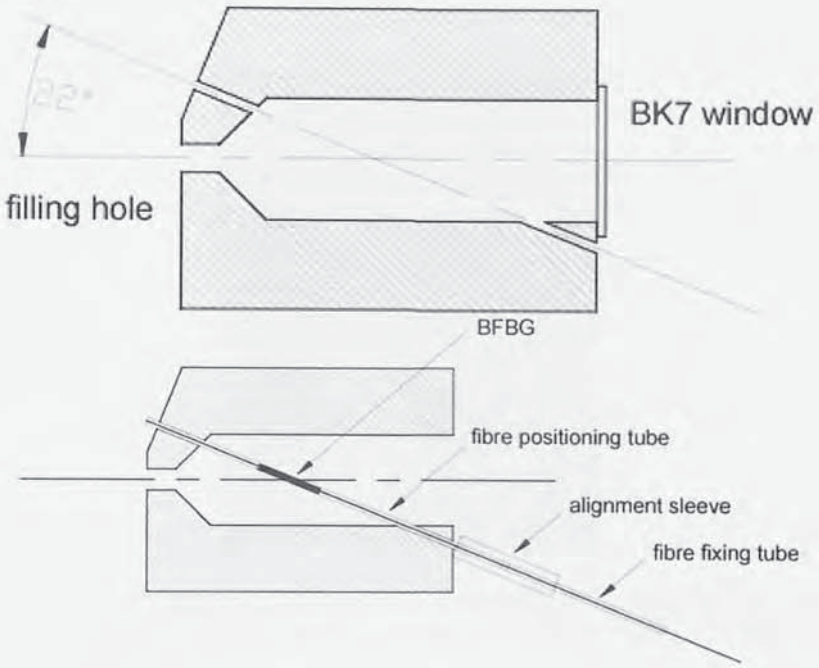

Figure 4.27 (a) (upper) The design of the grating housing which contains the index matching gel and (b) (lower) the fibre adjustment arrangement for rotating the fibre within the gel-filled housing enabling the system to be aligned.

This was achieved by the fabrication of a customised housing, shown in Figure 4.27a. A 1mm O/D, 250μm I/D capillary tube was sealed into the main chamber at an angle of 22° in accordance with Equation 2.19, through which the fibre could be threaded. A BK7 glass window was then fixed to the end of the block with a large (13mm) aperture, through which the radiation modes would pass approximately normal to the window. The device was then inverted and filled with index matching gel via the small (3mm) diameter filling hole. Following 48 hours at 80°C during which time the index matching gel was able to de-gas the filling hole was sealed with epoxy resin. It was necessary to make

provision for the fibre to be rotated within the alignment capillary tube so that the direction of radiation from the BFBG could be accurately adjusted. This was achieved by using an alignment tube with 1mm I/D which was permanently fixed to the capillary tube as indicated in Figure 4.27b. The fibre was then glued into another section of 1mm I/D capillary tubing and threaded through the gel filled capillary. Course rotational control was permitted by rotating the tube in which the fibre was fixed, and then using removable adhesive tape to fix the position. The finished alignment system is pictured in Figure 4.28 which shows the properly aligned BFBG radiating a 633nm light source through the BK7 window.

Figure 4.28 The index matching gel filled alignment device, shown with a properly aligned BFBG illuminated with 633nm He-Ne radiation which is visible at the grating location. Photo: David Birkin.

The focusing optics for the system were designed to be as simple and compact as possible. This was achieved with 'of-the-shelf' BK7 optics using a single 70mm focal length lens in the x-plane and two 50mm focal length lenses back-to-back in the y-plane. The x-plane optics are shown in Figure 4.29 and the y-plane optics are show in Figure 4.30. The lens mounts, CCD mount and base were designed to be highly adjustable to allow for alignment necessary as a result of grating imperfections.

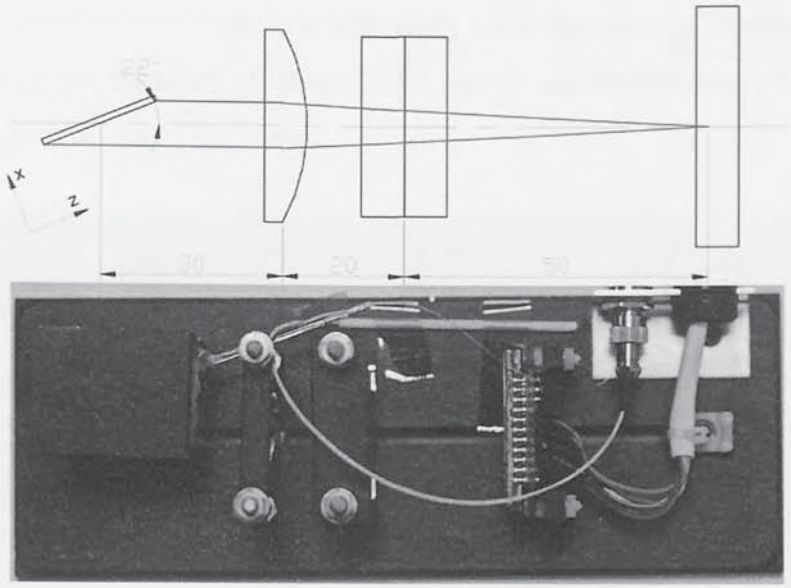

Figure 4.29 (a) (upper) A schematic showing the placement of the x-plane focusing optics and (b) (lower) a picture showing the manufactured prototype in the x-z orientation. Photo: David Birkin.

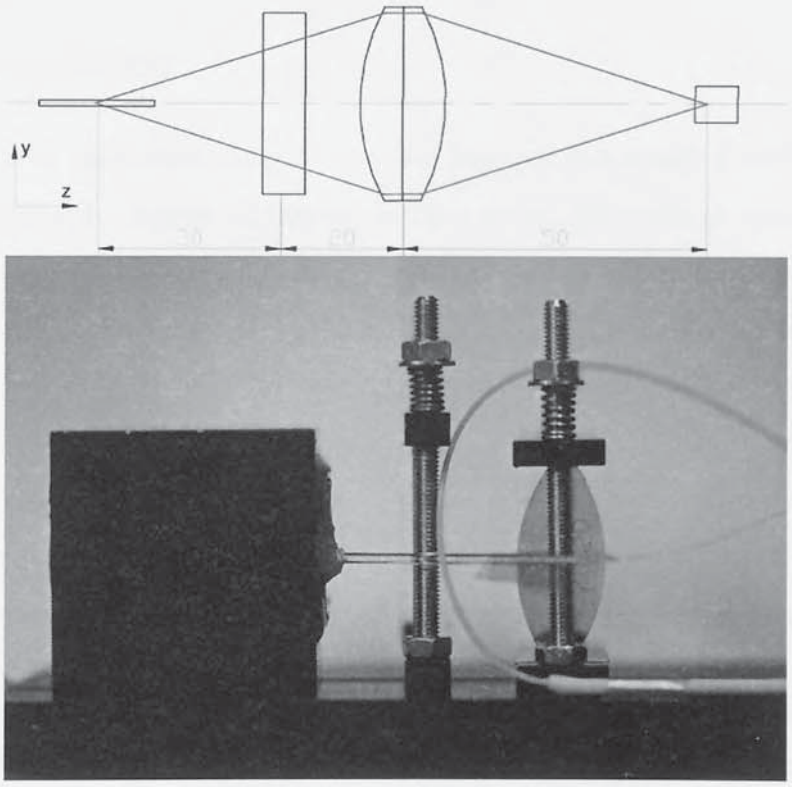

Figure 4.30 (a) (upper) A schematic showing the placement of the y-plane focusing optics and (b) (lower) a picture showing the manufactured prototype in the y-z orientation. Photo: David Birkin.

The final prototype is shown next to a laboratory OSA for scale in Figure 4.31a with the light shielding cover removed. Figure 4.31b shows the positioning of the alignment device, focusing optics and CCD array.

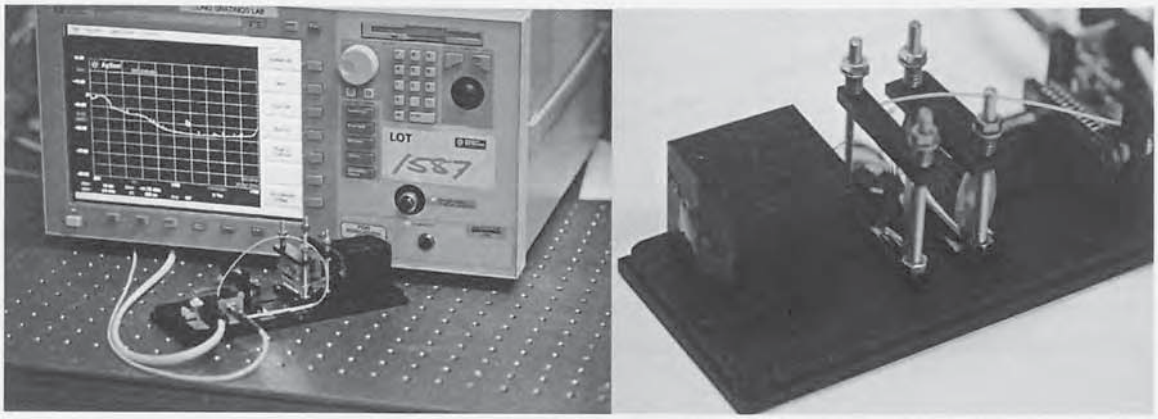

Figure 4.31 The finished prototype shown (a) (left) next to a laboratory spectrum analyser for scale and (b) (right) in detail indicating the position of all components. Photo: David Birkin.

4.5.2. Prototype testing

The prototype was calibrated using a tuneable laser as previously described. The laser was scanned across the region of interest in 5pm steps. 20 readings were taken at each discrete wavelength and the average plotted against wavelength in terms of peak position (Figure 4.32a) and peak intensity (Figure 4.32b). Figure 4.32a shows the transfer function of the system and may be used to determine the wavelength of an incident signal or sensor grating. There is a slight non-linearity evident in this transfer function which is attributed to a slight rotation of the x-pane optics causing non-uniform diffraction as a function of wavelength. The transfer function shows a spectral bandwidth of 64.5nm and an average physical pixilation (without software interpretation of the data) of 44pm per pixel.

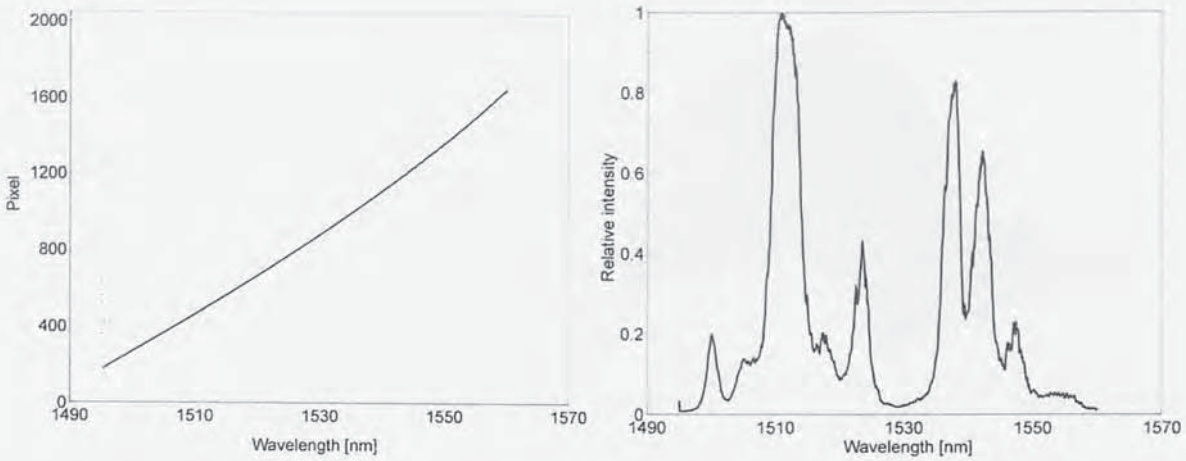

Figure 4.32 (a) (left) The transfer function of the system measured with a tuneable laser and (b) (right) the intensity calibration of the system which corresponds to the responsivity of the CCD array shown in Figure 4.7.

In order to calculate the SNR of the system it is necessary to consider the two interdependent variables in conjunction with the signal strength; the integration time of the CCD array and the wavelength of the reflected signal. This data is shown below in Figure 4.33. Figure 4.33a shows the SNR of the system with a simulated sensor FBG signal (the output of a tuneable laser) for an integration time of 1ms and an input power of -5dBm. The peak in the SNR corresponds to the 1537.2nm responsivity peak of Figure 4.7. Figure 4.33b shows a similar plot, but in 3 dimensions. The plot shows the SNR of a simulated senor from 1530nm to 1545nm, with integration times from 1ms to 150ms and an input power of -15dBm. There is now a steady decrease in the SNR at 1537.2nm with increasing integration time. This is a result of a slight side-lobe in the signal received by the CCD which quickly increases in amplitude as the integration time increases. Since the main signal is sufficiently strong to saturate the CCD at this wavelength, the signal does not keep ahead of the noise and the result is a severe degradation in the SNR. Dynamic control of the integration time is therefore a desirable extra for this system and is easily achievable in software. The offending side-lobe is likely to be a consequence of a poor quality BFBG, an air bubble in the index matching gel enclosure, poor system alignment or all three.

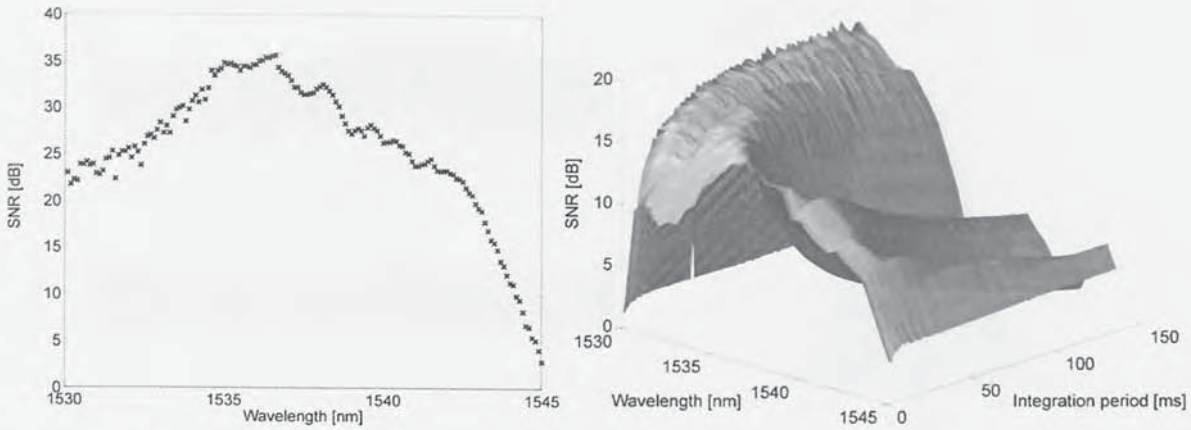

Figure 4.33 (a) (left) The signal to noise ratio against wavelength for a -5dBm source and (b) (right) the SNR surface plotted in three dimensions for wavelength and integration period for a -15dBm source.

The system drift was calculated in a similar way to that shown in Section 4.3.5.4. A tuneable laser was allowed to warm up and held at a constant wavelength of 1537.2nm. The peak was then detected in software using the CDA and a value recorded against time at a frequency of 10Hz. Figure 4.34a shows the result of this in terms of the direct measurement of wavelength (upper) and calibrated into 'pm' (lower). The lower plot also shows the drift with the sinusoidal variation, which may be attributed to instabilities within the tuneable laser, removed. The distribution histogram of the data shown in Figure 4.34b shows a typically normal distribution and yields a FWHM drift value well within ± 0.35pm. This represents a significant improvement in the stability, compared with the pre-prototype, and shows this design to be intrinsically stable.

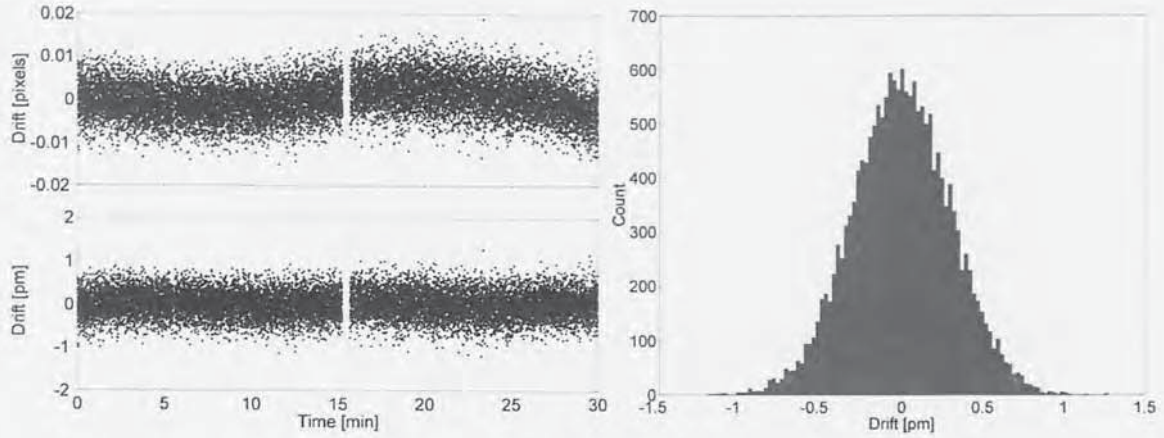

Figure 4.34 (a) (left) The system drift against time shown as measured in terms of pixels (upper) and converted to wavelength (lower) where the sinusoidal variations have been filtered out showing the true drift of the system. (b) (right) The distribution of the drift, clearly indicating a normal distribution.

4.5.3. Prototype demonstration with a commercial sensing system

Indigo Photonics recently unveiled their FSI – or Fibre Sensor Interrogator – which is a TDM based optical sensor interrogation system utilising synchronous detection techniques first deployed in radar systems, implemented in this instance using semiconductor optical amplifiers as switches [159] (the system is now marketed by Insensys LTD). The system will surely enjoy commercial success since it offers up to 16 channels at 100 sensors per channel with better than 1με resolution. The spectral interrogation in this system is performed (usually) by means of an edge filter. Unlike edge filter arrangements, the BFBG/CCD approach is not affected by increases in the broadband noise of the system and was thus deemed better able to cope with fluctuations created by the SOAs. To this end, it was decided to make a customised version of the FSI which used a BFBG/CCD array spectrometer.

The FSI was connected to an array of nominally 4 sensor gratings at the same wavelength separated by 2 meters of SMF fibre. The spectral output of the FSI was then connected to the BFBG/CCD array spectrometer. The output from the FSI is a stream of short pulses which are reflected from the grating selected by the FSI software interface. It is possible to select and interrogate each grating in turn via this software interface.

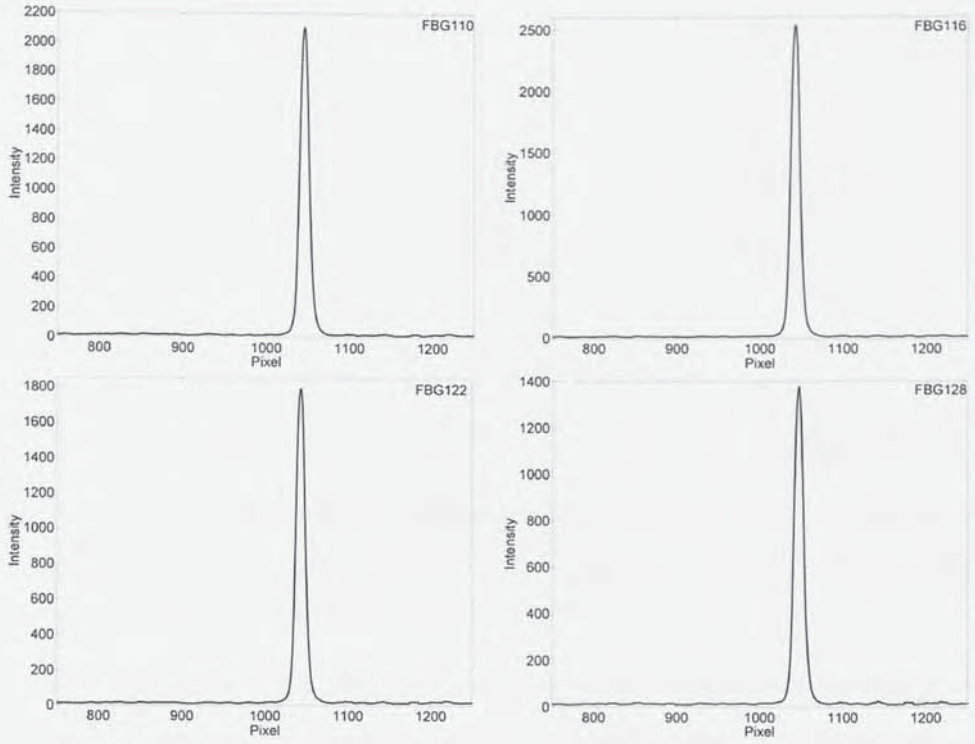

Figure 4.35 Examples of the spectra reflected from the Indigo Photonics FSI TDM system, as detected by a BFBG/CCD. Each plot shows a different sensor FBG in a relaxed condition.

Figure 4.35 shows the spectra of the gratings in the array and indicates a set of extremely clear sensor spectra. In order that the BFBG/CCD apparatus might be used to determine temperature, the system was calibrated by placing the sensor gratings in a computer controlled Peltier oven and saving 20 discrete wavelength values (measured in 'pixels') for each temperature. This is shown in Figure 4.36a and shows a good linear result. The interrogation system was then demonstrated by recording the temperature of a liquid as it cooled in air. This result is shown in Figure 4.36b.

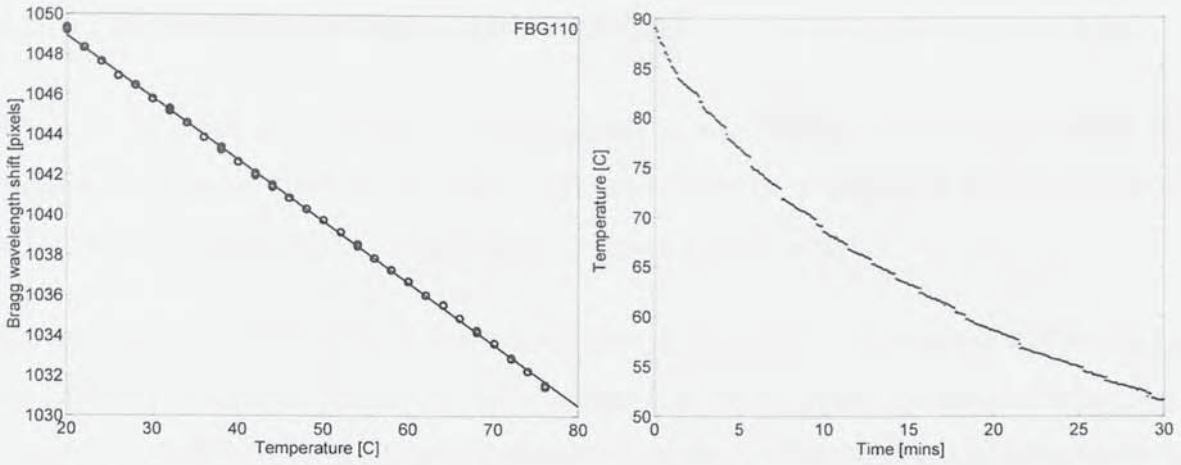

Figure 4.36 (a) (left) The temperature calibration plot of sensor FBG110 and (b) (right) an example of the system sensing a cooling cup of coffee with milk and two sugars. These plots indicate the success of the system when used in conjunction with the current state of the art WDM sensor decoder.

Although fairly straightforward, this is an extremely important result for this project since it shows that it is not only a practical reality, but that it has significant advantages in terms of technical operation and potential manufacture cost over an aspect of the current state of the art sensor interrogation system. An edge filter will give an inaccurate reading if there is an increase in background noise since this will increase the radiation falling on the detector. The BFBG/CCD spectrometer system is not affected by this since it measures wavelength directly rather than by making an intensity-dependent calculation.

4.6. IN-FIBRE POLARISER USING A BFBG

Reyes *et al* [160] showed that it was possible to use BFBGs as PDL controllers by twisting the grating structure. In-fibre polarimeters have been described by Westbrook *et al* [161] and Peupelmann *et al* [162] using complex grating arrays.

In this experiment, 45° BFBGs were fabricated in Ge-doped photosensitive fibre using the scanning phasemask technique and a 244nm CW laser source. To ensure the spectral response of the BFBGs with large tilt angles fell in the 1.55μm region, a phasemask with a large period (1800nm) was commissioned. The phasemask was rotated by 33.3° so as to induce slanted fringes at 45° within the fibre core in accordance with Equation 2.23:

Equation 2.23

$$\xi = \frac{\pi}{2} - \tan^{-1}\left[\frac{1}{n\tan(\xi_{PM})}\right]$$

The 45° slanted fringes were verified by examination with an oil immersion, high magnification microscope. As shown below in Figure 4.37, the internal fringe angle was 46.1°.

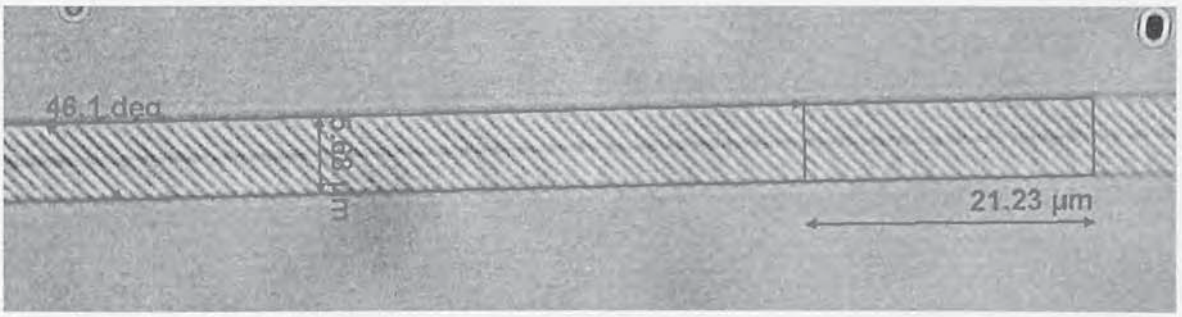

Figure 4.37 The fringes of a 45° blazed grating observed with an oil immersion microscope using a 100x objective.

The bespoke phasemask used in the experiment had a phase relief pattern of a modest 3×10mm which resulted in a maximum grating length of only 4.6mm when rotated to 33.3°. Because this resulted in low efficiency of cladding and radiation mode coupling, several grating sections were concatenate so as to produce a second grating of effective length 40mm. It should be noted that Battiato and Kostuk successfully inscribed 45°

gratings using a prism based holographic inscription technique [163] but were still only able to achieve a reported maximum grating length of 4mm.

Two characterization systems, as illustrated in Figure 4.38, were used to measure the polarisation property of the 45°-tilted FBGs. The first system was designed to measure the maximum and minimum polarisation dependent loss (PDL) and consisted of a broadband source, a fibre polariser and polarisation controller, and an optical spectrum analyzer. The second system was used to investigate the entire PDL response of the gratings (for different polarisation directions). In this system, a tuneable laser and a power meter were used in conjunction with a polarisation controller and a polarisation beam splitter with PM fibre pigtails and a fibre rotator.

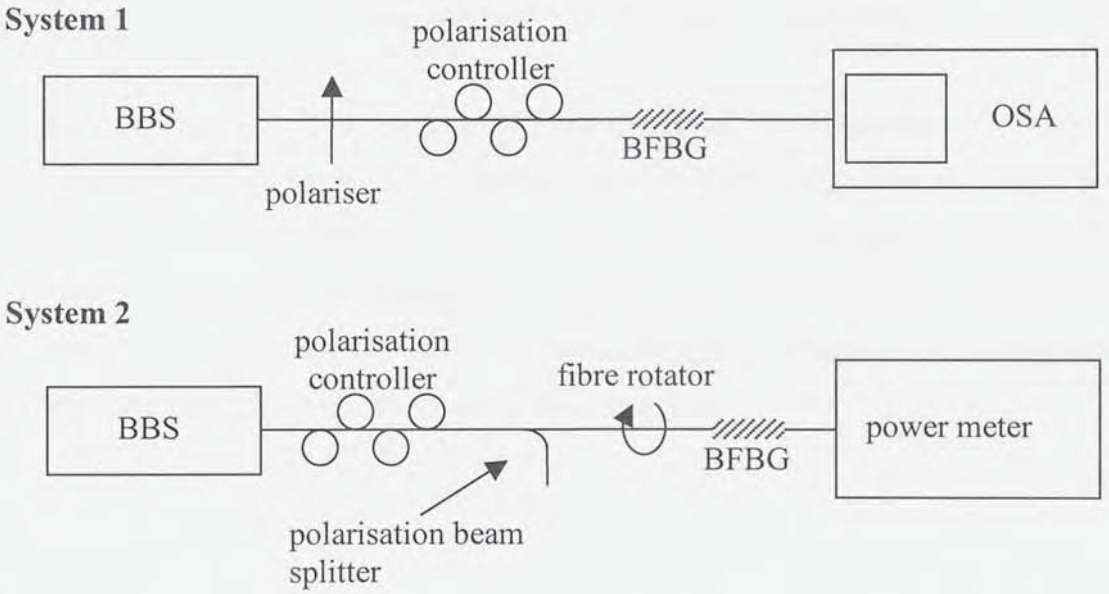

Figure 4.38 The two different experimental setups used to characterize the polarisation characteristics of the 45° BFBG.

By way of comparison, the normalized maximum PDL of both gratings were measured using system 1 of Figure 4.38 and are shown in Figure 4.39 below. The PDL of 4.6mm grating is only approximately 3dB compared with more than 28dB in the 40mm case.

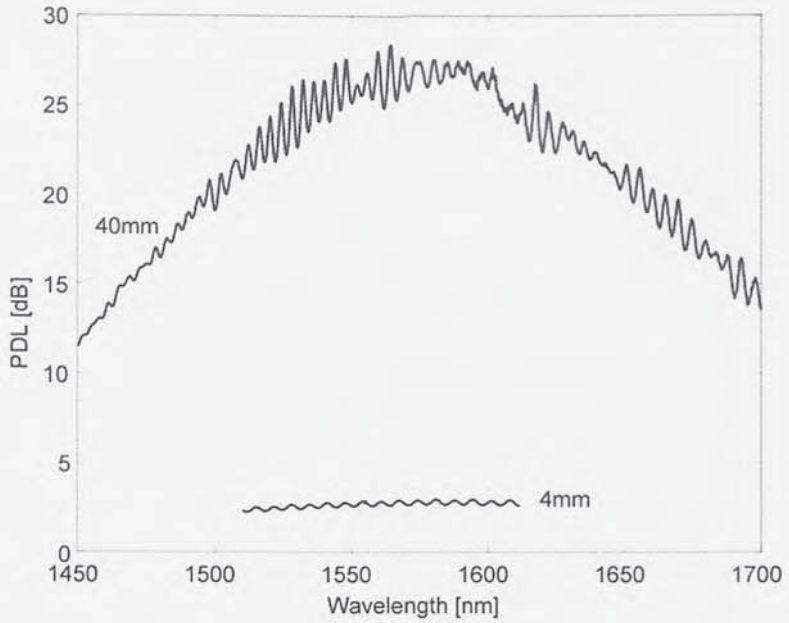

Figure 4.39 The PDL of the 4.6mm and the 40mm 45° BFBGs measured using system 1 shown in Figure 4.38

The full PDL response of the 4cm-BFBG was characterized with system 2 using linearly polarised light from 0° to 360°, generated by rotating the PM pigtail on the output port of the polarisation beam splitter, as shown in Figure 4.38. The transmission from the BFBG was measured as a function of the polarisation direction of the light, the results of which are plotted in Figure 4.40. The results show two expected maxima separated by 180° (at 140° and 320°) and minima orthogonal to these maxima.

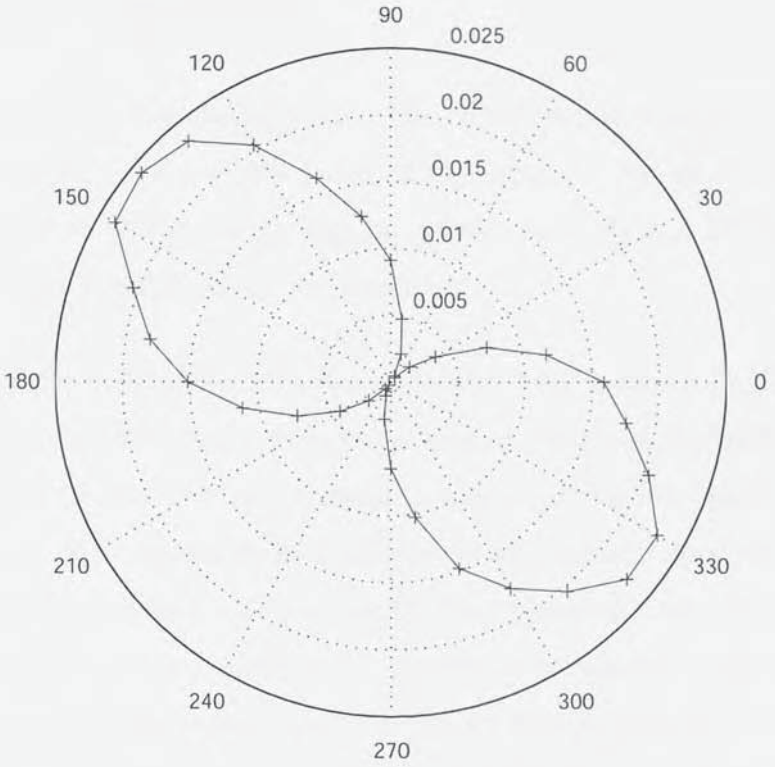

Figure 4.40 The PDL measurement of the 40mm grating over 360° of polarisation states. This was measured using system 2 of Figure 4.38

The polarising capability of the 40mm grating as polariser was also evaluated. Radiation at 1.55μm from a tuneable laser was first depolarised using a polarisation scrambler; the measured degree of polarisation was measured using a Newport polarisation analyser as 1.2%. The grating was then placed in the optical circuit before the analyser and the degree of polarisation was measured as 99.51%.

4.7. CHAPTER CONCLUSIONS

The work described by this chapter shows the novel implementation of several blazed grating based devices. The primary result of the work is that an extremely low cost spectrometer has been shown which may be quickly built using a BFBG, a CCD array and a few commonly available optical components.

This work shows the progression of a design intended for practical implementation, and the results correspond accordingly; the system was shown to be extremely accurate with an FWHM drift of <0.5pm over an extended time period. The final prototype, whilst not claiming to be a direct alternative to a laboratory style optical spectrum analyser, was clearly much smaller than such a device and far less expensive. More importantly though, the final system is rugged and with proper development will be capable of implementation in harsh environments. It was shown that an example WDM sensor array could be interrogated by the system using a broadband source, or a pulsed commercial system. These results indicate the successful design of an optical fibre sensor interrogation system.

It has been shown that a significant increase the bandwidth of a BFBG system may be achieved using superimposed BFBGs. This novel experiment superimposed 4- and 8-degree gratings and showed that the system functioned as expected yielding distinct radiation profiles associated with each grating. Figure 4.22 shows that the spectrum of a SBFBG corresponds to the convolution of its two constituent grating profiles and Figure 4.24 further shows that the optical power radiated by the device very accurately matches the loss profiles of Figure 4.22. This result indicates superb predictability of a system using superimposed blazed gratings.

Chapter 5

Type IA Fibre Bragg Gratings, Fabrication and Applications

5. TYPE IA FIBRE BRAGG GRATINGS, FABRICATION AND APPLICATIONS

5.1. PREAMBLE

This chapter comprehensively documents fabrication methods and applications of type IA gratings. The unique growth characteristics of type IA gratings are discussed at length and a novel fabrication method for regenerated gratings is introduced, explained and proven. The necessity for exposure uniformity is shown and experimental evidence is used to support a theoretical model of the mean index profile of type IA gratings. The chapter concludes with a detailed description of the fabrication of a self-referencing fibre sensor head which may be inscribed in a single fibre.

5.2. THE DISTINCTIVE GROWTH PROFILE OF THE TYPE IA FBG

The spectral characteristics of type IA gratings are unique; they are distinct from other grating types because they exhibit a large increase in the mean index of the core that is readily identifiable as a large red shift seen in the Bragg wavelength of the grating during inscription. This red shift is dependent on fibre type and hydrogenation conditions, but for a highly doped fibre is typically in the order of 15-20nm, and for SMF28 is 5-8nm.

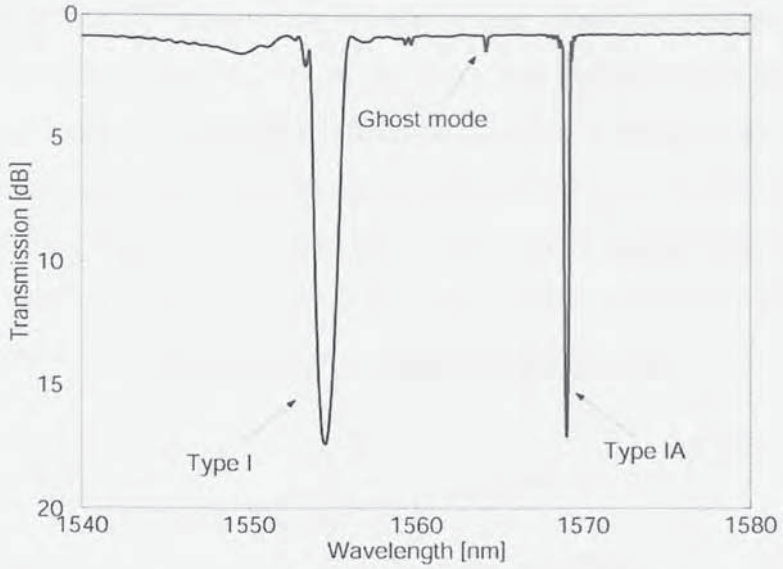

Figure 5.1 The spectrum of a standard grating (left) and a longer type IA grating (right) written in the same fibre with the same phasemask. The difference in wavelength is caused by the large increase in mean refractive index caused by type IA grating growth. This also accounts for the ghost mode as the mean index change is sufficient to cause the fibre to become multi-mode.

Figure 5.1 (above) shows the spectrum of a 4mm regenerated IA grating (right) and a 1mm standard type I grating (left). These gratings have been written in the same fibre with the same phasemask, yet their central reflecting peaks are 14.5nm apart after annealing. The large increase in mean refractive index caused by prolonged UV exposure has additionally increased the NA of the fibre to such an extent that it has become multi-mode. It is well known that for single mode fibres, the V-parameter must be ≤ 2.405. In the example above, the NA of the virgin fibre is 0.161 whereas the NA of the IA modified fibre is 0.247 (refer to Section 6.3.1). Using Equation 2.13, we may calculate the V-parameter as follows:

$$\left(\frac{2\pi}{1560\times10^{-9}}\right)\left(3.7\times10^{-6}\right)\left(0.161\right)=2.399$$

for the untreated fibre case, and:

$$\left(\frac{2\pi}{1560\times10^{-9}}\right)\left(3.7\times10^{-6}\right)\left(0.247\right)=3.681$$

for the IA treated case. This accounts for the second Bragg resonance, or ghost mode visible at 1564nm. Because this part of the fibre has become multimode, the grating reflects a second mode with different effective index in a similar way to the multiple peaks of long period gratings. If the Bragg wavelength is plotted against time as in Figure 5.2, the transient profile is also unique and shows three regions: the first is the rapid formation of a type I grating, this then decays and a linear period of mean index change begins before saturation occurs at which point the grating stabilises.

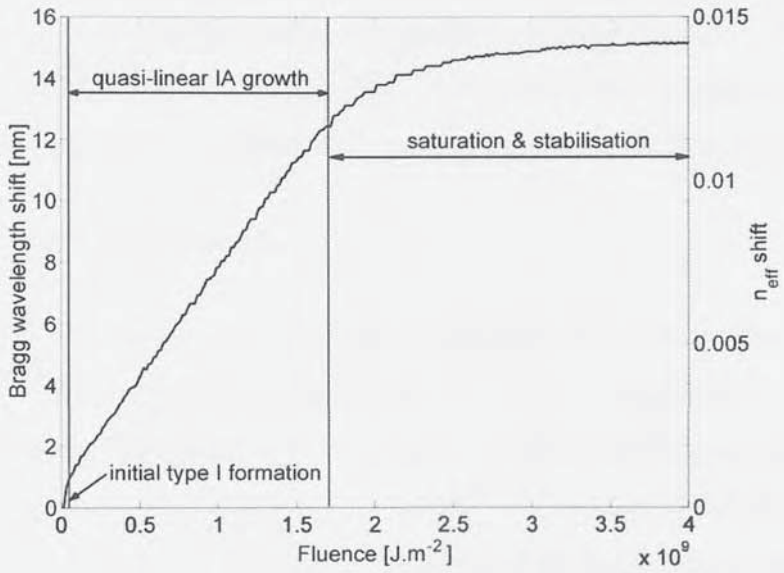

Figure 5.2 An example of the characteristic red shift displayed during prolonged UV exposure of hydrogenated germanosilicate fibre shown in terms of the spectral red-shift and associated refractive index change on a dual y-axis plot. The three distinct regions of IA growth are shown.

5.3. REGENERATED GRATING FABRICATION

Regenerated gratings are inscribed by the prolonged exposure to the inscribing laser. This has classically been performed in one of three ways: 1) by prolonged exposure in a holographic inscription setup; 2) by repeated scanning in a phasemask setup; or 3) by static exposure through a phasemask. Each method is generally suitable for most applications, but all have a common drawback. During a prolonged exposure, the quality of the grating is a function of the stability of the system during inscription since the fringe visibility will be degraded if the interference pattern is unstable. Clearly, the effect of any instability is multiplied when exposure time is doubled; thus regenerated gratings are significantly more difficult to inscribe with good fringe visibility than standard gratings.

5.3.1. Holographic fabrication

Chapter 3, Figure 3.3, shows a good quality holographic inscription setup, time has been spent assembling the components such that the vibrations transmitted to the interference fringes are minimised. Good quality lens mounts, firmly fixed to an optical bench which itself is isolated from ground vibrations by means of a system of air-springs, are a vital precursor to stable operation. However, even an extremely high quality setup such as that shown is degraded because the mechanical distance from the 50:50 beam splitter to the interference fringes is large. There are always unavoidable vibrations within the system and they are amplified by this distance causing the quality of an extended exposure to be reduced. In addition, it is difficult to inscribe gratings with uniform exposure profiles since the output of most UV lasers now available typically have a Gaussian cross section intensity profile; this problem is compounded if a beam expansion telescope is used to inscribe gratings of a longer length than the inscription laser beam diameter.

5.3.2. Static beam, phasemask exposure

The static phasemask exposure technique is by far the least demanding method of FBG inscription and requires the minimum of equipment, although high quality flexure stages are a prerequisite. The method works well for simple grating designs although apodisation is difficult. The drawback to any phasemask technique is that phasemasks are

often extremely expensive and although there are several published methods for extending the useful wavelength range of a phasemask (see Section 3.3.1.2) they are only usually applicable for small changes to the shorter side of the Bragg resonance. The principle of operation of a static phasemask system is shown below in Figure 5.3.

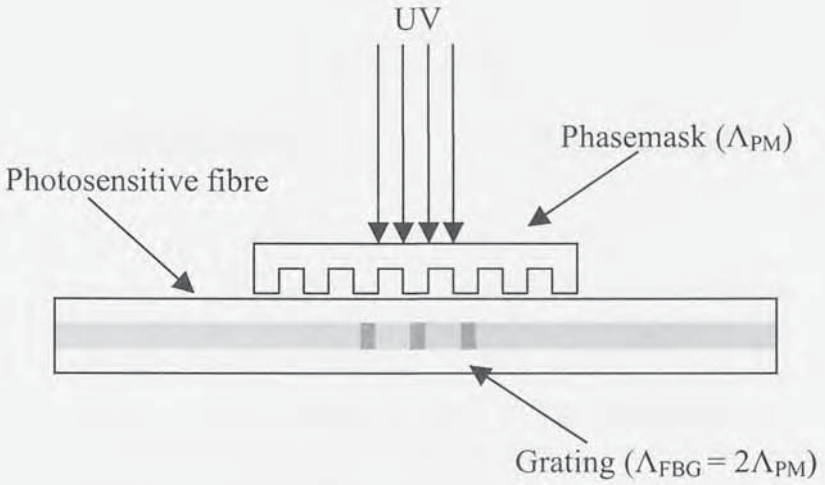

Figure 5.3 A schematic diagram showing the operation of a static phasemask inscription system. The UV laser is passed through a surface relief phasemask and the resulting fringe pattern is projected on to the optical fibre core, thereby inscribing a grating with period equal to twice that of the phasemask.

This system has some of the same drawbacks as the holographic system, it is not easy to produce exposure uniformity across the length of the grating and system vibrations reduce fringe visibility. This system is, however, generally more stable than holographic systems because the distance between phasemask and interference fringes is minimal (approximately 100μm).

5.3.2.1. Scanning beam, phasemask fabrication

Another well known method of FBG manufacture is the scanning beam, phasemask fabrication system. This system is again extremely straightforward in principle, however, it is extremely difficult to perfect and is the subject of a great deal of research in its own right. Rather than having a static beam, a mirror is placed on a translation stage (usually an extremely complicated piece of equipment costing a significant fraction of the total

system cost) that scans the beam along the length of the phasemask thus inscribing a grating within the fibre core. This is shown below in Figure 5.4.

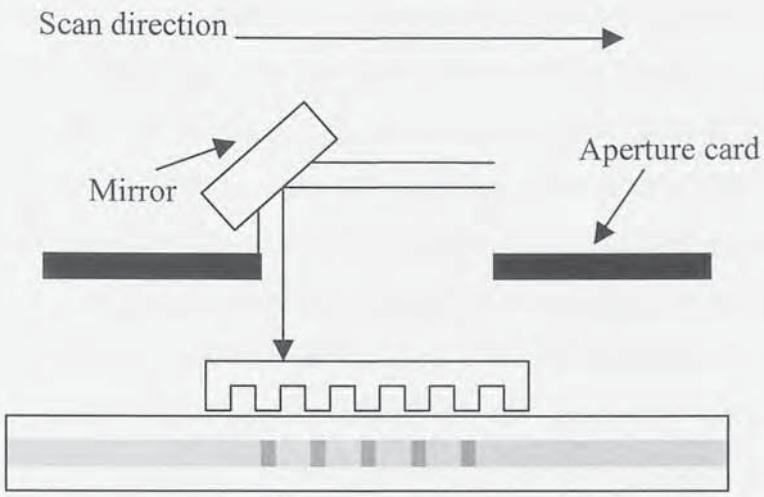

Figure 5.4 A modification of the static beam setup shown previously. This figure shows a scanning beam inscription setup using a phasemask and an aperture card to ensure uniform exposure of the grating.

Assuming an extremely high quality translation stage and associated equipment, the scanning beam fabrication method is of comparable stability to the static beam system but with the crucial advantages that gratings at least as long as the phasemask may be fabricated and that one may ensure a uniform intensity profile using a simple aperture card.

5.3.3. Blank beam fabrication

The principal drawback to all of the three methods listed above is that they require the microscopic interference pattern to be present for the full duration of the exposure. When fabricating standard (type I) gratings the process usually requires only a few seconds of UV exposure. This means that the fringe pattern is present for the minimum length of time thereby minimising stability concerns. However, when manufacturing regenerated gratings such as IA or IIA gratings, a significant amount of energy must be delivered to the fibre in order to change the properties of the fibre; this can typically take from 20mins to 5 hours. In this situation it would be far better to deliver the energy required to bring about the change in fibre properties and then to inscribe the grating afterward in the

normal way. The need for this will become apparent later in this chapter, especially when several thousand scans are required to deliver the required level of fluence to a fibre.

The principle of blank beam pre-exposure is therefore simple. A standard scanning beam inscription setup is modified by removing the phasemask, or translating it so that the inscribing beam may pass through a section with no phase relief pattern, the fibre may be pre-exposed to the UV radiation by repeated scanning of the fibre. In this way, the fibre may be pre-conditioned to the final state achieved during a prolonged exposure. Once the fibre is fully *mature*, the phasemask is reintroduced and a grating written in the modified fibre in the usual way. This method was first described during the post-deadline session of OFS 2003 [93] where the correlation between the mean index evolution and an absorption band at 1400nm was shown. Figure 5.5 shows the mean index evolution, which is akin to the maturity level of a type IA grating, and the associated increase in the absorption band at 1400nm. Both curves follow the three trends outlined in Section 5.2, Figure 5.2. The absorption band will be discussed at length in Chapter 6, Section 6.4.

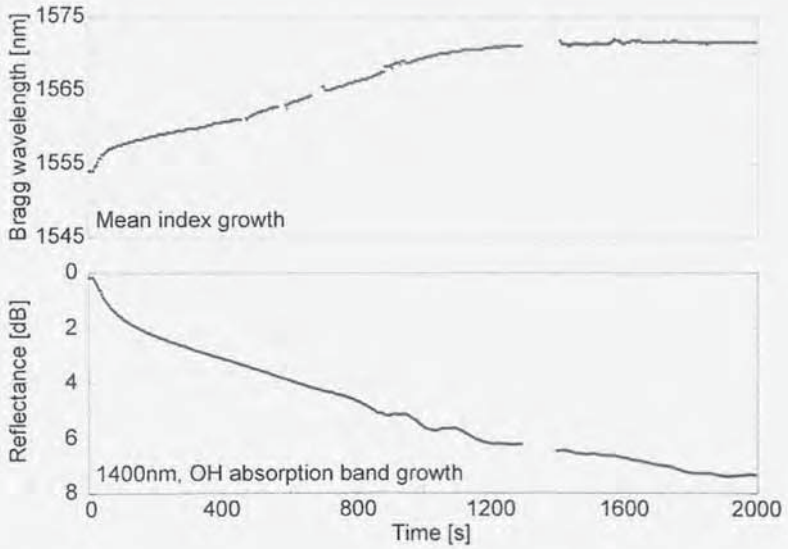

Figure 5.5 The relationship between the mean index change (or IA maturity) and the 1400nm absorption band under UV exposure. It is this relationship which enables IA index changes to be inscribed without writing a grating since the index change may be monitored by observing the absorption at 1400nm.

This absorption band is a consequence of the formation of OH ions within the fibre and has no dependence on the modulated index change required for a Bragg grating to be formed in the core. It is therefore possible to monitor the transmission loss at 1400nm and

glean accurate feedback as to the *maturity* of the fibre. When the absorption loss saturates, the fibre is fully mature and ready for inscription of any form of IA grating, be it slanted, long-period or standard.

Currently, this method has only been successful for the fabrication of type IA regenerated gratings; although it should be possible to apply the same technique to IIA gratings this has not yet been achieved.

5.4. FABRICATION OF IA GRATINGS

5.4.1. The dependence of IA growth on inscription intensity

A study was carried out to ascertain the dependence of the rate of IA formation on the inscription laser intensity with a view to calculating the optimum inscription wavelength and intensity.

Verillion IF01001410101 B/Ge co-doped fibre was hydrogenated at 225bar, 80°C for 68hours. A Coherent Sabre FreD laser at 244nm was used in conjunction with the holographic inscription setup shown in Figure 3.3 to inscribe four identical IA gratings with varying inscription powers of 10mm in length. The inscription power was varied by means of a calibrated set of neutral density filters whilst the laser maintained a constant 250mW output. The FBGs were monitored in transmission using a broadband source and an optical spectrum analyzer connected to a PC. The Bragg wavelength and the strength of the grating were logged every 6 seconds by PC.

Figure 5.6 shows the spectral location of the central Bragg resonance plotted against fluence as the gratings form in the fibres. Figure 5.6 gives a good indication of the characteristically large red shift that accompanies type IA grating formation and highlights the 3 distinct phases shown earlier in Section 5.2. Figure 5.6 shows two distinct intensity dependences:

The formation rate of the initial grating (type I grating, as defined in Section 3.3.2.4) exhibits negligible variation with inscription power

The formation rate of the regenerate grating (type IA grating, as defined in Section 3.3.2.4) exhibits large variation with inscription power

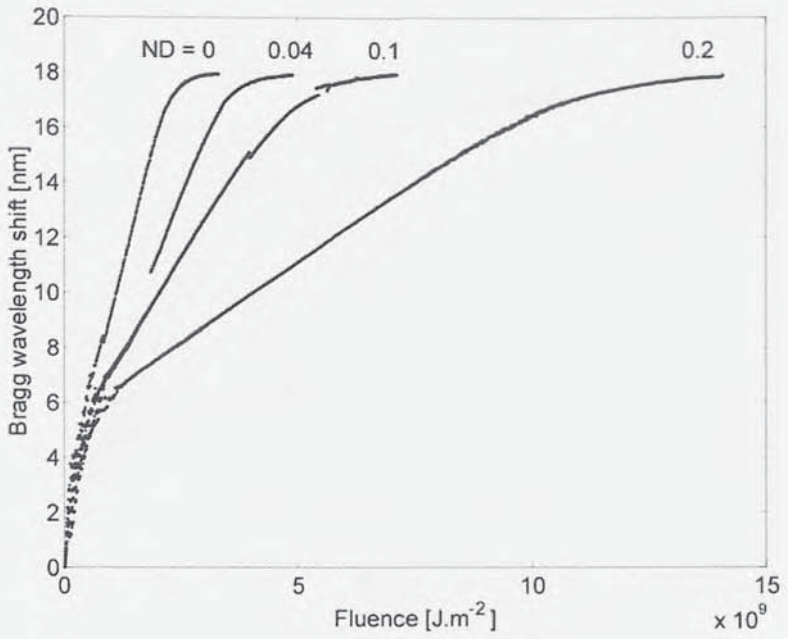

Figure 5.6 The rate of inscription of type IA gratings with decreasing UV inscription laser power is depicted. This example shows gratings written holographically in Verillion IF01001410101 B/Ge fibre.

In order to maximise the quality of the grating and to guarantee a uniform intensity profile, a scanning beam approach was adopted wherein the inscription laser scanned an aperture against a phasemask increasing the cumulative fluence with each scan of the laser in accordance with Section 5.3.2.1.

Fibercore PS1250/1500 B/Ge co-doped fibre was hydrogenated at 225bar for 68 hours at 80°C. The inscription laser was held at a constant 400mW and a calibrated neutral density filter set was utilised to adjust the power of the inscription laser. An OSA was used to save a spectrum of the sample gratings after each scan of the inscription laser. The laser was scanned at 1mms^{-1} across a 0.5mm aperture.

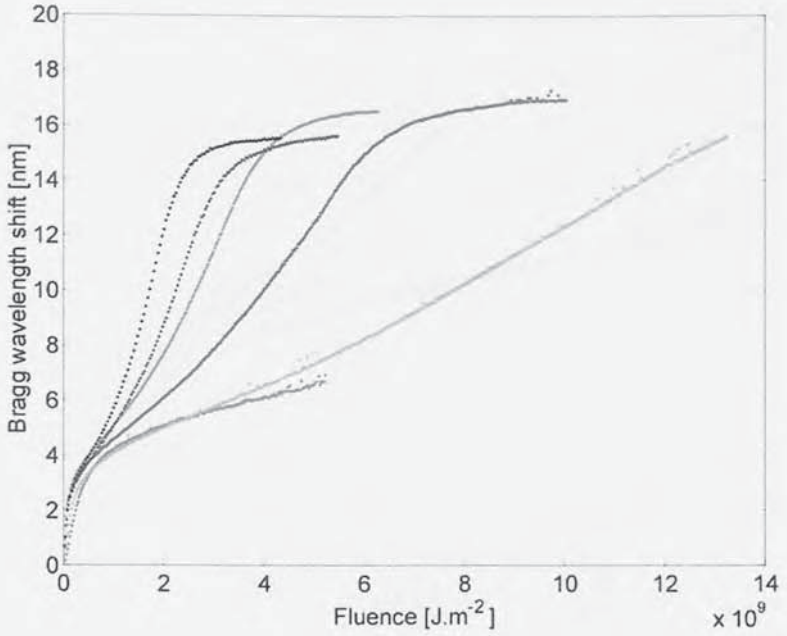

Figure 5.7 The rate of inscription of type IA gratings with decreasing UV inscription laser power is depicted. This example shows gratings written according to the scanning phasemask method in Fibercore PS1250/1500 B/Ge fibre. Refer to Table 5.1 for the inscription parameters and colour code of each plot.

The intensity of the inscription laser after the ND filter was calculated according to the simple relation $OD(\lambda) = -\log_{10} T(\lambda)$ where $OD(\lambda)$ is the optical density of the filter and $T(\lambda)$ is the transmissivity in % at wavelength λ. This equation has been applied to calculate the inscription intensities shown in Table 5.1.

Figure 5.7 shows the inscription rates for five mature type IA gratings (and 1 immature grating) written with inscription intensities as laid out in Table 5.1. The trends shown in Figure 5.6 are again shown here with the higher quality data. The transition from type I to IA is shown more clearly in Figure 5.8; this plot not only shows the distinct corner where the type IA process begins but highlights that the inscription laser intensity is only a significant factor for IA formation.

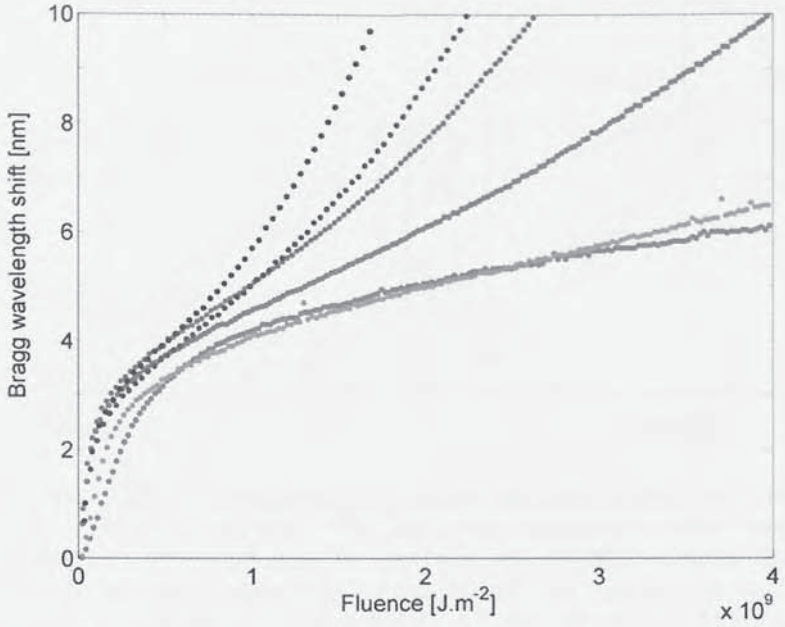

Figure 5.8 A zoomed in plot of Figure 5.7 showing the transition from type I to type IA and further showing that the inscription intensity dependence is significant only for the IA growth region.

This distinct change in growth profile indicates a fundamental change in the photosensitive mechanism which forms type I and IA gratings, and is an indication that IA gratings form as a result of multi-photon absorption. Closer inspection of the transition from type I to type IA is provided in Figure 5.9. In this series of figures the mean and modulated index change evolutions are plotted on dual y-axis charts. The mean index change is plotted in terms of wavelength shift in the Bragg resonance and the modulated index is shown simply in terms of maximum transmission loss.

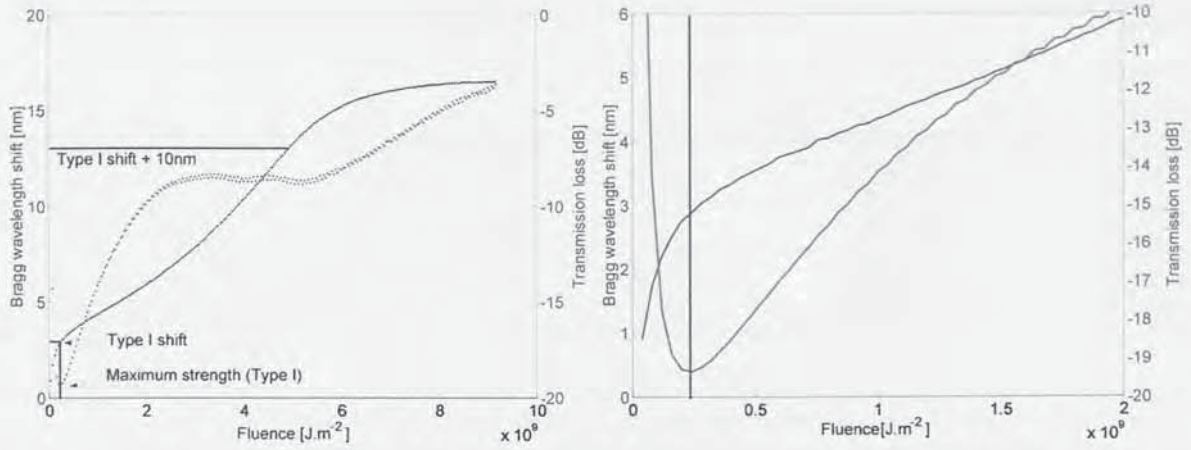

Figure 5.9 Dual y-axis plots showing the mean (blue) and modulated (red) index change of a type IA grating for (a) (left) the complete inscription period and (b) (right) the transition from type I to type IA. This plot is designed to show that the change in gradient of the mean index coincides precisely with the start of the decay of the type I grating, indicating the exhaustion of one of the underlying photosensitive mechanisms.

If we first examine Figure 5.9a, we can see that the initial grating forms extremely quickly, reaching a maximum transmission loss of -19.5dB in only 6 scans of the inscribing laser during which time the Bragg resonance has shifted 2.88nm. It then begins decaying rapidly and the mean index change slows somewhat. Note that the modulated index change does not follow a predictable pattern after this point; repetition of identical conditions frequently produces markedly different modulated index growth patterns. Figure 5.9b examines the transition from type I to IA more closely as it is a zoomed plot of Figure 5.9a. Note that the maximum reflectance is reached precisely at the same time as the mean index changes gradient. In order to compare these values we must define certain points on the growth curve. It is assumed that the point of maximum reflection represents the transition from I to IA; this will be termed $t\left(\lambda_{BR}^{I}\right)$. The wavelength change and fluence required to produce it is shown below in Table 5.1. Moreover, it is important to investigate the gradient of the mean index evolution from type I to IA wherein the marked difference in inscription power may be noted. This is done by calculating the fluence required to increase the central Bragg resonance a further 10nm from $t\left(\lambda_{BR}^{I}\right)$; this is termed $t\left(\lambda_{BR}^{I}+10\right)$ and is again summarised in Table 5.1. An increase of 10nm was chosen because it encapsulates the gradient of the linear part of the IA growth cycle.

FBG Ident	colour	ND Filter	Power	Max Δλ	Δλ to $t\left(\lambda_{BR}^{I}\right)$	Fluence to $t\left(\lambda_{BR}^{I}\right)$	Fluence to $t\left(\lambda_{BR}^{I}+10\right)$
			mW	nm	nm	J.m^{-2}	J.m^{-2}
1	black	0	400	15.56	2.91	2.00x10^{8}	**1.88x10^{9}**
2	blue	0.04	367	15.65	2.81	2.20 x10^{8}	**2.57 x10^{9}**
3	green	0.1	274	16.56	2.88	1.64 x10^{8}	**3.15 x10^{9}**
4	red	0.1 + 0.04	251	16.93	2.71	1.51 x10^{8}	**4.92 x10^{9}**
5	cyan	0.2	241		2.91	3.37 x10^{8}	**1.02 x10^{10}**
6	magenta	0.2 + 0.04	221		2.26	22.88 x10^{8}	**>4.9360 x10^{9}**

Table 5.1 A summary of the growth data of *Figure 5.7* indicating the colour codes used in the plot and the intensity of the inscription laser for each grating. The table also shows the fluence levels required to reach the milestones in the formation of IA gratings, as shown in *Figure 5.9*a.

Multi-photon absorption processes were described in Chapter 2, Section 2.2.4. It was shown a plot of photon density against successful molecular energy level transitions could be used to calculate the number of photons required to by quasi-simultaneously absorbed. Photon density is directly proportional to the intensity of the inscription laser and we may measure the successful molecular transitions in terms of the mean index shift. Figure 5.10 shows these results plotted on a logarithmic scale with overlaid x^n curves indicating the expected gradient for an n photon absorption process.

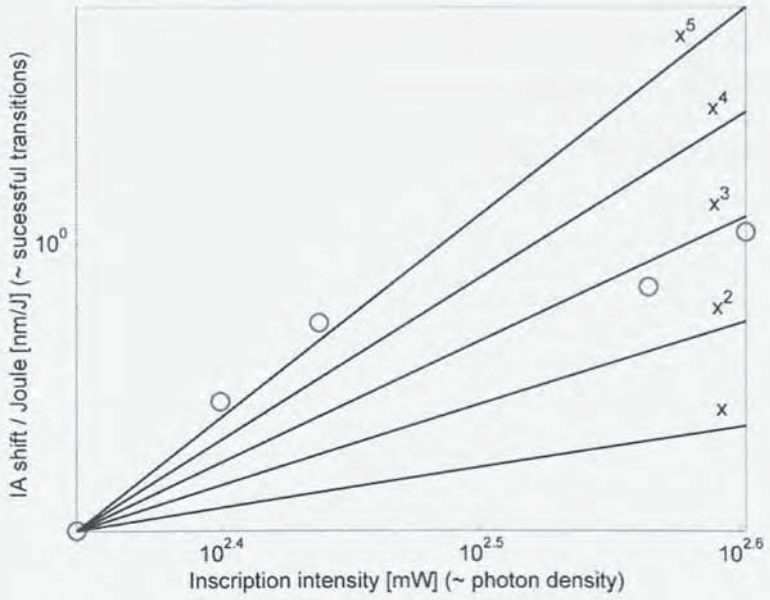

Figure 5.10 A logarithmic plot of inscription intensity vs. mean index shift per joule delivered to the sample. This is directly proportional a plot of photon density vs. successful transitions, and is used to show that the formation of type IA gratings is unlikely to be a single photon absorption process.

It should be pointed out, that Figure 5.10 represents the result of many repetitions of the experiment although unfortunately the results are far from conclusive. The curve most closely matching the data is x^3, although the fit is extremely poor. This is caused by inaccuracies in the alignment of the fibre within the interference fringes thus significantly reducing the intensity within the core. The inaccuracies are believed to originate from concentricity errors in the poly-acrylate fibre jacket through which the fibre is clamped in to the inscription apparatus. What we may safely conclude, however, is that the gradient is significantly higher than x^1 indicating that the type IA effect is most likely to be a result of multi-photon absorption at 244nm. We may also conclude that the type IA photosensitivity mechanism is distinct from the type I photosensitivity mechanism due to the differences in the growth rates, as indicated in Figure 5.8.

5.4.2. Temperature

A portion of the UV light used to inscribe gratings within the core of optical fibres is absorbed by the fibre. This may be seen as a slight blue glow at the spot where the laser is incident and is also responsible for a significant rise in the temperature of the glass. The thermal mass of a 125μm fused rod is very small and thus the heating remains localised to the point of interaction and cools almost instantaneously when the UV is removed. A simple way to demonstrate this, and to estimate the temperature within the fibre, is to examine the effect of turning off the laser when inscribing a holographic grating.

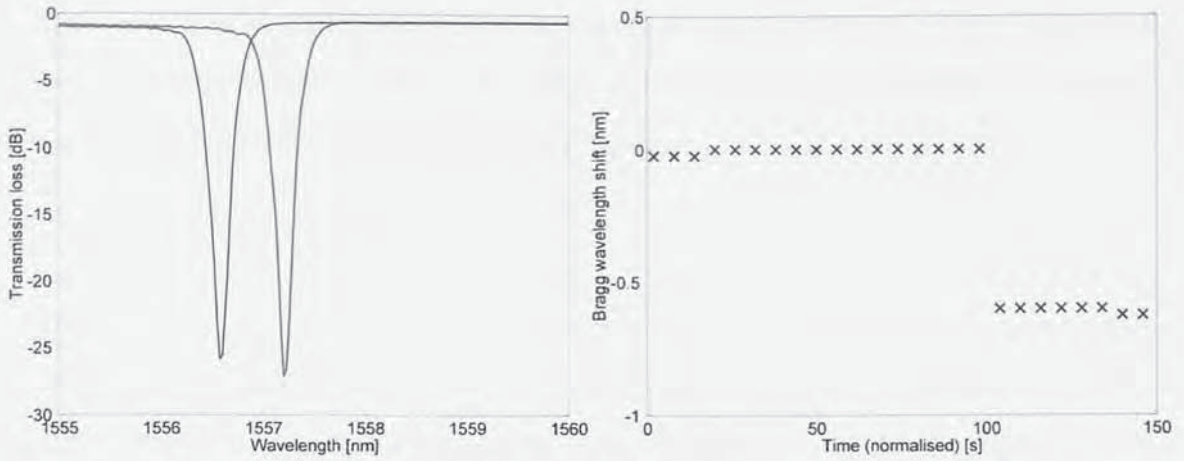

Figure 5.11 A demonstration of the heat generated in a germanosillicate fibre by the application of UV light. (a) (left) The red trace shows the Bragg wavelength with the laser on, and the blue shows the cooled trace after the laser has been turned off. (b) (right) A plot of Bragg reflection versus time showing the point at which the laser was tuned off indicating the rapid cooling of the fibre due to its small thermal mass.

Figure 5.11a shows this effect for a grating inscribed in germanosilicate fibre (refer to Section 5.4.1, Figure 5.6, ND = 0 for the precise details of this grating). The red trace represents a mature IA grating whilst the laser is still turned on; the blue shows it a short time later when it has shifted by 625pm. Figure 5.11b shows the timeline of this cooling with a resolution of around 6s. Although the resolution is not particularly fine, it is clear from this plot that the fibre has fully cooled within 6 seconds of the laser being turned off. The implied temperature shift equates to a temperature decrease of ~100°C which means the fibre was resting at ~125°C, and is our first hint that intensity dependent heating can affect the growth dynamics. This value is clearly dependent on intensity. Table 5.2 shows the details and implied temperature shifts for the remaining gratings illustrated in Section 5.4.1, Figure 5.6 which have decreasing levels of fluence. This is a good indication of the expected temperatures within the fibre.

ND Filter	Intensity $MW.m^{-2}$	λ_{BR} shift pm	ΔT °C
0	1.50	-625	**-104**
0.04	1.38	-500	**-83**
0.1	1.03	-375	**-63**
0.2	0.90	-350	**-58**

Table 5.2 Summary of the heating within a fibre exposed to UV radiation at a given fluence and an approximate temperature reached by the fibre calculated from the shift in Bragg wavelength.

A clear consequence of this is that when the laser has a sufficiently high intensity the fibre will become heated and will cause the outgassing of hydrogen during the inscription, thus causing the grating to self-anneal.

5.4.2.1. Self annealing

Self annealing occurs when the inscribing laser is absorbed by the fibre to such an extent that the heat generated causes the hydrogen within the fibre to diffuse out. This is depicted below in Figure 5.12 by the red trace. This shows a typical spectral plot of a self-annealing IA grating. The grating forms relatively quickly, but the Bragg wavelength then begins to decay and is reduced by almost 3nm before the experiment ends.

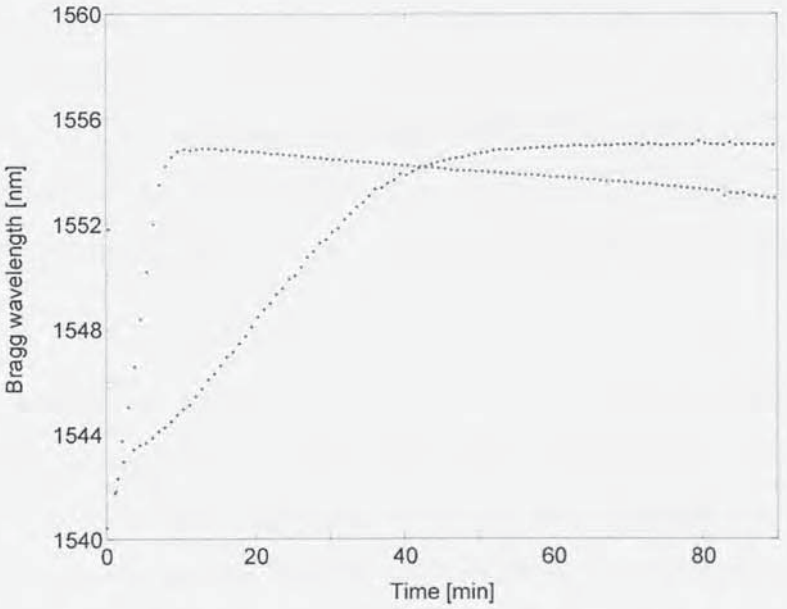

Figure 5.12 Type IA grating evolution under near identical conditions. The red trace shows a normal inscription, but the blue trace shows the effect of cooling the fibre to 5°C during inscription. The cooled fibre evolves significantly more slowly than the un-cooled fibre, thereby indicating that the heating effect of the inscription laser has a significant effect on the rate at which IA gratings form.

It was initially assumed that if the heating effect of the inscription laser could be removed then extremely high inscription powers could be employed, thus speeding the manufacture process significantly. In an attempt to achieve this, a Peltier device was placed close to the fibre during inscription and connected to a standard laboratory temperature controller set to -5°C. The grating evolution shown in blue by Figure 5.12

was significantly slower than the un-cooled inscription shown in red. This may be because the hydrogen used up in the IA process cannot be replenished by the hydrogen stored in the neighbouring fibre as quickly because the fibre is cooler and thus the diffusion rate (refer to Section 2.2.3.3, Equation 2.3) is significantly slower than the heated case. In either case, it shows that there are two contributing factors in the rate at which IA gratings form:

1. The intensity of UV light
2. The temperature of the fibre

5.4.3. The influence of strain on IA grating formation

It has already been discussed in Section 3.3.2.3 that IIA gratings form with less energy when the fibre in which they are being inscribed is placed under axial strain. It is believed that this is related to stress relaxation within the fibre. Due to the obvious similarities between IA and IIA gratings, it was pertinent to inscribe several gratings under increasing axial strain to ascertain if the same effects are responsible for the formation of IA gratings.

A standard scanning phasemask experiment was setup wherein successive scans of the UV laser across the phasemask caused the IA grating to grow in such a way that the mean and modulated index change could be monitored. A 1mm aperture was used to ensure that the gratings received a strictly uniform intensity profile across their length. Each end of the fibre sample was firmly clamped in customised fibre clamps, one of which was mounted to a load cell, whilst the other clamp was mounted on a translation stage enabling the fibre to be placed under a known amount of strain. In this experiment, 8 samples were created with strain levels ranging from almost zero to ~5000$\mu\varepsilon$.

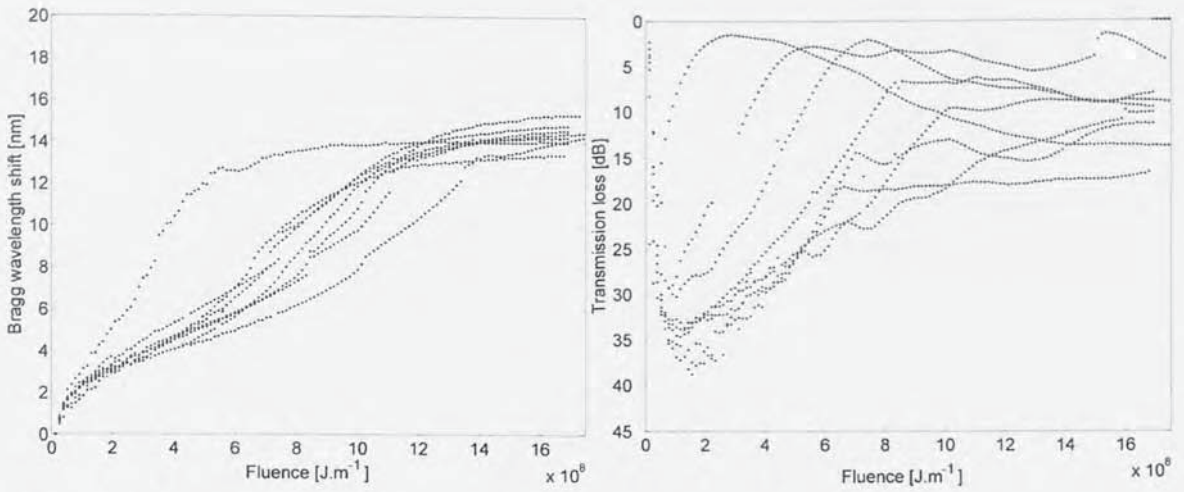

Figure 5.13 This figure shows the growth dynamics of a series of IA gratings written under increasing axial strain. It shows (a) (left) the wavelength evolution and (b) (right) the reflectance evolution of type IA gratings. The random nature of the growth characteristics indicates that the presence of strain does not have a significant effect on the growth dynamics, which is in contrast with IIA gratings.

Figure 5.13a shows the inscription rate for the gratings in terms of the mean index shift, as indicated by the central Bragg resonance evolution. The traces overlay each other within a reasonable level of noise; one trace represents a significantly faster evolution, which may have been caused by an increase in the intensity of the inscription laser. There is no order to the traces; indeed the traces (ST1 to ST8), which represent an increasing level of strain, do not form any trend and are randomly distributed within the overlaid traces. The same is true of Figure 5.13b which shows the reflectance evolution; there are no recognisable trends in the inscription process with increasing strain.

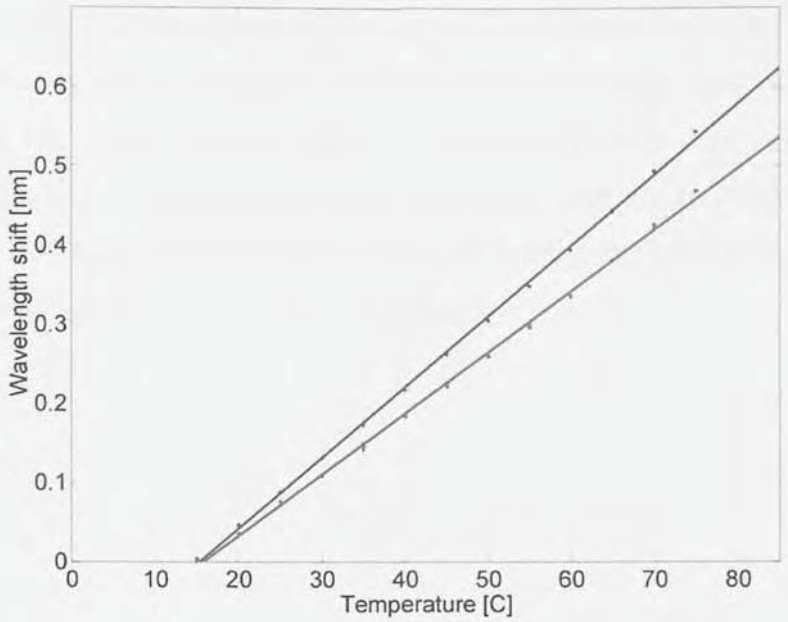

Figure 5.14 An example of the temperature coefficient plots for the gratings ST1 to ST8. This graph depicts ST4 and shows typical thermal coefficients for both gratings.

The gratings were then annealed at 80°C for ~100 hours. The annealing data again shows no sign of a trend. Figure 5.14 shows a typical temperature response curve for an example of one of the samples. The temperature coefficients for all gratings are shown in Table 5.3 and do not indicate any trend with respect to the inscription strain level; there is a variance in the measured coefficients but it does not indicate any discernable trend.

Reference	Inscription strain	$\lambda_{BR}^{I}(T)$	$\lambda_{BR}^{IA}(T)$	$\frac{\lambda_{BR}^{I}(T)}{\lambda_{BR}^{IA}(T)}$	$\lambda_{BR}^{IA}-\lambda_{BR}^{I}$	$\lambda_{BR}^{IA}-\lambda_{BR}^{I}$ annealed
	με	pm°C^{-1}	pm°C^{-1}	%	nm	nm
ST1	263	9.1	7.6	**19.929**	14.096	**13.879**
ST2	917	8.9	7.9	**12.056**	12.875	**12.701**
ST3	1583	8.4	7.9	**5.592**	13.554	**13.631**
ST4	2250	9.0	7.7	**15.661**	14.312	**14.148**
ST5	2903	8.9	8.0	**12.214**	13.247	**12.972**
ST6	3517	8.5	7.4	**14.001**	14.682	**14.385**
ST7	4170	8.8	8.0	**10.867**	14.928	**14.579**
ST8	4830	9.6	8.4	**14.282**	14.353	**14.151**

Table 5.3 The measured data for gratings ST1 to ST8 summarising the inscription strain levels, the thermal coefficients and the difference in Bragg wavelengths between type I and IA. There are no noticeable trends in the data.

Table 5.3 summarises all data gathered during this investigation into the effect of strain on the formation of type IA gratings. Whilst there is a larger than usual degree of variance across the fibre samples, there is no clear trend in any of the measured parameters which one might expect to see as a result of applied strain during inscription in the case of IIA gratings. This may indicate a fundamental difference between the underlying photosensitivity mechanisms of IA and IIA gratings.

5.5. EXPOSURE UNIFORMITY AND THE MEAN INDEX PROFILE

An important issue to consider when inscribing regenerated gratings is exposure uniformity. Beam expanded interferometer setups usually display an approximately Gaussian intensity profile across the interfering area. Similarly, with a scanning setup the edges of the scanned area may experience higher than average levels of exposure due to the time taken for the beam to change direction; they may also experience under-exposure if the scanning beam itself displays a strongly Gaussian intensity profile. This is most simply solved using a combination of the scanning technique and an aperture card, as shown in Figure 5.4. By scanning the beam over an area which is at least the grating length plus 2 times the beam width across an aperture card, the exposure is guaranteed to be exactly uniform since all parts of the exposed area must experience the same level of radiation. This is more important for regenerated gratings than standard gratings because if different parts of the grating are exposed to varying levels of energy, there will be gratings of different maturity levels (and ultimately different mean index values) along the sample resulting in extremely poor quality gratings.

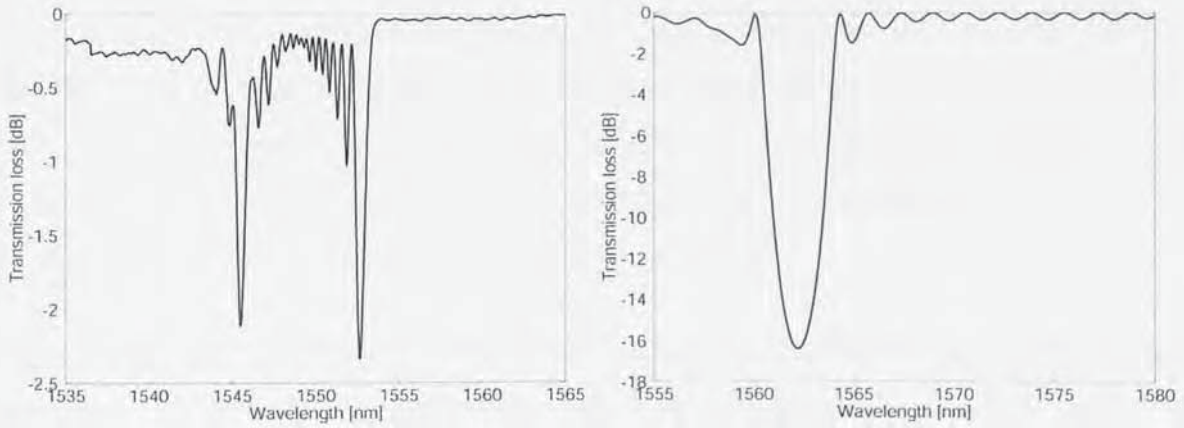

Figure 5.15 The spectrum of immature IA gratings manufactured by (a) (left) the holographic and (b) (right) the scanning beam phasemask methods. This figure highlights the requirement for exposure uniformity since (a) indicates a hybrid grating with a non-uniform mean index profile.

The need for exposure uniformity is demonstrated above by Figure 5.15. Figure 5.15a shows the spectra of a holographically inscribed IA grating approximately half-way towards full maturity; the grating was 10mm long, achieved by means of a beam expanding telescope. Figure 5.15b shows a 0.5mm grating inscribed with a scanning

phasemask approach and using an aperture card to ensure exposure uniformity. Figure 5.15a clearly indicates two Bragg resonances which correspond to a more mature grating in the centre where the radiation was more intense and less mature gratings at the edges. By contrast, Figure 5.15b shows the result of a truly uniform exposure profile and shows a comparatively clean spectrum of a maturing grating. This could alternatively have been achieved using a non-uniform velocity profile incorporating a slower velocity profile at the endpoints and a faster velocity in the central portion. Whilst this approach would decrease the overall fabrication time of the gratings by requiring a smaller scanning length, it would only really be of benefit in a large scale manufacturing scenario, since the complexities associated with measuring the intensity profile for many different exposure conditions would significantly counteract the time savings in an experimental situation.

Figure 5.15 also highlights the problem of maintaining good fringe visibility during prolonged exposure; the holographic grating is 20 times as long as the phasemask grating, yet it shows only 2.5dB peak transmission loss compared to more than 16dB in the phasemask case. Whilst the aim of Figure 5.15 is to contrast a good example with a poor one, the setup used to produce the holographic grating was by no of means poor quality. Although this is not an example of the best output from such a system, it is not atypical and goes a long way to showing the benefits of more advanced systems using phasemasks. This may be further seen by inspecting the first published examples of type IA gratings from the doctoral thesis of Yu Liu in 2001 [7].

Figure 5.16 shows a selection of temporally separated transmission spectra of an 8mm grating manufactured by the holographic technique in hydrogenated standard fibre. This example shows two clear peaks and echoes the spectrum shown in Figure 5.15a. The final spectrum shows a fully mature IA grating, but it also shows a hybrid grating which, in mean index terms, is somewhere between a type I and a type IA grating. Hybrid gratings were described theoretically by Shu *et al* [164] although they did not suggest any applications for these structures.

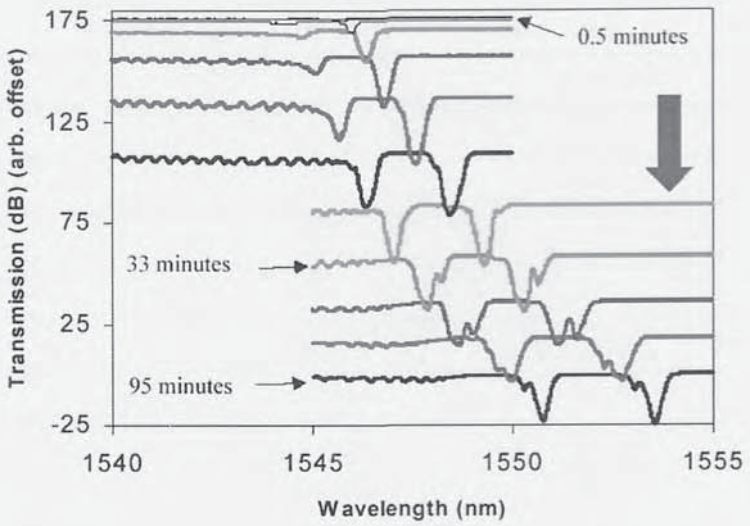

Figure 5.16 Reproduced from [7] (Figure 5.33). The figure shows the evolution of a IA grating under holographic inscription. This is an example of a poor IA inscription due to inscription non-uniformity as there are multiple levels of maturity present in the sample.

If the objectives to produce a clean transmission spectrum of a IA grating, it is unlikely to be possible with a holographic setup. Figure 5.17 shows a similar plot to Figure 5.16, but this figure was produced using data taken during the manufacture of a IA grating by the scanning beam technique with a fixed phasemask and aperture card. The benefit of this system is immediately apparent as there is only one peak throughout the entire evolutionary process. The final grating shows a clean transmission profile with small side-lobes and importantly only one Bragg resonance.

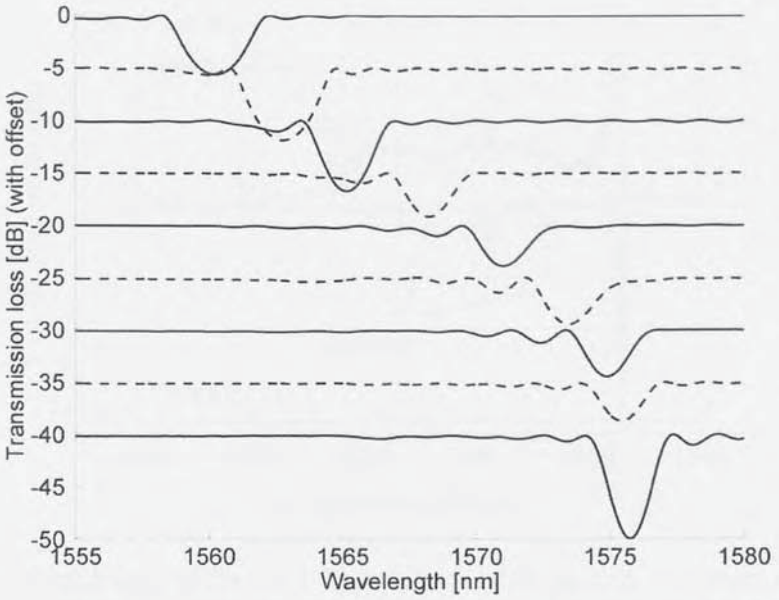

Figure 5.17 By contrast to Figure 5.16, this figure shows the spectral evolution of a 0.5mm IA grating manufactured by the scanning beam technique utilising a phasemask and 0.5mm aperture card to ensure uniform exposure. The result is a uniform grating throughout inscription with only a single maturity level present.

5.5.1. Fabry-Perot resonances in IA gratings

When IA gratings are manufactured, noise in both the reflection and transmission profiles is frequently seen in the region between the wavelengths associated with the type I grating and the maximum wavelength achieved by the IA grating. This was first seen in print in Y. Liu *et al*'s 2002 paper [108], reprinted below in Figure 5.18.

Figure 5.18 Reproduced from [108]. This figure shows a IA grating manufactured according to the holographic method. It shows noise on the blue side of the IA resonance which extends to the wavelength associated with a type I grating written in the same fibre. This is a result of a non-uniform exposure profile creating multiple peaks across the IA mean index increase.

Figure 5.18 shows the spectrum of a 10mm grating written in hydrogenated B/Ge co-doped (of an unspecified type, but most probably Nortel C2 fibre) with a two beam interferometric setup. The noise on the blue side of the IA resonance extends to the wavelength associated with a type I grating written in the same fibre. This trace was taken using an optical spectrum analyser and thus has a relatively large residual bandwidth (RBW), i.e. the minimum width (in wavelength terms) of a spectral artefact which may be resolved using the OSA is quite large. Figure 5.19 shows the spectrum of a 1.1mm grating, manufactured by the same two beam interferometric method as Figure 5.18 but the spectrum was acquired using a tuneable laser system comprising a tuneable laser with 5pm step size, a wavemeter and a InGaAs power meter. This tuneable laser system is capable of measuring the insertion loss and reflections from a fibre sample to an absolute resolution of 5pm.

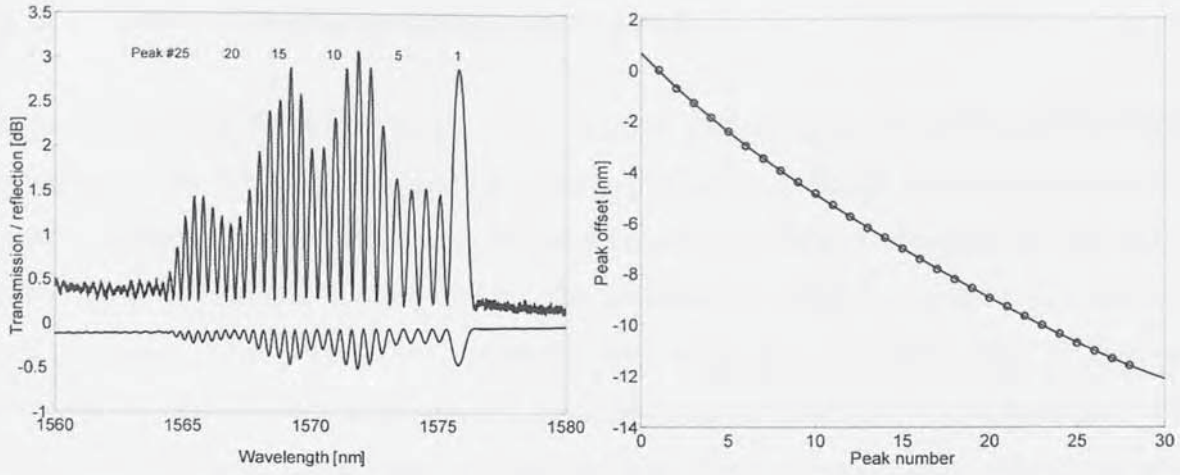

Figure 5.19 (a) (left) The spectrum of a IA grating, similar to that shown in Figure 5.18, which was acquired using a tuneable laser and power meter setup 5pm resolution. This shows that the noise seen in the early IA gratings was made up of multiple Bragg resonances caused by the existence of a broad range of mean index's. (b) (right) The offset of each peak shown in (a) indicating a trend in the peak-to-peak spacing of the resonant noise.

The IA peak of Figure 5.19 is smaller than that of Figure 5.18, which is in keeping with the difference in their physical lengths. It is clear from this high resolution spectrum that the noise on the blue side of the IA resonance shown by Y. Liu *et al* is in fact made up of a resonant structure, similar to that exhibited by a Fabry-Perot resonator. However it is clear from this high resolution data that the reflection and transmission data have modes which map each other identically and show that these are in fact Bragg modes. This indicates that the growth of the grating follows a complex process of inscription and erasure as the Bragg condition is alternately matched and mismatched during inscription leading to a non-uniform dc index of refraction change and multiple reflecting Bragg resonances.

5.6. DUAL GRATING SENSOR FABRICATION

Type IA gratings have previously been used as part of a dual grating arrangement wherein a type IIA and a IA grating, with significantly different thermal coefficients, were combined to form a sensor capable of decoupling strain and temperature [104-108]. Although not mentioned in these papers, the fabrication method for these IA-IIA sensors was extremely labour intensive. The reader will recall that the fundamental difference between the manufacture of IA and IIA gratings is that IA gratings require hydrogenated fibre, and IIA gratings require un-hydrogenated fibre. Clearly these conditions are mutually exclusive and require the fibre to be hydrogenated (or annealed) in between the fabrication of the first and second grating. This seemingly trivial step in the fabrication process would significantly increase the cost of commercial manufacturability for such a device because most of the labour cost in FBG manufacture is taken up by fibre preparation and alignment. Furthermore, removing and replacing the fibre once annealed also complicates the alignment process as it becomes necessary to accurately mark the position of the first grating, in order to produce the ideal situation of two directly adjacent gratings, thereby minimising temperature gradients across the sensor head. Yu Liu *et al* manufactured the two gratings in separate fibres, annealing the fibre containing the IA grating and then splicing the samples together. This situation is again non-ideal because it involves twice the manufacturing time and an extra period spent accurately cleaving and splicing the two fibres; it is unlikely that an operator could repeatedly splice such gratings to produce directly-adjacent gratings of different type.

In order to address this significant commercial problem, a compromise situation was designed wherein a type I and IA grating were combined, thus giving a smaller difference between the temperature coefficients of the two gratings, but significantly simplifying the inscription process by making it possible to inscribe both gratings at the same time and allowing them to be truly adjacent. The ideal method for fabrication of IA gratings, by means of blank beam pre-exposure (refer to Section 5.3.3) was used.

A section B/Ge fibre (Verillion IF01001410101), hydrogenated at 200Bar / 80°C for 64 hours, was pre-exposed to 244nm UV radiation. An aperture was used to ensure exposure

uniformity and the laser was scanned at $1mms^{-1}$. The intensity of the radiation was found to be 40mW at the fibre location. The laser was scanned a sufficient number of times to ensure that the OH absorption band had reached a maximum value (refer to Section 6.2.2 Figure 6.3), which in this case was of the order of 150-200 scans. To ensure that the gratings had a similar reflectance once annealed, trial and error was used to find a combination of grating length and inscription speed which yielded a good result. In this case the type IA gratings were 4mm long and written at $0.05mms^{-1}$ whereas the type I gratings were 1mm long and written at $0.5mms^{-1}$. By pre-exposing a 4mm section and then replacing the aperture with a phasemask it was possible to inscribe both gratings in a single action with no space between them thus giving a 5mm sensor head with an absolute minimum potential for temperature gradient across the sensor.

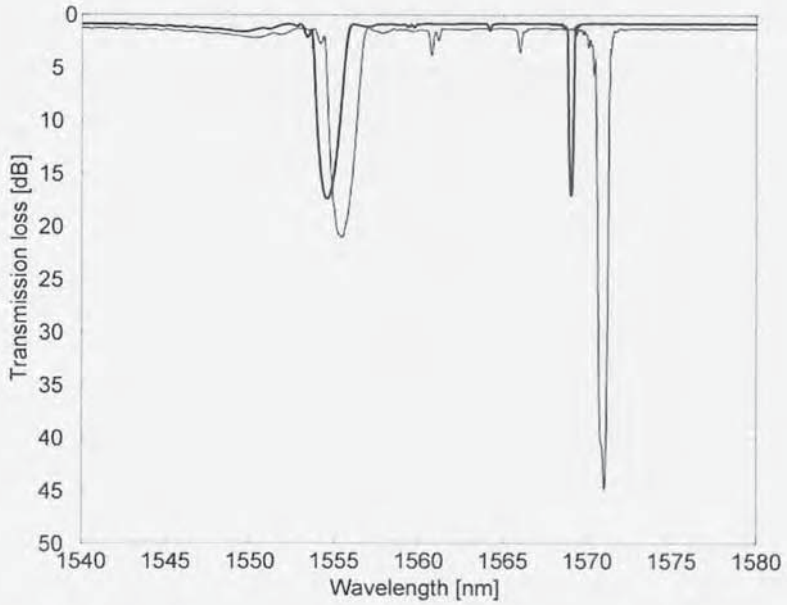

Figure 5.20 The spectrum of FBG8, a IA-I temperature compensating dual sensor head. The figure shows the gratings pre- (feint) and post- (bold) annealing and shows that proper choices of laser scan speed must be made so that the final sensor head has gratings with similar reflectances.

This process was repeated 8 times forming a batch of samples to assess the repeatability of the process and give an indication as to the commercial viability of production runs of such gratings. An example of the gratings manufactured by this technique is shown above in Figure 5.20. The gratings were annealed at 80°C for 70 hours. During this time, a multi-channel tuneable laser characterisation system with 5pm resolution was used to

save a spectrum for each grating pair every minute for the first 10 hours, and every 5 minutes thereafter. Clearly, prior to annealing the IA grating is significantly stronger than the type I; however, after annealing they have approximately the same reflectance. The annealing data may be seen in Section 6.6.2, specifically Figure 6.27 and Figure 6.28.

The temperature and strain responsivities of the IA-I sensor were measured by placing the sensor in a small insulated chamber whose internal temperature was controlled by a Peltier device and temperature controller of the type used to stabilise laser diodes. The change in the Bragg resonance with temperature is represented in Figure 5.21a for a specific example (FBG7). As anticipated there are different responses displayed for each grating type. The wavelength to strain response is shown in Figure 5.21b, where smaller but measurable differences are also recorded for the strain data. These primarily result from the differences in the centre wavelengths rather than a hardening of the glass during the formation of the IA grating, as discussed in Section 3.4.2.1.

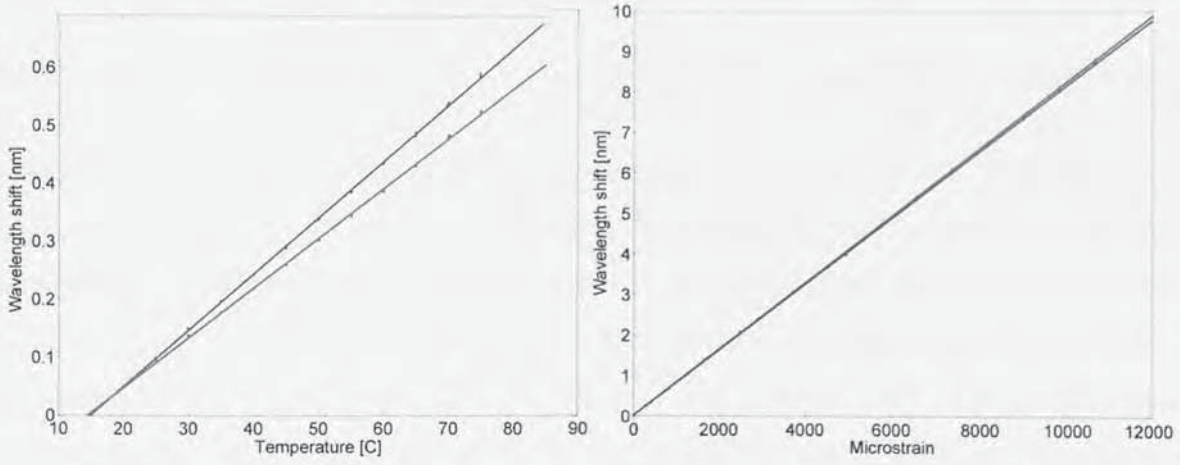

Figure 5.21 (a) (left) The thermal and (b) (right) the strain response of a IA-I dual grating sensor head (FBG8). Each case shows the response of the individual gratins in blue and red for the type I and IA gratings respectively. This shows that there is a significant difference in the temperature coefficients and a smaller, but measurable, difference in the strain coefficients from which temperature and strain may be independently measured.

Six of the eight gratings fabricated showed similar spectral, annealing, thermal and strain properties. This indicates superb potential repeatability for a properly constrained process. This data is summarised below in Table 5.4.

Reference	$\lambda_{BR}^{I}(\varepsilon)$	$\lambda_{BR}^{IA}(\varepsilon)$	$\frac{\lambda_{BR}^{I}(\varepsilon)}{\lambda_{BR}^{IA}(\varepsilon)}$	$\lambda_{BR}^{I}(T)$	$\lambda_{BR}^{IA}(T)$	$\frac{\lambda_{BR}^{I}(T)}{\lambda_{BR}^{IA}(T)}$	$\lambda_{BR}^{IA}-\lambda_{BR}^{I}$	$\lambda_{BR}^{IA}-\lambda_{BR}^{I}$ annealed
	$pm\mu\varepsilon^{-1}$	$pm\mu\varepsilon^{-1}$	%	$pm^{\circ}C^{-1}$	$pm^{\circ}C^{-1}$	%	nm	nm
FBG1	0.82	0.83	**-1.078**	9.7	8.5	**13.283**	15.844	**14.571**
FBG2	0.82	0.83	**-1.098**	10.0	8.9	**12.824**	15.951	**14.762**
FBG3	0.81	0.82	**-1.289**	9.7	8.6	**12.990**	15.271	**14.235**
FBG4	0.82	0.82	**-1.080**	9.4	8.7	**8.537**	14.064	**13.438**
FBG5	0.82	0.83	**-1.259**	8.6	8.2	**5.211**	15.178	**14.313**
FBG6	0.81	0.82	**-1.128**	9.6	8.5	**12.990**	15.726	**14.504**
FBG7	0.82	0.83	**-1.232**	9.6	8.5	**12.695**	15.590	**14.549**
FBG8	0.82	0.83	**-1.441**	9.6	8.5	**12.221**	15.476	**14.449**

Table 5.4 A summary of eight similar IA-I grating sensor heads. The table shows the temperature and strain coefficients of each grating, and the differences in the Bragg wavelengths of each grating pre- and post-annealing.

In order to determine the validity of the sensor design one may utilise the conventional matrix inversion technique, with the usual caveat; one must assume that strain and temperature are essentially independent, that is, the related strain–temperature cross term is negligible; refer to Section 2.7 for a discussion of this topic. Using the specific case of FBG7 shown in Figure 5.21, the ratios $\frac{\lambda_{BR}^{I}(T)}{\lambda_{BR}^{IA}(T)}=1.130$ and $\frac{\lambda_{BR}^{I}(\varepsilon)}{\lambda_{BR}^{IA}(\varepsilon)}=0.988$. These translate accordingly; an increase of 1mε corresponds to temperature rise of 85.15°C for a type I, and 97.42°C for a type IA grating. Assuming a 1pm error in wavelength measurement; the strain and temperature errors associated with these coefficients are $\pm 12\mu\varepsilon pm^{-1}$ and $\pm 1.2^{\circ}Cpm^{-1}$ respectively. For this example, the matrix condition number, calculated as described in Section 2.7, is 188. This makes the solution more accurate than those of Kalli *et al* [81, 120] and Frazao *et al* [121], the condition numbers of which are 203 and 272 respectively (for a full breakdown of the condition numbers of published dual grating measurand decoupling solutions, see Table 3.2). Therefore one may conclude that for the case outlined here, the IA-I dual grating sensor may be said to differentiate between strain and temperature to a high resolution for a fraction of the manufacturing complexity.

5.7. CHAPTER CONCLUSIONS

Type IA gratings are regenerated gratings fabricated in hydrogenated germanosilicate and boro-germanosilicate optical fibres. During inscription they undergo a unique mean index shift which is many times larger than observed with any other type of grating recorded to date. This mean index change occurs in three phases:

1. The initial phase is a very rapid yet small increase in mean refractive index, accompanied by a large modulated index change. This initial phase represents the formation of a standard, or type I, grating. The rate at which this change occurs does not vary with inscription laser intensity and may therefore be attributed to a single photon absorption process. The termination of this initial phase, notable due to a distinct change in the rate of mean index change, coincides precisely with the moment at which the grating is most reflective.

2. The majority of the mean index change occurs during the mid-phase of IA grating formation. During this period the grating amplitude varies from sample to sample and does not exhibit any good degree of uniformity between seemingly identical samples and conditions. However, this phase often exhibits decay to almost zero reflectivity before a re-growth to a final reflectivity which is significantly less than the maximum reflectivity achieved by the standard grating. The final reflectivity achieved is comparable to that achieved when inscribing a similar type IIA grating.

3. The final growth phase is a saturation phase where the mean index change rolls off to a maximum shift. In a typical example using boro-germanosillicate fibre of common dopant levels, a mean index shift of ~0.015 is achieved equating to a change in the Bragg wavelength of ~16nm in the 1550nm range.

The inscription process may be stopped at any time thereby enabling the tuning of a grating inscribed by the phasemask technique up to this maximum value.

The ideal fabrication method of type IA gratings is by the blank-beam method described by this chapter. In this method a section of hydrogenated fibre is exposed to uniform

intensity UV radiation whilst monitoring the strength of the 1400nm absorption band (the 1400nm absorption band is associated with the formation of hydroxides in the fibre and occurs at the same rate as the mean index change. Refer to Chapter 6 and Section 6.4).

The initial growth, up to the point of maximum reflectivity, requires single photon absorption; importantly however, the period of growth following this requires a multi-photon absorption process. Although it has not been possible to accurately predict the number of photons absorbed during this stage, it is clear that a photosensitivity mechanism somewhat different to that of type I gratings underlies the process (refer to Section 5.4.1 and particularly Figure 5.8).

Both IA and IIA gratings may be inscribed in germanium doped fibres, the inscription conditions and parameters are similar, except that IA gratings require the presence of hydrogen in order for them to form (refer to Section 6.2.2). The rate at which IIA gratings form is proportional to axial strain during inscription (refer to Section 3.3.2.3); by contrast, axial strain has no observable effect on the formation rate of type I gratings. This indicates a different photosensitivity mechanism to that of IIA gratings.

Finally, this chapter shows the fabrication conditions for a dual grating, self compensating, sensor. Unlike previously published configurations, this novel implementation does not require special treatment of the fibre between inscription of the two grating elements. By using a combination of types IA and I, it is possible to pre-expose one section and then use only a single phasemask scan to inscribe both grating types. This simple approach yields a matrix condition number better than 188.

Chapter 6

Type IA Fibre Bragg Gratings, Fundamental Investigation

6. TYPE IA FIBRE BRAGG GRATINGS, FUNDAMENTAL INVESTIGATION

6.1. PREAMBLE

This chapter builds upon the introduction to type IA gratings of Chapter 5 and discusses the results of a comprehensive investigation into the fundamental processes behind the formation of type IA gratings. It shows results of a comparative study into the formation of type IA gratings in fibres of differing dopants and dopant levels. It also shows a link between hydrogen saturation level within the core of the fibre and the evolution of IA gratings. This work shows, for the first time, that the concentration of hydrogen directly affects the inscription speed and temperature coefficient of type IA gratings. The presence and importance of the absorption band at 1400nm is shown in fibres of differing dopants and dopant levels and a novel method of selectively optically tuning an FBG is shown. The first report of the annealing characteristics of type IA gratings is made and a comparative study into the thermal stability of type I, IA and IIA gratings is documented.

6.2. TYPE IA FBG FORMATION UNDER VARIOUS CONDITIONS

Clearly the choice of fibre, or more precisely the level of core dopants, has a great effect on the gratings formed within, as do the techniques employed for increasing the photosensitivity of fibres.

6.2.1. Type IA formation in germanosilicate and boro-germanosilicate fibre

It is widely accepted that high levels of germanium (Ge) added to the core of optical fibres increases the photosensitivity of the fibre. A consequence of Ge-doping is that the refractive index of the fused silica increases – indeed Corning SMF28 uses 2-3 mol% Ge to increase the refractive index of the core above that of un-treated fused silica (SiO_2) giving the necessary step index for optical guiding and a NA of 0.14. Several fibre manufactures offer Ge-doped cores with extremely high levels of Ge doping, such as Fibercore FA1631211 where the NA increases to 0.30. The consequence of this high

level Ge doping is that these fibres become extremely difficult to splice to standard telecom fibre without significant losses (typically 1-10dB). In order that highly intrinsically photosensitive fibres may be manufactured and used in applications where splicing to standard fibre is necessary boron (B) is often added as a co-dopant since its presence as the opposite effect of Ge on the refractive index of fused silica in that it reduces the refractive index. By balancing the B and Ge levels, fibre manufacturers are able to make fibres which are highly photosensitive, without the requirement of costly hydrogenation, and which possess NA values extremely close to that of standard fibre. For example Verillion IF01001410101 fibre has an NA of 0.18 and Fibercore PS1250/1500 has an NA specified as 0.12 to 0.14; these fibres may be reliably spliced to Corning SMF28 with losses in the range of only 0.05-0.2dB (typically). Until this work, the effect of dopant levels and the differences between Ge and B/Ge co-doping had not been studied with relation to type IA gratings.

6.2.1.1. Grating inscription

Fibre samples from Verillion and Fibercore were hydrogenated at 80°C at 200Bar for 68 hours and allowed to cool for a further 24 hours after which time the pressure fell to 180Bar. The samples were then stored at -40°C for a short time until their use. Gratings were inscribed using the usual scanning phasemask technique with a 2mm aperture used to ensure an accurately uniform exposure profile along the length of the grating. The stage was scanned at 0.25mms-1 with 200mW optical power delivered to the fibre. The samples consisted of two different B/Ge co-doped and three different Ge doped samples as summarised in Table 6.1. Identical gratings were inscribed in each fibre with sufficient scans that the grating matured, as defined by the observation of the mean index shift saturating.

The formation of these gratings has been plotted in terms of the mean index shift, as depicted by the Bragg wavelength shift, and the integrated coupling constant as defined by Equation 2.7 which yields a comparison of the modulated index. This data is shown below in Figure 6.1 where there are 3 clear trends. The red and blue traces represent the Verillion and Fibercore B/Ge co-doped fibres respectively, whilst the green, black and

yellow traces are those of the Fibercore Ge doped traces. The gratings in B/Ge fibres form significantly faster than those in Ge doped fibres, indeed the Ge only fibres require more than 5 times more energy to form given the same laser intensity and hydrogenation conditions.

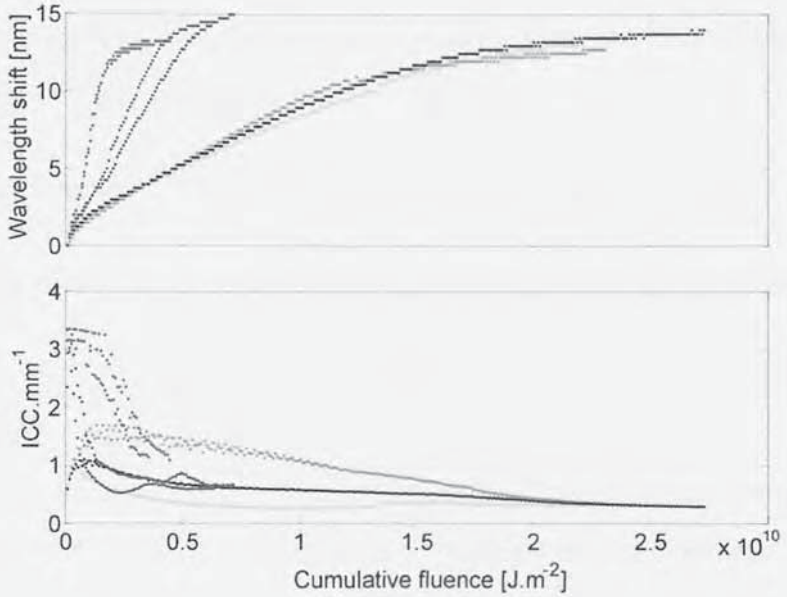

Figure 6.1 Evolution of type IA gratings shown in terms of the wavelength shift (upper) and integrated coupling coefficient (lower) in Verillion IF01001410101 B/Ge (red), Fibercore PS1250/1500 B/Ge (blue), Fibercore SD079-00B Ge (green), Fibercore SD748A-00AB Ge (black) and Fibercore Ge SD254-01B (yellow). This figure shows that fibres without boron-doping form IA gratings significantly slower than doped fibres.

The lower part of Figure 6.1 shows that both samples of B/Ge fibre produced type I gratings of similar peak amplitudes at approximately the same rate. Although the IA grating grew more rapidly in the Verillion sample, it did not reach the same mean index shift as the Fibercore sample.

Fibre Sample	$\lambda_{BR}^{I}(T)$	$\lambda_{BR}^{IA}(T)$	$\frac{\lambda_{BR}^{I}(T)}{\lambda_{BR}^{IA}(T)}$
	pm°C^{-1}	pm°C^{-1}	%
Verillion IF01001410101 B/Ge	8.5	7.7	10.4
Fibercore SD254-01B Ge	10.2	9.4	8.5
Fibercore SD079-00B Ge	10.6	9.8	8.2
Fibercore SD748A-00A B/Ge	11.1	10.3	7.8
Fibercore PS1250/1500 B/Ge	8.7	7.7	13.0

Table 6.1 A summary of the temperature coefficients for the fibres tested in this experiment.

The Bragg wavelengths and temperature coefficients of the samples are shown in Table 6.1. Table 6.1 shows that the choice of fibre has an effect on the individual grating temperature coefficients in keeping with the findings of Cavalerio *et al* [122] and Guan *et al* [123]. However, this variance in thermal coefficients not withstanding, the results for the boron free fibres seem to suggest that boron acts as a catalyst during the formation of IA gratings since the final properties are not dissimilar to the B/Ge doped fibres which required significantly less energy to form.

Section 6.4.1 discusses the 1400nm absorption bands for these samples.

6.2.2. Hydrogen levels: a comparison of IA and IIA grating formation

The similarities between IA and IIA gratings are fairly obvious. The fundamental difference is simply that IA gratings require hydrogen loading before inscription and IIA gratings expressly do not (refer to Section 2.2.3.2). This condition produces markedly different FBG growth profiles, both in terms of the growth to the point of a standard type I grating and beyond that to either a IA or IIA grating. The most obvious difference is in the mean index evolution of the gratings; it has by now been well documented in this thesis that IA gratings undergo a large red shift. By comparison, IIA gratings undergo a slight red shift followed by a small blue shift with the absolute wavelength shift being ~40 times smaller than that of IA gratings.

In order to accurately compare IA and IIA gratings, two identical samples of Fibercore PS1250/1500 were prepared; one was hydrogenated at 80°C / 200bar for 68 hours and the other was left as virgin fibre. A standard scanning beam inscription setup was used with a static phasemask and 0.5mm aperture card in order that the effect of cumulative fluence on the mean and modulated index change could be recorded. Figure 6.2 shows the data taken with the type IA grating shown in red, and the IIA in green (this convention shall be maintained for the remainder of this section). As expected, the IA grating shows a red shift of ~15nm, whereas the IIA shows a blue shift of <0.5nm.

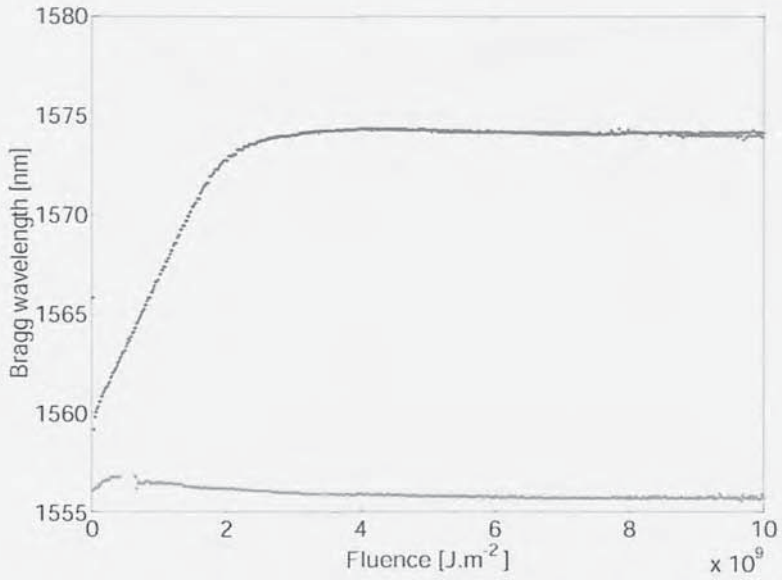

Figure 6.2 A comparative figure showing the differences between the mean index evolution of type IA and type IIA gratings. The IA grating undergoes a large red shift, whereas the IIA grating undergoes a significantly smaller blue shift. The red plot denotes the characteristics of a type IA grating and the green plot denotes a IIA grating.

The contrast in growth profiles does not end with the mean index change. The modulated index shift is also significantly different, as shown in Figure 6.3. The initial grating grown in both fibres is termed a type I; in the non-hydrogenated sample the maximum grating strength is <0.5dB whereas the hydrogenated sample produces a grating which is ~15dB more or less instantaneously. Following the initial formation of standard gratings, the grating in the non-hydrogenated sample is erased completely before regenerating to a maximum reflectivity and then decaying once more. By contrast, the hydrogenated sample does not decay completely but does decay significantly (by ~12dB) before regenerating to a reflectivity comparable to the IIA grating. From this point onwards, the IA and IIA gratings appear very similar in terms of their modulated index changes.

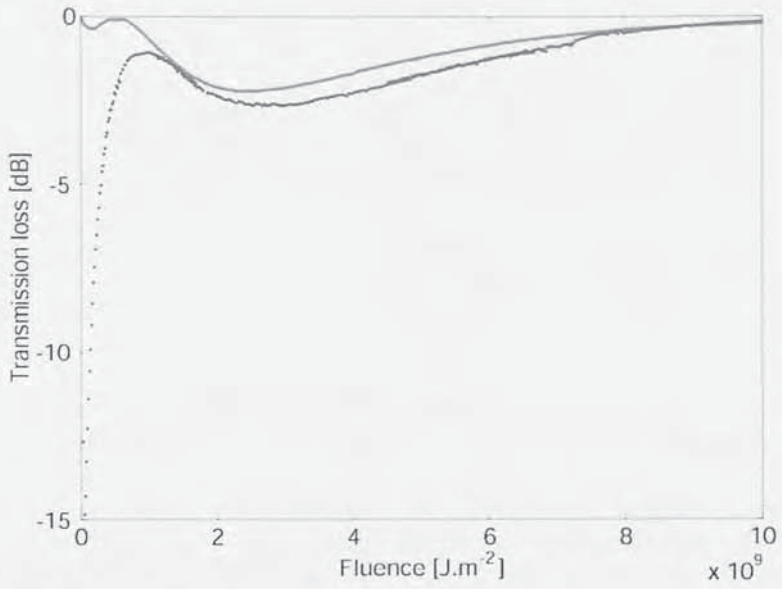

Figure 6.3 A comparative figure showing the differences between the modulated index evolution of type IA and type IIA gratings. The IA grating reaches peak reflectance within the first few seconds before decaying and re-forming slightly, whereas the IIA grating reaches an initial maximum before decaying completely and then re-forming to produce a significantly stronger grating. The red plot denotes the characteristics of a type IA grating and the green plot denotes a IIA grating.

It should be noted, however, that the point at which the modulated index change depicted in Figure 6.3 becomes similar for both gratings corresponds to the point in Figure 6.2 where the mean index change stabilises. The steady decay in reflectance of both samples may simply be caused by small fluctuations in the position of fibre or phasemask reducing the fringe visibility of the gratings.

6.2.2.1. Hydrogen outgassing

During the repeated manufacture of IA gratings over a large timescale and using many different batches of hydrogenated fibre of all types, it was noted that the quality of the gratings produced and the rate at which they matured was highly dependent on the concentration of hydrogen in the fibre. In order to demonstrate this and, to some extent, quantify the relationship, two batches of different fibre (Verillion IF01001410101 and Fibercore PS1250/1500) were hydrogenated at 80°C / 200 bar for 68 hours. The fibre was then stored at room temperature and 3 gratings were written in each sample at varying time intervals, as set out in Table 6.2.

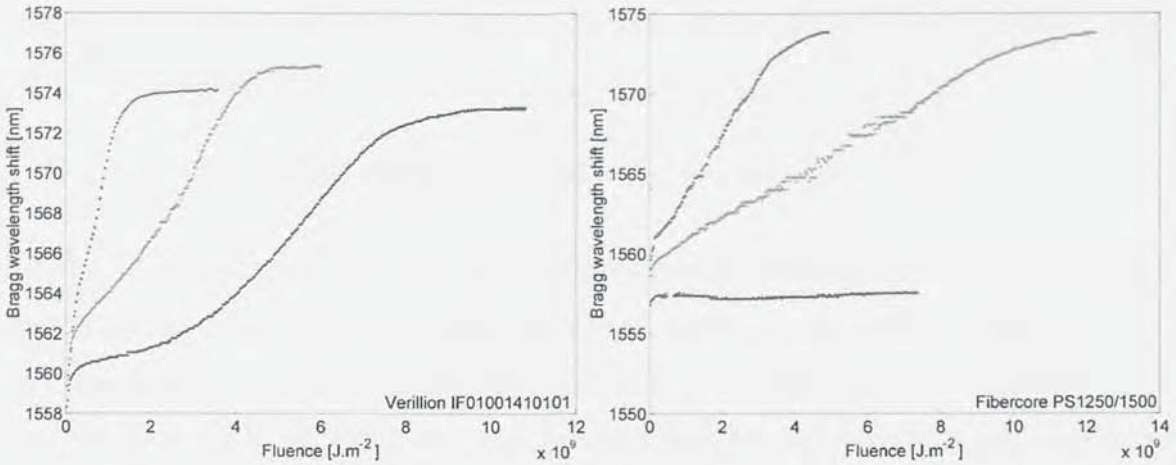

Figure 6.4 This figure shows the evolution of IA gratings written in (a) (left) Verillion IF01001410101 and (b) (right) Fibercore PS1250/1500. Each sample was hydrogenated and stored at RTP such the outgassing occurred. The traces represent successive gratings written with progressively less hydrogen. (b) Shows that after sufficient outgassing had occurred, a IIA grating formed. Refer to Table 6.2 for details of the hydrogen outgassing conditions and the colour code used.

Figure 6.4 shows the results of the experiment and clearly indicates that there is a relationship between the hydrogen content of the fibre and the rate at which the IA gratings form in the fibres. In the case of Figure 6.4b the final trace, shown in blue, shows an approximate IIA growth profile, indicating that the hydrogen is almost completely outgassed.

Verillion		t (hours)
Red	FBG1	0
Green	FBG2	23
Blue	FBG4	92

Fibercore		
Red	FBG2	22
Green	FBG3	48
Blue	FBG6	165

Table 6.2 Summary of the hydrogen outgassing times for the gratings shown above in Figure 6.4

It was discussed in Section 2.2.3.2 that Canning *et al* [46] have shown that pre-sensitisation of the fibre by hydrogen loading followed by hydrogen outgassing may be used to enhance the photosensitivity without forming a large OH band. However, it has

been shown in this section that type IA gratings do not form in pre-sensitised fibres without the presence H_2.

6.2.2.2. Hot or cold hydrogenation?

In order to determine if the type of hydrogenation, be it room temperature or heated, would have an effect on the formation of type IA gratings, two identical batches of fibre were prepared. Each batch consisted of Corning SMF28 standard telecoms fibre, Verillion B/Ge co-doped fibre and two different samples of Ge-only doped. One batch was hydrogenated at 80°C, 190Bar for 93 hours and allowed to cool to room temperature over 24 hours by which time the pressure had fallen to 160Bar; the other sample was hydrogenated for in excess of 4 months at 180Bar at room temperature. In the following section, data relating to the hot hydrogenation will be coloured red whereas the room temperature samples will be blue.

It is well known that fibres hydrogenated at a lower temperature will achieve a higher concentration of hydrogen within the core but will require a significantly longer time to reach saturation. Refer to Chapter 2, Section 2.2.3.3. Equation 2.2 shows that we may calculate the saturation level of hydrogen molecules within the core as follows:

Equation 2.2
$$\kappa_{sat} = 3.3481 p \exp\left[\frac{8670 J/mol}{RT}\right]$$

where κ_{sat} is the equilibrium solubility of the hydrogen, p is the pressure of the hydrogen in atmospheres, T is the temperature in Kelvin, and R is the gas constant (8.31451 J/K/mol).

Since both samples were hydrogenated for times sufficient for the equilibrium condition to be achieved we may calculate the hydrogen concentration within the fibre samples by applying Equation 2.2 to the hydrogenation conditions outlined above. The results are shown below in Table 6.3.

	Temperature K	Pressure atmospheres	Time hours	κ_{sat} ppm
Hot	353	178	93	11400
Cold	298	188	>384	21000

Table 6.3 A summary of the hydrogenation conditions for the hot and cold hydrogenated samples, sowing the time, temperature and pressure of hydrogenation and the calculated saturation level within the core of the fibre.

Gratings were inscribed using the usual scanning phasemask technique with a 1mm aperture used to ensure an accurately uniform exposure profile along the length of the grating. The stage was scanned at $1mms^{-1}$ with 130mW optical power delivered to the fibre. Figure 6.5 shows the growth rate for the hot and cold samples in the various fibre types. There is a clear trend that fibres hydrogenated at room temperature grew faster then those heated during the hydrogenation process; in alternative terms, the fibres containing more hydrogen formed type IA gratings with less energy.

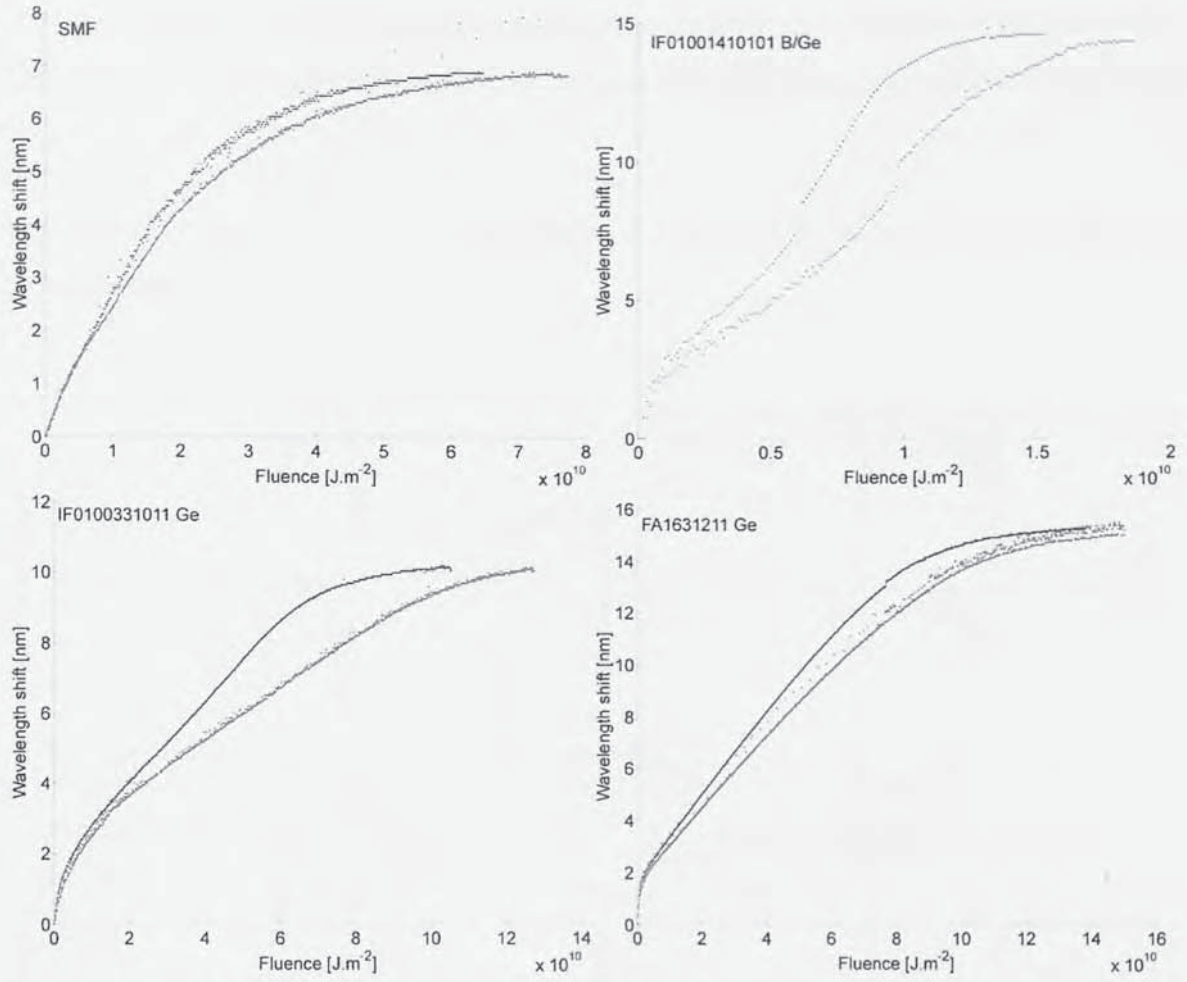

Figure 6.5 The growth rate of IA gratings in fibre types as indicated, for hot (red) and cold (blue) hydrogenation conditions. This figure shows that in all cases, the cold hydrogenated samples form faster than the hot samples. This shows that the inscription rate is related to the saturation of H_2 within the fibre.

In order that the IA gratings might have a reference grating whose properties are well understood, a 1mm type I grating was written within the same section of each fibre. Figure 6.6 shows the spectra of each sample before (upper) and after (lower) annealing at 80°C for 96 hours. Figure 6.6 highlights that the gratings written in Verillion IF01001410101 B/Ge co-doped fibre where both grating types differ significantly in amplitude and the type I grating appears to be slightly offset in wavelength. However, the remainder of the gratings are extremely similar between the hot and cold hydrogenated samples and do not seem to exhibit any significant spectral characteristics. The wavelength difference between Bragg resonances of the type I and IA gratings is summarised in Table 6.4 for the pre- and post-annealing gratings. The wavelength and

amplitude decay data for these gratings during annealing may be seen in Section 6.6.3. This may be an indication that H_2 acts as an essential catalyst in the reaction which forms IA gratings.

Note that the type I grating in the cold sample of FA1631211 was not inscribed due to an experimental oversight.

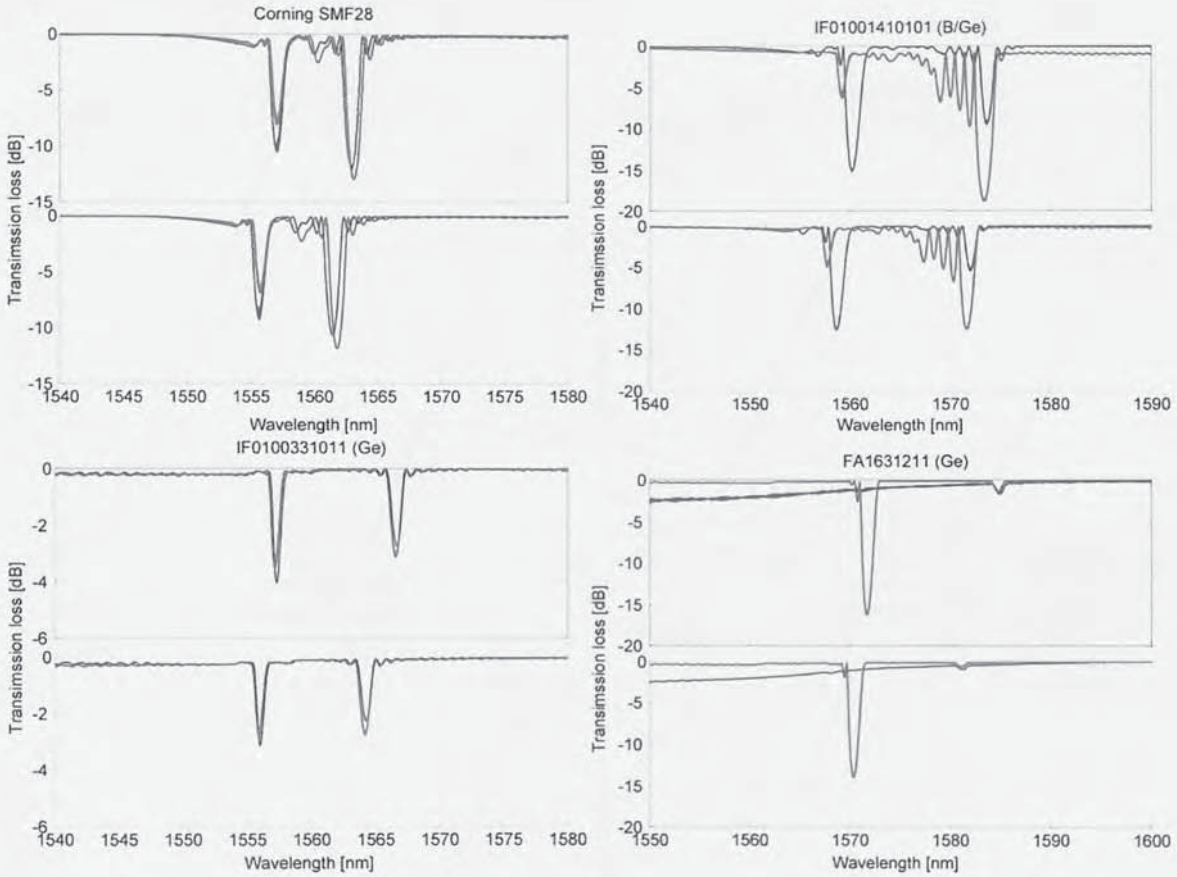

Figure 6.6 Pre- (upper traces) and post- (lower traces) annealing spectra for type I and type IA gratings written in fibre types as indicated, for hot (red) and cold (blue) hydrogenation conditions. This figure shows no significant spectral trend between the hydrogenation conditions.

The thermal coefficients of the gratings were also calculated by means of placing each individual grating on a temperature controlled block within an insulated chamber. The temperature was controlled by means of a Peltier device connected to a standard computer operated laboratory temperature controller. Temperature feedback was made possible by the placement of a calibrated thermistor and the Bragg wavelength was measured by passing broadband IR radiation from a powerful ASE source through the

fibre to an OSA with 0.06nm RBW. The centroid detection algorithm (CDA) was used to accurately locate the central Bragg resonance. A computer was used to set and record the temperature of the grating and to record the OSA traces. 20 readings were taken for each temperature and are plotted in Figure 6.7 for each grating and fibre type, as indicated. The thermal coefficient for the cold hydrogenated sample of Verillion FA1631211 could not be attained as the fibre did not survive handling after the annealing process. The thermal coefficients are summarised in Table 6.4.

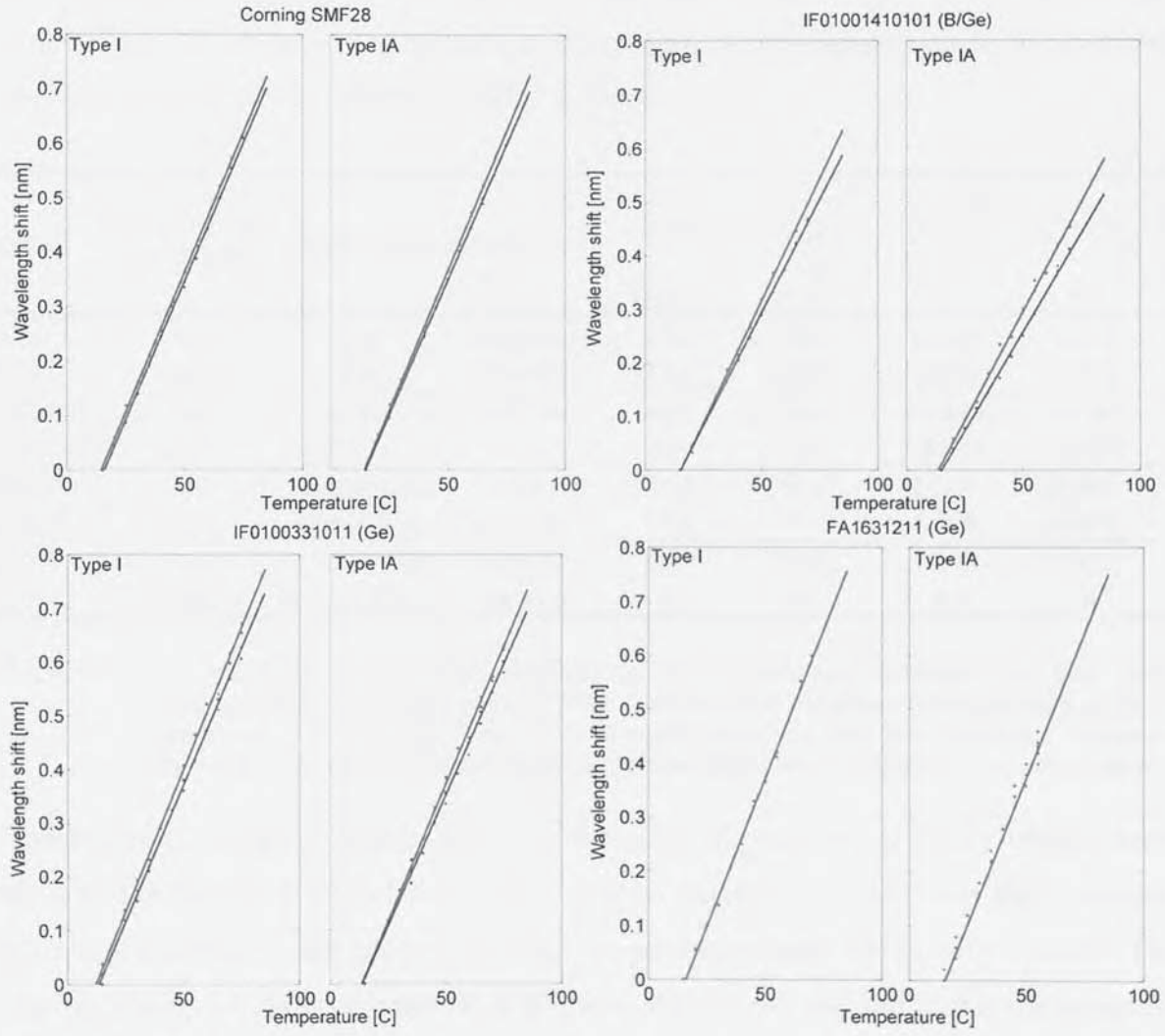

Figure 6.7 This figure shows the thermal coefficients for type I (left-hand traces) and type IA (right-hand traces) gratings written in various fibre types (as indicated) for hot (red) and cold (blue) hydrogenation conditions. This shows that in every measurable case, the thermal coefficient of both grating types was lower for the samples with higher concentration of H_2 molecules in the fibre.

It is clear from Figure 6.7 that in all cases where temperature coefficients could be calculated for both the hot and cold hydrogenated fibres (note that the cold FA1631211 sample was spoiled during the measurement) there is a clear and definite trend that the cold samples possess a lower temperature coefficient ($\lambda_{BR}(T)$). Moreover it is apparent from Figure 6.7 in conjunction with the table of summarised data, Table 6.4, that the difference between the $\lambda_{BR}(T)$ values for type I and IA gratings is larger when the samples were hydrogenated at 25°C in preference to 80°C. Although this surprising result may not be completely explained, it has clear implications for situations where the thermal properties of IA gratings may be used to compensate for temperature shifts in a sensing application (refer to IA-I sensors, Chapter 5, Section 5.6).

Reference	Hydrogenation conditions	Fibre type	Manufacturer	$\lambda_{BR}^{I}(T)$	$\lambda_{BR}^{IA}(T)$	$\frac{\lambda_{BR}^{I}(T)}{\lambda_{BR}^{IA}(T)}$	$\lambda_{BR}^{IA}-\lambda_{BR}^{I}$	$\lambda_{BR}^{IA}-\lambda_{BR}^{I}$ annealed
				pm°C^{-1}	pm°C^{-1}	%	nm	nm
SMF28	hot	Std	Corning	10.2	10.2	**0.039**	5.848	**5.761**
SMF28	cold	Std	Corning	10.2	9.9	**2.434**	6.076	**6.032**
IF01001410101	hot	B/Ge	Verillion	9.1	8.1	**11.853**	14.147	**13.925**
IF01001410101	cold	B/Ge	Verillion	8.4	7.4	**14.334**	13.474	**13.375**
IF0100331011	hot	12mol%Ge	Verillion	10.6	10.3	**3.247**	9.387	**8.284**
IF0100331011	cold	12mol%Ge	Verillion	10.2	9.8	**4.329**	9.365	**8.277**
FA1631211	hot	21mol%Ge	Verillion	11.0	10.8	**1.648**	13.067	**10.757**
FA1631211	cold	21mol%Ge	Verillion	xx	xx	**xx**	xx	**xx**

Table 6.4 A summary of the data highlighting the differences between hot and cold hydrogenation in various types of fibre. It shows that the fibres hydrogenated at 25°C produced gratings with lower thermal coefficients and that the difference between the type I and the IA thermal coefficients was larger with a higher H_2 saturation level.

These results compare excellently with those of Brennan *et al* [111] which were discussed in Section 3.3.2.4. Brennan *et al* studied the effects of extremely high pressure hydrogen loading on the growth of FBGs in germanosilicate fibres with ~9mol% Ge doping. Figure 6.8 shows the results of Brennan *et al*'s work and shows that the presence of more hydrogen in the core of the fibre reduces the level of energy required to bring about the mean index change. Brennan *et al* did not report the temperature coefficients of the final gratings, but it would be reasonably to assume that they exhibit a similar dependence as those outlined above.

Figure 6.8 Reproduced from [111]. The growth curves of gratings written under similar conditions for 30mins for different hydrogenation pressures, as indicated. This figure complements the results shown above and confirms the result that the rate at which IA gratings may be inscribed is related to the saturation of H_2 molecules within the core.

6.3. REFRACTIVE INDEX MODEL

It is clear from the large red shift during inscription that the refractive index profile of type IA gratings is markedly different from standard gratings and that it consists significant mean and modulated refractive index components. This is depicted in Figure 6.9. During the grating inscription process the period of the grating does not change, therefore we may readily calculate the increase in mean refractive index from the measured shift in the Bragg resonance. An example case exhibited a shift of 18.50nm which equates to a mean refractive index increase of ~1.8x10-2. The modulated refractive index may be approximated according to Equation 2.14:

Equation 2.14
$$\Delta n_{\text{mod}} = \left({}^{\lambda_{BR}}\!/_{\pi L} \right) \tanh^{-1}\left(\sqrt{1 - T_{\min}} \right)$$

In this example case we have λ_{BR} = 1565nm, Tmin = -10.4dB and L = 2mm which yields $\Delta n_{\text{mod}} \approx 4.65\text{x}10^{-4}$.

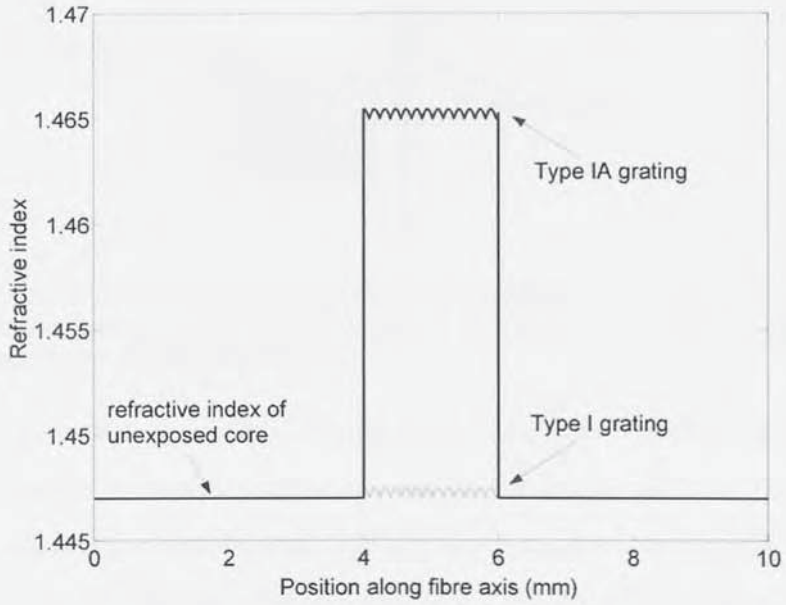

Figure 6.9 The refractive index model for IA gratings. The small modulated index change is offset by the large mean index change of IA gratings. It is this huge mean index change that differentiates IA gratings from all other types.

Figure 6.9 shows the ideal case where all parts of the grating receive the same exposure and consequently only one central Bragg resonance is present.

6.3.1. Increase in numerical aperture of germanosilicate fibre

If blank beam UV radiation is used to create the large characteristic mean in the core refractive index, it is possible to increase the NA of the fibre without writing a grating. This may be desirable for applications where there is a need to tailor the acceptance angle of a fibre. In order to show this principle, two samples of hydrogenated Verillion B/Ge co-doped fibre were prepared. In one sample a scanning UV laser at 244nm was used to fabricate a type IA mean index change in a 10mm section of the core, the centre of which was then cleaved, giving a fibre end with a modified NA. The control fibre was a section of identical fibre with a similar cleave made in an untreated section.

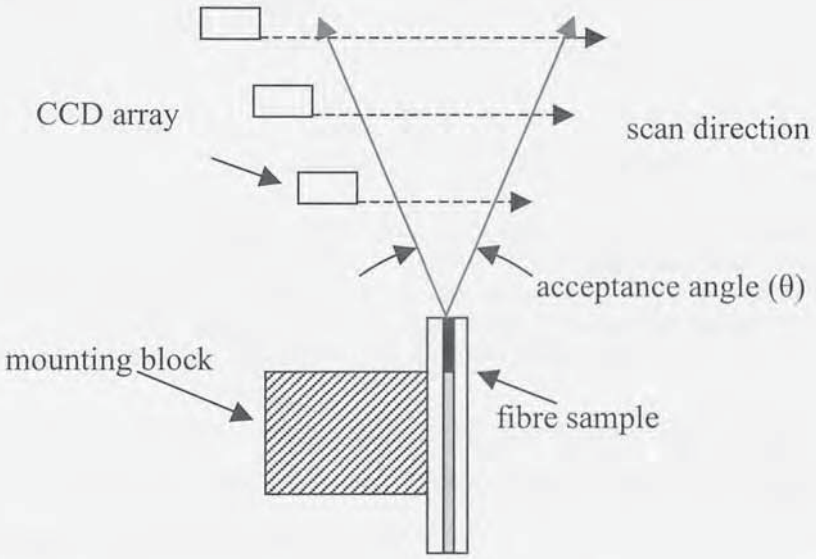

Figure 6.10 Schematic showing the arrangement of apparatus used to map the far-field image of radiation being emitted from samples of IA treated and virgin B/Ge fibre in a bid to calculate the NA of the samples.

These samples were then securely mounted as indicated by Figure 6.10 in a specifically designed experiment to measure the diameter of the beam radiated from the fibre at varying heights above the cleaved end. The apparatus used a scanning CCD array, coated for sensitivity in the IR region (refer to Chapter 4, Section 4.3.2, Figure 4.7), which was controlled by a motorised translation stage. The fibres were connected to a tuneable laser outputting 1mW at 1511.2nm (chosen to coincide with the peak responsivity of the CCD coating). The beam diameters at increasing heights above the fibre were calculated from a contour plot formed by overlaying the individual profiles saved from the CCD at 0.1mm

intervals. These are shown for the treated and untreated fibre samples in Figure 6.11a and Figure 6.11b respectively.

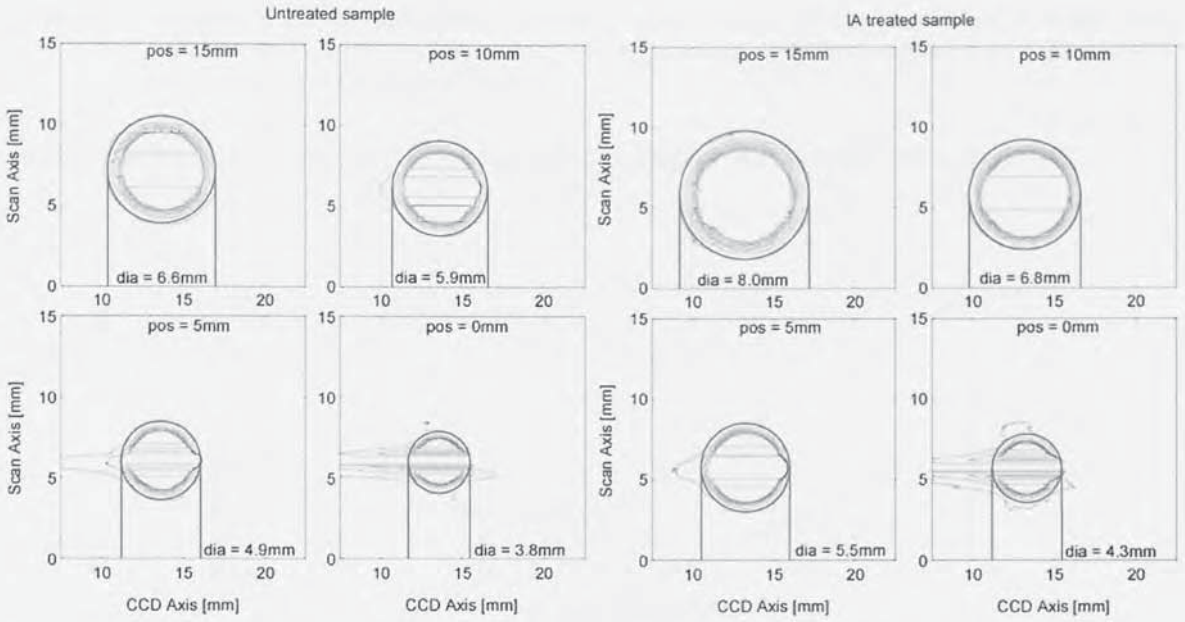

Figure 6.11 Contour plots showing the beam diameters of 1511.2nm radiation emitted from samples of virgin (left) and IA treated (right) Verillion fibre at various heights (as indicated) above the fibre cleave. The plots show that the NA of the IA treated fibre is significantly larger than the virgin fibre. The horizontal contours in some figures are a result of the radiation saturating the CCD array.

The measured diameters are related to height above the fibre cleaves by Figure 6.12 which also shows the gradient of the acceptance cone vector. The acceptance angles may be calculated from Figure 6.12 as follows:

Equation 6.1 $$\theta = \arctan(G)$$

Where θ is the acceptance angle and G is the gradient of the acceptance cone vector. The acceptance angle may also be calculated from classical geometrical optics as follows:

Equation 6.2 $$\theta = \arcsin(NA)$$

Where NA is the numerical aperture of the fibre. These equations have been applied to the data to produce Table 6.5, which contrasts experimental and theoretical results.

Fibre Sample	NA	θ, Equation 6.2	G	θ, Equation 6.1
Virgin	0.161	9.3	0.188x	10.6
IA treated	0.247	14.3	0.248x	13.9

Table 6.5 Summary of the calculated and measured values for the acceptance angle of IA treated and virgin Verillion B/Ge fibre showing excellent agreement between the calculated and measured NAs.

Clearly the measured and calculated acceptance angles are in excellent agreement.

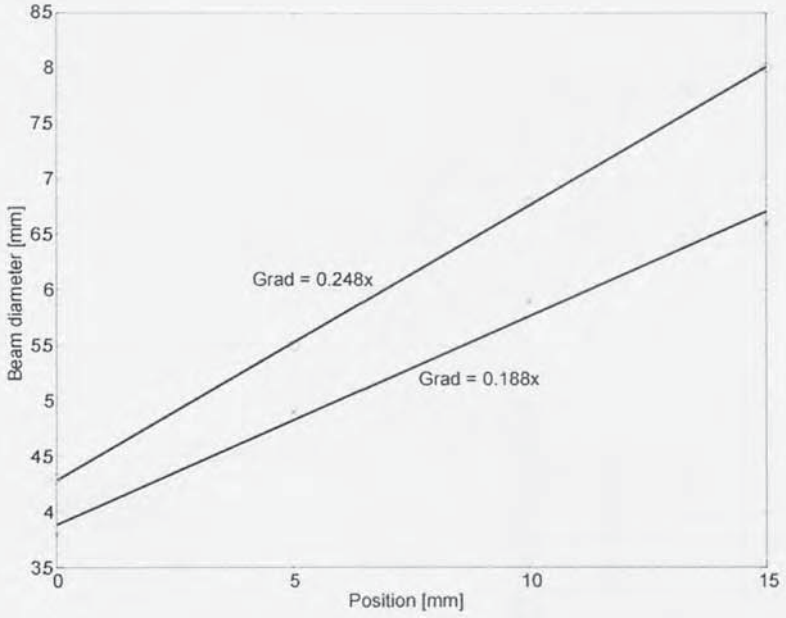

Figure 6.12 A plot showing the gradients of the acceptance cone vectors for IA treated (x) and virgin (o) Verillion B/Ge fibre. It shows that IA treatment increases the acceptance angle of the fibre.

6.3.2. Minimum index change resolution

The type IA effect manifests itself not as a grating with large fringe visibility, but as an increase in the mean refractive index of the core. It is therefore important to measure the minimum axial resolution of the IA index change. In order to do this the side diffraction pattern generated through side illumination by a visible He-Ne laser at 633nm was utilised.

In an unexposed section of Verillion B/Ge fibre, the refractive indices of the core and cladding are $n_1 = 1.4738$ and $n_2 = 1.4650$ respectively. This yields a Δn of $\sim 6 \times 10^{-3}$ and an NA of 0.161. In the case of a section of exposed fibre containing a type IA mean index

change the NA has increased to 0.247 (refer to Table 6.5). This increase in the numerical aperture causes a significantly different diffraction pattern when visible radiation is focused into the core.

When a small laser spot is focused in to the core of a standard optical fibre (as shown in Figure 6.13), the difference in refractive index of the core and cladding form a diffraction

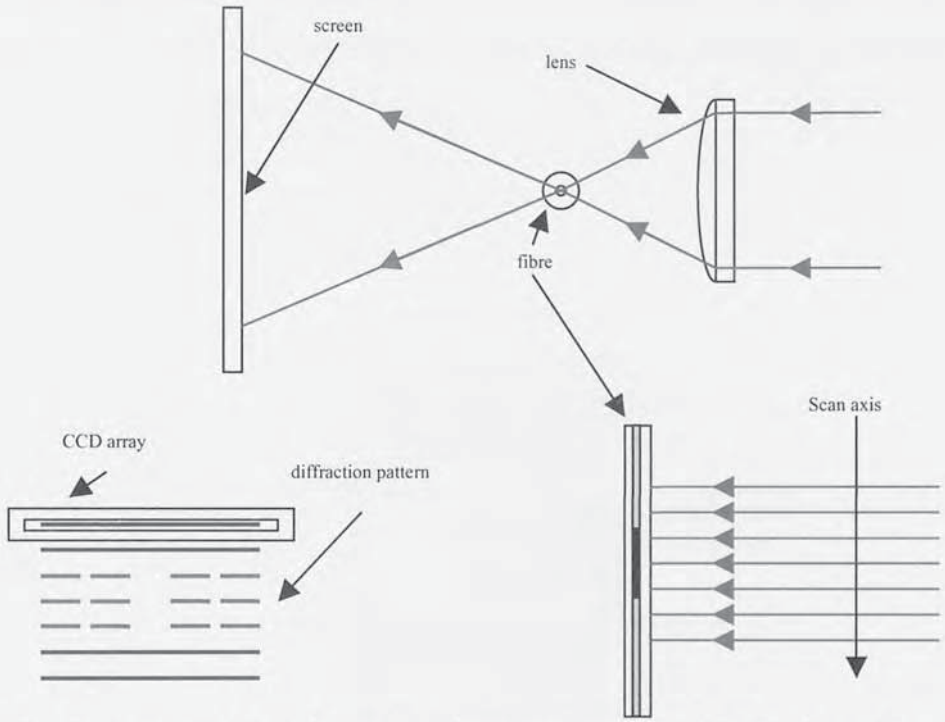

pattern that is seen as a line when viewed on a screen placed behind the fibre with respect to the illuminating source. In this case, the beam steering and focusing optics were mounted on a computer controlled translation stage and the fibre was securely fixed between accurately positioned clamps. The screen was replaced with a Sony ILX511 CCD array (refer to Chapter 4, Section 4.3.2, Figure 4.6) whose lateral position was also determined by the position of the translation stage. To this end, the intensity profile of the visible radiation diffracted by the fibre core-cladding interface could be accurately mapped along the axis of the fibre by moving the translation stage and storing the profile captured by the CCD. By overlaying many such profiles it is possible to build up a complete picture of the difference between the core-cladding refractive indices along the fibre axis.

Figure 6.13 Schematic experimental outline showing the dispersive effect of an optical fibre when illuminated from the side by a visible laser source (top), the positioning of the CCD array in the experiment with respect to the diffraction pattern (bottom, left), and the manner in which the source should be scanned along the axis of the fibre (bottom, right).

A IA mean index change was induced with a uniform intensity profile by using a scanning blank-beam inscription set up with a 2mm aperture. The fibre was then aligned in the apparatus and He-Ne diffraction patterns were saved every 50μm along the axis of the fibre for a 5mm section encompassing the IA grating. This data is shown in the form of a contour plot by Figure 6.14 below.

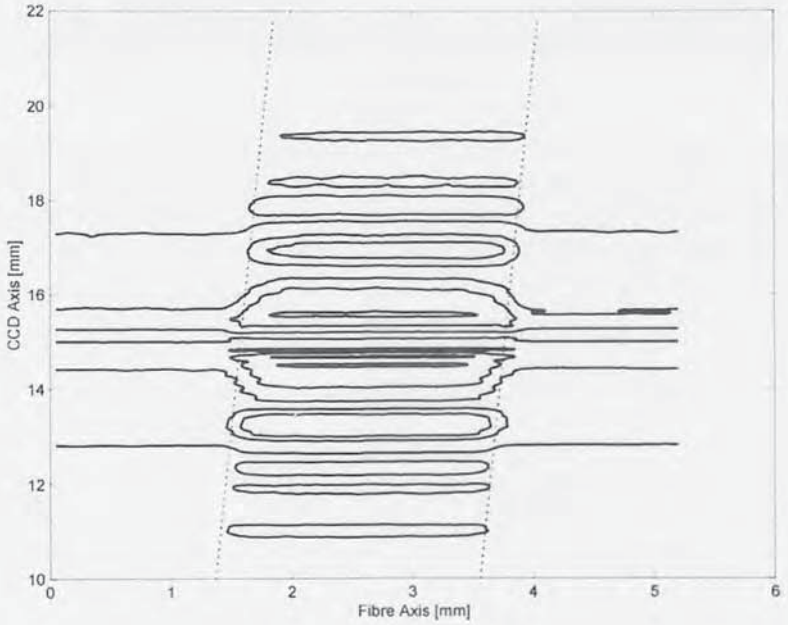

Figure 6.14 A contour plot showing the image of diffracted light from the fibre. The central peak intensities show the position of the IA mean index change in the fibre.

Figure 6.14 clearly shows the difference in diffraction pattern between the virgin fibre and the area containing the IA grating (within the dashed lines). There is a slight tilt on the profile, caused by a misalignment of the CCD. Although extremely illustrative, this plot alone is not particularly useful in ascertaining the minimum resolution of the IA index change. Figure 6.15, shows the intensity of the fringes shown in Figure 6.14 above. This plot clearly shows that there is decay in the mean index from its peak value to that of virgin fibre which takes place over approximately 0.5mm. This would indicate that the IA mean index shift is a diffuse process and may suggest that it is caused by a heating effect.

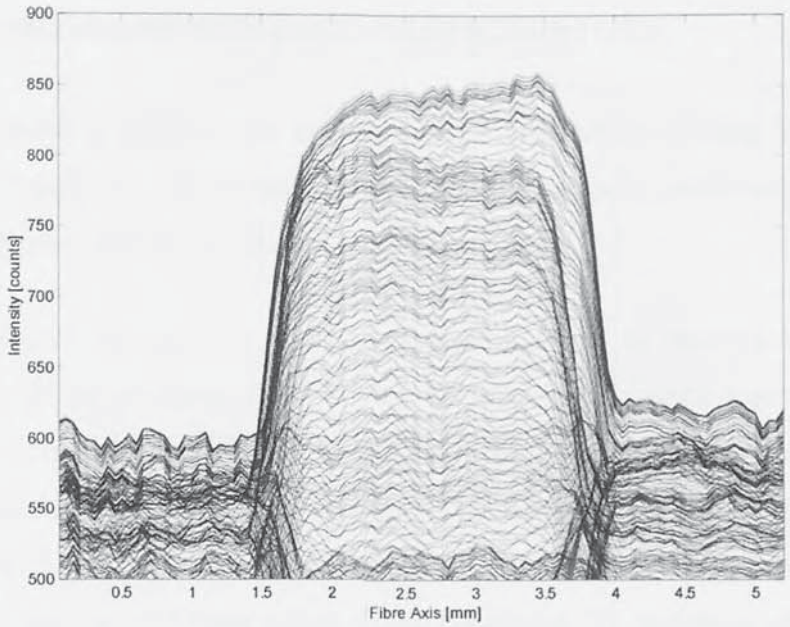

Figure 6.15 A plot showing the overlaid intensities of the diffraction patterns along the fibre axis of a type IA grating. The central peak corresponds to the position of the grating in the fibre and may be used to calculate the resolution of the IA index change as the slope of the sides represents the decay in the mean index at the edge of the IA change.

6.4. 1400NM ABSORPTION BAND CHARACTERISTICS

The absorption band at 1400nm has already been introduced in Section 5.3.3 wherein it was shown by Figure 5.5 that the rate of mean index change is paralleled by the growth rate of the absorption band at 1400nm.

Figure 6.16a shows the growth of the absorption band in hydrogenated Verillion IF01001410101 B/Ge co-doped fibre during IA inscription. Each trace represents an additional scan from a 244nm UV laser at 1mm/s over a 5mm exposure length and shows how the absorption band matures and saturates. This confirms the results of Canning *et al* [46] (see Section 2.2.3.2) and shows excellent agreement with their data (see Figure 2.1), wherein the OH band at ~1400nm grows under continued UV exposure before saturating in strength. Note that the peak of the curve is just beyond 1400nm under continuous UV exposure, indicating that the anticipated contributions from a mixture of SiOH (1390 nm) and GeOH (1410nm) bands are biased in favour of the GeOH bonds for this fibre. Deconvolution of the data shows the presence of two peaks as shown in Figure 6.16b. The solid trace represents the absorption band as measured with an optical spectrum analyser. The dashed and dotted traces represent the de-convolved Gaussian peaks within the absorption band and the bold solid trace shows the addition of these two traces which closely follows the experimental data. The deconvolved peaks are located at 1401.1nm (assigned to GeOH contribution) and 1424.1nm (as yet unassigned). There is also no evidence of a hydride band at 1500nm that is most often associated with GeH; this may indicate the rapid conversion of the hydride to a more stable hydroxyl form.

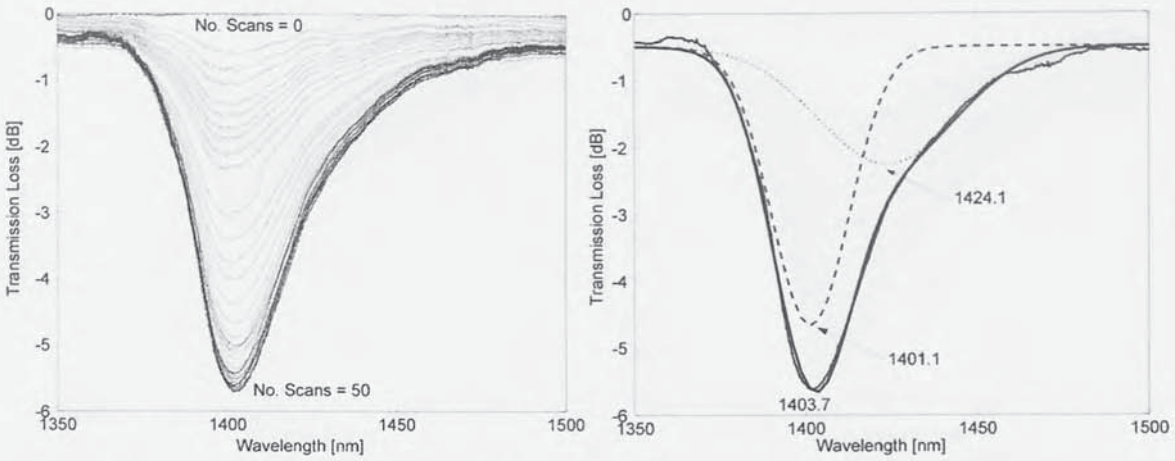

Figure 6.16 (a) (left) The absorption band at 1400nm, shown for continuing exposure and (b) (right) the absorption band at 1400nm deconvolved to show its constituent peaks. This figure shows that the OH band is made up from competing OH species.

6.4.1. OH Band structure in different fibre types

The gratings manufactured in Section 6.2.1.1 in the fibre types summarised in Table 6.1 were monitored for transmission loss at 1400nm. The OH bands formed by these different fibre types are shown in Figure 6.17. For each figure, successive scans with the inscribing laser are represented by another OSA trace which shows increasing loss with every pass until saturation. Note that the broadband loss also increases with continuing exposure.

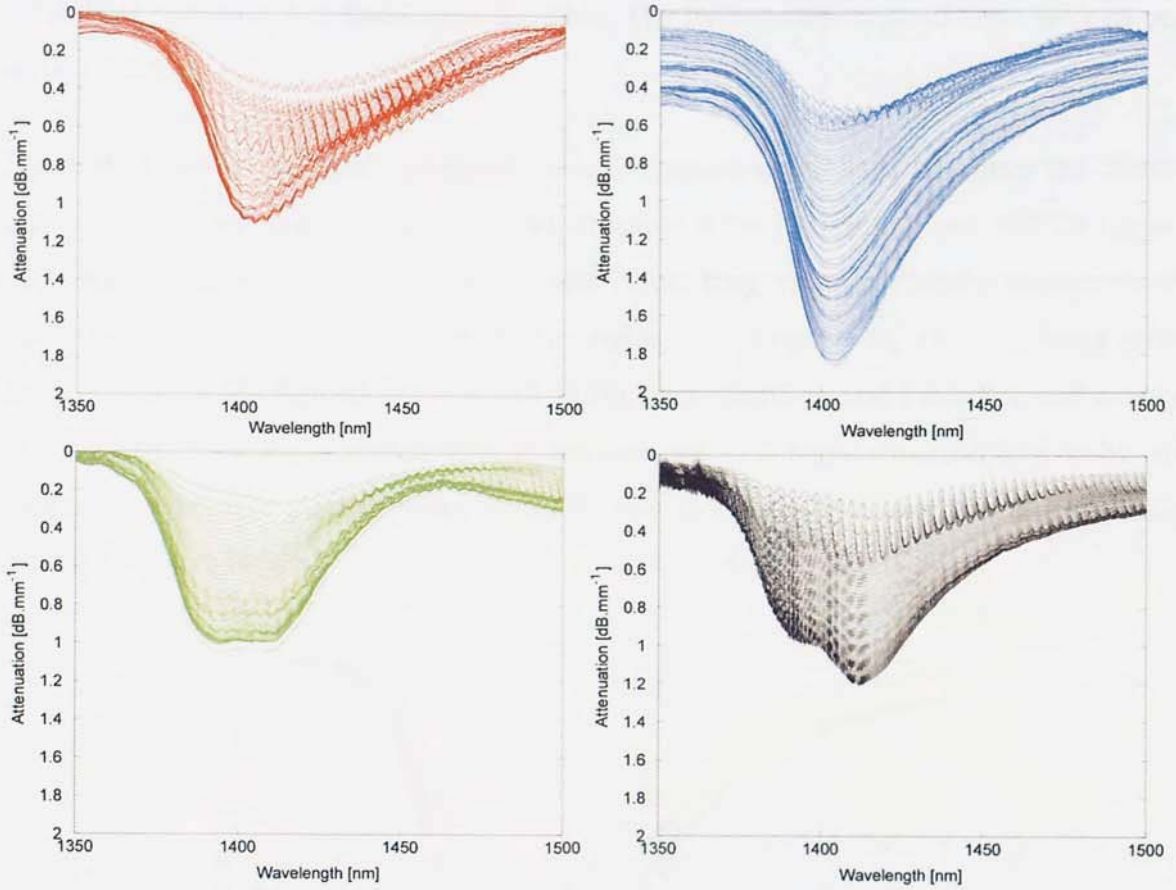

Figure 6.17 Evolution of the OH band associated with the formation of IA gratings during inscription in Verillion IF01001410101 B/Ge (red), Fibercore PS1250/1500 B/Ge (blue), Fibercore SD079-00B Ge (green) and Fibercore SD748A-00AB Ge (black). This figure shows that the competing OH species have are weighted according to fibre dopants and doping levels.

There are significant spectral similarities between the different fibre types shown in Figure 6.17. The B/Ge co-doped fibres (top two plots, red and blue) both show the same fundamental shape as deconvolved in Figure 6.16b, whereas the three Ge doped fibres show the presence of another peak at around 1390nm possibly due to the influence of SiOH.

6.4.1.1. OH Band formation in 20mm blank beam exposed sections

In order to further explore the differences between the shapes of the OH bands in different fibres another experiment was performed where 20mm sections of the sample fibres were exposed to blank-beam UV radiation. The scan speed was 1mms^{-1} with

200mW of optical power incident to the fibre. The hydrogenation conditions were as per section 6.2.1.1.

Figure 6.18 shows the result of this extended exposure normalised to equate the 20mm exposure to a 1mm section. The traces which show B/Ge fibre (blue) and SMF28 (cyan) both exhibit fairly simple spectral characteristics; they show a slightly asymmetrical Gaussian with the extended portion on the higher wavelength side. The remaining plots show the OH bands formed in Ge doped fibres from Verillion and Fibercore and clearly show at least two main peaks. This is because the OH band structure is a trade off between the relative contributions of SiOH and GeOH, which explains the dithering around 1380 to 1410nm.

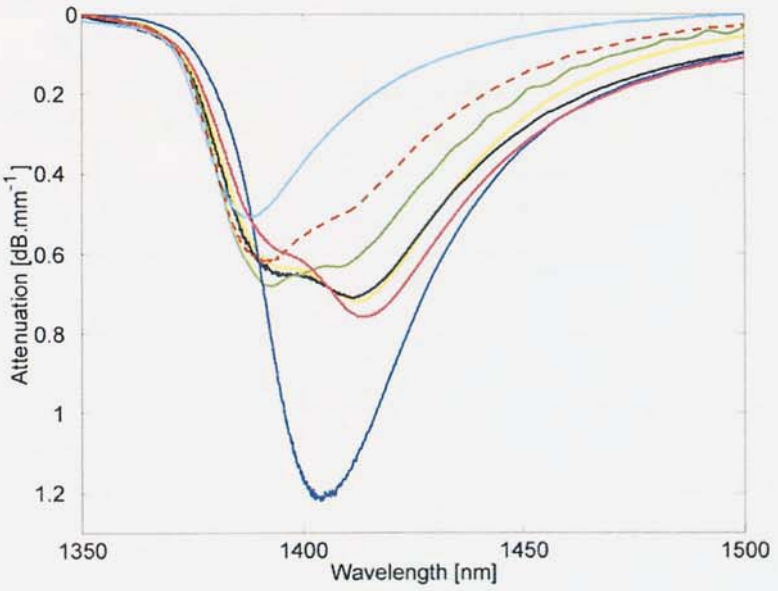

Figure 6.18 The OH band created by uniform exposure of a 20mm section of fibre to UV radiation. Shown for Fibercore PS1250/1500 B/Ge (blue), Fibercore SD079-00B Ge (green), Fibercore SD748A-00AB Ge (black), Fibercore Ge SD254-01B (yellow), Verillion IF0100331001 Ge (red-dashed), Verillion FA1631211 Ge (magenta) and Corning SMF28 (cyan). This figure shows the contrast between the OH bands of different fibres more clearly.

The wavelength associated with the primary and secondary absorption peaks for each trace in Figure 6.18 is shown below in Table 6.6.

Fibre ref	Manufacturer	Colour convention	Fibre type	NA	Main peak		Secondary peak	
					nm	dB/mm	nm	dB/mm
SMF28	Corning	Cyan	STD	0.14	1388	0.51	xx	xx
PS1250/1500	Fibercore	Blue	B/Ge	0.14	1404	1.22	xx	xx
IF0100331001	Verillion	Red-dashed	Ge	0.23	1392	0.62	1406	0.51
SD079-00B	Fibercore	Green	Ge	0.24	1393	0.68	1408	0.63
SD748A-00AB	Fibercore	Black	Ge	0.26	1412	0.71	1397	0.66
SD254-01B	Fibercore	Yellow	Ge	0.30	1412	0.72	1395	0.64
FA1631211	Verillion	Magenta	Ge	0.30	1414	0.76	1397	0.60

Table 6.6 Summary of the absorption band peaks and dopant levels for the fibres tested.

6.5. OH BAND HEATING

6.5.1. OH Band heating using a tuneable laser

It has been extensively demonstrated in this section that for type IA index changes an absorption band exists at ~1400nm that is typically ~1.2dBmm^{-1} for a B/Ge co-doped fibre. It is therefore logical that if a fibre containing a type IA grating were to be pumped with a laser source coinciding with the absorption band, the fibre would be heated in the IA region.

In order to demonstrate this principle an experiment was devised which illuminated a IA-I dual grating with a broadband source in the spectral region of the gratings and a powerful Santec tuneable laser (with a range of 1410nm to 1490nm) as depicted in Figure 6.19. The IA-I grating pair consisted of a 2mm IA grating, manufactured by the blank beam pre-exposure method in Fibercore PS1250/1500 directly adjacent to a 2mm type I grating.

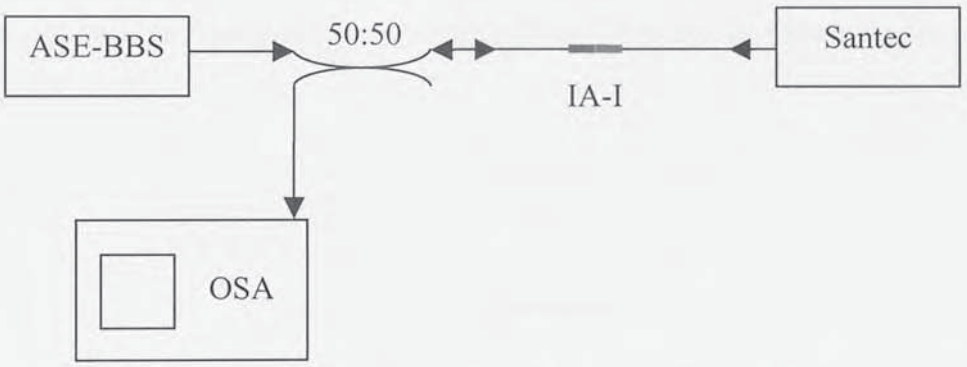

Figure 6.19 A schematic showing the connection of equipment used to demonstrate the IA heating effect.

The Bragg wavelengths of the IA-I dual grating were monitored in reflection by the OSA. Although the peak absorption of this fibre type occurs at 1404nm (refer to Table 6.6) the tuneable laser was not capable of emitting a wavelength below 1410nm, thus the laser was set to this closest value.

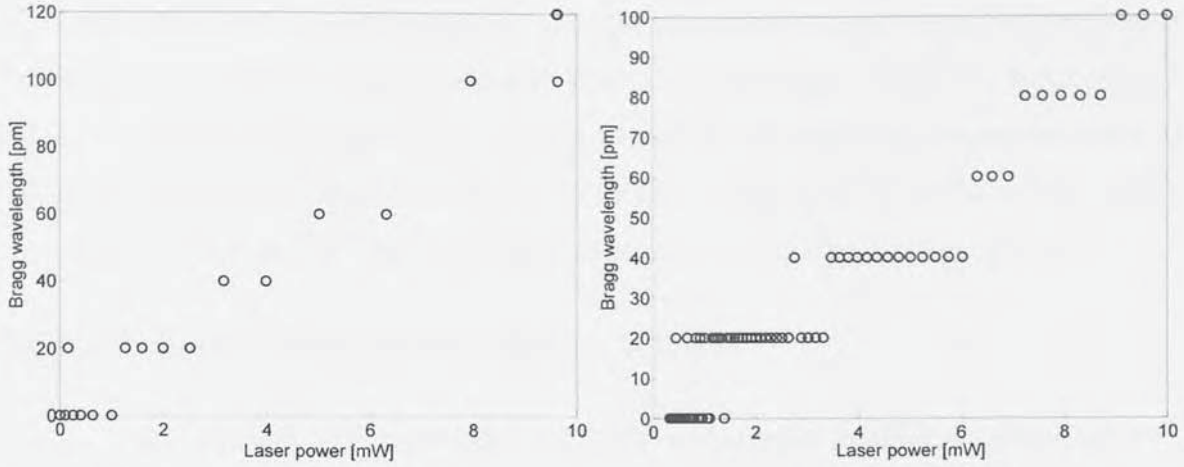

Figure 6.20 The shift in the Bragg wavelength of a IA grating heated with a 1410nm tuneable laser of varying power levels which was controlled manually (a) (left) and by computer (b) (right). This shows that the Bragg wavelength of a IA grating may be controlled remotely with strictly optical means.

Figure 6.20 shows the shift in Bragg wavelength with increasing laser power at 1410nm. Figure 6.20a shows the shift for various power levels under manual control and Figure 6.20b shows the result for many more points this time controlled by computer. Unfortunately the Bragg wavelength shifts are small and so a limiting factor in this data is the minimum resolvable wavelength change of the OSA and is shown in the pixelated data of Figure 6.20.

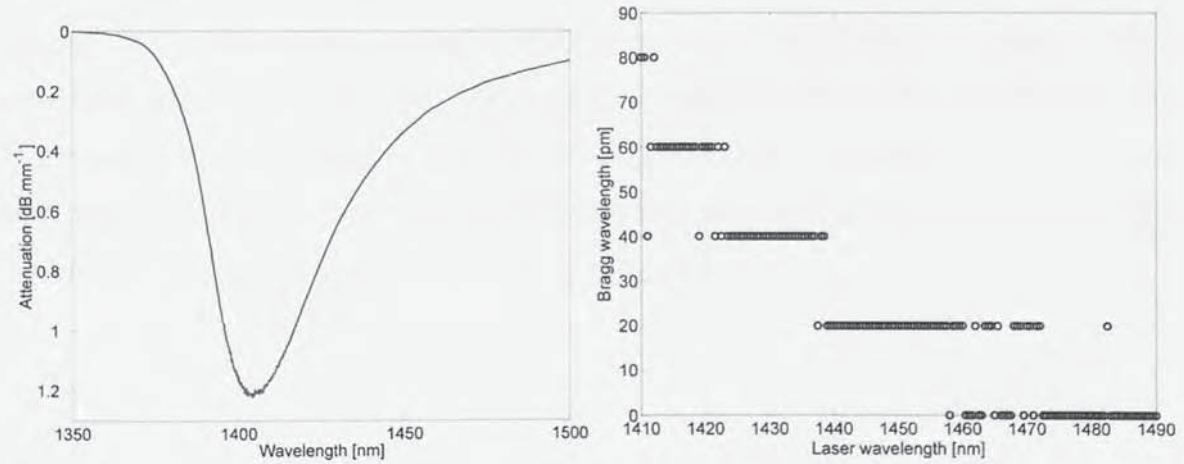

Figure 6.21 (a) (left) The OH band of the IA grating tested in this experiment, and (b) (right) the shift in the Bragg wavelength of the IA grating when the tuneable laser was held t a constant power and the wavelength was shifted up the edge of the OH band. This further shows that the Bragg wavelength of a IA grating may be controlled remotely with strictly optical means.

The next step in this experiment was to shift the wavelength of the tuneable laser whilst maintaining a constant output power and thus to use the shape of the OH band (Figure 6.21a) as an edge thus varying the amount of energy absorbed and hence the level of tuning in the Bragg wavelength. Figure 6.21b shows the effect of scanning the Santec laser from 1410nm to 1490nm whilst maintaining a constant 10mW output power.

6.5.2. OH Band heating using a Raman amplifier

Raman amplifiers are now commonly available with output powers in excess of 5W. Although the peak wavelength is 1425nm, placing it in a weaker region of absorption, the extremely high energy levels compensate for this to some extent.

The experimental apparatus shown in Figure 6.19 was reconfigured so that the Santec laser was replaced by the Raman source with variable output power. The IA-I grating was then monitored in reflection using the OSA as before.

Figure 6.22 shows the overlaid reflection spectra of the IA-I dual grating. The results show the principle of operation of an extremely useful property. Although the gratings are directly adjacent to one another, the 1425nm radiation is only absorbed by the fibre portion which was pre-exposed to UV radiation and contains the higher wavelength IA grating. Since the type I grating is written in virgin fibre with no strong 1400nm absorption band it is not heated. The negligible thermal mass of the fibre prevents any significant level of conduction from the two regions. Thus the application of the Raman laser causes the IA grating to spectrally shift whilst the type I grating remains at a fixed wavelength, making an optically tuneable grating pair.

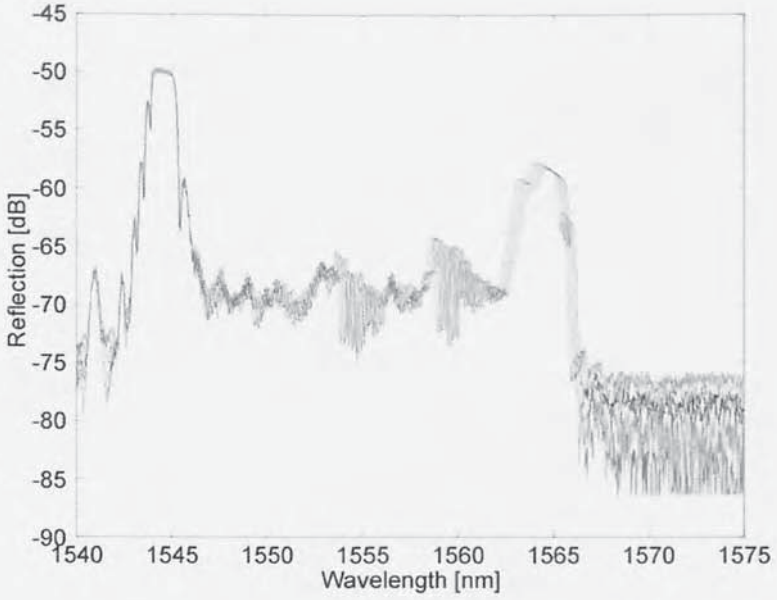

Figure 6.22 The overlaid reflection spectra of a IA-I dual grating under the heating effect of a Raman laser source being used to heat the IA grating. The type I grating remains at a constant wavelength whilst the IA grating shifts despite the gratings being directly adjacent to one another.

This data is more obvious in Table 6.7 wherein the relative shifts of the IA and I gratings are summarised. This information is also shown by Figure 6.23, indicating a linear relationship between Raman power and wavelength shift. Note that although there is a slight fluctuation in the wavelength of the type I grating, this may be attributed to experimental error.

Raman Power mW	$\Delta\lambda_{BR}^{IA}$ pm	$\Delta\lambda_{BR}^{I}$ pm
0	0	-3
25.1	105	0
52.9	245	17
79.22	367	17
103.45	455	-3
124.8	525	17

Table 6.7 A summary of the wavelength shifts of the type I and IA gratings when heated with a Raman source at 1425nm.

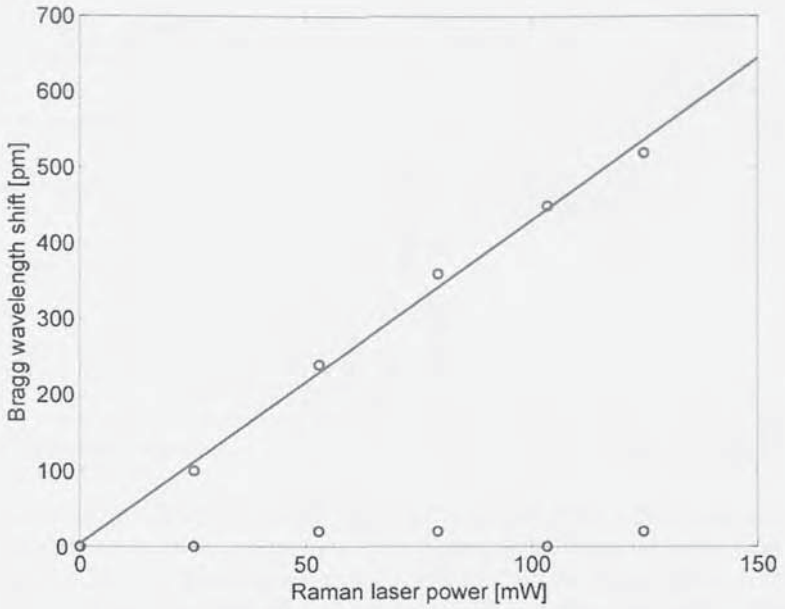

Figure 6.23 A plot of the wavelength shifts of the type I and IA gratings when heated with a Raman source at 1425nm. This figure clearly shows a controllable change in the Bragg wavelength of the IA grating and a constant Bragg wavelength of the type I grating.

If we next consider the effect of the Raman source being absorbed along the length of the grating; it is logical to conclude that the heating effect will be non-uniform along the length of the absorbing section of fibre and that the result will be an induced chirp along the grating. Clearly, higher Raman powers will induce a larger chirp and an increase in the FWHM reflectance bandwidth of the IA grating.

The decay in the intensity of the Raman source along the length of the IA grating may be summarised be the simple equation, Equation 6.3.

Equation 6.3 $$I(p) = I(p-1).\left(1-10^{\frac{A}{10}}\right), \quad [I(p) \propto \Delta T]$$

where *I(p)* is the Raman intensity at a point p, A is the absorption per unit length of the Raman radiation measured in dB and ΔT is the induced temperature increase. Figure 6.24a shows this relation for the power levels used to create Figure 6.24b and an estimation of the absorption coefficient of $1.2 dBmm^{-1}$.

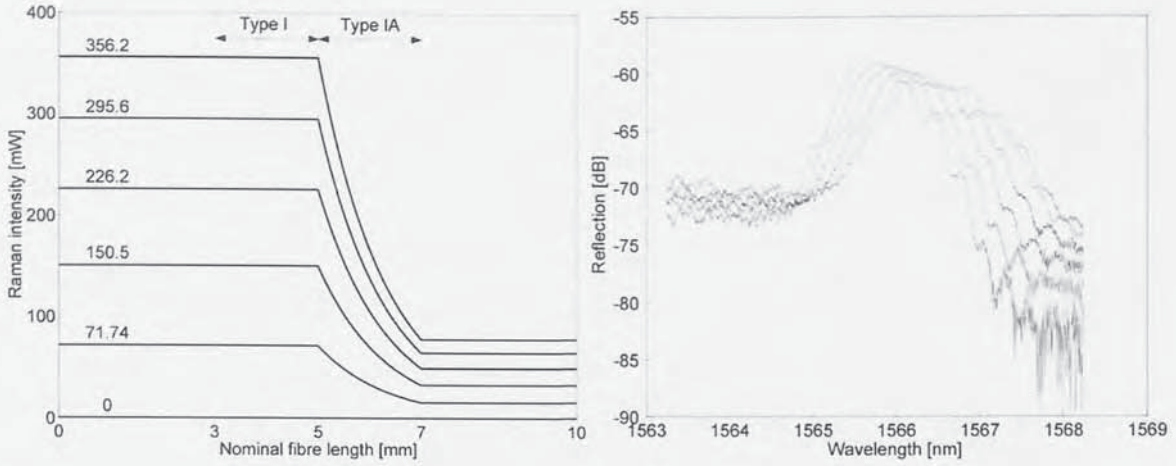

Figure 6.24 (a) (left) A simulation showing the decay in the intensity of the Raman laser along the length of a 2mm IA grating. (b) (right) The overlaid reflection spectra of a IA grating under the heating effect of a Raman laser. This figure shows that it is also possible to tune the chirp of a IA grating by purely remote optical means.

Figure 6.24b shows this effect for slightly higher powers than those used in the previous experiment. Table 6.8 Shows the summary of this data and details both a clear increase in the Bragg wavelength and the FWHM bandwidth of the reflectance peak.

Raman Power	$\Delta\lambda_{BR}^{IA}$	FWHM
mW	pm	nm
0	0	1.31
71.74	160	1.36
150.5	250	1.45
226.2	420	1.55
295.6	590	1.65
356.2	620	1.73

Table 6.8 A summary of the wavelength shift and FWHM expansion of a type IA grating when heated with a Raman source at 1425nm.

The information shown above in Table 6.8 is plotted below in Figure 6.25 again indicating linear relationships between the FWHM bandwidth and the Raman intensity and also the Bragg wavelength shift and Raman intensity.

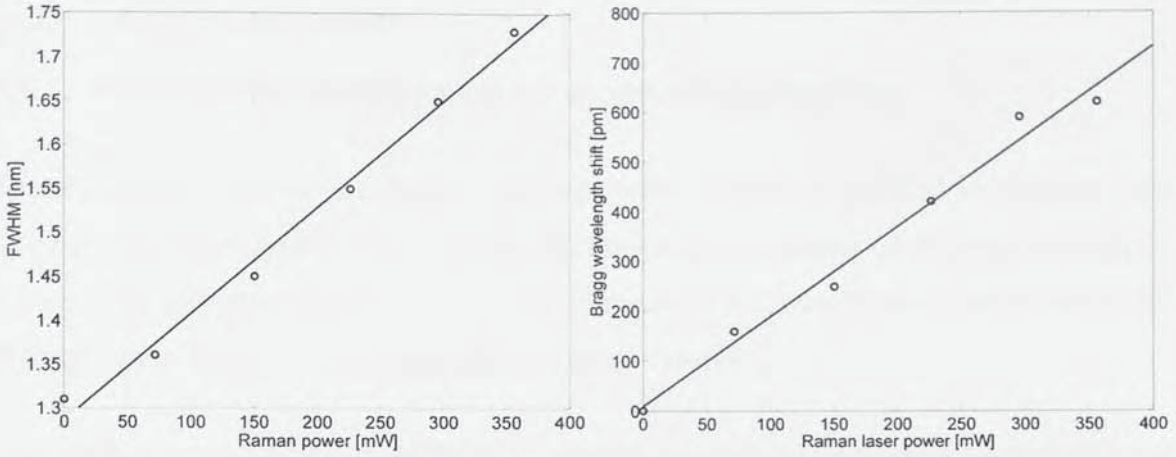

Figure 6.25 (a) (left) A plot showing the linear relation between the FWHM bandwidth of a IA grating and the intensity of the Raman laser. (b) (right) A plot showing the linear relation between the Bragg wavelength shift of a IA grating and the intensity of the Raman laser.

This experiment has unequivocally shown that it is possible to selectively heat a grating within an array of other gratings by purely optical methods. Since all grating types could be written in a section of pre-exposed fibre this method of optical tuning could be used for all existing FBG applications making the technique invaluable to a multitude of regimes such as selective wavelength tuning in a DFB laser or edge filter adjustment in sensing applications.

6.6. ANNEALING STUDY

6.6.1. Experimental arrangement for monitoring annealing

The annealing properties of type IA gratings were studied in order to investigate their thermal stability and any similarities to the annealing properties of other grating types. An experimental arrangement was devised to measure the transmission profile of several gratings whilst being held at predetermined temperatures.

The samples were fusion spliced to FC:PC pigtails to reduce coupling losses before being connected to an 8 channel DWDM test system comprising a tuneable laser with 5pm step size, a wavemeter, launch power meter and a rack of 8 InGaAs photodiodes with >100dB dynamic range. The tuneable laser was connected to the wavemeter, before feeding the samples such that a highly accurate measure of the discrete wavelength might be obtained. The samples were placed in a Sanyo environmental chamber (-40°C to 180°C range). This apparatus is shown schematically in Figure 6.26.

A LabView script was written to automatically control the test equipment, enabling the equipment to save an accurate transmission profile at a predetermined time interval for the duration of the experiment. After running such an experiment the individual traces were processed using another custom software program which calculated the Bragg wavelength and peak transmission loss for each dataset.

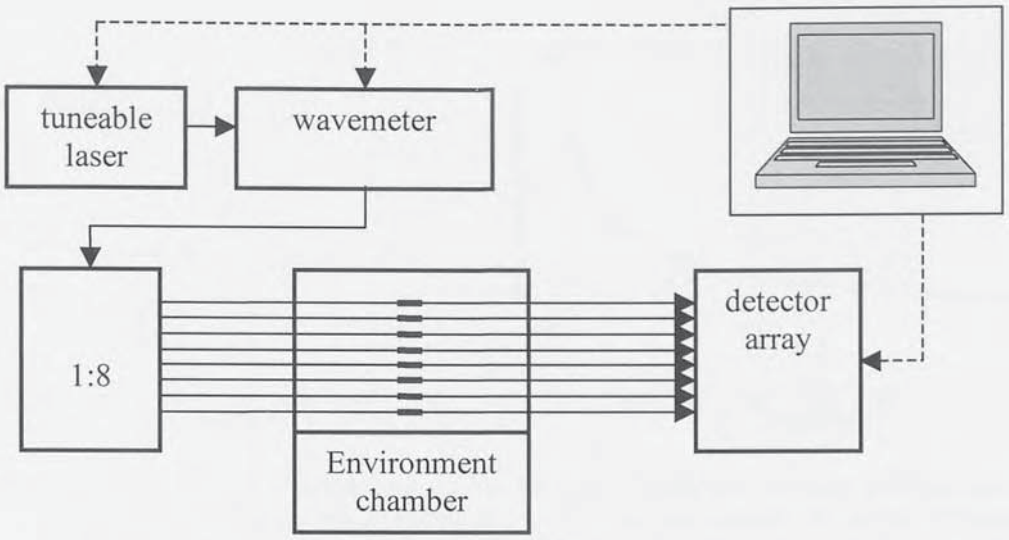

Figure 6.26 Schematic showing the tuneable laser system used to characterise the gratings during the heating cycle in the tubular oven. This system enabled 5pm resolution with 100dB dynamic range on all 8 channels.

6.6.2. Standard annealing at 80°C of IA-I dual sensors

This subsection details the annealing data for the gratings manufactured in Section 5.6 which were 8 IA-I dual grating sensors manufactured in B/Ge fibre (Verillion IF01001410101), hydrogenated at 200Bar / 80°C for 64 hours. The type I grating was 1mm long and was written at $0.5mms^{-1}$ whereas the type IA grating was 4mm long and written at $0.05mms^{-1}$ after 200 blank beam scans at $1mms^{-1}$ to induce the IA index change.

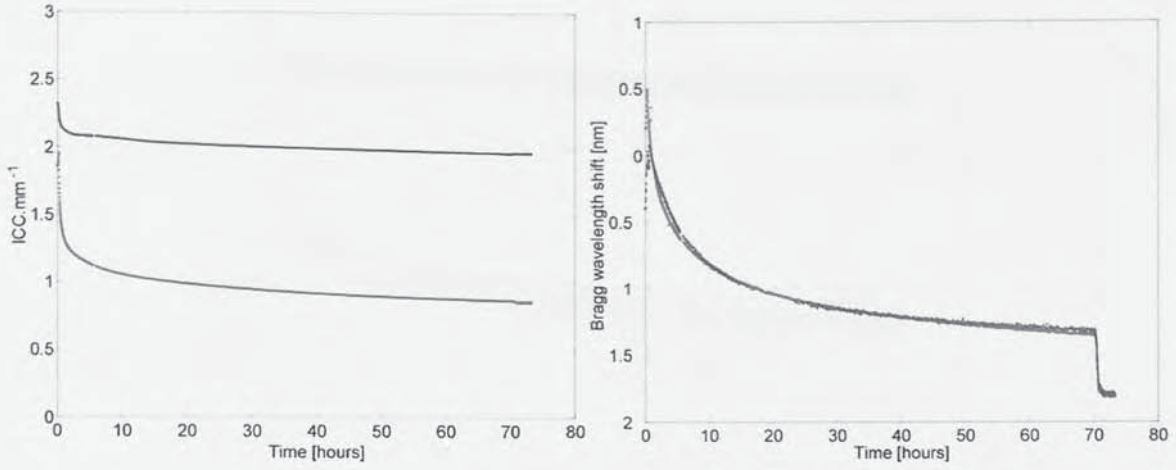

Figure 6.27 (a) (left) The 80°C annealing curves for type I (blue) and IA (red) gratings for sample reference FBG4 shown in terms of the ICC per unit length. (b) (right) The annealing curves shown in terms of the Bragg wavelength shift during annealing. This figure shows that the modulated index of the IA grating anneals significantly faster than the type I, but their mean indexes anneal similarly due to H_2 outgassing.

The gratings were placed in the apparatus as described in Section 6.6.1 and annealed at 80°C for 70 hours. Figure 6.27 shows the annealing curves for an example grating (FBG7). In Figure 6.27a the annealing curves for the two gratings in terms of ICC.mm^{-1} as laid out in Section 2.3, Equation 2.7 is shown. This plot explicitly shows that the type I grating anneals significantly more slowly than the IA grating. Figure 6.27b shows the decay of the mean index during the annealing process as metered by the Bragg wavelength of the grating during the annealing. This figure shows that in this case, both type I and IA gratings undergo the same rate of mean index change.

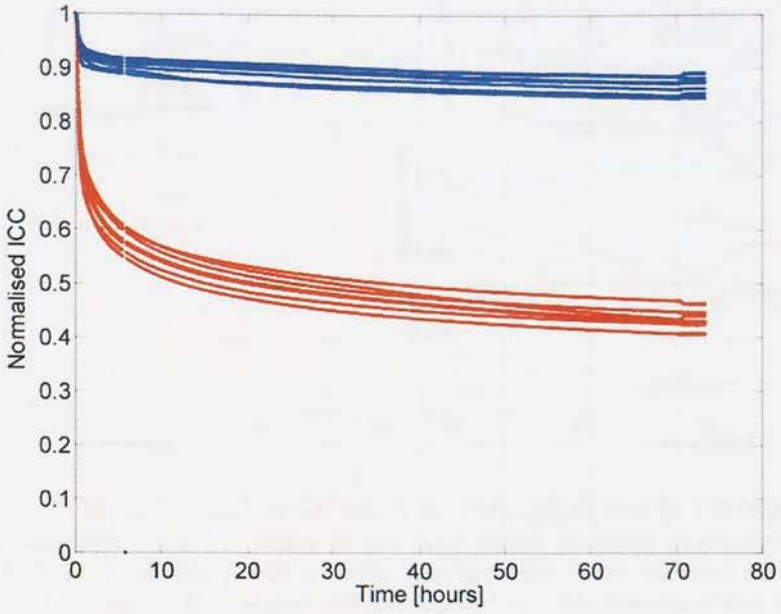

Figure 6.28 The 80°C annealing curves for type I (blue) and IA (red) gratings for 8 samples shown in terms of the normalised ICC. This shows that the annealing curves for IA gratings follow a uniform trend.

Figure 6.28 shows the annealing curves for all 8 samples in terms of the normalised to t=0 ICC value, η. This figure clearly shows that there is a definite trend to the annealing process with only a small amount of variance between samples.

Figure 6.28 also shows a curiosity at the end of the annealing cycle. At t=70hrs, the gratings were allowed to cool naturally to room temperature whilst the monitoring software was still running at a slightly higher sample rate. Figure 6.29 shows this period in more detail for both gratings. What is clear is that the majority of the type I gratings increase in reflectivity whilst the majority of the IA gratings decrease in reflectivity. Recalling that the type I and IA gratings are written in directly adjacent pairs, it is unclear why this would be the case but highlights another contrast between the two grating types.

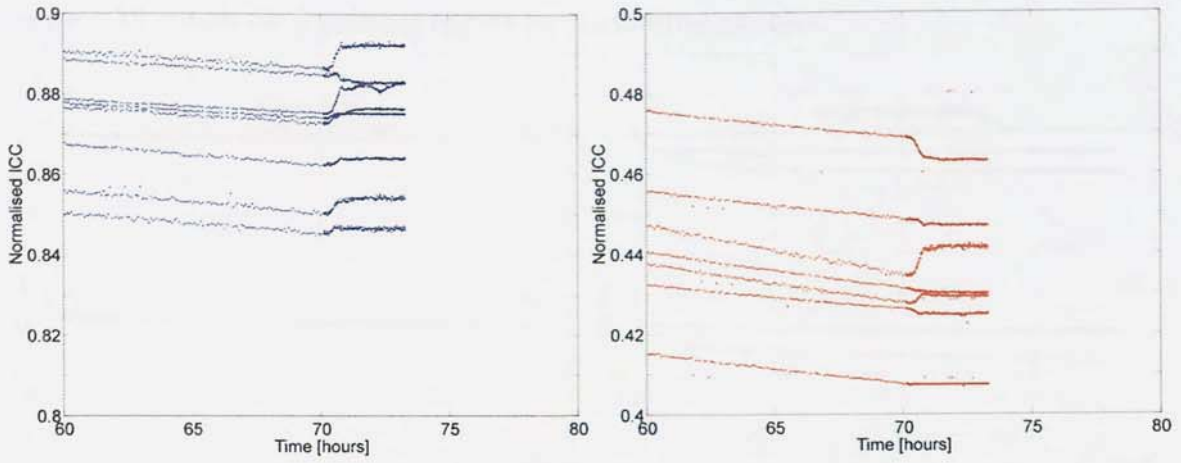

Figure 6.29 The 80°C annealing curves for type I (a) (left) (blue) and IA (b) (right) (red) gratings for 8 samples shown in terms of the normalised coupling coefficient and zoomed to show the end of the process when the gratings were allowed to cool naturally to 25°C at 70 hours. This shows a curiosity in the reflectances of the two grating types as the fibres cool.

6.6.3. Hot and Cold Verillion samples

This subsection details the annealing data for the gratings manufactured in Section 6.2.2.2 which were type IA-I dual gratings written in two identical batches of fibre; each consisting of SMF28, B/Ge co-doped fibre and two different samples of Ge-only doped fibre as laid out in Table 6.4, partially repeated below. One batch was hydrogenated at 80°C, 190Bar for 93 hours and allowed to cool to room temperature over 24 hours by which time the pressure was 160Bar; the other samples were hydrogenated for in excess of 4 months at 180Bar at room temperature. 1mm gratings of each type were inscribed as per Section 6.2.2.2.

Reference	Hydrogenation conditions	Fibre type	Manufacturer
SMF28	hot	Std	Corning
SMF28	cold	Std	Corning
IF01001410101	hot	B/Ge	Verillion
IF01001410101	cold	B/Ge	Verillion
IF0100331011	hot	12mol%Ge	Verillion
IF0100331011	cold	12mol%Ge	Verillion
FA1631211	hot	21mol%Ge	Verillion
FA1631211	cold	21mol%Ge	Verillion

Table 6.9 Table 6.4 The details of the fibres tested in this section.

Figure 6.30 shows the annealing curves for these fibre samples.

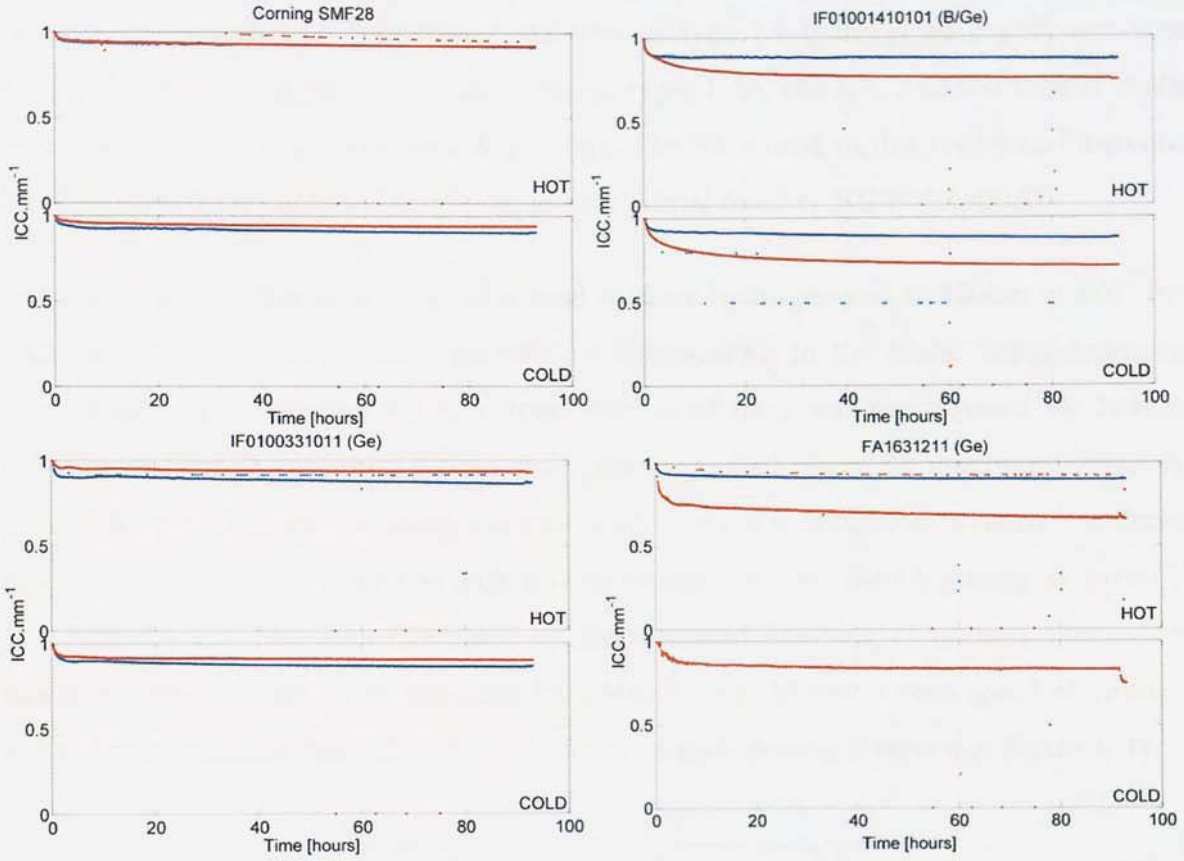

Figure 6.30 80°C Annealing plots for type I (blue) and type IA (red) gratings written in various fibre types (as indicated) for hot (upper) and cold (lower) hydrogenation conditions shown in terms of the normalised ICC. This figure does not show any significant differences in the annealing properties of the fibres under different hydrogenation conditions.

Although this is a useful figure showing the annealing properties of several different fibre types, it does not show any significant trends between the hydrogenation conditions.

6.7. HIGH TEMPERATURE STABILITY

In order to evaluate the temperature stability of type IA gratings an experiment was designed to make a direct comparison between types I, IA and IIA. The test looked at six type I, six type IA and two type IIA gratings. The fibre used in this trail was Fibercore PS1250/1500 B/Ge co-doped single mode fibre (serial number 30246B/A-00A).

The type I and IA gratings were fabricated in fibre hydrogenated at 200bar at 80C for 64hours. The IA gratings were manufactured according to the blank beam exposure method detailed in Section 5.3.3, a 3mm section of fibre was pre-exposed by 244nm radiation at $1mms^{-1}$ until the 1400nm absorption band had reached a maximum value. A 2mm FBG was then written using a scanning phasemask technique at $0.1mms^{-1}$. A 2mm type I grating was then inscribed with a 1mm separation from the IA grating at $2mms^{-1}$. The type IIA gratings were fabricated by the shuttered scanning phasemask method in non-hydrogenated fibre (from the same PS1250/1500 batch) with a scan speed of $1mms^{-1}$ and a shutter width of 2mm. A typical spectrum of each grating is shown in Figure 6.31.

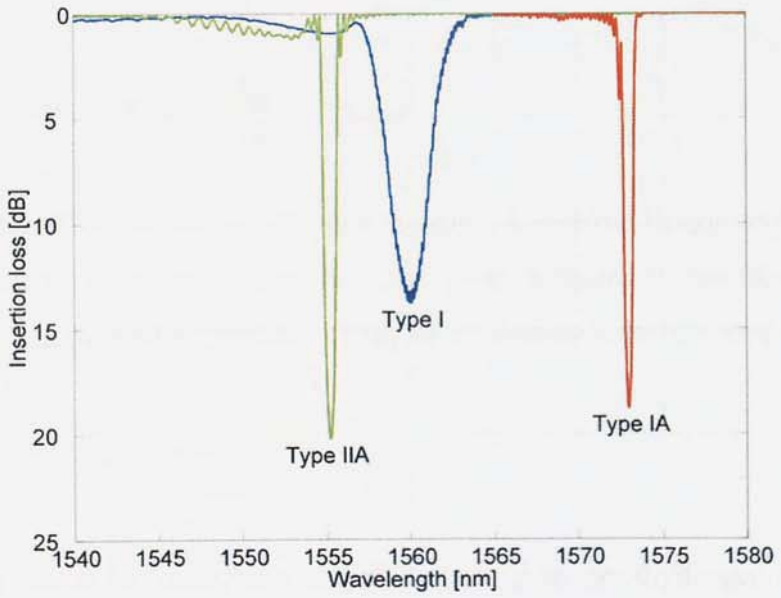

Figure 6.31 The spectra of type I (blue), IA (red), and IIA (green) gratings prior to annealing written in B/Ge fibre. Each grating has the same period and demonstrates the differences in the mean index of the three gratings.

All gratings were manufactured in the middle of a 1m section of fibre and mounted in a modified version of the apparatus outlined in section 6.6.1. The gratings were placed inside a high temperature Carbolite tubular furnace in place of the Sanyo environmental chamber. The gratings were held at 100C, 200C, 300C, 400C and 500C

6.7.1.1. Data processing

In order to ascertain the thermal stability of the gratings the mean and modulated index changes of the samples were calculated. This was done by means of a software program designed to sift through the 8000 or so individual spectral traces and produce tables of the central reflecting wavelengths and peak insertion losses for each grating as a function of time. This information was then converted to mean and modulated index change as follows:

Mean index change

The mean index change was calculated according to the following rearrangement of Equation 2.9:

Equation 6.4 $$\Delta n_{eff}(t) = \frac{\lambda_{BR}(t)}{2\Lambda} - n_{initial}$$

where Δn_{eff} is the effective refractive index at time t, λ_{BR} is the Bragg wavelength at time t, $n_{initial}$ is the initial refractive index of the fibre core (supplied by the fibre manufacturer as 1.4441) and Λ is the grating period. Λ may be accurately approximated as follows:

Equation 6.5 $$2\Lambda = \frac{\lambda_{initial}}{n_{initial}}$$

where $\lambda_{initial}$ is found by inscribing a type I grating in non-hydrogenated fibre. Care should be taken that the grating is sufficiently immature that it has not exhibited a significant level of the red shift seen during the earliest stages of IIA grating manufacture. This is shown below in Figure 6.32, which yields a value of 1077.515nm for twice the period of the gratings when applied to Equation 6.5.

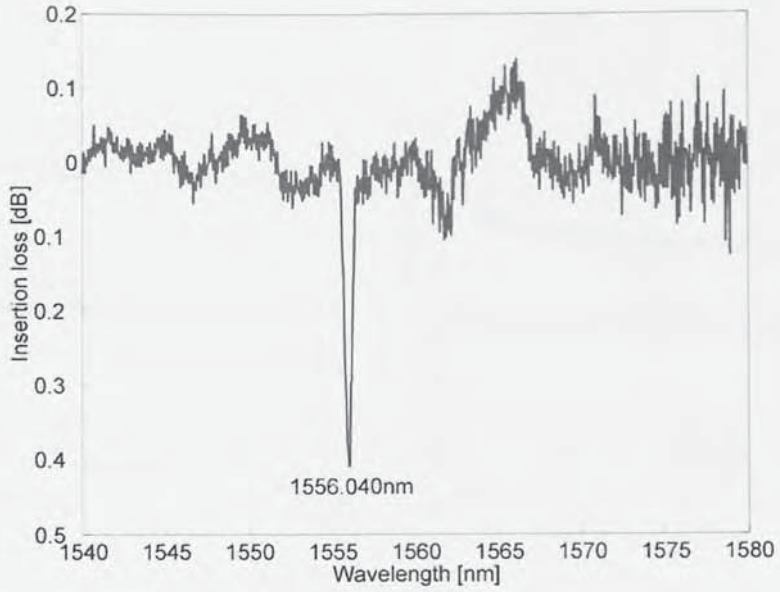

Figure 6.32 Showing the λ_{BR} of a type I grating in non-hydrogenated Fibercore PS1250/1500 with n_{eff} = 1.4441 as used to calculate the period of the inscribed gratings during the annealing experiment.

It is also desirable to normalise the recorded values of central reflectance for the effects of thermal shift in the Bragg resonance. This is most simply done by applying $\lambda_{BR}(t) = T(t).\lambda_{BR}(T)$, where T($t$) is the temperature at time t, and λ_{BR}(T) is the thermal coefficient of the individual gratings. The average values shown in Table 6.10 were used, since it was not possible to measure the thermal coefficients of these particular samples as the high final temperatures used in this experiment carbonised the fibre beyond use.

Grating type	Thermal coefficient (pmC^{-1})
I	8.0
IA	6.0
IIA	11.0

Table 6.10 Summary of average thermal coefficients used to calculate the shift in the Bragg resonances during annealing. This data represents an approximation used to normalise the mean index change under different temperatures.

The result of Equation 6.5 was substituted back into Equation 6.4 and normalised to t=0 for successive values of λ_{BR} thus producing a dataset containing the mean index change against time for the gratings at increasing ambient temperature. This data is shown in Figure 6.33 below.

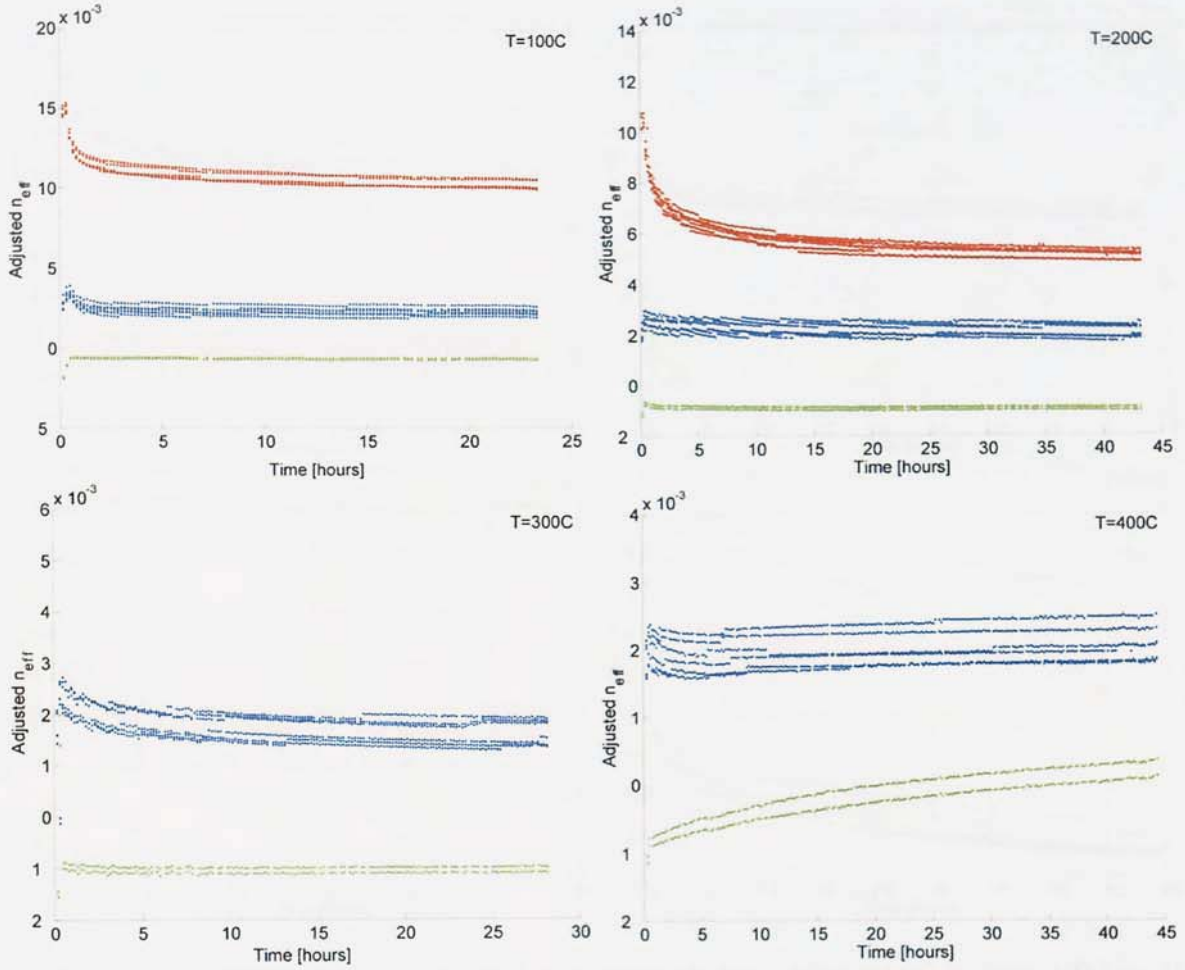

Figure 6.33 The decay in the mean index experienced by type I (blue), IA (red) and IIA (green) gratings during heating at 100C (top, left), 200C (top, right), 300C (bottom, left) and 400C (bottom, right). This figure is the first evidence that the mean index change of IA gratings also decays under moderate temperatures.

Modulated index change

The modulated index change was shown in terms of the normalised ICC, as discussed in Section 2.3 and defined by Equation 2.7. The modulated index change is shown below in Figure 6.34.

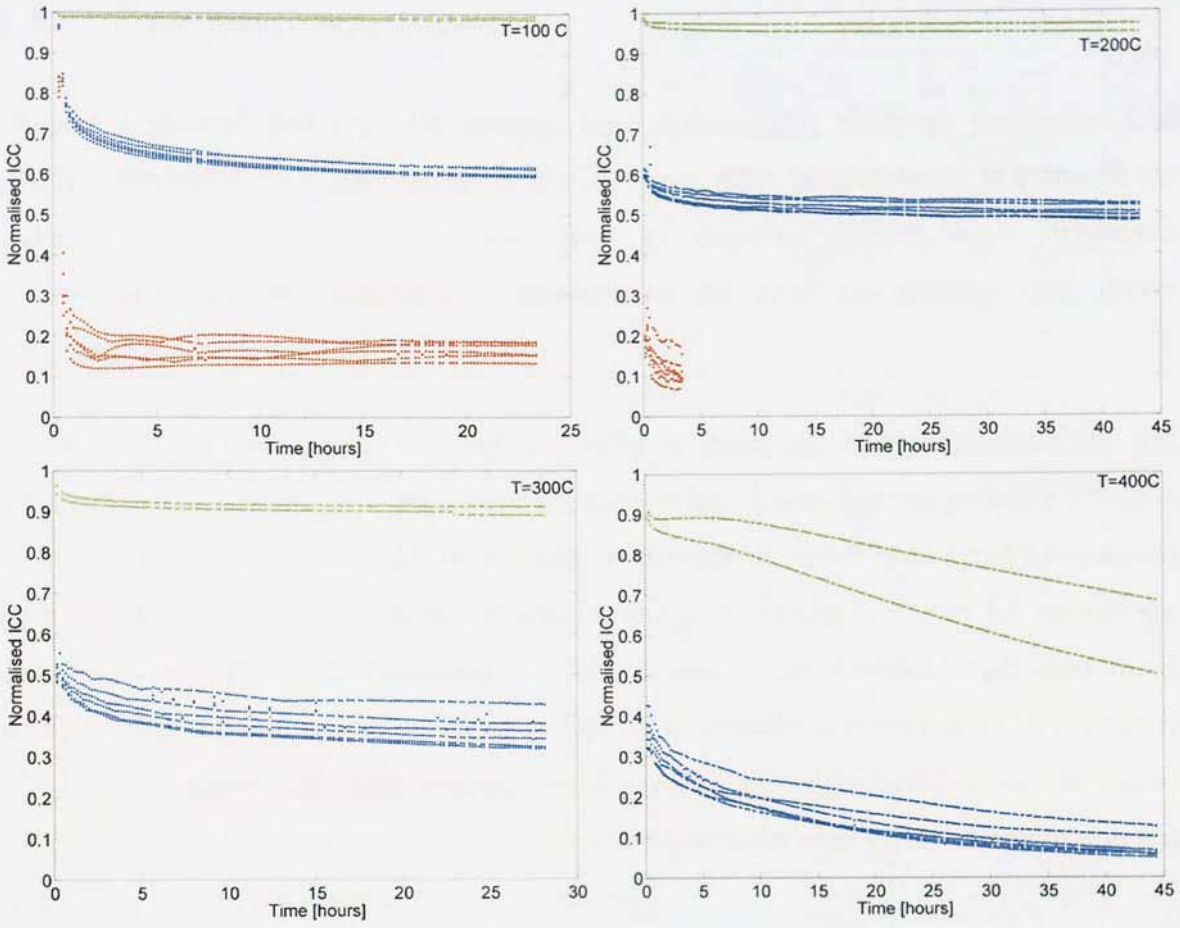

Figure 6.34 The decay in the normalised integrated coupling constant (κ) by type I (blue), IA (red) and IIA (green) gratings during heating at 100C (top, left), 200C (top, right), 300C (bottom, left) and 400C (bottom, right). This figure shows that the type IA gratings present the lowest thermal stability, being erased at only modest temperatures. This has profound implications on the potential uses of IA gratings.

This data shows a vital result concerning the high temperature stability of type IA gratings. Figure 6.34 indicates that IA gratings undergo a drastic initial decay at 100°C which implies that they are thermally unstable at this temperature. Figure 6.33 shows that the mean index change is severely reduced at this temperature However, the results of Figure 6.28 and Figure 6.30 show that the modulated index change of IA gratings remains stable at lower annealing temperatures of 80°C, whilst Figure 6.27b shows that the mean index change decays at a comparable rate to type I gratings at 80°C. These results show that the maximum temperature IA gratings may be reliably used is less than 80°C. Figure 6.34 also confirms well known reports as to the stability of different types of Bragg grating showing that IIA gratings are more stable than type I gratings.

6.8. CHAPTER CONCLUSIONS

Chapter 5 showed that type IA gratings have substantially different inscription and physical properties than other reported grating types. This chapter looks at some of the underlying parameters including the effect of dopants, dopant levels, hydrogen concentration and the annealing characteristics for type IA gratings and draws comparisons with grating types I and IIA.

Boron has long been added to fibre pre-forms to both enhance photosensitivity and reduce the refractive index of the core. This chapter has shown that the presence of boron within the glass has a profound effect both on the rate at which type I and IA gratings form and the maximum reflectivity of type I gratings. Referring to Figure 6.1 we can see that ICC value of boron containing samples is more than 3 times larger than those without. Additionally we can see that the fluence to inscribe a mature type IA grating is ~0.6J.m^{-2} for boron containing glasses, whilst germanium only glasses require in excess of 2.7J.m^{-2}. It has not been possible to confidently conclude what effect, if any, boron has on the temperature coefficient of type IA gratings.

The fundamental difference between IA and IIA grating inscription regimes is that IA gratings require the presence of hydrogen. This chapter has shown that the concentration of hydrogen within the core directly affects the rate at which IA gratings form and the thermo-optic coefficient of the mature IA grating; gratings inscribed in fibre samples with a higher hydrogen concentration form faster and have lower temperature coefficients. It has also been shown that by allowing all hydrogen within the sample to outgas a type IIA grating is formed. This shows that it is not possible to inscribe IA gratings using the pre sensitisation technique of Canning *et al* (refer to Section 2.2.3.2) which infers a different photosensitivity mechanism between type I and type IA gratings.

The refractive index model of type IA gratings shows a large mean index change which is substantially larger than reported elsewhere. However, it has also been shown that the minimum length of such an index change is more than 0.5mm. This may be the result of a diffuse effect spreading through the fibre which is not substantially localised to the area

exposed to prolonged UV exposure. It is logical to envisage this as a heating effect in keeping with the demonstration of fibre heating caused by UV exposure in Section 5.4.2. A use for this large mean index change has been suggested and demonstrated; the consequential increase in NA could be used to decrease splicing losses between optical fibres.

There has been substantial evidence of the absorption band at 1400nm and its relation to the formation of hydroxides within the fibre under UV Exposure. It has been shown that the final shape of the absorption band is related to the concentration of fibre dopants, and is believed to be ultimately determined by the ratio of Si-OH and Ge-OH. A novel use for this OH band has been proposed; it is possible to locally heat a type IA grating using radiation within the absorption band and is thereby possible to selectively tune its resonance by purely optical means.

Annealing experiments have shown similarities between the modulated index change of types I and IA, but also shown that type IA gratings are substantially less stable at higher temperatures. It should be noted that the use of type IA gratings at temperatures above 80°C for prolonged periods of time should be avoided, and exposure to temperatures greater than ~150°C to 200°C is likely to result in the complete erasure of the gratings.

Chapter 7

Thesis Conclusions

7. THESIS CONCLUSIONS

Blazed Grating Spectroscopy

This thesis has shown the novel implementation of several blazed grating based spectrometer devices. The primary result of the work on this subject is that an extremely low cost spectrometer was assembled using only standard, low cost, components. The final prototype showed excellent stability and high accuracy when operating with a range of WDM sensor arrays and in various test environments.

An important result stemming from this work was the use of superimposed BFBGs to enlarge the spectral bandwidth of the system. This worked because the radiation angle and spectral range of BFBGs is dependant on the blaze angle of the grating. By superimposing gratings of different blaze angles it was possible to design a system where the radiation profiles of the two gratings complemented each other, thereby resulting in a larger bandwidth.

This work will find use in the manufacture of spectrometers and fibre sensor interrogation apparatus. Refer to the conclusions of Chapter 4 for a more detailed conclusion of this work.

Type IA Gratings and Temperature Compensating Sensors

Type IA gratings have been studied in depth and shown to be a unique grating type similar to, although distinct from, types I and IIA. It was shown that the formation of IA gratings occurs in three distinct phases; initially a standard type I grating is formed which then decays in the second phase, usually to almost zero reflectivity, before regenerating and saturating with a large offset in the mean index signalling the end of the third phase. The final reflectivity of type IA gratings approximates that of IIA gratings written in similar conditions and is much less than the maximum reflectivity achieved by the initial inscription phase.

It was shown that a typical IA grating undergoes a mean index change equivalent to a shift in the Bragg wavelength of up to 16nm and that by stopping the inscription process at the correct time it is possible to tune the intended wavelength of a phasemask by up to this value.

Work has been presented detailing methods of fabricating IA gratings. The ideal inscription method proposed was the blank beam method which uses uniform UV radiation to pre-expose a section of hydrogenated fibre. This inscription method has the advantage of not requiring highly stable apparatus during the prolonged exposure and yields uniform gratings of a more pure spectral profile.

By varying the intensity of the inscription laser, it has been shown that the initial growth phase (attributed to the formation of standard gratings) is not strongly dependant on intensity. However, after the standard grating reaches maximum reflectivity a marked change in the growth characteristic occurs and the rate of mean index change varies strongly with inscription intensity. It was argued that this is likely to result from a single photon absorption in the initial phase followed by a multi-photon absorption process in the latter phases.

Work has been presented detailing the fabrication and characterisation of dual grating sensors which may be used to simultaneously decouple temperature and strain. The sensor head comprises a standard type I grating fabricated directly adjacent to a type IA grating, having a lower temperature coefficient and slightly higher strain coefficient. Fabrication of the IA-I sensor was shown to be significantly more straightforward than other dual grating devices as the blank-beam pre-exposure technique may be used to avoid the need to change or anneal fibres in between grating inscription. Using a standard matrix technique it is possible to interrogate the sensor head and decouple strain and temperature with a matrix condition number better than 188.

Novel work was presented pertaining to the effects of core dopants and dopant levels. It was shown that boron should be used to accelerate the inscription process of type IA

gratings and that a higher concentration of hydrogen in the fibre results in a lower final thermal coefficient.

A method of reducing splicing losses by increasing the numerical aperture of germanium doped fibres was presented. This method uses blank-beam exposure to induce a IA mean index change in the section of fibre prior to cleaving. It was shown by direct measurement and theoretical calculation that this method increases the acceptance angle of the fibres.

A strong absorption band, which forms simultaneously with IA gratings, was shown for several types of fibres. It was shown that this absorption band is related to the formation of hydroxide species and that the final shape is determined by the core dopants, dopant levels and hydrogen levels. It was also shown that by pumping a IA grating with a 1400nm source, it is possible to optically tune the central reflecting wavelength whilst not effecting a directly adjacent grating.

This work will find use in situations where separate measurements of temperature and strain are required. It will also be of use in any situation where it is desirable to optically tune the resonance of an FBG.

7.1. SUGGESTED FUTURE WORK

Blazed Grating Spectrometer

Previous reports of BFBG spectrometers used expensive InGaAs arrays with much larger pixels because they offer significant improvements over coated CCD arrays in terms of responsivity linearity. If a BFBG could be manufactured to operate at 600nm, then the existing BFBG spectrometer prototype could be made to operate in the flatter and more responsive region of Figure 4.7b. A system operating at this wavelength would also benefit from low-cost light sources in this spectral region.

In the current BFBG spectrometer design, excessive temperature excursions cause the glass window shown in Figure 4.27 and Figure 4.28 to deform as a result of thermal

expansion of the index matching fluid and thereby impede system performance. If fibre alignment and index matching component could be replaced by a solid prism the thermal dependence of the system would be significantly improved.

Section 4.4 showed the successful implementation of a BFBG spectrometer in which the bandwidth was improved by superimposing two gratings of different blaze angles. It should be possible to repeat this with a number of overlaid gratings and thereby increase the bandwidth of the system to a larger maximum level.

Type IA Gratings

Figure 5.2 (for example) shows the mean index change of a type IA grating during inscription. The temperature coefficients at the end of the initial growth period (up to the point of type I formation) and at the end of IA inscription are known, but it is not known how the temperature coefficient changes in between these two points. By inscribing multiple gratings at levels of maturity corresponding to points along this curve, it would be possible to then plot the evolution of the temperature response during fabrication and may thereby give significant insight into the photochemical changes taking place within the fibre.

Among the most significant sections of this thesis is Section 5.4.1 which shows that there are at least two photosensitive mechanisms involved in the fabrication of type IA gratings. Figure 5.8 shows that the formation of type I gratings requires single photon absorption, but the transformation from type I to type IA requires multiple photon absorption. Unfortunately, despite repeated attempts, it has not been possible to safely conclude the number of photons absorbed during the transformation. This is a consequence of small fluctuations in the intensity of the inscribing UV laser on the fibre sample, probably caused by sub-micron misalignments of the fibre in the inscription apparatus. It may be possible to eliminate these fluctuations with feedback from beam position sensors (see the works of Mikael Svalgaard, e.g. [165, 166]) and thereby accurately predict the number of photons absorbed during IA formation.

Heating a hydrogenated section of germanosilicate fibre above ~200°C results in the formation of an absorption band similar to those shown in Section 6.4, but does not impart a mean index change. Furthermore, Section 6.3.2 shows that the minimum resolution in locality of an index change is ~0.5mm and indicates a diffuse nature through the slope of the index change shown by Figure 6.15. This diffuse nature is an indication that fibre heating may be responsible for the change. This may indicate that the formation of the OH band is incidental to the formation of IA gratings and is simply the consequence of UV induced fibre heating (see Section 5.4.2). Alternatively, type IA formation may require both elevated temperature and the presence of hydrogen (Figure 5.12 indicates that elevated temperatures act as a catalyst to IA formation). Clearly the OH band is required for IA fabrication using the blank-beam pre-exposure method (Section 5.3.3) but the significance, or lack thereof, of the absorption band may be of interest to photo-chemists and should therefore be the subject of further work.

Section 5.5 shows the importance of exposure uniformity in order to produce a *clean* type IA grating. However, if the exposure were to be deliberately and controllably non-uniform a grating with any desired mean index profile could be manufactured; this would enable the chirping of a uniform period grating up to ~16nm.

Section 6.2.2.2 shows that samples containing a higher concentration of hydrogen form IA gratings faster, and that the gratings have lower temperature coefficients than similar samples with a lower concentration. This work should be expanded to investigate the upper and lower limits of hydrogenation and to investigate the minimum achievable temperature coefficients at extremely high hydrogen levels. It has been shown by Section 6.2.2.1 that hydrogen pre-sensitisation (refer to Section 2.2.3.2) does not result in the formation of IA gratings. Alternatives to hydrogenation, such as deuterium loading or flame brushing, should be tested with relation to the production of IA gratings.

8. PUBLICATIONS & REFERENCES

8.1. PUBLICATIONS ARISING FROM THIS WORK

8.1.1. Type IA work

1. AG. Simpson, K. Kalli, K. Zhou, L. Zhang, and I. Bennion, "*An ideal method for the fabrication of temperature compensating IA-I strain sensors,*" presented at OFS16, Nara, Japan, PD4, 2003.

2. AG. Simpson, K. Kalli, K. Zhou, L. Zhang, and I. Bennion, "*Formation of type IA fibre Bragg gratings in germanosilicate optical fibre,*" Electronics Letters, vol. 40, iss. 3, pp. 163-164, 2004.

3. AG. Simpson, K. Kalli, K. Zhou, L. Zhang, and I. Bennion, "*Blank beam fabrication of regenerated type IA gratings,*" Measurement Science & Technology, vol. 15, iss. 8, pp. 1665-1669, 2004.

4. AG. Simpson, K. Kalli, L. Zhang, K. Zhou, and I. Bennion, "*Type IA fibre Bragg grating photosensitivity and the development of optimum temperature invariant Type I - IA strain sensors,*" presented at SPIE, Photonics Europe, Salle Sforza/Spaak, paper reference 5459-14, 2004.

5. AG. Simpson, K. Kalli, K. Zhou, L. Zhang, and I. Bennion, "*Abnormal photosensitivity effects and the formation of type IA FBGs,*" presented at BGPP, 2003, Monterey, USA, MD32, 2003.

6. K. Kalli, AG. Simpson, K. Zhou, L. Zhang, D. Birkin, T. Ellingham, and I. Bennion, "*Wavelength tuning, chirping and thermally induced decay of type IA FBGs using purely optical methods,*" Optical Fibre Sensors 17 (OFS17), 2005, awaiting publication.

7. K. Kalli, AG. Simpson, K. Zhou, L. Zhang, and I. Bennion, "*Impact of hydrogenation conditions on the temperature and strain coefficients of type I and type IA dual grating sensors,*" Optical Fibre Sensors 17 (OFS17), 2005, awaiting publication.

8.1.2. BFBG work

8. AG. Simpson, K. Zhou, L. Zhang, L. Everall, and I. Bennion, "*Optical sensor interrogation with a blazed fibre Bragg grating and a charge-coupled device linear array,*" Applied Optics, vol. 43, iss. 1, pp. 33-40, 2004.

9. AG. Simpson, K. Zhou, P. Foote, L. Zhang, and I. Bennion, "*Polarisation independent, high resolution spectral interrogation of FBGs using a BFBG-CCD array for optical sensing applications,*" presented at SPIE, Photonics East, Rhode Island, USA, 2003.

10. K. Zhou, AG. Simpson, L. Zhang, I. Bennion, "*Low-cost in-fibre WDM devices using tilted FBGs,*" presented at CLEO, Baltimore, USA, 2003.

11. K. Zhou, AG. Simpson, L. Zhang, and I. Bennion, "*Side detection of strong radiation-mode out-coupling from blazed FBGs in single-mode and multimode fibres,*" IEEE Photonics Technology Letters, vol. 15, iss. 7, pp. 936-938, 2003.

12. K. Zhou, AG. Simpson, X. Chen, L. Zhang, and I. Bennion, "*High extinction ratio in-fibre polarizer based on a 45 -tilted fibre Bragg grating,*" Optics Letters, Awaiting publication (2005).

13. K. Zhou, AG. Simpson, X. Chen, L. Zhang, and I. Bennion, "*Two-dimensional optical power distribution of side-out-coupled radiation from tilted FBGs in multimode fibre,*" Electronics Letters, vol. 39, iss. 8, pp. 651-653, 2003.

14. K. Zhou, AG. Simpson, X. Chen, L. Zhang, and I. Bennion, "*Fibre Bragg grating sensor interrogation system using a CCD side detection method with superimposed blazed gratings*," IEEE Photonics Technology Letters, vol. 16, iss. 6, pp. 1549-1551, 2004.

15. K. Zhou, AG. Simpson, L. Zhang, I. Bennion, "*Wide bandwidth, high resolution spectral interrogation using a BFBG-CCD array for optical sensing applications,*" presented at Optical Fibre Sensors - 16, Nara, Japan, 2003.

16. K. Zhou, AG. Simpson, L. Zhang and I. Bennion, "*High accuracy interrogation of a WDM FBG sensor array using radiation modes from a B-FBG,*" presented at BGPP, Monterey ,USA, 2003.

17. K. Zhou, AG. Simpson, X. Chen, L. Zhang, I. Bennion, "*Superimposed blazed grating based CCD side detection system and its application in sensor interrogation,*" presented at ECOC, 2004.

8.2. REFERENCES

[1] K. O. Hill, Y. Fujii, D. C. Johnson, and B. S. Kawasaki, "Photosensitivity on optical fibre waveguides: application to reflection filter fabrication," *Applied Physics Letters*, vol. 32, pp. 647-649, 1978.

[2] D. K. W. Lam and B. Garside, "Characterization of single-mode optical fibre filers," *Applied Optics*, vol. 20, pp. 440-445, 1981.

[3] G. Meltz, W. W. Morey, and W. H. Glenn, "Formation of Bragg Gratings in Optical Fibres By a Transverse Holographic Method," *Optics Letters*, vol. 14, Iss. 15, pp. 823-825, 1989.

[4] D. Z. Anderson, V. Mizrahi, T. Erdogan, and A. White, "Production of in-fibre gratings using a diffractive optical element," *Electronics Letters*, vol. 29, pp. 566-567, 1993.

[5] K. O. Hill, B. Malo, F. Bilodeau, D.C. Johnson, and J. Albert, "Bragg gratings fabricated in monomode photosensitive optical fibre by UV exposure through a phase mask," *Applied Physics Letters*, vol. 62, pp. 1035-1037, 1993.

[6] G. Meltz, W. W. Morey, and W. Glenn, "In-Fibre Bragg grating tap," presented at Optical Fibre Communications, TUG1, pp24 1990.

[7] Y. Liu, "Advanced fibre gratings and their application," Ph.D. Thesis, *Photonics Research Group*, Aston University, Birmingham, 2001.

[8] I. Bennion, J. A. R. Williams, L. Zhang, K. Sugden, and N. Doran, "UV-written in-fibre Bragg gratings," *Optical and Quantum Electronics*, vol. 28, pp. 93-135, 1996.

[9] K. O. Hill and G. Meltz, "Fibre Bragg Grating Technology Fundamentals and Overview," *Journal of Lightwave Technology*, vol. 15, Iss. 8, pp. 1263-1276, 1997.

[10] A. Othonos, "Fibre Bragg gratings," *Rev. Sci. Instrum*, vol. 68, Iss. 12, pp. 4309-4341, 1997.

[11] A. Othonos and K. Kalli, "Bragg gratings in optical fibres," in *Handbook of advanced electronic and photonic materials ad devices*, vol. 9, Nonlinear optical materials, H. Nalwa, Ed., 2001.

[12] A. D. Kersey, M. A. Davis, H. J. Patrick, M. LeBlanc, K. P. Koo, C. G. Askins, M. A. Putnam, and E. J. Friebele, "Fibre grating sensors," *Journal of Lightwave Technology*, vol. 15, Iss. 8, pp. 1442-1463, 1997.

[13] Y. J. Rao, "In-Fibre Bragg grating sensors," *Meas. Sci. Technol.*, vol. 8, pp. 355-375, 1997.

[14] L. Zhang, W. Zhang, and I. Bennion, "In-Fibre Grating Optic Sensors," in *Fibre Optic Sensors*, F. Yu and S. Yin, Eds. New York: Marcel Dekker Inc, 2002.

[15] D. A. Jackson and D. Webb, "Optical fibre Bragg grating sensors for strain measurement," in *Handbook of Laser Technology and Applications: Volume 1: Principles*, vol. 3, CE Webb and J. Jones, Eds., 2003, pp. Part D.

[16] B. Lee, "Review of the present status of optical fibre sensors," *Optical fibre technology*, vol. 9, pp. 57-79, 2003.

[17] R. Kashyap, *Fibre Bragg gratings*: Academic Press, ISBN 0124005608, 1st Edition, 1999.

[18] A. Othonos and K. Kalli, *Fibre Bragg gratings*: Artech House Publishers, ISBN 0890063443, 1st Edition, 1999.

[19] C. Fiori and R. Devine, "Evidence for a wide continuum of polymorphs in a-SiO2," *Physical Review B*, vol. 33, pp. 2972-2974, 1986.

[20] N. Lawandy, "Light induced transport and delocalisation in transparent amorphous systems," *Optics Communications*, vol. 74, pp. 180-184, 1989.

[21] D. P. Hand and J. S. Russell, "Photoinduced refractive index changes in fibre Bragg gratings," *Applied Physics Letters*, vol. 15, pp. 102-104, 1990.

[22] A. Attard, "Fermi level shift in $Bi_{12}SiO_{20}$ vis photon-induced trap level occupation," *Journal of Applied Physics*, vol. 71, pp. 933-937, 1992.

[23] M. G. Sceats, G. R. Askins, and S. Poole, "Photo-induced index changes in optical fibres," *Annual Reviews in Material Science*, vol. 23, pp. 381-410, 1993.

[24] D. Williams, "Photosensitivity and self-organisation in optical fibres and waveguides," presented at SPIE, vol 2044, pp 55-68, 1993.

[25] K. D. Simmons, S. Larochelle, V. Mizrahi, G. I. Stegeman, and D. L. Griscom, "Correlation of Defect Centres With a Wavelength-Dependent Photosensitive Response in Germania-Doped Silica Optical Fibres," *Optics Letters*, vol. 16, Iss. 3, pp. 141-143, 1991.

[26] R. M. Atkins, "Measurement of the Ultraviolet-Absorption Spectrum of Optical Fibres," *Optics Letters*, vol. 17, Iss. 7, pp. 469-471, 1992.

[27] D. P. Hand and P. S. Russell, "Photoinduced Refractive-Index Changes in Germanosilicate Fibres," *Optics Letters*, vol. 15, Iss. 2, pp. 102-104, 1990.

[28] J. Nishii, H. Yamanaka, H. Hosono, and H. Kawazoe, "Preparation of Bragg gratings in sputter-deposited GeO2-SiO2 glasses by excimer-laser irradiation," *Optics Letters*, vol. 21, Iss. 17, pp. 1360-1362, 1996.

[29] D. L. Williams, S. T. Davey, R. Kashyap, J. R. Armitage, and B. J. Ainslie, "Direct Observation of UV Induced Bleaching of 240-Nm Absorption-Band in Photosensitive Germanosilicate Glass-Fibres," *Electronics Letters*, vol. 28, Iss. 4, pp. 369-371, 1992.

[30] R. M. Atkins and V. Mizrahi, "Observations of Changes in UV Absorption-Bands of Single mode Germanosilicate Core Optical Fibres On Writing and Thermally Erasing Refractive-Index Gratings," *Electronics Letters*, vol. 28, Iss. 18, pp. 1743-1744, 1992.

[31] R. M. Atkins, V. Mizrahi, and T. Erdogan, "248nm Induced Vacuum UV Spectral Changes in Optical-Fibre Preform Cores - Support For a Color Center Model of Photosensitivity," *Electronics Letters*, vol. 29, Iss. 4, pp. 385-387, 1993.

[32] B. Malo, K. A. Vineberg, F. Bilodeau, J. Albert, D. C. Johnson, and K. O. Hill, "Ultraviolet-Light Photosensitivity in Ge-Doped Silica Fibres - Wavelength Dependence of the Light-Induced Index Change," *Optics Letters*, vol. 15, Iss. 17, pp. 953-955, 1990.

[33] F. Bilodeau, D. C. Johnson, B. Malo, K. A. Vineberg, K. O. Hill, T. F. Morse, A. Kilian, and L. Reinhart, "Ultraviolet-Light Photosensitivity in Er-3+-Ge-Doped Optical Fibre," *Optics Letters*, vol. 15, Iss. 20, pp. 1138-1140, 1990.

[34] T. E. Tsai, E. J. Friebele, and D. L. Griscom, "Thermal-Stability of Photoinduced Gratings and Paramagnetic Centers in Ge-Doped and Ge/P-Doped Silica Optical Fibres," *Optics Letters*, vol. 18, Iss. 12, pp. 935-937, 1993.

[35] W. X. Xie, P. Niay, P. Bernage, M. Douay, J. F. Bayon, T. Georges, M. Monerie, and B. Poumellec, "Experimental-Evidence of 2 Types of Photorefractive Effects Occurring During Photo inscriptions of Bragg Gratings Within Germanosilicate Fibres," *Optics Communications*, vol. 104, Iss. 1-3, pp. 185-195, 1993.

[36] P. Cordier, J. C. Doukhan, E. Fertein, P. Bernage, P. Niay, J. F. Bayon, and T. Georges, "TEM Characterization of Structural-Changes in Glass Associated to Bragg Grating Inscription in a Germanosilicate Optical-Fibre Preform," *Optics Communications*, vol. 111, Iss. 3-4, pp. 269-275, 1994.

[37] P. Niay, P. Bernage, S. Legoubin, M. Douay, W. X. Xie, J. F. Bayon, T. Georges, M. Monerie, and B. Poumellec, "Behaviour of Spectral Transmissions of Bragg

Gratings Written in Germania-Doped Fibres - Writing and Erasing Experiments Using Pulsed or CW UV Exposure," *Optics Communications*, vol. 113, Iss. 1-3, pp. 176-192, 1994.

[38] K. S. Chiang, M. G. Sceats, and D. Wong, "Ultraviolet Photolytic-Induced Changes in Optical Fibres - the Thermal-Expansion Coefficient," *Optics Letters*, vol. 18, Iss. 12, pp. 965-967, 1993.

[39] B. Malo, J. Albert, D. C. Johnson, F. Bilodeau, and K. O. Hill, "Elimination of Photoinduced Absorption in Ge-Doped Silica Fibres By Annealing of Ultraviolet Color-Centers," *Electronics Letters*, vol. 28, Iss. 17, pp. 1598-1599, 1992.

[40] M. Douay, W. X. Xie, T. Taunay, P. Bernage, P. Niay, P. Cordier, B. Poumellec, L. Dong, J. F. Bayon, H. Poignant, and E. Delevaque, "Densification involved in the UV-based photosensitivity of silica glasses and optical fibres," *Journal of Lightwave Technology*, vol. 15, Iss. 8, pp. 1329-1342, 1997.

[41] D. L. Williams, B. J. Ainslie, J. R. Armitage, R. Kashyap, and R. Campbell, "Enhanced UV Photosensitivity in Boron Co doped Germanosilicate Fibres," *Electronics Letters*, vol. 29, Iss. 1, pp. 45-47, 1993.

[42] L. Dong, J. L. Cruz, L. Reekie, M. G. Xu, and D. Payne, "Enhanced photosensitivity in tin-co doped germanosilicate optical fibres," *IEEE Photonics Technology Letters*, vol. 7, pp. 1048-1050, 1995.

[43] R. M. Atkins, P. J. Lemaire, T. Erdogan, and V. Mizrahi, "Mechanisms of Enhanced UV Photosensitivity Via Hydrogen Loading in Germanosilicate Glasses," *Electronics Letters*, vol. 29, Iss. 14, pp. 1234-1235, 1993.

[44] P. J. Lemaire, R. M. Atkins, V. Mizrahi, and W. A. Reed, "High-Pressure H-2 Loading As a Technique For Achieving Ultrahigh UV Photosensitivity and Thermal Sensitivity in Geo2 Doped Optical Fibres," *Electronics Letters*, vol. 29, Iss. 13, pp. 1191-1193, 1993.

[45] P. Y. Fonjallaz, H. G. Limberger, R. P. Salathe, F. Cochet, and B. Leuenberger, "Tension Increase Correlated to Refractive-Index Change in Fibres Containing UV-Written Bragg Gratings," *Optics Letters*, vol. 20, Iss. 11, pp. 1346-1348, 1995.

[46] J. Canning, M. Aslund, and P. Hu., "Ultraviolet-induced absorption losses in hydrogen-loaded optical fibres and in presensitized optical fibres,," *Optics Letters*, vol. 25, Iss. 22, pp. 1621-1623, 2000.

[47] N. K. Viswanathan, W. V. Dower, D. M. Paolucci, and M. Barrera, "Enhancing fibre photosensitivity using dilute hydrogen in high-pressure mixtures," presented at BGPP, Monterey, CA., vol MC5, pp 49-52, 2003.

[48] H. Poignant, "Influence of H_2 loading on the kinetics of type IIA fibre Bragg grating photo inscription," presented at IEE Colloquium on optical fibre gratings, 1997.

[49] P. Lemaire, "Reliability of optical fibres exposed to hydrogen: prediction of long-term loss increases," *Optical Engineering*, vol. 30, pp. 780-781, 1991.

[50] J. Crank, *The mathematics of diffusion, Page 30*. Oxford, UK: Clarendon-Press, 1975.

[51] F. Bliodeau, B. Malo, J. Albert, DC. Johnson, KO. Hill, Y. Hibino, Y. Abe, and M. Kawachi, "Photosensitisation of optical fibre and silica-on-silicon/silica waveguides," *Optics Letters*, vol. 18, pp. 953-955, 1993.

[52] D. L. Williams and R. P. Smith, "Accelerated Lifetime Tests On UV Written Intra-core Gratings in Boron Germania Co doped Silica Fibre," *Electronics Letters*, vol. 31, Iss. 24, pp. 2120-2121, 1995.

[53] S. Kannan, J. Z. Y. Guo, and P. J. Lemaire, "Thermal stability analysis of UV-induced fibre Bragg gratings," *Journal of Lightwave Technology*, vol. 15, Iss. 8, pp. 1478-1483, 1997.

[54] S. Ishikawa, A. Inoue, M. Harumoto, T. Enomoto, and H. Kanamori, "Adequate aging condition for fibre Bragg grating based on simple power low model," presented at Optical Fibre Sensors (OFS1998), pp183-184, 1998.

[55] H. Patrick, S. L. Gilbert, A. Lidgard, and M. D. Gallagher, "Annealing of Bragg Gratings in Hydrogen-Loaded Optical-Fibre," *Journal of Applied Physics*, vol. 78, Iss. 5, pp. 2940-2945, 1995.

[56] M. Aslund and J. Canning, "Annealing properties of gratings written into UV-presensitized hydrogen-out diffused optical fibre," *Optics Letters*, vol. 25, Iss. 10, pp. 692-694, 2000.

[57] T. Erdogan, V. Mirrahi, P. Lemaire, and D. Monroe, "Decay of ultraviolet-induced fibre Bragg gratings," *Journal of Applied Physics*, vol. 76, Iss. 1, pp. 73-80, 1994.

[58] S. R. Baker, H. N. Rourke, V. Baker, and D. Goodchild, "Thermal decay of fibre Bragg gratings written in boron and germanium co doped silica fibre," *Journal of Lightwave Technology*, vol. 15, Iss. 8, pp. 1470-1477, 1997.

[59] Y. Masuda and e. al, "Wavelength evolution of fibre Bragg gratings fabricated from hydrogen-loaded optical fibre during annealing.," *Journal of Lightwave Technology*, vol. 22, Iss. 3, pp. 934-941, 2004.

[60] K. E. Chisholm, K. Sugden, and I. Bennion, "Effects of thermal annealing on Bragg fibre gratings in boron/germania co-doped fibre," *Journal of Physics D-Applied Physics*, vol. 31, Iss. 1, pp. 61-64, 1998.

[61] S. Pal, J. Mandal, T. Sun, and K. T. V. Grattan, "Analysis of thermal decay and prediction of operational lifetime for a type I boron-germanium co doped Fibre Bragg grating," *Applied Optics*, vol. 42, Iss. 12, pp. 2188-2197, 2003.

[62] J. Senior, *Optical Fibre Communications*: Prentice Hall, 1st Edition, 1992.

[63] Y. Li, M. Froggatt, and T. Erdogan, "Volume Current Method for Analysis of Tilted Fibre Gratings," *Journal of Lightwave Technology*, vol. 19, Iss. 10, pp. 1580-1591, 2001.

[64] J. L. Wagner, T. A. Strasser, J. N. Pedrazzani, J. DeMarco, and D. DiGiovanni., "Fibre grating optical spectrum analyzer tap," presented at ECOC, pp 65-68, 1997.

[65] R. W. S. J. Mihailov, P. Lu, H. Ding, X. Dai, C. Smelser and L. Chen, "UV-Induced polarisation-dependant loss (PDL) in tilted fibre Bragg gratings: application of a PDL equaliser," *IEE Proc. Optoelectronics*, vol. 149, pp. 211, 2002.

[66] R. W. S. J. Mihailov, T. J. Stocki and D. C. Johnson, "Fabrication of tilted fibre-grating polarisation-dependant loss equaliser," *Electronics Letters*, vol. 37, Iss. 5, 2001.

[67] T. Erdogan and J. E. Sipe, "Tilted fibre phase gratings," *Journal of the Optical Society of America a-Optics Image Science and Vision*, vol. 13, Iss. 2, pp. 296-313, 1996.

[68] K. Zhou, Private papers, 2003.

[69] K. Zhou, G. Simpson, X. Chen, L. Zhang, and I. Bennion, "High extinction ratio in-fibre polarizer based on a 45 -tilted fibre Bragg grating," *Optics Letters*, pp. In Press, 2004.

[70] A. Cooke, "The Thermo-Optic Effect," see *www.coe.uncc.edu/~alcooke/1*, 2002.

[71] G. Hocker, "Fibre-optic sensing of pressure and temperature," *Applied Optics*, vol. 18, Iss. 9, pp. 1445, 1979.

[72] C. B. A. G. Hocker, "Fibre optic strain gauge," *Applied Optics*, vol. 17, Iss. 2867-9, 1978.

[73] P. Fuhr, "Thermal Considerations for Fibre-Optic Sensor Components," *Sensor Technology and Design*, vol. Part 4, 2002.

[74] R. Maier, "Temperature dependence of the stress response of fibre Bragg gratings," *Measurement Science & Technology*, vol. 15, Iss. 8, pp. 1601-1606, 2004.

[75] S. W. James, R. P. Tatam, A. Twin, M. Morgan, and P. Noonan, "Strain response of fibre Bragg grating sensors at cryogenic temperatures," *Measurement Science & Technology*, vol. 13, Iss. 10, pp. 1535-1539, 2002.

[76] M. J. O'Dwyer, C. C. Ye, S. W. James, and R. Tatam, "Thermal dependence of the strain response of optical fibre Bragg gratings," *Measurement Science and Technology*, vol. 15, Iss. 8, pp. 1607-1613, 2004.

[77] G. M. H. Flockhart, R. R. J. Maier, J. S. Barton, W. N. MacPherson, J. D. C. Jones, K. E. Chisholm, L. Zhang, I. Bennion, I. Read, and P. D. Foote, "Quadratic behaviour of fibre Bragg grating temperature coefficients," *Applied Optics*, vol. 43, Iss. 13, pp. 2744-2751, 2004.

[78] J. Jones, "Review of fibre sensor techniques for temperature-strain discrimination," presented at OFS12, pp 36-39, 1997.

[79] D. Jackson, "Interferometers," in *Optical fibre sensors: systems and applications*, vol. 2, Culshaw and Dakin, Eds., 1989, pp. Ch 10, p239-280.

[80] W. Jin, "Simultaneous measurement of strain and temperature: Error analysis," *Optical Engineering*, vol. 36, pp. 598-609, 1997.

[81] G. P. Brady, K. Kalli, D. J. Webb, D. A. Jackson, L. Reekie, and J. Archambault, "Simultaneous measurement of strain and temperature using first- and second-order diffraction wavelengths of Bragg gratings," *IEE Proc. Optoelectronics*, vol. 144, Iss. 3, pp. 156-161, 1997.

[82] W. H. Press, B. P. Flannery, A .S. Teukolsky, and W. Vetterling, *Numerical Recipes*: Cambridge University Press, 2nd Edition, 1987.

[83] P. Sivanesan, J. S. Sirkis, Y. Murata, and S. Buckley, "Optimal wavelength pair selection and accuracy analysis of dual fibre grating sensors for simultaneously measuring strain and temperature," *Optics Engineering*, vol. 41, Iss. 10, pp. 2456-2463, 2002.

[84] G. A. Meltz, W. W. W. H. Morey, and A. L. M. Wilson, "US#5,061,032: Optical waveguide embedded light redirecting and focusing Bragg grating arrangement," US Patent: United Technologies Corporation (Hartford, CT), 1989.

[85] J. M. Moran and I. Kaminow, "Properties of holographic gratings photo induced in polymethylmethacrylate," *Applied Optics*, vol. 12, Iss. 8, pp. 1964-1970, 1973.

[86] B. Eggleton, P. Krug, and L. Poladian, "Experimental demonstration of compression of dispersed optical pulses by reflection from self-chirped optical fibre Bragg gratings," *Optics Letters*, vol. 19, pp. 877-880, 1994.

[87] R. Kashyap, J. R. Armitage, R. Wyatt, S. T. Davey, and D. L. Williams, "All-Fibre Narrow-Band Reflection Gratings At 1500 Nm," *Electronics Letters*, vol. 26, Iss. 11, pp. 730-732, 1990.

[88] H. Limberger, "Photosensitivity and self-organization in optical fibres and waveguides," presented at SPIE, vol 2044, pp 272-285, 1993.

[89] X. Liu, J. S. Aitchison, R. M. DeLaRue, S. Thoms, L. Zhang, J. A. R. Williams, and I. Bennion, "Electron beam lithography of phase mask gratings for near field holographic production of optical fibre gratings," *Microelectronic Engineering*, vol. 35, Iss. 1-4, pp. 345-348, 1997.

[90] J. D. Prohaska, E. Snitzer, S. Rishton, and V. Boegli, "Magnification of Mask Fabricated Fibre Bragg Gratings," *Electronics Letters*, vol. 29, Iss. 18, pp. 1614-1615, 1993.

[91] Q. Zhang, D. A. Brown, L. Reinhart, T. F. Morse, J. Q. Wang, and G. Xiao, "Tuning Bragg Wavelength By Writing Gratings On Pre-strained Fibres," *IEEE Photonics Technology Letters*, vol. 6, Iss. 7, pp. 839-841, 1994.

[92] K. C. Byron and H. N. Rourke, "Fabrication of Chirped Fibre Gratings By Novel Stretch and Write Technique," *Electronics Letters*, vol. 31, Iss. 1, pp. 60-61, 1995.

[93] A. G. Simpson, K. Kalli, K. Zhou, L. Zhang, and I. Bennion, "An ideal method for the fabrication of temperature compensating IA-I strain sensors," presented at OFS16, Nara, Japan, paper PD4, 2003.

[94] L. Dong, J. L. Archambault, L. Reekie, P. S. J. Russell, and D. N. Payne, "Single-Pulse Bragg Gratings Written During Fibre Drawing," *Electronics Letters*, vol. 29, Iss. 17, pp. 1577-1578, 1993.

[95] J. L. Archambault, L. Reekie, and P. S. J. Russell, "100-Percent Reflectivity Bragg Reflectors Produced in Optical Fibres By Single Excimer-Laser Pulses," *Electronics Letters*, vol. 29, Iss. 5, pp. 453-455, 1993.

[96] J. Canning, D. Moss, M. Aslund, and M. Bazylenko, "Negative index gratings in germanosilicate planar waveguides," *Electronics Letters*, vol. 34, Iss. 4, pp. 366-367, 1998.

[97] W. X. Xie, P. Niay, P. Bernage, M. Douay, T. Taunay, J. F. Bayon, E. Delevaque, and M. Monerie, "Photo inscription of Bragg gratings within preform plates of high NA germanosilicate fibres: Searching for an experimental evidence of type II A photosensitivity in preform plates," *Optics Communications*, vol. 124, Iss. 3-4, pp. 295-300, 1996.

[98] L. Dong, W. F. Liu, and L. Reekie, "Negative-index gratings formed by a 193-nm excimer laser," *Optics Letters*, vol. 21, Iss. 24, pp. 2032-2034, 1996.

[99] P. E. Dyer, R. J. Farley, R. Giedl, and K. C. Byron, "Amplification of Fibre Bragg Grating Reflectivity By Post- Writing Exposure With a 193nm ArF Laser," *Electronics Letters*, vol. 30, Iss. 14, pp. 1133-1134, 1994.

[100] P. E. Dyer, R. J. Farley, R. Giedl, K. C. Byron, and D. Reid, "High Reflectivity Fibre Gratings Produced By Incubated Damage Using a 193nm ArF Laser," *Electronics Letters*, vol. 30, Iss. 11, pp. 860-862, 1994.

[101] N. Groothoff and J. Canning, "Enhanced type IIA gratings for high-temperature operation," *Optics Letters*, vol. 29, Iss. 30, pp. 2330-2352, 2004.

[102] J. Canning and M. Aslund, "Correlation of ultraviolet-induced stress changes and negative index growth in type IIA germanosilicate waveguide gratings," *Optics Letters*, vol. 24, Iss. 7, pp. 463-465, 1999.

[103] X. W. Shu, D. H. Zhao, L. Zhang, and I. Bennion, "Use of dual-grating sensors formed by different types of fibre Bragg gratings for simultaneous temperature and strain measurements," *Applied Optics*, vol. 43, Iss. 10, pp. 2006-2012, 2004.

[104] Y. Liu, X. Shu, F. Floreani, L. Zhang, JAR. Williams, and I. Bennion, "Abnormal spectral evolution and temperature sensitivity reduction in regenerated FBGs in hydrogenated fibres with UV overexposure," presented at POWAG, paper WA4, 2002.

[105] X. W. Shu, Y. Liu, D. H. Zhao, B. Gwandu, F. Floreani, L. Zhang, and I. Bennion, "Dependence of temperature and strain coefficients on fibre grating type and its application to simultaneous temperature and strain measurement," *Optics Letters*, vol. 27, Iss. 9, pp. 701-703, 2002.

[106] X. Shu, "Effectively simultaneous temperature and strain measurement utilising a dual-grating sensor formed by Type IA and Type IIA FBGs," presented at IEEE Sensors 2002, pp 1740-1745, 2002.

[107] X. Shu, Y. Liu, D. Zhao, B. Gwandu, F. Floreani, L. Zhang, and I. Bennion, "Fibre grating type dependence of temperature and strain coefficients and application to simultaneous temperature and strain measurement," presented at Optical Fibre Sensors, vol TuB4, pp 83-86, 2002.

[108] Y. Liu, J. A. R. Williams, L. Zhang, and I. Bennion, "Abnormal spectral evolution of fibre Bragg gratings in hydrogenated fibres," *Optics Letters*, vol. 27, Iss. 8, pp. 586-588, 2002.

[109] J. F. Brennan, D. Sloan, J. Dent, and D. L. LaBrake, "The behaviour of silica optical fibres exposed to very high-pressure hydrogen environments," presented at Optical Fibre Sensors, San Diego, pp 81-85, 1999.

[110] J. F. Brennan, D. Sloan, J. Dent, and D. L. LaBrake, "The behaviour of silica optical fibres exposed to very high-pressure hydrogen environments," presented at Optical Society of America, TOPS XXIX, pp 101-105, 1999.

[111] J. F. Brennan, D. A. Sloan, M. May, and D. L. LaBrake, "The photosensitivity and UV-induced optical loss of silica optical fibres exposed to very high-pressure hydrogen environments," presented at SPIE 3847, pp 42-47, 1999.

[112] H. Kawano, H. Muentz, Y. Sato, J. Nishimae, and A. Sugitatsu, "Reduction of transmission spectrum shift of long-period fibre gratings by a UV-preexposure method," *Journal of Lightwave Technology*, vol. 19, Iss. 8, pp. 1221-1228, 2001.

[113] F. M. Haran, J. K. Rew, and P. Foote, "A strain-isolated fibre Bragg grating sensor for temperature compensation of fibre Bragg grating strain sensors," *Measurement Science and Technology*, vol. 9, pp. 1163-1166, 1998.

[114] W. W. Morey, G. Meltz, and J. Weiss, "Evaluation of a fibre Bragg grating hydrostatic pressure sensor," presented at OFS8, Monterey, CA., post-deadline paper 4.4, 1992.

[115] A. D. Kersey, T. A. Berkoff, and W. Morey, "Fibre-optic Bragg grating strain sensor with drifting-compensated high-resolution interferometric wavelength-shift detection," *Optics Letters*, vol. 18, pp. 72-74, 1993.

[116] MG. Xu, J. L. Archambault, L. Reekie, and J. Dakin, "Thermally compensated bending gauge using surface-mounted fibre gratings," *International Journal of Optoelectronics*, vol. 9, Iss. 281-283, 1994.

[117] G. W. Yoffee, PA. Krug, F. Ouellette, and D. Thorncraft, "Passive temperature-compensating package for optical fibre gratings," *Applied Optics*, vol. 34, Iss. 30, pp. 6859-6861, 1995.

[118] T. Iwashima, "Temperature compensation technique for fibre Bragg gratings using liquid crystalline polymer tubes," *Electronics Letters*, vol. 33, pp. 417-419, 1997.

[119] M. G. Xu, J. L. Archambault, L. Reekie, and J. P. Dakin, "Discrimination between strain and temperature effects using dual wavelength fibre sensors," *Electronics Letters*, vol. 30, Iss. 13, pp. 1085-1087, 1994.

[120] K. Kalli, G. Brady, DJ. Webb, DA. Jackson, L. Zhang, and I. Bennion, "Possible approach for simultaneous measurement of strain and temperature with second harmonics in a fibre Bragg grating sensor," presented at OFS10, Glasgow, postdeadline paper 2.1, 1994.

[121] O. Frazao, M. J. N. Lima, and J. L. Santos, "Simultaneous measurement of strain and temperature using type I and type IIA fibre Bragg gratings," *Journal of Optics a-Pure and Applied Optics*, vol. 5, Iss. 3, pp. 183-185, 2003.

[122] P. M. Cavalerio, F. M. Araujo, L. A. Ferreira, J. L. Santos, and F. Farahi, "Simultaneous measurement of strain and temperature using Bragg gratings written in germanosilicate and boron-co doped germanosilicate fibres," *IEEE Photonics Technology Letters*, vol. 11, Iss. 12, pp. 1635-1637, 1999.

[123] B. Guan, H. Tam, S. Ho, W. Chung, and X. Dong, "Simultaneous strain and temperature measurement using a single fibre Bragg grating," *Electronics Letters*, vol. 36, Iss. 12, 2000.

[124] S. W. James, M. L. Dockney, and R. Tatam, "Simultaneous independent temperature and strain measurement using in-fibre Bragg grating sensors," *Electronics Letters*, vol. 32, Iss. 12, pp. 1133-1134, 1996.

[125] B. L. Minho Song, Sang Bae Lee, Sang Sam Choi, "Interferometric temperature-insensitive strain measurement with different-diameter fibre Bragg gratings," *Optics Letters*, vol. 22, Iss. 11, pp. 790-792, 1997.

[126] M. G. Xu, L. Dong, L. Reekie, and J. Cruz, "Temperature independent strain sensor using a chirped grating in a tapered fibre," *Electronics Letters*, vol. 31, Iss. 10, pp. 823-825.

[127] Z. J. Lu and F. Blaha, "Application issues of fibre optic sensors in aircraft structures," presented at SPIE, Fibre Optic Smart Structures IV, vol 1588, pp 276-281, 1991.

[128] K. Talat, "Smart skins and optic-optic sensors application and issues," presented at SPIE Fibre Optic Smart Structures III, vol 1370, pp 103-114, 1990.

[129] R. E. Morgan, S. L. Ehlers, and K. Jones, "Composite embedded fibre optic data links and related material / connector issues," presented at SPIE Fibre Optic Smart Structures IV, vol 1588, pp 189-197, 1991.

[130] H. K. Kang, J. W. Park, C. Y. Ryu, CS. Hong, and C. Kim, "Development of fibre optic ingress / egress methods for smart composite structures," *Smart Materials and Structures*, Iss. 9, pp. 149-156, 2000.

[131] Sjogren, "Manufacturing technique for embedding detachable optic-optic connections in aircraft composite components," *Smart Materials and Structures*, vol. 9, pp. 855-858, 2000.

[132] B. Sjorgren, "Static strength of CFRP laminates with embedded fibre-optic edge connectors," *Composites: Part A*, vol. 32, pp. 189-196, 2001.

[133] A. K. Green and E. Shafir, "Termination and connection methods for optical fibres embedded in aerospace composite components," *Smart Materials and Structures*, vol. 8, pp. 269-273, 1999.

[134] A. K. Green, M. Zaidman, E. Shafir, M. Tur, and S. Gali, "Infrastructure development for incorporating fibre-optic sensors in composite materials," *Smart Materials and Structures*, vol. 9, pp. 316-321, 2000.

[135] R. S. Westbrook, K. S. Feder, P. I. Reyes, P. Steinvurzel, B. J. Eggleton, R. G. Ernst, L. A. Reith, and D. M. Gill, "Application of fibre Bragg grating filter/tap module to a wavelength-locked low-chirp directly-modulated 10Gb/s RZ transmitter," presented at Optical Fibre Communications, vol ThG49, pp 680-681, 2002.

[136] H. S. Park, S. H. Yun, I. K. Hwang, S. B. Lee, and B. Y. Kim, "All-fibre add-drop wavelength-division multiplexer based on inter-modal coupling," *IEEE Photonics Technology Letters*, vol. 13, Iss. 5, pp. 460-462, 2001.

[137] K. W. Gaff, F. Ladouceur, and J. D. Love, "Two-wavelength planar add/drop WDM filter employing a three- mode coupling Bragg grating," *Electronics Letters*, vol. 36, Iss. 13, pp. 1142-1144, 2000.

[138] E. Marin, R. Ghosh, J. P. Meunier, X. Daxhelet, and S. Lacroix, "Bragg gratings in 2 x 2 symmetric fused fibre couplers: Influence of the tilt on the wavelength response," *IEEE Photonics Technology Letters*, vol. 11, Iss. 11, pp. 1434-1436, 1999.

[139] S. Baek, Y. Jeong, and B. Lee, "Characteristics of short-period blazed fibre Bragg gratings for use as macro-bending sensors," *Applied Optics*, vol. 41, Iss. 4, pp. 631-636, 2002.

[140] G. Laffont and P. Ferdinand, "Tilted short-period fibre-Bragg-grating-induced coupling to cladding modes for accurate refractomerty," *Measurement Science & Technology*, vol. 12, Iss. 7, pp. 765-770, 2001.

[141] R. Kashyap, R. Wyatt, and R. J. Campbell, "Wide-Band Gain Flattened Erbium Fibre Amplifier Using a Photosensitive Fibre Blazed Grating," *Electronics Letters*, vol. 29, Iss. 2, pp. 154-156, 1993.

[142] H. Labidi, C. Debarros, R. Letteron, and I. Riant, "Slanted Bragg grating with ultra-low polarization dependant loss," presented at Optical Fibre Communications, pp 113, 2002.

[143] M. Y. Fu, W. F. Liu, T. C. Chen, and H. J. Sheng, "Acousto-optic-induced cladding-mode reflection in a blazed- superstructure fibre grating," *IEEE Photonics Technology Letters*, vol. 15, Iss. 10, pp. 1392-1394, 2003.

[144] C. W. Haggans, H. Singh, W. F. Varner, J. W. Li, and M. Zippin, "Narrow-band rejection filters with negligible back reflection using tilted photoinduced gratings in single-mode fibres," *IEEE Photonics Technology Letters*, vol. 10, Iss. 5, pp. 690-692, 1998.

[145] Y. Liu, L. Zhang, and I. Bennion, "Fabricating fibre edge filters with arbitrary spectral response based on tilted chirped grating structures," *Measurement Science & Technology*, vol. 10, Iss. 1, pp. L1-L3, 1999.

[146] G. Meltz, W. W. Morey, and A. Wilson, "Optical waveguide embedded light redirecting and focusing Bragg grating arrangement," . US, 1991.

[147] C. S. Koeppen and J. Wagener, "Article comprising a dispersive waveguide tap," . US, 2000.

[148] I. M. Perez and T. Bibby, "Fibre optic Bragg grating demodulator and sensor incorporating same," . US, 1997.

[149] J. M. Miller, N. deBeaucoudrey, P. Chavel, J. Turunen, and E. Cambril, "Design and fabrication of binary slanted surface-relief gratings for a planar optical interconnection," *Applied Optics*, vol. 36, Iss. 23, pp. 5717-5727, 1997.

[150] T. D. Liao, S. Sheard, M. Li, J. G. Zhu, and P. Prewett, "High-efficiency focusing waveguide grating coupler with parallelogramic groove profiles," *Journal of Lightwave Technology*, vol. 15, Iss. 7, pp. 1142-1148, 1997.

[151] C. Jauregui and J. Lopez-Higuera, "Interrogation of fibre Bragg gratings with a tilted fibre Bragg grating," *Measurement Science & Technology*, vol. 15, pp. 1596-1600, 2004.

[152] C. Jauregui, A. Quintela, F. J. Madruga, A. Cobo, and J. Lopez-Higuera, "Fibre Bragg grating interrogation scheme based on the radiated near-field of a tilted fibre grating," presented at Optical Fibre Sensors, 16, Nara, Japan, vol ThP34, pp 702-705, 2003.

[153] C. Jauregui, A. Quintela, F. J. Madruga, A. Cobo, and J. Lopez-Higuera, "Tilted chirped fibre Bragg gratings radiation behaviour," presented at Optical Fibre Sensors, 16, Nara, Japan, vol ThP33, pp 706-709, 2003.

[154] C. Jauregui, A. Quintela, O. M. Conde, A. Cobo, and J. M. Lopez-Higuera, "Civil Engineering Transducer's Interrogation Unit," presented at SPIE, Industrial and Highway Sensors Technology, Rhode Island, USA, vol 5272, pp 332-340, 2003.

[155] C. Jauregui, A. Quintela, and J. M. Lopez-Higuera, "Interrogation unit for fibre Bragg grating sensors that uses a slanted fibre grating," *Optics Letters*, vol. 29, Iss. 7, pp. 676-678, 2004.

[156] S. Wielandy and S. C. Dunn, "Tilted superstructure fibre grating used as a Fourier-transform spectrometer," *Optics Letters*, vol. 29, Iss. 14, pp. 1614-1616, 2004.

[157] K. S. Feder, P. S. Westbrook, J. Ging, P. I. Reyes, and G. E. Carver, "In-fibre spectrometer using tilted fibre gratings," *IEEE Photonics Technology Letters*, vol. 15, Iss. 7, pp. 933-935, 2003.

[158] A. Ezbiri, S. E. Kanellopoulos, and V. A. Handerek, "High resolution instrumentation system for fibre-Bragg grating aerospace sensors," *Optics Communications*, vol. 150, Iss. 1-6, pp. 43-48, 1998.

[159] G. D. Lloyd, L. A. Everall, K. Sugden, I. Bennion, 'Resonant cavity based fibre Bragg grating interrogation using ratiometric detection', *Opt. Commun.*, **244**, (1-6), pp.193-197, 2004.

[160] P. Reyes and P. S. Westbrook, "Tuneable PDL of twisted-tilted fibre gratings," *IEEE Photonics Technology Letters*, vol. 15, Iss. 6, pp. 828-830, 2003.

[161] P. S. Westbrook, T. A. Strasser, and T. Erdogan, "In-line polarimeter using blazed fibre gratings," *IEEE Photonics Technology Letters*, vol. 12, Iss. 10, pp. 1352-1354, 2000.

[162] J. Peupelmann, E. Krause, A. Bandemer, and C. Schaffer, "Fibre-polarimeter based on grating taps," *Electronics Letters*, vol. 38, Iss. 21, pp. 1248-1250, 2002.

[163] J. M. Battiato and R. K. Kostuk, "45 degrees slanted fibre Bragg grating design with prism coupled holographic exposure," *Electronics Letters*, vol. 38, Iss. 22, pp. 1323-1324, 2002.

[164] X. W. Shu, K. Sugden, D. H. Zhao, F. Floreani, L. Zhang, and I. Bennion, "Complex growth behaviour of hybrid-type fibre Bragg gratings," *Electronics Letters*, vol. 39, Iss. 3, pp. 274-276, 2003.

[165] M. Svalgaard, "Ultraviolet light induced refractive index structures in germanosilica," in *Research Center Com.* Denmark: Technical University of Denmark, 1997.

[166] M. Svalgaard and K. Faerch, "UV written variable optical attenuator," presented at BGPP, Monterey, CA, paper TuA5, 2003.

[167] F. Ouellette, "Fibre Bragg Gratings," *SPIE OE Magazine, special focus section*, pp. 38-42, 2001.